Ultrafast Dynamics of Gas Phase Anions

Christopher West

Department of Chemistry

University of Durham

2015

A thesis submitted in partial fulfilment of the requirements for the degree of

Doctor of Philosophy

Declaration

The material contained within this thesis has not previously been submitted for a degree at the University of Durham or any other university. The research reported within this thesis has been conducted by the author unless indicated otherwise.

Copyright Notice

Abstract

The ultrafast dynamics of a number of molecules have been studied in the gas phase through the use of frequency- angle- and time-resolved photoelecron imaging. A particular emphasis has been applied to the behaviour of biologically relevant molecules following photoexcitation. The gaseous ions were produced from an electrospray ionisation source and interrogated by a purpose-built velocity-map imaging photoelectron spectrometer with a minimum temporal resolution of ~50 fs.

Firstly, the details of a global kinetic fitting routine for a time-resolved photoelectron spectrum are presented. Through fitting the constituent photoelectron images to a kinetic fit, the photoelectron angular anisotropy of the consituent features of the time-resolved spectrum is preserved. Secondly, the dynamics of the green fluorescent protein model chromophore following UV excitation were explored, identifying internal conversion of the initially produced excited state population to a lower lying excited state before photodetachment. Thirdly, frequency- and angle-resolved photoelectron imaging is employed to investigate the dynamics of anionic resonances of para-*benzoquinone, that have been implicated in facilitating electron attachment to this moiety. Fourthly, the photoelectron spectra of a series of carboxylic acids are presented in order to assess the feasibility of producing anions by attaching carboxylic acids to neutral chromophores. Fifthly, a time-resolved photoelectron spectrum of the biological chromophore and carboxylic acid, all-*trans-*retinoic acid is presented. Finally, highly anisotropic photoelectron spectra of the dianion, antimony tartrate are presented. In order to explain the anisotropy, classical trajectories of electrons on the molecular electrostatic potential energy surface are calculated. From this, the observed anisotropy can be assigned the the shape of the molecular repulsive Coulomb barrier.*

Acknowledgements

This thesis is the result of three years of work and could not have been completed without the support of many people.

First of all, I would like to thank my supervisor, Dr Jan Verlet, for your unwavering patience, help, instruction and support over the past 3 years.

Next, I would like to thank everyone that I have worked with over past three years for making the experience so rewarding and enjoyable: Lars-Olof Pålsson, Dan Horke, Adam Chatterley, Laurence Stanley, Anna Hughes, Ashley Johns, Paweł Nowakoski, James Bull, David 'David, can I ask you a couple of questions about Matlab?' Woods, Josh Rogers, Erkki Antonkov, Megan Ferguson, Allie Tyson and Cate Anstöter.

Outside of work, I have been unwaveringly supported by both family and friends. Particular thanks go to my parents (I will explain this thesis to you one day) and, in no particular order and woefully incomplete, Matt Frye, Ollie Bartlett, Guy Barrett, James Nelson, Georgina Bonfanti, Mike Tynan, Ben Beswick, Patrick Holmes, the Trevelyan College MCR and the Trevelyan College Pool teams.

Finally, I would like to thank all of the staff of the Trevelyan college bar, without whom this thesis would either not have been written, or would have been finished about a year ago.

Contents

Publications

Parts of this Thesis are based upon the following Publications:

Chapter 4: 'Communication: Autodetachment versus Internal Conversion from the S_1 state of the isolated GFP Chromophore Anion', C. W. West, A. S. Hudson, S. L. Cobb and J. R. R. Verlet, *J. Chem. Phys.*, **139**, 071104 (2013)

'Excited State Dynamics of the Isolated Green Fluorescent Protein Chromophore Anion Following UV Excitation', C. W. West, J. N. Bull, A. S. Hudson, S. L. Cobb and J. R. R. Verlet, *J. Phys. Chem. B*, **119**, 3982 (2015)

Chapter 5: 'Anion Resonances of *para*-Benzoquinone Probed by Frequency-Resolved Photoelectron Imaging', C. W. West, J. N. Bull, E. Antonkov and J. R. R. Verlet, *J. Phys. Chem. A*, **118**, 11346 (2014)

Chapter 8: 'Photoelectron Imaging of the Isolated Antimony Tartrate Dianion', C. W. West, J. N. Bull, D. A. Woods and J. R. R. Verlet, *Chem. Phys. Lett.*, **645**, 138 (2016)

List of Abbrieviations

AD = Autodetachment

ADE = Adiabatic detachment energy

AEA = Adiabatic electron affinity

AT = Antimony tartrate

ATR = All-*trans* retinal

ATRA = All-*trans* retinoic acid

BBO = β-Barium borate

BH = Born-Huang

BO = Born-OppenheimerCI = Conical intersection

DAI = Decay associated image

DAS = Decay associated spectrum

eBE = Electron binding energy

eKE = Electron kinetic energy

ESI = Electrospray ionisation

FC = Franck-Condon

GFP = Green Fluorescent Protein

HBDI = *para*-Hydroxybenzilidene-2,3-dimethylimidazolinone

HOMO = Highest occupied molecular orbital

IC = Internal conversion

IVR = Intramolecular vibrational energy redistribution

LUMO = Lowest unoccupied molecular orbital

MCA = Multiply charged anion

MCP = Micro-channel plate

MO = Molecular orbital

PAD = Photoelectron angular distribution

pBQ = *para*-Benzoquinone

PE = Photoelectron

PEPICO = Photoelectron-photoion coincidence spectroscopy

PES = Potential energy surface

POP = Polar onion peeling algorithm

RCB = Repulsive Coulomb barrier

TCSPC = Time-correlated single photon counting

TE = Thermionic emission

TRPEI = Time-resolved photoelectron imaging

TRPES = Time-resolved photoelectron spectroscopy

UPS = Ultraviolet photoelectron spectroscopy

VAD = Vibrational autodetachment

VDE = Vertical detachment energy

VEA = Vertical electron affinity

VMI = Velocity Map Imaging

XPS = X-ray photoelectron spectroscopy

Chapter 1. Introduction

In this chapter, a brief introduction to the motivation behind the work undertaken in this thesis and a short discussion of the fundamental concepts underlying the physical processes investigated are presented. The principles of the production of an excited electronic state by absorption of a photon, the production of a wave packet on the excited state surface and the mechanisms by which an isolated molecule in an excited electronic state may decay back to the ground electronic state are discussed. The principles of photoelectron spectroscopy, including photodetachment, methods by which the detached electron might be detected and photoelectron angular distributions, are presented. In order to trace the evolution of a wave packet on an excited state surface, it is necessary to employ a time-resolved spectroscopic method. Numerous time-resolved spectroscopic methods are discussed, with a focus on pump-probe spectroscopy and hence time-resolved photoelectron spectroscopy. Finally, a short discussion of the recent application of photoelectron spectroscopy to the study of the dynamics of a variety of molecular systems is presented.

1.1 Blink and You'll Miss It: The Need for Observations on an Electronic Timescale

The French Drop is one of the most famous and performed magic tricks in the world. The traditional order of the trick is as follows: 1. the magician presents a coin to the audience, holding it between the thumb and first two fingers of the right hand; 2. the magician transfers the coin to the left hand and holds it in his fist in clear view of the audience; 3. the magician taps their fist with their magic wand and reveals their empty palm to an astonished and rapturous audience. If the magician is feeling particularly wealthy, the coin can be retreived from the ear of, and subsequently presented to, a small child. An astute observer watching closely and stood both slightly behind and

above the performer would notice that the coin never in fact enters the left hand; as the magician moves to transfer the coin, the thumb is relaxed, the coin falls into the palm of the right hand and the left hand grasps nothing. The audience is left none the wiser, as the movement is both covered by the other hand and too fast for the casual observer to see.

The excited state dynamics of a molecular species following photoexcitation are extremely fast. In the solid phase, the ground electronic state is typically recovered on the order of nanoseconds,[1,2] with few processes such as phosphorescence occuring on timescales which can approach the order of 10s of seconds, although in the majority of cases this occurs on a millisecond timescale.[1] In the gas phase, the dynamics tend to occur on an even faster timescale. With these timescales in mind, it is difficult to seriously compare molecular dynamics to the drop of a coin; the coin takes ~0.1 s to fall into one's hand, $\sim 10^8$ orders of magnitude slower than the majority of the excited state processes in the gas phase, and is $\sim 10^8$ orders of magnitude larger than a molecular species. Indeed, it is considerably easier to observe the coin falling than internal conversion within the molecule. However, care is still requrired to observe the coin, as the speed at which it falls is difficult to track with the human eye – blink and you'll miss it. The coin and an electronic excited state are therefore similar; without careful, consistent observation on an appropriate timescale, whether sleight of hand or the dynamics of an excited state, the observers will be sat like bemused children, wondering where it went.

1.2 Dynamics of Excited States

1.2.1 Principles of Photoexcitation

First, we must consider the processes involved in the absorption of a photon by an atom or a molecule in order to induce a non-forbidden electronic transition to produce an electronically excited state of that species. As a general approximation, the energy of the photon is absorbed by the molecule to promote an electron into a higher energy molecular orbital. In contrast to vibrational and rotational transitions, in which the photons absorbed lie in the infrared and microwave regions of the electromagnetic spectrum,[1] higher photon energies are required to induce electronic transitions. As such, the photons absorbed typically lie in the ultraviolet and visible region. However, in order to describe the molecular processes at play, we must consider the system in terms of quantum mechanics. The complete description of any system can be found by solving the Schrödinger equation for all nuclei and electrons, which, for a one electron system, is given as:[1-4]

$$\hat{H}\,\Psi(q,Q_1,Q_2,\ldots Q_N) = E\Psi(q,Q_1,Q_2,\ldots Q_N) \qquad (1.1)$$

where q is the position of the electron, Q_N is the position of the N^{th} nucleus, Ψ is the total wavefunction, E is the total energy and $\hat{H}$ is the Hamiltonian of the system:

$$\hat{H} = T_{\text{e}} + T_{\text{N}} + V \qquad (1.2)$$

where T_N and T_e are the kinetic energy of the nuclei and the electron respectively and V is the potential energy of the system.

Equation (1.1) cannot be solved analytically for any system that contains more than one nucleus,[3] hence it may not be solved for a molecule. As such, at the outset of any quantum mechanical treatment, we must invoke the Born-Oppenheimer (BO) approximation. In this, as the mass of an electron is far less than the mass of a nuclei ($m_{\text{Proton}}/m_{\text{Electron}}$ = 1836.2),[2] the nuclei of a system can be assumed to be stationary on

the timescale of electron motion. The wavefunction of the electron may now be found in the static field of the nuclei and the Schrödinger equation may therefore be written as:[1-4]

$$T_e\Psi(Q_1, Q_2, \ldots Q_N) + V\Psi(Q_1, Q_2, \ldots Q_N) = E_e\,\Psi(Q_1, Q_2, \ldots Q_N), \quad (1.3)$$

where E_e gives the eigenstates of the molecule, accounting for the kinetic energy of the electrton and the Coulombic interactions between all particles. While equation (1.3) is only solvable for a single electron system, the BO approximation reduces the complexity of the equations governing the behaviour of many electron systems considerably.

An important concept introduced in equation (1.2) is *V*, the potential energy, which is dependent upon the nuclear geometry in the BO approximation. *V* can be described by a $3N$–6 dimensional surface, where *N* is the number of atoms in the molecule, and is essential for the understanding and visualisation of molecular dynamics.

The wave-particle duality of an electron and its subsequent description as a wavefunction leads to an interesting and famous result. Consider Fourier's theorem:[5]

$$f(x) = \sum_{n=-\infty}^{\infty} c_n e^{inx} \quad (1.4)$$

which states that any periodic function can be described by the sum of an infinite number of sine and cosine functions. As such, any function that is non-sinusoidal must contain contributions from a number of sinusoidal functions oscillating at different frequencies. In order to illustrate this effect, Figure 1.1 shows a series of summed cosine waves, of the form:

$$f(x) = \sum_{k=1}^{n} \cos(kx) \quad (1.5)$$

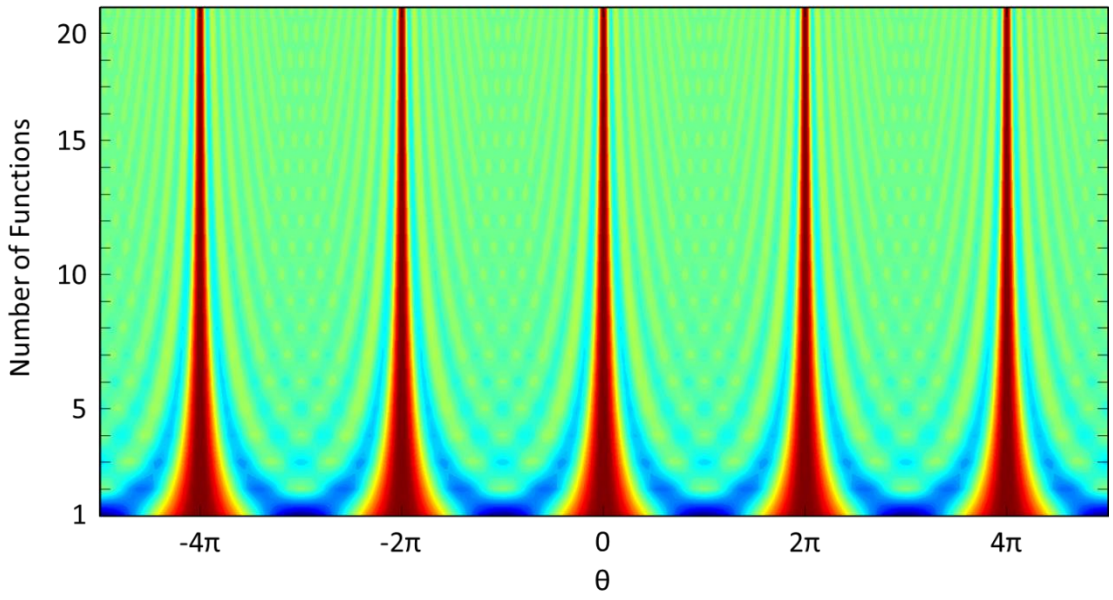

Figure 1.1 Demonstration of constructive and destructive interference by the sum of a number of cosine functions.

As the number of frequencies in the summation increases, the function tends towards a series of high amplitude, highly localised peaks; as the time resolution of the peaks in the spectrum increases, the 'resolution' of the frequency decreases. Hence, a direct result of wave-particle duality is that one cannot define both the energy and the lifetime of an electron accurately and simultaneously. This can be summarised in the famous form:

$$\Delta t \Delta E \geq \hbar/2, \qquad (1.6)$$

which is a consequence of the uncertainty principle, as proposed by Heisenberg.[6,7] This is an extremely important result for quantum mechanics and exists in numerous different forms to decribe different complementary relationships – position and momentum is perhaps the most well known relationship defined by the uncertainty principle.[3] This result also has significant implications for the generation of ultrafast laser pulses and in fact provides the underlying principle for mode-locking,[8] the method used to produce femtosecond pulses in titanium:sapphire lasers. In this, a number of lasing modes are allowed to propagate simultaneously and the interference between the

waves results in a train of femtosecond length pulses, by the mechanism illustrated in Figure 1.1. However, as previously discussed, the temporal resolution requires a broad range of wavelengths and hence the energetic resolution of femtosecond pulses is considerably worse than acheivable with longer pulsed or continuous wave lasers.[8]

We may now turn our attention back to electronic excitation. In this, by the interaction between the molecular electronic dipole moment, $\boldsymbol{\mu}_e$, and the incident electric field of a photon, $\mathbf{E}$, the photon may be absorbed in order to promote the molecule to an electronic excited state, according to the selection rules:[1-4]

$$\Delta \Lambda = 0, \pm 1, \tag{1.7}$$

$$\Delta S = 0, \tag{1.8}$$

where Λ is the total angular momentum quantum number and S is the total spin quantum number. Following photoexcitation, V might be expected to differ significantly from that in the ground state if the occupancy of the bonding molecular orbitals is reduced and so the equilibrium geometry is expected to be vary accordingly. However, under the BO approximation, the nuclei are stationary and the rearrangement concerns only electrons. The transition is therefore said to vertical, where all coordinates bar the energy and the electrons remain constant, an approximation termed the Franck-Condon principle.[9-11]

This principle may be considered quantitatively by considering the probability of the transition. The transition dipole moment, $\mathbf{d}_{if}$, between an initial and final state, Ψ_i and Ψ_f respectively, may be written:[3]

$$\boldsymbol{d}_{if} = \left\langle \Psi_f(\mathbf{r},\mathbf{R}) \middle| \boldsymbol{\mu}_e \bullet \mathbf{E} \middle| \Psi_i(\mathbf{r},\mathbf{R}) \right\rangle \tag{1.9}$$

in Dirac bra-ket notation,[3] where $\mathbf{r}$ and $\mathbf{R}$ describe the electronic and nuclear coordinates respectively. In this, both electronic and nuclear degrees of freedom are contained within $\boldsymbol{\mu}_e$. Under the BO approximation, the nuclei are stationary and the

transition dipole moment can be defined as the constant $\mathbf{d}_{if}^{e}$, the electronic transition dipole moment, at this geometry, allowing the separation of the electronic and nuclear degrees of freedom.

$$\mathbf{d}_{if}^{e} = \left\langle \Psi_f(\mathbf{r}) \middle| \boldsymbol{\mu}_e \bullet \mathbf{E} \middle| \Psi_i(\mathbf{r}) \right\rangle \qquad (1.10)$$

We may now express $\mathbf{d}_{if}$ in terms of $\mathbf{d}_{if}^{e}$ and subsequently in terms of the wavefunction overlap between the initial and final states in the stationary geometry, which is typically denoted as the overlap integral $S_{if}(\mathbf{R})$.[1-4]

$$\mathbf{d}_{if} = \mathbf{d}_{if}^{e} \left\langle \Psi_f(\mathbf{R}) \middle| \Psi_i(\mathbf{R}) \right\rangle = \mathbf{d}_{if}^{e} S_{if}(\mathbf{R}) \qquad (1.11)$$

The probability of the transition is then proportional to $\left|S_{if}(\mathbf{R})\right|^2$, which may be termed the Franck-Condon factor.[2] In short, the probability of the transition between two states is given by the overlap of the wavefunctions of the intial and final states in the geometry of the initial state.

As previously discussed, a necessary result of the uncertainty principle is that ultrafast laser pulses must have a broad energy profile. This is significant in terms of photoexcitation, as it will result in a range of photoexcited states being produced by excitation with an ultrafast laser pulse, as opposed to the single excitation that one might expect when utilising a single frequency. This range of vibrationally excited states will be defined by the shape of the excitation pulse (typically a Gaussian distribution) and the orbital overlap at each frequency in the static geometry. The superposition of excited states produced by such an excitation can be described mathematically as:[3]

$$\Psi(\mathbf{r},\mathbf{R}) = \sum_n A_n \psi_n(\mathbf{r},\mathbf{R}) e^{-iE_n t/\hbar} \qquad (1.12)$$

$$= \sum_n \left(\mathbf{d}_{if} \otimes f(Pulse) \right) \psi_n(\mathbf{r},\mathbf{R}) e^{-iE_n t/\hbar}$$

where ψ_n is the n^{th} vibrational wavefunction, E_n is the energy of the function, A_n is a weighting factor describing the shape of the excitation pulse, $f(Pulse)$, and the Franck-Condon factor at each n, and t is the evolution time of the system. This equation is similar to that of Fourier's theorem, equation (1.4), and the superposition effectively behaves in a similar fashion; it appears as a highly localised region of high intensity with little to no amplitude elsewhere, a phenonemon known as a wave packet.[3]

An important variable in equation (1.12) is t, the evolution time of the system. As t varies, so does the position at which the frequencies constructively interfere. This effectively means that the wave packet can oscillate across the potential energy surface (PES) as a coherent feature with t. If the energy level spacings between the vibrational levels are unequal, as in the anharmonic oscillator model, then the wave packet may dephase and change shape with time, as opposed to oscillating indefinitely on evenly spaced energy levels.[3]

1.2.2 Decay Mechanisms

If there is no mechanism for energy loss from the photoexcited states, then the wave packet will remain oscillating indefinitely on the excited state PES. However, this is not the case and the photoexcited molecule will attempt to recover thermal eqilibrium. Therefore, when one attempts to determine the dynamics of an excited state, one is attempting to determine the evolution of the initially produced wave packet with time. There are numerous processes by which the molecule can redistribute or lose excess energy, both radiative and non-radiative, which are denoted on the Jablonski diagram shown in Figure 1.2.

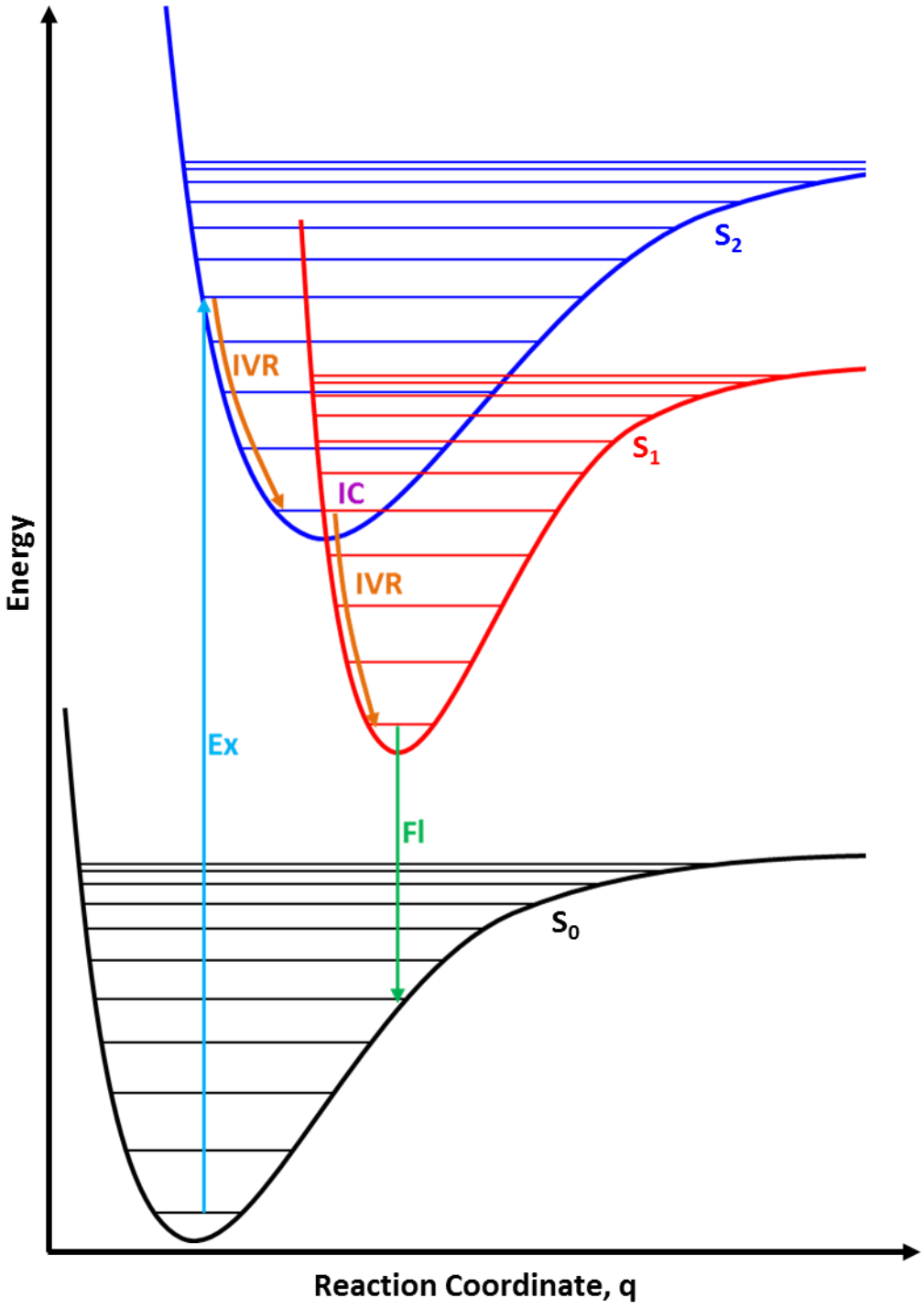

Figure 1.2 Jablonski diagram illustrating the major decay mechanisms of an electronically excited state along a reaction coordinate. The excited state (S_2) is produced by an initial photoexcitation (Ex) of the electronic ground state (S_0) and begins to decay by intramolecular vibrational energy relaxation (IVR). The S_2 state decays through a conical intersection (CI) to a second excited state (S_1), which may decay to the S_0 state by fluorescence (Fl).

1.2.2.1 Intra-Molecular Vibrational Energy Relaxation

In the solution and solid phases, following photoexcitation to a vibrationally-hot electronic excited state, the excess energy is quickly redistributed to the kinetic modes of the surrounding molecules via inter-molecular vibrational energy relaxation and the molecule falls to the Maxwell-Boltzmann distribution of vibrational states in the excited electronic state. In this gas phase, the molecule is isolated and therefore this pathway is not accessible; the initial excitation energy is conserved within the molecule. Instead, the energy may be redistributed through the vibrational modes of the initially excited molecule, in intra-molecular vibrational energy redistribution (IVR).[12] When considering the PES of the excited state along a single reaction coordinate (for example, the stretch of a bond linking two chromophores or the rotation about a double bond following a $\pi^* \leftarrow \pi$ transition) this allows for the minimum energy geometry to be achieved while conserving the vibrational energy in different vibrational modes. IVR typically occurs on the order of tens of picoseconds.[1]

This is significant when considering the fate of the wave packet. In small molecules, the number of vibrational modes is small enough that the originally excited mode may be recovered, i.e. the vibrational energy redistribution is reversible. The wave packet may then be recovered following dephasing. In larger molecules, however, the number of vibrational modes is large and the density of states results in a near-continuum. This is an incoherent system, hence the wave packet will irreversibly dephase.[3]

1.2.2.2 Internal Conversion

While IVR deals with energy redistribution on an excited state surface, most other decay mechanisms involve the conversion of the excited state to an alternate electronic state. Internal conversion (IC) is the predominant mechanism for this process

and describes an electronic transition between two states with the same spin via the coupling of modes of the same energy on the initial and final states.[3,12] In a reasonably large system, as with IVR, the density of vibrational modes can be approximated to a continuum of states. The rate of the transition can therefore be described by Fermi's golden rule:[13]

$$W_{fi} = 2\pi\hbar\left|V_{fi}\right|^2\rho\left(E_f\right) \qquad (1.13)$$

where W_{fi} is the transition rate, $\left|V_{fi}\right|^2$ is the square modulus of the transition matrix element which describes the overlap of the wavefunctions of the vibrational modes and $\rho\left(E_f\right)$ is the density of states.[3] An important result of this equation is that IC is more efficient between close lying excited states. Finally, in order to couple the two electronic states, the transition must be totally symmetric. Therefore, a promoting mode of the correct symmetry is usually required:[3]

$$\Gamma_i \otimes \Gamma_m \otimes \Gamma_f \supseteq \Gamma_{\mathrm{TS}} \qquad (1.14)$$

where i and f label the initial and final states, m is the promoting mode and Γ_{TS} is the totally symmetric irreducible representation of the relevant point group.

As previously stated, IC is forbidden between electronic excited states with differing spin. However, in states with sufficient spin-orbit coupling, this rule can break down and the state may be converted into a state with differing spin. This process is known as inter-system crossing (ISC) and, due to the dependence on spin-orbit coupling, is most prevelant in systems containing heavy atoms such as metal complexes.[2]

1.2.2.3 Conical Intersections

This coupling between excited states is known as non-adiabatic coupling or vibronic coupling and describes the coupling of electronic and nuclear vibrational motion.[14-17] A crucial consequence of this coupling is that the BO approximation does

not hold; one cannot consider the interaction between electronic and nuclear motion if the nuclei are stationary! As such, the Born-Huang (BH) or coupled electronic state approximation,[18] which holds that T_N in equation (1.2) is both non-zero and a diagonal matrix, is employed. Within this approximation, a non-radiative transition may occur between two electronic excited states via non-adiabatic coupling and is most likely to occur in molecular geometries where the potential energy surfaces intersect.[14]

This is not an unexpected result; from equation (1.13), it follows that the maximum rate occurs when $\Delta E = 0$, or when the PES of the coupled excited states are degenerate. The point at which the electronic states are degenerate is known as a conical intersection (CI),[14,16,17,19-23] so called because the shape of the PES as the reaction coordinate moves away from the degeneracy appears as a double cone. In order for the PES to be degenerate, the equation:[14]

$$\Gamma_i \otimes \Gamma_{geom} \otimes \Gamma_f \supseteq \Gamma_{\mathrm{TS}}, \qquad (1.15)$$

where i and f label the initial and final states, *geom* is the nuclear geometry at the CI and Γ_{TS} is the totally symmetric irreducible representation of the relevant point group, must be satisfied. As such, if the excited states have differing symmetries, then the condition can be trivially met to form an accidental symmetry-allowed CI. The transition is known as accidental as the electronic states do not need to be degenerate at the point of requisite symmetry. If the electronic states are symmetrically degenerate (both belong to a E or T representation), then a symmetry-required CI is formed.[14,16,17] The Jahn-Teller distortion is a result of the formation of a symmetry-required CI. However, the conditions can only be produced in an N – 2 dimensional space, where N is the number of degrees of freedom. In a diatomic system, N = 1 and as such, the electronic states may never be degenerate; this is known as the non-crossing rule. IC and non-adibatic dynamics occuring through CIs can be extremely fast, typically

occuring on sub-picosecond timescales and often limited by the vibrational period of the modes required to access the CI. [14,16,17]

1.2.2.4 Radiative Transitions

Photoemission is effectively the reverse process of photoexcitation; the molecule converts from an excited state to the ground state by emission of a photon.[1,2,12] When the initial and final states have the same spin, this process is known as fluorescence. If the initial and final states have differing spin, then the process is known as phosphorescence. As phosphorescence is a quantum-mechanically-forbidden process due to the change in spin quantum number, the lifetime of phosphorescence can be extremely long and exceed milliseconds,[2] whereas fluorescence lifetimes are typically on the order of nanoseconds.[12] Both lifetimes are far longer than those for IVR, hence radiative processes tend to occur from the lowest energy geometry of the excited state. This geometry is typically different from the FC geometry, hence the energy gap between the intial and final states is different from that in the FC region. The difference in energy and hence the difference between the energy of the photon that is initially absorbed and that which is emitted is termed the Stoke's Shift.[1,2,4]

1.2.2.5 Photofragmentation

Finally, we consider the loss of energy via bond dissociation. It is possible for the molecule to decay to an alternate ground state by photodissociation. It is sometimes possible for a molecule to absorb a photon to an unbound electronic state, leading to bond fission and the loss of a group from the molecule; dissociation. It is also possible for a bound electronic state to undergo IC through an intersection on the potential energy surfaces into a dissociative state; this is known as predissociation.[2]

Another possible pathway for the production of photofragments is excitation with multiple photons. If the incident radiation is insufficient to fragment the molecule,

then the fragmentation threshold may be reached by absorbing multiple photons over the timescale of the laser pulse. This is greatly assisted if the incident radiation is resonant with an excited electronic state that can decay to the ground electronic state within the timescale of the laser pulse, at which point the initial excitation becomes resonant once more and allows for efficient multiple absorption.[24-26]

While we have predominantly considered bond dissociation as the major product of photofragmentation, the smallest fragment that one can produce following photoexcitation is an electron. This phenomenom can be exploited to investigate the electronic structure of the molecule by photoelectron (PE) spectroscopy.

1.3 Photoelectron Spectroscopy

1.3.1 Principles of Photoelectron Spectroscopy

The photoelectric effect, the observation of electrons from the surface of a metal following irradiation with photons, was first observed by Heinrich Hertz[27] in 1887, after observing that it was easier to generate sparks from electrodes when they were illuminated with ultraviolet light. The effect was the subject of much interest, as no electrons were liberated until the threshold frequency of the incident radiation for the metal in question had been reached, regardless of the intensity of the radiation. The phenomenon was eventually explained in 1905 by Einstein,[28] in between formulating both his theories of heat capacities and the special theory of relativity, who based the explanation on the conservation of energy in a collision between an incident photon and an electron embedded within the metal. In order to detach an electron, the energy of the incident radiation must exceed the work function of the metal, Φ, explaining the frequency dependence of the effect, and the excess energy is conserved by the kinetic energy of the liberated electron, eKE. This can be summarised as:

$$eKE = h\upsilon - \Phi, \qquad (1.16)$$

where Φ is analagous to the ionisation potential of the system. In closed-shell Hartree-Fock theory, Koopman's theorem holds that the first ionisation potential of a system is equal to the negative of the orbital energy of the highest occupied molecular orbital.[29] As Hartree-Fock theory assumes that the geometries of the unionised and ionised molecule are identical, this is equivalent to a vertical transition leading to ionisation of the molecule, i.e. the photoelectric effect. Therefore, we can write:

$$eKE = h\upsilon - I, \qquad (1.17)$$

where I is the ionisation potential of the orbital from which the electron is detached. Subsequently, a photon of sufficient energy may detach an electron from each molecular orbital in the system, assuming that the ionisation energy of the orbital is surpassed. This observation is the underlying principle behind PE spectroscopy; by irradiating the subject system with radiation of sufficient energy and measuring the kinetic energy of the liberated electrons, it is possible to determine the orbital energies of the molecular orbitals from which the electrons were detached.

PE spectroscopy was developed into an analytical technique in the early 1960s[30] and can be broadly, if somewhat arbitrarily, separated into X-Ray PE spectroscopy (XPS) and ultraviolet PE spectroscopy (UPS). Although conceptually they vary only by the frequency of the radiation used to ionise the system of interest, experimentally the two groups vary significantly. In general, XPS probes the core orbitals of the system, whereas UPS ionises the valence orbitals. In this thesis, we shall focus on UPS, as the electronic transitions to form the excited states and their subsequent dynamics involve the valence orbitals.

In UPS, the system of interest is ionised with photons of an energy between 3 eV < $h\upsilon$ < 10 eV, which can easily be generated by second harmonic generation and

sum frequency generation of the fundamental frequency of neodymium yttrium aluminium garnet (1064 nm, 1.165 eV), neodymium yttrium lithium fluoride (1062 nm, 1.168 eV) and titanium sapphire lasers (800 nm, 1.55 eV). These photon energies are unlikely to be sufficient to ionise cations and may only ionise neutral molecules with unusually low binding energies (one of the lowest known ionisation energy for a neutral molecule is 5.95 eV for tetrakis(N,N',N'',N'''-tetramethylethylenediylidenetetraamine[31]). However, this range of energies is typically sufficient to detach electrons from most anions, and it is the application of UPS to anion spectroscopy that shall be the focus of this thesis.

1.3.2 Environmental Considerations

PE spectroscopy is entirely dependent upon the accurate determination of the kinetic energy of the detached electrons. It is therefore imperative that collisional loss of energy from the electrons to atmospheric molecules is minimised. As such, almost all PE spectroscopic studies are performed *in vacuo*. The systems that may be studied by PE spectroscopy must therefore be stable over the timescale of the measurement. The application of XPS and UPS to solid state substrates such as metals and surfaces has been well established.[32-35] The application to solution phase systems has been hampered by the propensity of most liquids to have a low vapour pressure and hence to evaporate under experimental conditions. Liquid microjets have emerged as a promising solution.[36-39] In this, the PEs are detached from within a jet of solution fired into a vacuum chamber and the solution phase is therefore constantly regenerated. Finally, XPS and UPS have been applied extensively to gas phase systems, both for isolated molecules[40-43] and for clusters,[44-46] and it is on these systems that we shall focus for the remainder of this thesis.

Molecular beams have long been used to produce gaseous molecules[47-49] and have been used extensively in PE spectroscopy.[47,50,51] For the production of a molecular beam, a gas is expanded through a pinhole into a chamber held at lower pressure. If the pressure ratio exceeds a critical value (dependent on the gas), then the velocity of the molecules can reach supersonic speeds and hence results in a free jet expansion. This is characterised by a collision free '*zone of silence*' immediately in front of the pinhole, surrounded by a series of compression waves as the supersonic particles collide with the particles in the vacuum. A skimmer is placed in order to extract a small section of the expansion from within the zone of silence and so before the collisonal region, producing a beam of molecules with approximately equal velocities and very few collisions between particles.[47,52] Typically, a carrier gas (often Ar) is flowed over the sample of interest, potentially while being heated, in order to produce the sample beam. This technique is typically used to produce neutral molecules, although it is possible to ionise a neutral molecular beam by laser ionisation[47,50,51,53] or an electron gun[47,54-57] to produce an ionic beam, or by seeding the carrier gas with ions produced by a single polarity ion source, such as a plasma source.[58]

There are multiple techniques for generating gaseous ions that have been developed by the mass-spectrometry community, such as electron ionisation,[54,59] glow discharge,[24,60,61] inductively coupled plasma[24] and matrix assisted laser desorption/ionisation.[62] However, it was the development of electrospray ionisation (ESI) as a simple, soft technique for producing gaseous ions free of counter ions[62-66] that has revolutionised ionic PE spectroscopy. In this, a high voltage is applied to a needle through which a solution containing the system of interest is passed. The electric field induced by the applied voltage forms the droplet on the end of the needle into a Taylor cone.[62] The apex of the conical meniscus theoretically becomes infinitely small, but in

practice breaks into small droplets when the surface tension relaxation time becomes larger than the charge relaxation time. The solvent droplets then begin to evaporate and undergo Coulomb fission as the electrostatic repulsion between the solute molecules overcomes the surface tension constraining the droplet. The solute may then desorb from the droplet once a threshold radius is reached for this process to become feasible (the ion evaporation molecule, most commonly for small molecules),[66,67] or the evaporation and fission cycle continues until only droplets containing a single solvent molecule remain and the solvent simply evaporates (the charge residue model, predominantly for larger ions).[68,69] ESI is also able to produce multiply charged anions (MCAs), which had not previously been possible by other methods.[70] The first to utilise this technology for anion UPS were the Wang group, who combined ESI with a magnetic bottle spectrometer,[71] and the technique has become more widespread as the underlying technology advances.[41,70,72-74]

1.3.3 Anion UPS

The general description for electron detachment into the neutral continuum of the molecule can be written:

$$S_0 + h\upsilon \rightarrow D_0 + e^- \qquad (1.18)$$

where S_0 is the ground electronic state of the anion and D_0 is the ground state of the neutral radical. The ionisation threshold required for electron emission is defined by the molecular geometry at the point of emission. The adiabatic ionisation energy (ADE) is the minimum amount of energy required to initiate electron loss. This can be described as the difference in energy between the vibrational ground states of the initial and photodetached species. However, the vertical detachment energy (VDE) is the difference between the ground vibrational state of the initial species and a vibrationally excited state of the ionised species which shares a molecular geometry with the initial

ground state, i.e. in the Franck-Condon geometry. Indirect or adiabatic electron detachment occurs in the geometry of the ionised species, whereas direct or vertical electron detachment occurs in the geometry of the unionised species.[2]

The photodetachment cross-section of an anion is dependent upon the kinetic energy of the detached electron in the relationship set out by Wigner,[75] such that the cross-section at 0 eV is equal to zero. This is due to a centrifugal barrier caused by the interaction between the angular momentum of the PE and the photodetached species. If the anion is multiply charged, then the species produced following photodetachment will also be negatively charged. The interaction between the long range repulsion between the anion and the PE and the centrifugal barrier results in the presence of the repulsive Coulomb barrier (RCB). First observed by Wang and co-workers by UPS,[76] the presence of the RCB results in only electrons with sufficient kinetic energy to overcome the RCB being ejected, leading to a characteristic cut-off in the PE spectra of MCAs at low energy. The nature of the RCB can be conveniently probed by PE spectroscopy.[42,43,76]

As previously discussed, the VDE of anions are lower than those observed in neutral and cationic molecules and is often below the energy required to access the first electronic excited state. It is often the case that it is possible to access an anionic resonance that is unbound with respect to electron detachment by UV excitation:

$$S_0 + h\upsilon \rightarrow S_n^* \qquad (1.19)$$

where S_n^* is an anionic resonance. While this is the case for all molecules, the lower VDE for anionic species results in a far greater number of unbound resonances having been observed within the ultraviolet spectral range for anions than for neutrals and cations. In fact, it is often (erroneously) stated that anions do not have bound electronic states. Detachment from an anionic resonance produced by photoexcitation in this

fashion is known as autodetachment. The dynamics that subsequently occur on the excited state surface will be a competition between IVR, IC and other relaxation mechanisms as the molecule attempts to recover the ground electronic state and electron autodetachment:

$$S_n^* \rightarrow D_0 + e^- \quad (1.20)$$

$$S_n^* \xrightarrow{IVR} S_n^\dagger \rightarrow D_0 + e^- \quad (1.21)$$

$$S_n^\dagger \xrightarrow{IC/ISC} S_{n-1}^* \rightarrow D_0 + e^- \quad (1.22)$$

Crucially, as time progresses and further dynamics occur on the excited state, the kinetic energy of the detached electrons will vary. Careful dection of the kinetic energy of the detached electrons can allow for a window into the dynamics occuring on the excited state surface.

Finally, we consider thermionic emission (TE).[77-79] TE is a statistical detachment process that results in a characteristic PE feature that appears as an exponential decay, peaking at an electron kinetic energy of 0 eV. As previously discussed, the cross section for photodetachment of an electron with 0 eV is zero,[75] hence these electrons cannot arise from a direct detachment process. As energy is conserved in the molecular system, the electronic ground state of a molecule produced PE by IC from an initially photoexcited electronic state is vibrationally hot. It is possible for an electron to 'boil-off' in an attempt to reduce the energy of the system. This is a ground state process that will result in a statistical range of PE kinetic energies.

1.3.4 Photoelectron Detection

PE spectroscopy is dependent upon the accurate determination of the *eKE*. In the early days of PE spectroscopy, numerous methods were employed in order to analyse the PE emission, including retarding field analysis and deflection analysis. Retarding field analysis involves applying a retarding potential to the emission, such that only

electrons with sufficient energy may reach the detector.[80-82] By measuring the PE current and varying the retarding potential, the spectrum may be obtained. In deflection analysis, multiple types of analysers exist, but rely on deflecting the PE emission onto a detector set off axis to the direction of the emission by the application of an external potential.[80-82] These techniques both require scanning of potentials in order to determine the spectrum and may only measure a small solid angle of the emission. The techniques are therefore inefficient. With the advent of pulsed lasers, it was possible to measure the entire spectrum simultaneously by detecting the PE emission's time-of-flight.[83] The efficiency of this technique was greatly improved by the introduction of the 'magnetic bottle'.[84]

As an alternative, the technique of Velocity Map Imaging (VMI) was developed by Chandler and Houston[85] and the design refined by Eppink and Parker.[86] In this, the spherical cloud of electrons produced by photodetachment of a small packet of gaseous molecules is accelerated by an electrode held at a negative voltage onto a pair of micro-channel plates (MCP) in a chevron arrangement to amplify the signal, and then onto a phosphor screen, the output of which is captured by a charge-coupled device. During this, the electron cloud expands according to the kinetic energy of the electrons and produces an image of a series of concentric spheres projected onto a 2D plane. The radius of the spheres is determined by the velocity of the PE s. The position of the PE on the detector is entirely dependent upon the velocity of the electron and independent of the position at which the electron was detached. The *eKE* may then be extracted through an inverse Abel transform.[87] Through this, the spatial information contained within the electron cloud, such as the PE angular anisotropy, is preserved.

1.3.5 Photoelectron Anisotropy

The conservation of the spatial information within the PE cloud by VMI allows for the direct observation of PE anisotropy. PE spectroscopy can be viewed as an electron scattering from an atomic or molecular core structure, hence the PE wavefunction can be expressed as the sum of a series of spherical harmonic functions:[88-90]

$$\psi_{\mathrm{e}} = \sum_{lm} c_{lm} e^{i\delta_l} Y_{lm}(\theta, \phi) \qquad (1.23)$$

where ψ_e is the PE wavefunction, l is the orbital angular momentum quantum number, m is a laboratory frame projection quantum number, c_{lm} is a coefficient containing radial and angular information about the state from which the electron was scattered, δ_l is a scattering induced phase shift and $Y_{lm}(\theta, \phi)$ are the spherical harmonic functions, which are also known as partial waves. The PE angular distribution (PAD) is given by the coherent square of this wavefunction:[88-90]

$$\begin{aligned} I(\theta, \phi) &\propto \psi_{\mathrm{e}}^{*} \psi_{\mathrm{e}} \\ &= \sum_{lm} \sum_{lm} c_{l'm'}^{*} c_{lm} e^{i(\delta_l - \delta_{l'})} Y_{l'm'}^{*}(\theta, \phi) Y_{lm}(\theta, \phi) \\ &= \sum_{LM} B_{LM} Y_{LM}(\theta, \phi) \end{aligned} \qquad (1.24)$$

where $I(\theta, \phi)$ is the PE intensity in three dimensional polar coordinates relative to the polarisation of the incident radiation, l' and m' are l and m in the final state, $|l - l'| \leq L \leq l + l'$ and $M = m + m'$ by the vector combination of the angular momenta, and B_{LM} is a coefficient dependent on several factors and describes the contribution of each partial wave to the PAD and the interference with the other partial waves. An important consequence of equation (1.24) is that the PAD is dependent upon the orbital from which the electron is scattered and hence can be described by symmetrical considerations.[91]

In a gas phase experiment, the sample is an isotropic distribution of isolated molecules. Cooper and Zare showed through symmetrical considerations that single photon ionisation of such a distribution of open or closed shell molecules by linearly polarised light would result in a PAD constrained by the equation:[92]

$$I(\theta) \propto 1 + \beta_2 P_2(\cos(\theta)) \qquad (1.25)$$

where θ is the angle between the polarisation of the incident radiation, $\boldsymbol{\varepsilon}$, and the ejection direction of the PE, and $P_2(\cos(\theta))$ is the second order Legendre polynomial. This results in an angular distribution that is cylindrically symmetric about the laser polarisation, which functions as the laboratory frame *z*-axis. The β_2 parameter may vary between –1 and +2 and may be used to provide qualitative information about the molecular orbitals and resonances of the photoionised system. However, in order to extract the maximum amount of information about the partial waves from the PAD, it is necessary to prealign the molecular distribution into an anisotropic distribution, by, for instance, ionising a distribution that was produced by initial photoexcitation to an excited state.[10,45]

Sanov and co-workers have developed an elegant method for extracting information about the detachment process from the observed PAD of low kinetic energy electrons detached from anions based on symmetrical arguments – the *s*-*p* model.[93-96] At low kinetic energies, by the Wigner threshold law, the wavefunction of the outgoing PEs is dominated by low angular momentum partial waves, specifically those with l = 0 and 1 (*s* and *p* waves respectively).[75] The *s*-*p* model takes the symmetry of the orbital from which the electron is detached, $\Gamma(\Psi_e)$, and the molecular frame components of the transition dipole moment, $\Gamma(\mu_x)$, $\Gamma(\mu_y)$ and $\Gamma(\mu_z)$, and considers the symmetry of the partial waves that contribute to the outgoing PE wave, $\Gamma(e^-)$, such that:

$$\Gamma(\Psi_e) \otimes \Gamma(\mu_i) \otimes \Gamma(e^-) \supseteq \Gamma_{TS} \qquad (1.26)$$

where $i = x$, y or z and Γ_{TS} is the totally symmetric irreducible representation of the point group of the system. In order for equation (1.26) to hold, then:

$$\Gamma(\Psi_e) \otimes \Gamma(\mu_i) \equiv \Gamma(e^-) \qquad (1.27)$$

By inspection of the relevant point group table, it is then possible to determine the symmetry of the outgoing waves in the molecular frame and hence the angular momentum: $l = 0$ corresponds to an s type wave, $l = 1$ corresponds to a p type wave and momenta of $l \geq 2$ are disregarded. s type waves give rise to an isotropic distribution, whereas p type waves give rise to an anisotropic distribution that peaks either perpendicular or parallel to $\boldsymbol{\varepsilon}$, dependent on the symmetry of the wave; if the transition in the x axis, $\Gamma(\mu_x)$, gives rise to a p_x type wave, then the anisotropy peaks parallel to $\boldsymbol{\varepsilon}$. While the s-p model has been shown to be valid for small molecules,[93] the quantitative prediction of the PE angular distribution for large molecular systems and at higher electron kinetic energies remains very difficult and involves time and resource consuming calculations.[97-99] Nevertheless, the PAD remains an extremely useful and sensitive insight into the dynamics of electron photodetachment.

1.4 Measurements in the Time Domain

Perhaps the first example of a time-resolved experiment is 'Sallie Gardener at a Gallop',[100] a 1878 series of 24 photos of a galloping horse taken at short time intervals in order to establish whether a horse's hooves all leave the ground at the same point. If we take the first photo in the series as the 'time zero' point, then each subsequent photograph represents a measure of the system as it evolves in time. This is the underlying principle of all time-resolved measurements; a perturbation is applied to a system and the state of the system is measured as it evolves in time. Time-domain measurements can be broadly divided into two groups: single excitation (where the time

domain measurement comes from measuring the time of emission following the initial perturbation) and multiple excitation (where the time domain measurement comes from the time delay between the two laser pulses).

1.4.1 Single Excitation Measurements

The quintessential single excitation experiment is time-resolved luminescence spectroscopy, or time-correlated single photon counting (TCSPC).[1,101-103] In this, a single excitation pulse is used to promote a system to an excited state that may decay by fluorescence or phosphorescence. The emission is then typically filtered to select a certain wavelength and detected by, for example, a photomultiplier tube or a single-photon avalanche diode. The current from the detector is binned in time relative to the initial excitation pulse, allowing for a histogram to be constructed of the decay of the photoemission signal. The lifetime of the emission may then be extracted from this. While predominantly performed in the solid or liquid phases, gas phase TCSPC studies are not uncommon.[26,104-107]

Fluorecence lifetime imaging is a rapidly expanding field that combines microscopy with time-resolved fluorescence spectroscopy.[108-111] A sample, such as a cell, is doped with a fluorescent dye and placed on the microscope. The sample is then illuminated with a laser pulse in order to excite the dye, and the emission is observed through the microscope. The emission is detected by the same principle as TCSPC, except that a position sensitive detector such as a CCD camera is used instead of a photomultiplier tube.[112] Subsequently, there has been considerable effort to develop fluorescent probes with lifetimes that vary with the environment of the probe. Förster resonance energy transfer[111] is a dipole-dipole interaction where the excitation energy can be transferred non-radiatively from one chromophore to another if the absorption spectrum of the latter overlaps with the emission spectrum of the former. The efficiency

of this mechanism is dependent on the distance between the chromophores, proportional to r^6 where r is the distance between the chromophores. This dependency has been extensively employed to follow intracellular reactions as an extension of fluorescence lifetime imaging. The Förster resonance energy transfer acts as a competing decay mechanism of the excited state, hence, with increased efficiency, the observed fluorescence lifetime will be reduced despite the rate of fluorscence being unchanged. If a protein and a substrate are tagged with complementary chromophores, then, by following the change in the observed fluorescence lifetime, it is possible to pinpoint the location and frequency of protein based reactions in the cellular environment.

An extension of PE spectroscopy is PE -photoion coincidence spectroscopy (PEPICO). When a neutral or cationic molecule is ionised, a PE and a cation are produced simultaneously. The electric fields required for VMI will repell one and accelerate the other, separating the disparate clouds and allowing for detection of both. By measuring the kinetic energy of all fragments simultaneously, a complete picture of energy redistribution on an excited state surface can be obtained.[113-120]

1.4.2 Multiple Excitation Measurements

Single excitation time-domain measurements are dependent upon detecting some particle emitted from the molecule following the initial excitation. Here, we have focussed on detecting photons emitted by fluorescence or phosphorescence following an initial photoexcitation. Other techniques on the same principle exist, notably time-resolved electron attachment, where the lifetime of ions formed by bombardment of neutral molecules with variable kinetic electrons is determined.[121,122] Techniques involving multiple excitations rely on an initial excitation to produce an excited state, followed by a second excitation to induce a second transition, the result of which is detected. The time delay between the two excitation pulses is recorded and gives the

time resolution of the experiment. This is known as pump-probe spectroscopy, where the initial excitation is known as the pump and the second excitation, where the state of the system is determined relative to the time delay between the two excitations, is known as the probe.

An extension of fluorescence lifetime measurements is fluorescence upconversion,[123,124] a two photon technique. In this, the system of interest is photoexcited by an ultrafast laser pulse. The resultant photoemission is collected and directed through a non-linear optical crystal. A second ultrafast laser pulse is directed through the crystal concurrently and the angle is adjusted to maximise the sum-frequency generation, where the two photons effectively combine to give a single photon of the summed energy. The sum frequency photons are then detected and, by varying the time delay between the initial photoexcitation pulse and the upconversion pulse, it is once again possible to construct a histogram of the decay of the photoemission signal and therefore extract the fluorescence lifetimes. This technique allows for greater time resolution than TCSPC, which is dependent upon the time-resolution of the photomultiplier tube and the data acquisition set-up.

Transient absorption is a widely used time-resolved experiment that exemplifies multiple excitation techniques.[1,2] In this, a sample promoted into an excited state by an ultrafast laser pulse. A second pulse is then introduced to produce white light with which the sample is irradiated. The absorbance is recorded across the range of interest and, by varying the time delay between the two pulses, the change in the absorption spectrum with time can be determined. As the absorption spectrum is necessarily tied to the accessible electronic transitions and energy level spacings, the changes in the absorption spectrum can be used to trace the evolution of the excited states. This technique typically requires a greater density of molecules than can be produced by

conventional gas phase techniques, so this transient absorption has not been widely employed in the gas phase.

Numerous examples of time-resolved photofragment spectroscopy studies have been reported, which can be largely grouped into two categories: where the fragmentation is induced by the probe pulse and the fragments then detected (typically by mass spectrometry)[125] and where the fragmentation is induced by the pump pulse and the probe pulse is used to detect the fragment (typically by ionisation of a neutral fragment, so the fragment is then charged and therefore can be detected by traditional methods).[126-128]

1.4.3 Time-Resolved Photoelectron Spectroscopy

It is the extension of PE spectrscopy into the time domain on which we shall focus for the rest of the chapter. The intrinsic principle of PE spectroscopy is to promote the system above the ionisation potential. In time resolved PE spectroscopy (TRPES), the energy required is typically provided by multiple photons. An ultrafast laser pulse is used to promote the species to an excited state and defines t_0 of the experiment. This is followed by a second, probe pulse at a delay of Δt, which promotes the species over the detachment energy and causes electron emission to an electronic state, typically the ground state, of the ionised species. From monitoring the PE spectrum over a series of delays, it is possible to determine the lifetime of the initial excited state and to determine its fate. As such, TRPES can be described as the combination of three processes: the creation of a wave packet in the excited state of a species by the pump pulse, the evolution of this wave packet on the excited state surface for a time delay Δt and, finally, the detection of the wave packet by the probe pulse. An important advantage of this technique is the relaxed selection rules of photoionisation – the detached PE can take any symmetry required to satisfy equation (1.26), hence

ionisation is always an allowed transition. The underlying principles of TRPES are illustrated in Figure 1.3.

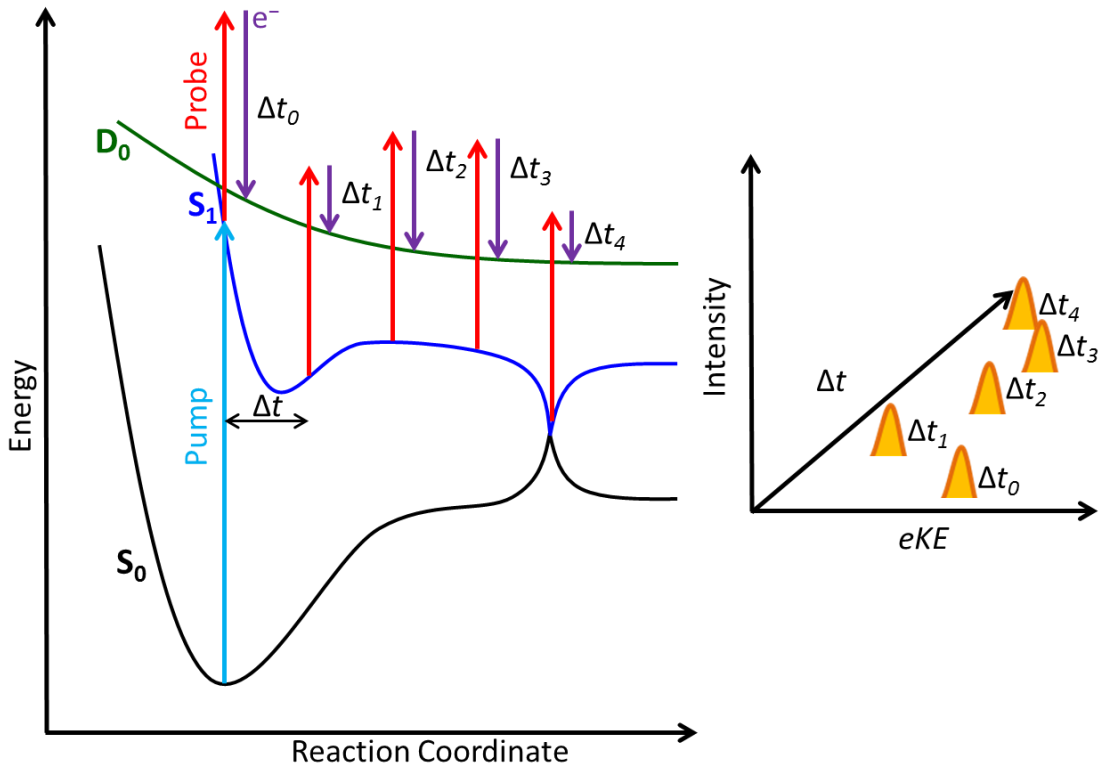

Figure 1.3 Schematic diagram illustrating the fundamental processes underlying TRPES. A pump photon promotes an electron in an anionic species, S_0, into an excited state, S_1. The excited state is then probed by a probe photon after a delay, Δt, to promote the anion into a continuum state. The molecule may then decay to the ground state of the neutral molecule, D_0, following emission of an electron. By recording the intenisty, kinetic energy and distribution of the PEs as a function of pump-probe delay, it is possible to track the evolution of the excited state with time.

1.5 State of the Art

Gas phase PE spectroscopy of neutrals and anions has been used to study a great number of systems. Ultrafast spectroscopic studies are based upon the intricate transition state experiments of Zewail and co-workers,[129] for which Zewail was awarded the 1999 Nobel Prize in Chemistry. While the first TRPES studies were performed in the mid-1980's,[130] the first femtosecond-resolution TRPES studies were reported in the mid-1990's.[131-136] More recently, the first examples of femtosecond time-resolved PE

imaging were reported by Wang *et al.*[137] and Davies *et al.*[113] Over the past two decades, time-resolved gas phase PE spectroscopy has been used extensively to explore a variety of systems. Here, a brief review of recent advances in the field of PE spectroscopy used to investigate the ultrafast molecular dynamics of gas phase molecules is presented.

1.5.1 Deoxyribonucleic Acid

PE spectroscopy has been extensively employed to investigate the dynamics of DNA. The PE spectra, electronic structure and excited state dynamics of the DNA bases have been the subject of considerable interest due to the instability of the DNA strands to ionising radiation.[138] Energy released into cells by ionising radiation is frequently converted into secondary electrons with kinetic energies between 1-20 eV. These electrons, when attached to DNA strands, induce both single and double strand breakages from kinetic energies as low as 3 eV.[139] However, the energies involved are far below the estimated ionisation potentials of the nucleotides or the dissociation energy of the phosphate backbone.[140-142] Recent theoretical studies[143,144] have suggested that the cleavage is due to the occupation of an empty π^* orbital on the nucleobase by the free electron. This may then undergo electron transfer onto the sugar-phosphate backbone, resulting in the breaking of a C-O σ bond.

An important factor in understanding the source of this molecular damage is the adiabatic ionisation energy of the nucleotides. In order to determine this energy, numerous computational,[145,146] PE spectroscopy[147-153] and electron affinity studies[154-156] have been performed on the isolated gas phase nucleotides. Yang *et al.*[152] employed single photon PE spectrum to investigate isolated gas phase deprotonated nucleotides and oglio-nucleotides. This revealed that the PE spectrum of guanine has a considerably lower onset than the other nucleotides, a finding replicated by the two-photon resonance enhanced electron detachment technique used by Chatterley *et al.*[153] This feature has

been assigned to electron detachment from a low energy π orbital in guanine, whereas the lowest-lying features in the spectra for the other nucleotides have been assigned to detachment from the negatively charged phosphate group.

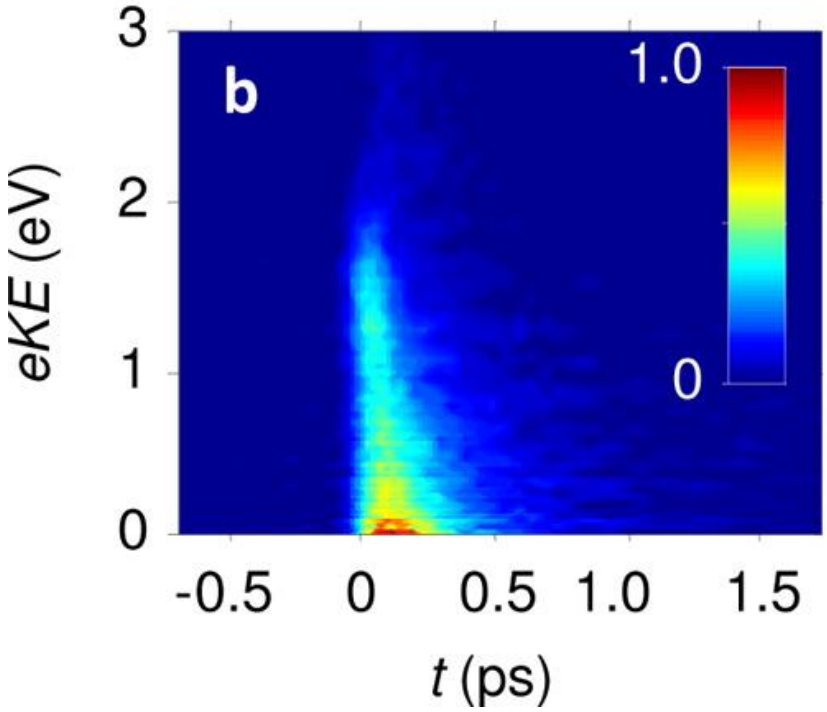

Figure 1.4 TRPES of the anionic adenosine nucleobase, using a 266 nm pump pulse and 400 nm probe pulse. Reproduced from Chatterley *et al.*[157]

The excited state dynamics of DNA nucleotides have been extensively studied in solution.[158] Bisgaard *et al.* have previously presented femtosecond TRPES of the gas phase neutral nucleotides adenine, cytosine, thymine and uracil.[159] In this and in further work,[160] the decay channels of the excited state of adenine are assigned in detail. The dynamics of the nucleotides in the gas-phase have been investigated by time-resolved PE spectroscopy by Chatterley *et al.*,[157,161] by initially accessing the $^1\pi\pi^*$ excited state located on the nucleobase and subsequently detaching an electron with a second laser pulse. The TRPES exploring the dynamics of the adenosine nucleobase is presented in Figure 1.4. The excited states of adenine and guanine nucleotides were found to decay primarily by internal conversion to the ground state with no involvement of

intermediary electronic states and to be relatively insensitive to the environment.[157,161] The thymine nucleotide was found to exhibit similar dynamics to the isolated nucleobase, whereas the cytosine nucleotide was found to have considerably slower dynamics than the associated nucleobase.[161] However, the excited state dynamics following electron attachment to DNA nucleotides have not yet been studied extensively in the gas phase. In pursuit of this goal, the Neumark group have very recently reported TRPEI studies of iodide–thymine and –uracil clusters.[162,163] The pump pulse ionises the iodide ion, whereupon the detached electron may attach to the nucleotide. The probe pulse may then ionise the anionic nucleotide. These studies revealed that the anionic state decays to the neutral state biexponentially, indicating multiple decay channels. However, the lack of the phosphate backbone is expected to have a significant effect upon the excited state dynamics.

Investigations of the photophysics of DNA and RNA nucleotides bound to platinum cyanide complexes in the gas phase have been presented by Sen *et al.*[74,164-166] The authors supplement numerous laser action spectra and photofragmentation mass spectra[164-166] with low-temperature PE spectra of the dianionic $Pt(CN)_4^{2-}$ moiety both isolated and complexed to uracil, thymine, cytosine and adenine.[74] The spectral features of the $Pt(CN)_4^{2-}$ dianion were found to shift to higher binding energy when bound to a nucleobase and a broad, featureless band was observed for all nucleobases following excitation at 193 nm, which was assigned to delayed electron detachment. Crucially, the band was only oberved in two nucleobases (thymine and adenine) following excitation at 266 nm. This was assigned to the promotion of a long-lived excited state in these species following excitation at 266 nm, allowing for effective coupling to the photodetachment continuum.[74] As such, the PE spectrum of the complex is intrinsically

linked to the dynamics of the complexed nucleobase and so may be viewed as a dynamic tag.

1.5.2 Metal and Metal Salt Clusters

A major area of study in which PE spectroscopy has been invaluable is in the study of the electronic and physical structure of small anionic metal clusters.[20,46] A vast range of studies have been performed on small clusters of pure metals, such as copper,[167,168] silver,[167] gold,[167,169] niobium[170] and mercury,[171] and expanded to study metal atoms in anionic clusters of solvent. An excellent example of such a study is the work of Deng *et al.*,[73] which seeks to probe the systems initially formed in salt nucleation. Electrospray ionisation produces a series of charged droplets from which solvent may evaporate rapidly.[65,66,69] The rapid reduction in the amount of solvent in the droplet leads to the formation of supersaturated droplets and eventually pure ionic salt clusters. This process is, in theory, analagous to the nucleation of salts from solution and can therefore be used as a model system in which to probe the changes in the electronic structure as the bulk solid forms. By this process, Deng *et al.* were able to form and probe $K_x(SCN)^-_{x+1}$, $K_y(SCN)^{2-}_{y+2}$ and $K_z(SCN)^{3-}_{z+3}$ clusters. It was observed that the singly charged anion clusters were super halogen clusters. The multiply charged clusters were found to be suppressed at high temperatures and become increasingly prevalent as the mass of the complex increased. Overall, the system acted as a good model for solute aggregation.[73]

Conversely, if one can form a series of anions solvated by an increasing number of solvent molecules, then, by probing the system at each cluster size, an insight in solvation from initial interactions to bulk solution can be obtained.[44,172-177] A recent example is the work of Zeng *et al.*,[177] in which the PE spectra of $Li(H_2O)_n^-$ and $Cs(H_2O)_n^-$ (n = 1-6) were reported along with supporting *ab initio* calculations. These

systems are of interest as the lithium clusters can be described as a cation and two solvated electrons. Therefore, this system may act as a gas phase model of two electron solvation and subsequently provide insight to the electron-electron interaction present in several biologically important reactions involving solvated electron pairs.[177] Lithium was found to be surrounded by water molecules, whereas Caesium lies on the surface of the water cluster. The structure of the clusters was found to be dependent on a number of different factors in addition to the forces due to the excess electrons, which could provide significant information for the understanding of the hydration of alkali metals in addition to the solvated electron pair.[177]

1.5.3 Photodissociation

Investigations of the ultrafast dynamics of photodissociation have traditionally been limited by the availability of both tunable femtosecond pulses and dissociable molecules. It is necessary to be able to initiate the photodissociation by absorption of a photon produced by the available femtosecond systems. It is extremely preferable that only a single bond may be broken at that wavelength, to ease identification of the fragments. This is by no means a necessity, however, and the fragmentation channels are entirely dependent upon the system studied. As such, TRPES studies of photodissociation dynamics have tended to be constrained to anions and weakly bound clusters.[127,128,170,175]

The Lineberger group have employed TRPES in order to investigate the dynamics and fate of the products of photodissociation in small halide and pseudo-halide clusters. The photodissociation dynamics of ICN^-, probing in this instance the rotational energy of the dissociated CN, have been investigated by PE spectroscopy and TRPES.[178,179]

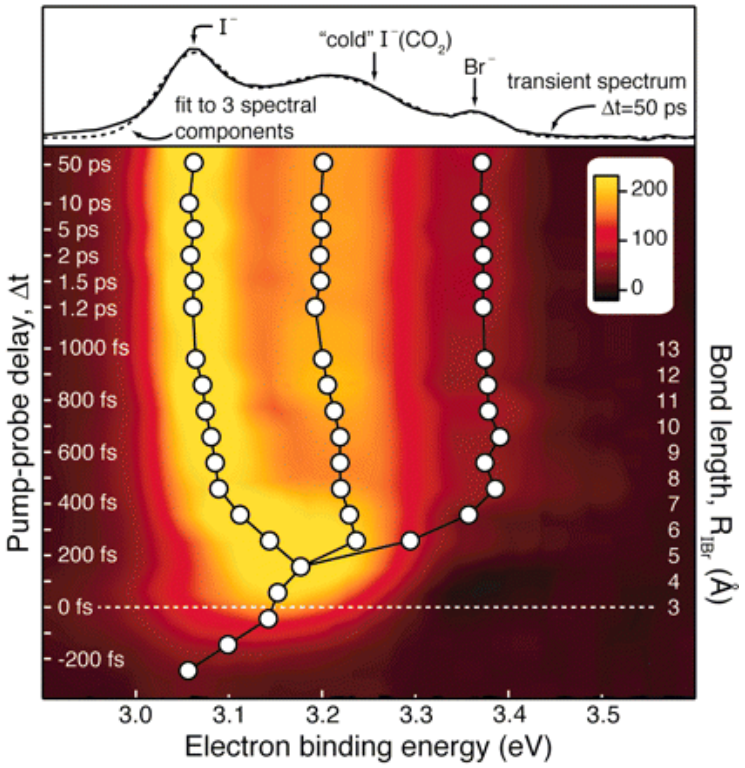

Figure 1.5 The time-resolved photoelectron spectrum of $IBr^-(CO_2)$ plotted against the pump-probe delay and the radial spectrum at 50 ps. The peak for Br^- can be seen to evolve at approximately 350 fs. Reproduced with permission from Sheps *et al*.[180]

In addition, TRPES[180-182] and computational studies[176,183] have been employed to investigate the photodissociation dynamics of $IBr^-(CO_2)_n$ clusters. IBr^- dissociates following photoexcitation at 780 nm to form predominantly I^- and Br, although the formation of I and Br^- is also an important product channel.[176] An important result from these studies was the observation that the presence of carbon dioxide solvating the IBr^- considerably increases the proportion of Br^- produced. This implies that a charge transfer reaction from the I^- to the Br occurs during dissociation that is mediated by the solvent molecules.[176] In order to investigate this, Sheps *et al.* have examined the evolution of Br^- following the photofragmentation of the $IBr^-(CO_2)$ cluster *via* a TRPES study, presented in Figure 1.5.[180] In this, the initial excitation promoted the system to the second excited (A') electronic state. This is a dissociative state that favours the production of I^- and vibrationally excited Br.

The electron transfer between the participating atoms was found to occur at 350 fs after the pump pulse. The distance between I and Br at this pump-probe time delay was calculated to be 7 Angstroms.[180] Molecular dynamics simulations suggest that the long range charge transfer is due to participation from a CO_2 bending mode, facilitating a shift in the localisation of the excess charge away from the iodide anion and towards the bromine atom. This is a notable example of solvent driven long range charge transfer. The Lineberger group have also recently reported a similar study in which photodissociation of the cluster is initiated by excitation to a higher (B) electronic state. This state is also dissociative, but promotes the production of Br^- and vibrationally excited $I(CO_2)$.[182] In this, the reverse solvent-mediated charge transfer was observed from the Br^- anion to the I atom. However, a greater proportion of electron transfer between the species was observed compared to the I to Br charge transfer.

1.5.4 Small Organic Molecules

Due in part to their prevalence in nature and applicability in light harvesting metal complexes, there has been considerable interest in investigating the molecular dynamics of organic molecules that may absorb photons in the visible and ultraviolet range.[20,184,185] Due to its aromatic nature and the wide prevalence of the phenyl sub-unit in nature, benzene has been the subject of considerable interest for several decades. While initial PE studies of benzene focussed upon the assignment and ordering of the molecular orbitals,[186-188] the dynamics of the S_1 excited state were subsequently investigated by picosecond[189] and femtosecond[190,191] TRPES. TRPES was also applied to investigate internal conversion from the S_2 state.[192]

The Fielding group have recently applied gas phase TRPES to neutral benzene molecules in a molecular beam in order to investigate the ultrafast dynamics at the onset of the channel 3 region of benzene.[193] An initial pump pulse at a wavelength of 243 nm

promoted the molecule to the S_1 excited state, which was then probed at various wavelengths centred between 235 and 260 nm. While it was found that a large proportion of the excited states rapidly internally convert to the S_0 state, a significant proportion undergoes intersystem crossing to the T_1 state on an ultrafast timescale.[193] Additionally a small proportion of molecules were found to oscillate between the S_1 and T_2 states. These results indicate that the ultrafast decay of the S_1 excited state previously attributed to internal conversion[191] is actually a result of competition between internal conversion and intersystem crossing. Theoretical investigations suggest that the unexpectedly high rate of intersystem crossing is due to the accessing of a vibrational mode favourable to intersystem crossing.[194] The S_2 excited state of benzene has recently been probed through TRPES by Shen *et al.*,[195] who produced the excited state through two photon absorption of 400 nm and probed at 267 nm. Two lifetimes were observed: a sub 100-femtosecond lifetime assigned to the $S_1 \leftarrow S_2$ transition and a 5 picosecond lifetime assigned to the loss of the S_1 state. The authors note that the second lifetime is shorter than previous observations, which is ascribed to the opening of an additional decay channel; intersystem crossing between the vibrationally excited S_1 state and the T_3 state.[195]

In addition to their work on the excited states of benzene, the Fielding group have recently employed TRPES to determine the dynamics for the first two excited states (S_1 and S_2) of styrene.[196] It was found that, while both excited states decay *via* internal conversion through conical intersections, the rate of internal conversion from S_1 to S_0 was five times slower if it was preceded by internal conversion from an S_2 state produced with excess vibrational energy. Nunn *et al.* concluded that the conical intersection between the S_1 and S_0 states did not occur on the intial geometry relaxation coordinate following photoexcitation and was therefore barrier activated, whereas the

converse was true for the $S_1 \leftarrow S_2$ transition.[196] The internal conversion from the S_2 state therefore produces an S_1 excited state population that is geometrically 'further' from the $S_0 \leftarrow S_1$ conical intersection, resulting in the observed increase in lifetime.

TRPES has been extensively employed to investigate the excited state dynamics of indole, which is of particular interest due to its presence in the amino acid tryptophan.[197-200] The dynamics of the mixed Rydberg-valence 3s/πσ* state produced by photoexcitation at 267 nm and 258 nm have been well characterised.[198] In this, it was found that population existed on the excited state surface at large N-H separations for long timescales before the excited state decays by dissociation or internal conversion. This was linked to the rapid evolution of the mixed Rydberg-valence excited state character as the along the N-H separation and indicates the importance of careful consideration of mixed Rydberg-valence states in the assignment of excited state dynamics. As the excitation energy is decreased, however, the involvement of this state in the excited state dynamics becomes negligible.[199]

The excited state dynamics of aniline have been the subject of considerable interest, due to numerous studies drawing opposing conclusions. Wren *et al.* have reported the gas phase PE spectrum of the anilinide anion,[201] in which the authors note the clear progression of a vibrational mode. Spesyvtsev *et al.* have observed the excited state dynamics of aniline in the gas phase through TRPES following excitation at 269-238 nm.[202] In this, it was concluded that the $S_2(3s/\pi\sigma^*)$ excited state was produced following excitation at all wavelengths, which would then decay through two possible channels: ultrafast internal conversion to the $S_1(\pi\pi^*)$ state via a conical intersection and subsequent relaxation to the electronic ground state by a far slower process, and a non-radiative channel that appeared to involve motion along the N-H stretch coordinate on the πσ* dissociative potential energy surface. Although the precise nature of this

channel was not able to be discerned by this study, the timescales recorded were extremely similar to lifetimes reported by Livingstone *et al.* in their recently reported TRPES investigation into the excited state dynamics of indole and 5-hydroxyindole.[197] The Townsend group assigned these lifetimes to motion on the dissociative πσ* potential energy surface, leading Spesyvtsev *et al.* to suggest that similar motion may occur in aniline.[202]

However, these observations appear to conflict with the observations of Ashfold and co-workers[203] and Stavros and co-workers,[204] who employed H atom Rydberg tagging and time resolved H atom imaging, respectively. These works inferred the presence of a $S_1(\pi\pi^*)/S_2(3s/\pi\sigma^*)$ coupling interaction and so the reverse of the non-adiabatic coupling observed by the Fielding group. Townsend and co-workers have recently performed TRPES studies on aniline following photoexcitation at 250 nm, *N*,*N*-dimethylaniline and 3,5-dimethylaniline in order to investigate the internal molecular coordinates involved in the excited state coupling.[205,206] In this, it was found that both excited states were initially excited and that the $S_2(3s/\pi\sigma^*)$ population may decay by internal conversion to the $S_1(\pi\pi^*)$ or via a postulated dissociation mechanism along the N-H/Me stretch coordinate. The aromatic ring system was linked to the internal conversion between the $S_2(3s/\pi\sigma^*)$ and $S_1(\pi\pi^*)$ excited states, as methylation of the aromatic ring results in only the direct dissociative mechanism being observed.[190]

Time-resolved PE spectroscopy has also been exploited to investigate the ring opening reaction of 1,3-cyclohexadiene following UV excitation.[207] Excitation of 1,3-cyclohexadiene at 270 nm produces an excited state population on an extremely repulsive section of the 1B excited state surface, which induces ultrafast internal conversion *via* a conical intersection to the 2A state. This state then decays back to the ground 1A state *via* a second conical intersection. At this point, the system branches

into two populations: the system may undergo a ring-opening reaction to form 1,3,5-hexatriene or return to the initial 1,3-cyclohexadiene strucutre. The branching ratio of this process has been the subject of some controversy, with gas and liquid phase experiments yielding differing branching ratios.[208,209] Adachi *et al.* employed gas phase TRPES to promote 1,3-cyclohexadiene into the excited state and subsequently probe the relaxation dynamics.[207] The probe pulse used is a 13.6 eV (90 nm), 40 fs pulse, which is sufficient to ionise the molecule from the ground state and so allows for observation of complete ground state recovery. It was determined that 30% of the initial excited state population undergoes the ring opening reaction, in good accord with experimental observations in the liquid phase and theoretical calculations for the gas phase. This study is a clear example of the utility of TRPES where the ground state recovery may be probed to comprehensively determine the fate of an excited state population.

Finally, TRPES has recently been used to explore the deactivation dynamics of the $\pi\pi^*(V)$ state of ethene at sub-20 fs resolution.[210] The system is promoted into the desried excited state by an ultrafast pump pulse at 159 nm and the photoelectron detached by an ultrafast probe pulse at 198 nm. The resultant TRPE spectrum is presented in Figure 1.6.

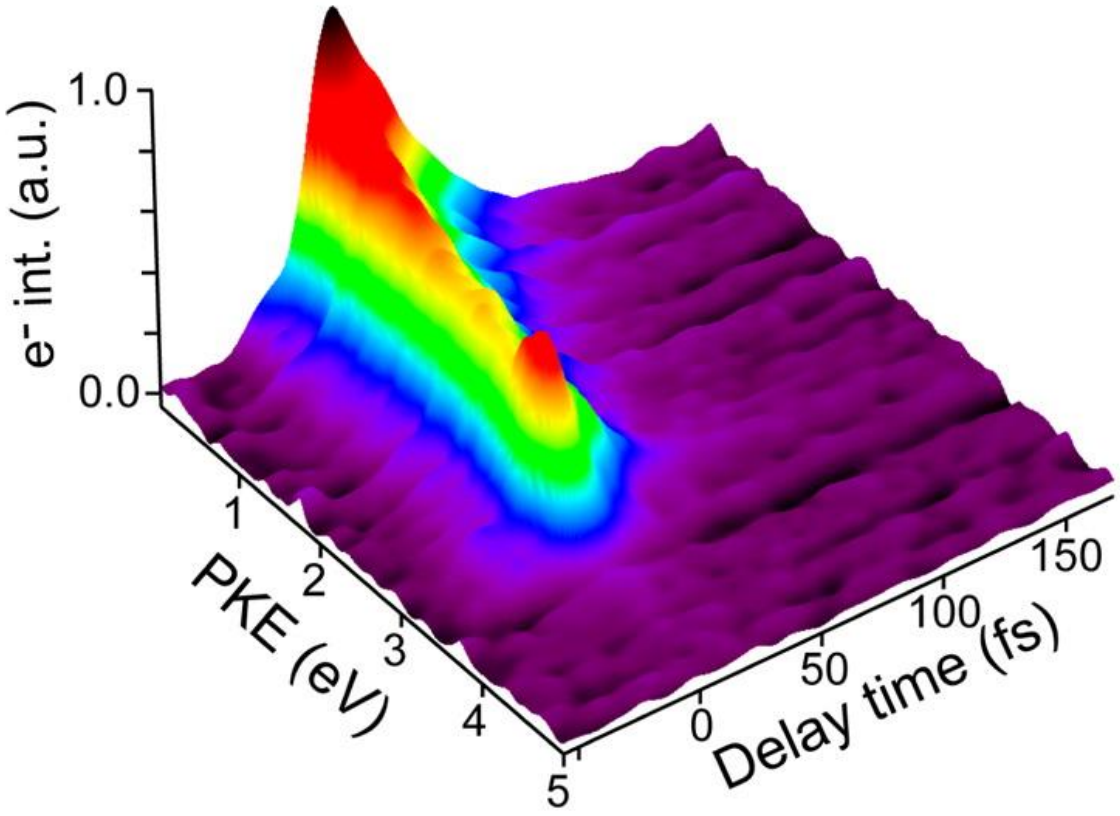

Figure 1.6 TRPES of ethene, following excitation to the $\pi\pi^*(V)$ state. Reproduced with permission from Kobayashi *et al.*[210] Copyright 2015 American Chemical Society

A clear downward trend in the photoelectron kinetic energy distribution can be observed, occuring on a sub-20 fs timescale. This was ascribed to a combination of a twist around the C–C bond and a pyrimidalization motion. Through careful examination of the TRPES, a partial wave packet revival at 3 eV at 18 fs after the initial photoexcitation can be observed. This was attributed to recovery of an equivalent geometry to the Franck-Condon geometry through a 180^o twist of the C–C bond. The unprecedented time-resolution of this work provides a fantastic example of the application of TRPES to exploring ultrafast molecular dynamics.

1.6 Summary

In this chapter, I have aimed to introduce the fundamental concepts that underly the work undertaken in this thesis. A brief summary of the production and evolution of

an excited electronic state was presented. The principles of PE spectroscopy, including photodetachment, methods of detection and PE angular anisotropy, were then summarised. Numerous methods of time-resolved spectroscopies with which to trace the evolution of a wave packet on an excited state surface were discussed, with a focus on pump-probe spectroscopy and time-resolved PE spectroscopy. Finally, a short discussion of the recent application of PE spectroscopy to the study of the dynamics of molecular systems was presented.

The remainder of the thesis is structured as follows: a brief overview of the experiment is given in Chapter 2. Chapter 3 describes the development of a new global kinetic fitting program that fits to the total PE intensity of the PE image, as opposed to the PE spectrum. Chapter 4 describes the dynamics of the excited states of the anionic model green fluorescent protein chromophore. Chapter 5 moves on to the study of the radical anionic excited states produced following electron attachment to a proto-typical electron acceptor, where the initial states produced by electron attachment are instead produced by photoexcitation of the ground state of the radical anion. Chapter 6 presents the PE spectra of a series of phenyl carboxylic acids, π-conjugated carboxylic acids and amino acids. Chapter 7 then details a TRPES study of the excited state dynamics of isolated all-*trans* retinoic acid. Finally, Chapter 8 details the study of a highly symmetric dianion and the simulation of electron trajectories on a representative electrostatic excited state surface in order to simulate the dependence of the observed PE anisotropy on the repulsive Coulomb barrier.

1.7 References

(1) Hollas, J. M. *Modern Spectroscopy*; 4th Edn ed.; John Wiley & Sons, Ltd: Chichester, 1987.

(2) Atkins, P.; de Paula, J. *Atkins' Physical Chemistry*; 8th Edn ed.; Oxford University Press: Oxford, 2006.

(3) Atkins, P.; Friedman, R. *Molecular Quantum Mechanics*; Oxford University Press: Oxford, 2005.

(4) Balzani, V.; Ceroni, P.; Juris, A. *Photochemistry and Photophysics*; Wiley-VCH Verlag Gmbh & Co. KGaA: Weinheim, 2014.

(5) Fourier, J. *The Analytical Theory of Heat*; Dover Publication: Dover, 1822.

(6) Heisenberg, W. *Zeitschrift Fur Physik* **1927**, *43*, 172.

(7) Kennard, E. H. *Zeitschrift Fur Physik* **1927**, *44*, 326.

(8) Hannaford, P. *Femtosecond Laser Spectroscopy*; Springer Science + Business Media, 2005.

(9) Franck, J. *Transactions of the Faraday Society* **1926**, *21*, 0536.

(10) Condon, E. *Physical Review* **1926**, *28*, 1182.

(11) Condon, E. U. *Physical Review* **1928**, *32*, 0858.

(12) Gilbert, A.; Baggott, J. *Essentials of Molecular Photochemistry*; Blackwell Scientific Publications: Great Britain, 1991.

(13) Fermi, E. *Nuclear Physics*; University of Chicago Press: Chicago, 1950.

(14) Domcke, W.; Yarkony, D. R.; Koppel, H. *Conical Intersections: Electronic Structure, Dynamics & Spectroscopy*; World Scientific Publishing Co. Pte. Ltd.: Singapore, 2004.

(15) Robb, M. A.; Bernardi, F.; Olivucci, M. *Pure and Applied Chemistry* **1995**, *67*, 783.

(16) Yarkony, D. R. *Journal of Physical Chemistry A* **2001**, *105*, 6277.

(17) Yarkony, D. R. *Reviews of Modern Physics* **1996**, *68*, 985.

(18) Born, M.; Huang, K. *Dynamical Theory of Crystal Lattices*; Oxford University Press: Oxford, 1954.

(19) Bernardi, F.; Olivucci, M.; Robb, M. A. *Chemical Society Reviews* **1996**, *25*, 321.

(20) Hertel, I. V.; Radloff, W. *Reports on Progress in Physics* **2006**, *69*, 1897.

(21) Worth, G. A.; Cederbaum, L. S. *Annual Review of Physical Chemistry* **2004**, *55*, 127.

(22) Domcke, W.; Stock, G. *Advances in Chemical Physics D* **1997**, *100*, 1.

(23) Koppel, H.; Domcke, W.; Cederbaum, L. S. *Advances in Chemical Physics* **1984**, *57*, 59.

(24) Adams, F.; Gijbels, R.; Van Grieken, R. *Inorganic Mass Spectrometry*; John Wiley & Sons, Ltd.: New York, 1988.

(25) Forbes, M. W.; Nagy, A. M.; Jockusch, R. A. *International Journal of Mass Spectrometry* **2011**, *308*, 155.

(26) Yao, H.; Jockusch, R. A. *Journal of Physical Chemistry A* **2013**, *117*, 1351.

(27) Hertz, H. *Annalen Der Physik* **1887**, *267*, 983.

(28) Einstein, A. *Annalen Der Physik* **1905**, *17*, 132.

(29) Koopmans, T. *Physica* **1934**, *1*, 104.

(30) Turner, D. W.; Aljobory, M. I. *Journal of Chemical Physics* **1962**, *37*, 3007.

(31) Cetinkaya, B.; King, G. H.; Krishnamurthy, S. S.; Lappert, M. F.; Pedley, J. B. *Chemical Communications* **1971**, *1971*, 1370.

(32) Fadley, C. S.; Baird, R. J.; Siekhaus, W.; Novakov, T.; Bergstrom, S. A. L. *Journal of Electron Spectroscopy and Related Phenomena* **1974**, *4*, 93.

(33) Brundle, C. R. *Surface Science* **1975**, *48*, 99.

(34) Hansson, G. V.; Uhrberg, R. I. G. *Surface Science Reports* **1988**, *9*, 197.

(35) Fadley, C. S. *Progress in Surface Science* **1984**, *16*, 275.
(36) Winter, B. *Nuclear Instruments and Methods in Physics Research Section A: Accelerators, Spectrometers, Detectors and Associated Equipment* **2009**, *601*, 139.
(37) Seidel, R.; Thurmer, S.; Winter, B. *Journal of Physical Chemistry Letters* **2011**, *2*, 633.
(38) Ottosson, N.; Faubel, M.; Bradforth, S. E.; Jungwirth, P.; Winter, B. *Journal of Electron Spectroscopy and Related Phenomena* **2010**, *177*, 60.
(39) Winter, B.; Faubel, M. *Chemical Reviews* **2006**, *106*, 1176.
(40) Mabbs, R.; Grumbling, E. R.; Pichugin, K.; Sanov, A. *Chemical Society Reviews* **2009**, *38*, 2169.
(41) Wang, L.-S. *Journal of Chemical Physics* **2015**, *143*, 040901.
(42) Wang, X.-B.; Wang, L.-S. In *Annual Review of Physical Chemistry*; Annual Reviews: Palo Alto, 2009; Vol. 60, p 105.
(43) Chatterley, A. S.; Horke, D. A.; Verlet, J. R. R. *Physical Chemistry Chemical Physics* **2014**, *16*, 489.
(44) Bragg, A. E.; Verlet, J. R. R.; Kammrath, A.; Cheshnovsky, O.; Neumark, D. M. *Science* **2004**, *306*, 669.
(45) Hertel, I. V.; Radloff, W. *Reports on Progress in Physics* **2006**, *69*, 1897.
(46) Verlet, J. R. R. *Chemical Society Reviews* **2008**, *37*, 505.
(47) Campargue, R. *Atomic and Molecular Beams: the State of the Art 2000*; Springer-Verlag Berlin Heidelberg: Berlin, 2001.
(48) Johnson, T. H. *Physical Review* **1928**, *31*, 103.
(49) van de Meerakker, S. Y. T.; Bethlem, H. L.; Vanhaecke, N.; Meijer, G. *Chemical Reviews* **2012**, *112*, 4828.
(50) Ono, Y.; Linn, S. H.; Prest, H. F.; Gress, M. E.; Ng, C.-Y. *Journal of Chemical Physics* **1980**, *73*, 2523.
(51) Prigogine, I.; Rice, S. A.; Ng, C.-Y. *Molecular Beam Photoionization Studies of Molecules and Clusters*; John Wiley & Sons, Inc.: Hoboken, NJ, USA, 1983; Vol. 52.
(52) Scoles, G. *Atomic and Molecular Beam Methods*; Oxford University Press: Oxford, 1988; Vol. 1.
(53) Trott, W. M.; Blais, N. C.; Walters, E. A. *Journal of Chemical Physics* **1978**, *69*, 3150.
(54) Märk, T. D.; Dunn, G. H. *Electron Impact Ionization*; Springer-Verlag/Wien: Austria, 1985.
(55) Neynaber, R. H.; Marino, L. L.; Rothe, E. W.; Trujillo, S. M. *Physical Review* **1961**, *124*, 135.
(56) Tate, J. T.; Smith, P. T. *Physical Review* **1932**, *39*, 270.
(57) Fite, W. L.; Brackmann, R. T. *Physical Review* **1959**, *113*, 815.
(58) Van Zyl, B.; Utterback, N. G.; Amme, R. C. *Review of Scientific Instruments* **1976**, *47*, 814.
(59) Gehrke, M.; Kapila, S.; Nam, P.; Flanigan, V. In *Detection and Remediation Technologies for Mines and Minelike Targets IV Conference* Orlando, Fl, 1999; Vol. 3710, p 299.
(60) Cody, R. B.; Laramée, J. A.; Durst, H. D. *Analytical Chemistry* **2005**, *77*, 2297.
(61) Marcus, R. K. *Glow Discharge Spectroscopies*; Plenum Press: New York, 1993.

(62) El-Aneed, A.; Cohen, A.; Banoub, J. *Applied Spectroscopy Reviews* **2009**, *44*, 210.
(63) Hines, R. L. *Journal of Applied Physics* **1966**, *37*, 2730.
(64) Fenn, J. B.; Mann, M.; Meng, C. K.; Wong, S. F.; Whitehouse, C. M. *Science* **1989**, *246*, 64.
(65) Fenn, J. B.; Mann, M.; Meng, C. K.; Wong, S. F.; Whitehouse, C. M. *Mass Spectrometry Reviews* **1990**, *9*, 37.
(66) Nguyen, S.; Fenn, J. B. *Proceedings of the National Academy of Sciences of the United States of America* **2007**, *104*, 1111.
(67) Iribarne, J. V.; Thomson, B. A. *Journal of Chemical Physics* **1976**, *64*, 2287.
(68) Dole, M.; Mack, L. L.; Hines, R. L. *Journal of Chemical Physics* **1968**, *49*, 2240.
(69) Kebarle, P.; Peschke, M. *Analytica Chimica Acta* **2000**, *406*, 11.
(70) Wang, X. B.; Wang, L. S. In *Annual Review of Physical Chemistry*; Annual Reviews: Palo Alto, 2009; Vol. 60, p 105.
(71) Wang, L. S.; Ding, C. F.; Wang, X. B.; Barlow, S. E. *Review of Scientific Instruments* **1999**, *70*, 1957.
(72) Handschuh, H.; Gantefor, G.; Eberhardt, W. *Review of Scientific Instruments* **1995**, *66*, 3838.
(73) Deng, S. H. M.; Kong, X.-Y.; Wang, X.-B. *Journal of Chemical Physics* **2015**, *142*, 024313.
(74) Sen, A.; Hou, G.-L.; Wang, X.-B.; Dessent, C. E. H. *Journal of Physical Chemistry B* **2015**, *119*, 11626.
(75) Wigner, E. P. *Physical Review* **1948**, *73*, 1002.
(76) Wang, X.-B.; Ding, C.-F.; Wang, L.-S. *Physical Review Letters* **1998**, *81*, 3351.
(77) Andersen, J. U.; Bonderup, E.; Hansen, K. *Journal of Physics B-Atomic Molecular and Optical Physics* **2002**, *35*, R1.
(78) Baguenard, B.; Pinare, J. C.; Bordas, C.; Broyer, M. *Physical Review A* **2001**, *63*, 023204.
(79) Campbell, E. E. B.; Levine, R. D. *Annual Review of Physical Chemistry* **2000**, *51*, 65.
(80) Baker, A. D.; Betteridge, D. *Photoelectron Spectroscopy: Chemical and Analytical Aspects*; Pergamon Press: Oxford, 1972; Vol. 53.
(81) Eland, J. H. D. *Photoelectron Spectroscopy*; Butterworth & Co. Ltd.: London, 1974.
(82) Letokhov, V. S. *Laser Photoionization Spectroscopy*; Academic Press Inc. Ltd.: London, 1987.
(83) Wiley, W. C.; McLaren, I. H. *Review of Scientific Instruments* **1955**, *26*, 1150.
(84) Kruit, P.; Read, F. H. *Journal of Physics E-Scientific Instruments* **1983**, *16*, 313.
(85) Chandler, D. W.; Houston, P. L. *Journal of Chemical Physics* **1987**, *87*, 1445.
(86) Eppink, A.; Parker, D. H. *Review of Scientific Instruments* **1997**, *68*, 3477.
(87) Roberts, G. M.; Nixon, J. L.; Lecointre, J.; Wrede, E.; Verlet, J. R. R. *Review of Scientific Instruments* **2009**, *80*, 7.

(88) Reid, K. L. *Molecular Physics: An International Journal at the Interface between Chemistry and Physics* **2012**, *110*, 131.
(89) Reid, K. L. *Annual Review of Physical Chemistry* **2003**, *54*, 397.
(90) Underwood, J. G.; Reid, K. L. *Journal of Chemical Physics* **2000**, *113*, 1067.
(91) Yang, C. N. *Physical Review* **1948**, *74*, 764.
(92) Cooper, J.; Zare, R. N. *Journal of Chemical Physics* **1968**, *48*, 942.
(93) Culberson, L. M.; Blackstone, C. C.; Sanov, A. *Journal of Physical Chemistry A* **2013**, *117*, 11760.
(94) Khuseynov, D.; Blackstone, C. C.; Culberson, L. M.; Sanov, A. *Journal of Chemical Physics* **2014**, *141*, 124312.
(95) Sanov, A. In *Annual Review of Physical Chemistry, Vol 65*; Johnson, M. A., Martinez, T. J., Eds. 2014; Vol. 65, p 341.
(96) Sanov, A.; Grumbling, E. R.; Goebbert, D. J.; Culberson, L. M. *Journal of Chemical Physics* **2013**, *138*, 054311.
(97) Oana, C. M.; Krylov, A. I. *Journal of Chemical Physics* **2009**, *131*, 124114.
(98) Liu, Y.; Ning, C. *Journal of Chemical Physics* **2015**, *143*, 144310.
(99) Oana, C. M.; Krylov, A. I. *Journal of Chemical Physics* **2007**, *127*, 234106.
(100) In *Sallie Gardner at a Gallop*,http://www.imdb.com/title/tt2221420/ 1878, (2015)
(101) Becker, W.; Bergmann, A.; Biskup, C. *Microscopy Research and Technique* **2007**, *70*, 403.
(102) Duncan, R. R.; Bergmann, A.; Cousin, M. A.; Apps, D. K.; Shipston, M. J. *Journal of Microscopy* **2004**, *215*, 1.
(103) Palsson, L. O.; Wang, C.; Russell, D. L.; Monkman, A. P.; Bryce, M. R.; Rumbles, G.; Samuel, I. D. W. *Chemical Physics* **2002**, *279*, 229.
(104) Felker, P. M. *Journal of Physical Chemistry* **1992**, *96*, 7844.
(105) Zimmerman, F. P.; Koban, W.; Roth, C. M.; Herten, D.-P.; Schulz, C. *Chemical Physics Letters* **2006**, *426*, 248.
(106) Sagoo, S. K.; Jockusch, R. A. *Journal of Photochemistry and Photobiology A: Chemistry* **2011**, *220*, 173.
(107) Zhang, Y.; Oliver, T. A. A.; Ashfold, M. N. R.; Bradforth, S. E. *Faraday Discussions* **2012**, *157*, 141.
(108) Bastiaens, P. I. H.; Squire, A. *Trends in Cell Biology* **1999**, *9*, 48.
(109) Berezin, M. Y.; Achilefu, S. *Chemical Reviews* **2010**, *110*, 2641.
(110) Gomes, A.; Fernandes, E.; Lima, J. *Journal of Biochemical and Biophysical Methods* **2005**, *65*, 45.
(111) Wallrabe, H.; Periasamy, A. *Current Opinion in Biotechnology* **2005**, *16*, 19.
(112) Valeur, B.; Brochon, J.-C. *New Trends in Fluorescence Spectroscopy: Applications to Chemical and Life Sciences*; Springer-Verlag Berlin Heidelberg: Berlin, 2001.
(113) Davies, J. A.; LeClaire, J. E.; Continetti, R. E.; Hayden, C. C. *Journal of Chemical Physics* **1999**, *111*, 1.
(114) Gador, N.; Samoylova, E.; Smith, V. R.; Stolow, A.; Rayner, D. M.; Radloff, W.; Hertel, I. V.; Schultz, T. *Journal of Physical Chemistry A* **2007**, *111*, 11743.

(115) Hayden, C. C.; Davies, J. A. *Abstracts of Papers of the American Chemical Society* **1999**, *218*, U315.

(116) Lehmann, C. S.; Ram, N. B.; Irimia, D.; Janssen, M. H. M. *Faraday Discussions* **2011**, *153*, 173.

(117) Mayer, P. M.; Staedter, D.; Blanchet, V.; Hemberger, P.; Bodi, A. *Journal of Physical Chemistry A* **2013**, *117*, 2753.

(118) Rijs, A. M.; Janssen, M. H. M.; Chrysostom, E. T. H.; Hayden, C. C. *Physical Review Letters* **2004**, *92*, 123002.

(119) Stert, V.; Radloff, W.; Schulz, C. P.; Hertel, I. V. *European Physical Journal D* **1999**, *5*, 97.

(120) Vredenborg, A.; Roeterdink, W. G.; Janssen, M. H. M. *Journal of Chemical Physics* **2008**, *128*, 204311.

(121) Asfandiarov, N. L.; Pshenichnyuk, S. A.; Fokin, A. I.; Nafikova, E. P. *Chemical Physics* **2004**, *298*, 263.

(122) Allan, M. *Chemical Physics* **1983**, *81*, 235.

(123) Xu, J.; Knutson, J. R. *Methods in Enzymology* **2012**, *450*, 159.

(124) Chosrowjan, H.; Taniguchi, S.; Tanaka, F. *The FEBS Journal* **2015**, *282*, 3003.

(125) Brodbelt, J. S. *Chemical Society Reviews* **2014**, *43*, 2757.

(126) Gelbart, W. M. *Annual Review of Physical Chemistry* **1977**, *28*, 323.

(127) Sato, H. *Annual Report of Progress in Chemistry Section C* **2004**, *100*, 73.

(128) Schinke, R. *Annual Review of Physical Chemistry* **1988**, *39*, 39.

(129) Dantus, M.; Rosker, M. J.; Zewail, A. H. *Journal of Chemical Physics* **1987**, *87*, 2395.

(130) Neumark, D. M. *Annual Review of Physical Chemistry* **2001**, *52*, 255.

(131) Greenblatt, B. J.; Zanni, M. T.; Neumark, D. M. *Chemical Physics Letters* **1996**, *258*, 523.

(132) Baumert, T.; Thalweiser, R.; Gerber, G. *Chemical Physics Letters* **1993**, *209*, 29.

(133) Fischer, I.; Villeneuve, D. M.; Vrakking, M. J. J.; Stolow, A. *Journal of Chemical Physics* **1995**, *102*, 5566.

(134) Fischer, I.; Vrakking, M. J. J.; Villeneuve, D. M.; Stolow, A. *Chemical Physics* **1996**, *207*, 331.

(135) Cyr, D. R.; Hayden, C. C. *Journal of Chemical Physics* **1996**, *104*, 771.

(136) Assion, A.; Geisler, M.; Helbing, J.; Seyfried, V.; Baumert, T. *Physical Review A* **1996**, *54*, R4605.

(137) Wang, L.; Kohguchi, H.; Suzuki, T. *Faraday Discussions* **1999**, *113*, 37.

(138) Schussler, H.; Navaratnam, S.; Distel, L. *Radiation Physics and Chemistry* **2005**, *73*, 163.

(139) Boudaiffa, B.; Cloutier, P.; Hunting, D.; Huels, M. A.; Sanche, L. *Science* **2000**, *287*, 1658.

(140) Hush, N. S.; Cheung, A. S. *Chemical Physics Letters* **1975**, *34*, 11.

(141) Bravaya, K. B.; Kostko, O.; Dolgikh, S.; Landau, A.; Ahmed, M.; Krylov, A. I. *Journal of Physical Chemistry A* **2010**, *114*, 12305.

(142) Colson, A. O.; Besler, B.; Close, D. M.; Sevilla, M. D. *Journal of Physical Chemistry* **1992**, *96*, 661.

(143) Simons, J. *Accounts of Chemical Research* **2006**, *39*, 772.

(144) Gu, J. D.; Xie, Y. M.; Schaefer, H. F. *Journal of the American Chemical Society* **2006**, *128*, 1250.

(145) Roca-Sanjuan, D.; Rubio, M.; Merchan, M.; Serrano-Andres, L. *Journal of Chemical Physics* **2006**, *125*.

(146) Close, D. M.; Ohman, K. T. *Journal of Physical Chemistry A* **2008**, *112*, 11207.

(147) Hendricks, J. H.; Lyapustina, S. A.; deClercq, H. L.; Snodgrass, J. T.; Bowen, K. H. *Journal of Chemical Physics* **1996**, *104*, 7788.

(148) Stokes, S. T.; Grubisic, A.; Li, X.; Ko, Y. J.; Bowen, K. H. *Journal of Chemical Physics* **2008**, *128*.

(149) Orlov, V. M.; Smirnov, A. N.; Varshavsky Ya, M. *Tetrahedron Letters* **1976**, *48*, 4377.

(150) Lin, J.; Yu, C.; Peng, S.; Akiyama, I.; Li, K.; Lee, L. K.; Lebreton, P. R. *Journal of Physical Chemistry* **1980**, *84*, 1006.

(151) Trofimov, A. B.; Schirmer, J.; Kobychev, V. B.; Potts, A. W.; Holland, D. M. P.; Karlsson, L. *Journal of Physics B-Atomic Molecular and Optical Physics* **2006**, *39*, 305.

(152) Yang, X.; Wang, X. B.; Vorpagel, E. R.; Wang, L. S. *Proceedings of the National Academy of Sciences of the United States of America* **2004**, *101*, 17588.

(153) Chatterley, A. S.; Johns, A. S.; Stavros, V. G.; Verlet, J. R. R. *Journal of Physical Chemistry A* **2013**, *117*, 5299.

(154) Desfrancois, C.; AbdoulCarime, H.; Schermann, J. P. *Journal of Chemical Physics* **1996**, *104*, 7792.

(155) Desfrancois, C.; Periquet, V.; Bouteiller, Y.; Schermann, J. P. *Journal of Physical Chemistry A* **1998**, *102*, 1274.

(156) Wesolowski, S. S.; Leininger, M. L.; Pentchev, P. N.; Schaefer, H. F. *Journal of the American Chemical Society* **2001**, *123*, 4023.

(157) Chatterley, A. S.; West, C. W.; Roberts, G. M.; Stavros, V. G.; Verlet, J. R. R. *Journal of Physical Chemistry Letters* **2014**, *5*, 843.

(158) Middleton, C. T.; de La Harpe, K.; Su, C.; Law, Y. K.; Crespo-Hernandez, C. E.; Kohler, B. In *Annual Review of Physical Chemistry*; Annual Reviews: Palo Alto, 2009; Vol. 60, p 217.

(159) Ullrich, S.; Schultz, T.; Zgierski, M. Z.; Stolow, A. *Physical Chemistry Chemical Physics* **2004**, *6*, 2796.

(160) Bisgaard, C. Z.; Satzger, H.; Ullrich, S.; Stolow, A. *Chemphyschem* **2009**, *10*, 101.

(161) Chatterley, A. S.; West, C. W.; Stavros, V. G.; Verlet, J. R. R. *Chemical Science* **2014**, *5*, 3963.

(162) Parsons, B. F.; Sheehan, S. M.; Yen, T. A.; Neumark, D. M.; Wehres, N.; Weinkauf, R. *Physical Chemistry Chemical Physics* **2007**, *9*, 3291.

(163) Yandell, M. A.; King, S. B.; Neumark, D. M. *Journal of the American Chemical Society* **2013**, *135*, 2128.

(164) Sen, A.; Dessent, C. E. H. *Journal of Physical Chemistry Letters* **2014**, *5*, 3281.

(165) Sen, A.; Dessent, C. E. H. *Journal of Chemical Physics* **2014**, *141*, 241101.

(166) Sen, A.; Luxford, T. F. M.; Yoshikawa, N.; Dessent, C. E. H. *Physical Chemistry Chemical Physics* **2014**, *16*, 15490.

(167) Ho, J.; Ervin, K. M.; Lineberger, W. C. *Journal of Chemical Physics* **1990**, *93*, 6987.

(168) Leopold, D. G.; Ho, J.; Lineberger, W. C. *Journal of Chemical Physics* **1986**, *86*, 1715.

(169) Wang, L.-M.; Wang, L.-S. *Nanoscale* **2012**, *4*, 4038.

(170) Amrein, A.; Simpson, R.; Hackett, P. *Journal of Chemical Physics* **1991**, *95*, 1781.

(171) Verlet, J. R. R.; Bragg, A. E.; Kammrath, A.; Cheshnovsky, O.; Neumark, D. M. *Journal of Chemical Physics* **2004**, *121*, 10015.

(172) Kammrath, A.; Griffin, G. B.; Verlet, J. R. R.; Young, R. M.; Neumark, D. M. *Journal of Chemical Physics* **2007**, *126*.

(173) Lippert, H.; Stert, V.; Hesse, L.; Schulz, C. P.; Hertel, I. V.; Radloff, W. *Journal of Physical Chemistry A* **2003**, *107*, 8239.

(174) Mbaiwa, F.; Wei, J.; Van Duzor, M.; Mabbs, R. *Journal of Chemical Physics* **2010**, *132*, 134304.

(175) Piani, G.; Becucci, M.; Bowen, M. S.; Oakman, J.; Hu, Q.; Continetti, R. E. *Physica Scripta* **2008**, *78*, 058110.

(176) Sanford, T.; Han, S. Y.; Thompson, M. A.; Parson, R.; Lineberger, W. C. *Journal of Chemical Physics* **2005**, *122*, 11.

(177) Zeng, Z.; Liu, C.-W.; Hou, G.-L.; Feng, G.; Xu, H.-G.; Gao, Y. Q.; Zheng, W.-J. *Journal of Physical Chemistry A* **2015**, *119*, 2845.

(178) Miller, E. M.; Sheps, L.; Lu, Y. J.; Case, A. S.; McCoy, A. B.; Lineberger, W. C. *Journal of Chemical Physics* **2012**, *136*, 7.

(179) Case, A. S.; Miller, E. M.; Martin, J. P.; Lu, Y.-J.; Sheps, L.; McCoy, A. B.; Lineberger, W. C. *Angewandte Chemie-International Edition* **2012**, *51*, 2651.

(180) Sheps, L.; Miller, E. M.; Horvath, S.; Thompson, M. A.; Parson, R.; McCoy, A. B.; Lineberger, W. C. *Science* **2010**, *328*, 220.

(181) Sheps, L.; Miller, E. M.; Lineberger, W. C. *Journal of Chemical Physics* **2009**, *131*, 8.

(182) Sheps, L.; Miller, E. M.; Horvath, S.; Thompson, M. A.; Parson, R.; McCoy, A. B.; Lineberger, W. C. *Journal of Chemical Physics* **2011**, *134*, 9.

(183) Thompson, M. A.; Martin, J. P.; Darr, J. P.; Lineberger, W. C.; Parson, R. *Journal of Chemical Physics* **2008**, *129*, 12.

(184) Crispin, X.; Marciniak, S.; Osikowicz, W.; Zotti, G.; Van der Gon, A. W. D.; Louwet, F.; Fahlman, M.; Groenendaal, L.; De Schryver, F.; Salaneck, W. R. *Journal of Polymer Science Part B-Polymer Physics* **2003**, *41*, 2561.

(185) Hare, P. M.; Crespo-Hernandez, C. E.; Kohler, B. *Proceedings of the National Academy of Sciences of the United States of America* **2007**, *104*, 435.

(186) Potts, A. W.; Price, W. C.; Streets, D. G.; Williams, T. A. *Faraday Discussions* **1972**, *54*, 168.

(187) Chewter, L. A.; Sander, M.; Mullerdethlefs, K.; Schlag, E. W. *Journal of Chemical Physics* **1987**, *86*, 4737.

(188) Ford, M.; Lindner, R.; Muller-Dethlefs, K. *Molecular Physics* **2003**, *101*, 705.

(189) Smith, J. M.; Zhang, X.; Knee, J. L. *Journal of Physical Chemistry* **1995**, *99*, 1768.

(190) Clara, M.; Hellerer, T.; Neusser, H. J. *Appl. Phys. B* **2000**, *71*, 431.

(191) Worth, G. A.; Carley, R. E.; Fielding, H. H. *Chemical Physics* **2007**, *338*, 220.

(192) Radloff, W.; Stert, V.; Freudenberg, T.; Hertel, I. V.; Jouvet, C.; Dedonder-Lardeux, C.; Solgadi, D. *Chemical Physics Letters* **1997**, *281*, 20.

(193) Minns, R. S.; Parker, D. S. N.; Penfold, T. J.; Worth, G. A.; Fielding, H. H. *Physical Chemistry Chemical Physics* **2010**, *12*, 15607.

(194) Penfold, T. J.; Spesyvtsev, R.; Kirkby, O. M.; Minns, R. S.; Parker, D. S. N.; Fielding, H. H.; Worth, G. A. *Journal of Chemical Physics* **2012**, *137*, 204310.

(195) Shen, H.; Zhang, B. *Acta Physico-Chimica Sinica* **2015**, *31*, 1662.

(196) Nunn, A. D. G.; Minns, R. S.; Spesyvtsev, R.; Bearpark, M. J.; Robb, M. A.; Fielding, H. H. *Physical Chemistry Chemical Physics* **2010**, *12*, 15751.

(197) Livingstone, R.; Schalk, O.; Boguslavskiy, A. E.; Wu, G.; Bergendahl, L. T.; Stolow, A.; Paterson, M. J.; Townsend, D. *Journal of Chemical Physics* **2011**, *135*, 194307.

(198) Zawadzki, M. M.; Thompson, J. O. F.; Burgess, E. A.; Paterson, M. J.; Townsend, D. *Physical Chemistry Chemical Physics* **2015**, *17*, 26659.

(199) Godfrey, T. J.; Yu, H.; Biddle, M. S.; Ullrich, S. *Physical Chemistry Chemical Physics* **2015**, *17*, 25197.

(200) Godfrey, T. J.; Yu, H.; Ullrich, S. *Journal of Chemical Physics* **2014**, *141*, 044314.

(201) Wren, S. W.; Vogelhuber, K. M.; Ichino, T.; Stanton, J. F.; Lineberger, W. C. *Journal of Physical Chemistry A* **2012**, *116*, 3118.

(202) Spesyvtsev, R.; Kirkby, O. M.; Fielding, H. H. *Faraday Discussions* **2012**, *157*, 165.

(203) King, G. A.; Oliver, T. A. A.; Ashfold, M. N. R. *Journal of Chemical Physics* **2010**, *132*, 214307.

(204) Roberts, G. M.; Williams, C. A.; Young, J. D.; Ullrich, S.; Paterson, M. J.; Stavros, V. G. *Journal of the American Chemical Society* **2012**, *134*, 12578.

(205) Thompson, J. O. F.; Livingstone, R. A.; Townsend, D. *Journal of Chemical Physics* **2013**, *139*, 034316.

(206) Thompson, J. O. F.; Saalbach, L.; Crane, S. W.; Paterson, M. J.; Townsend, D. *Journal of Chemical Physics* **2015**, *142*, 114309.

(207) Adachi, S.; Sato, M.; Suzuki, T. *Journal of Physical Chemistry Letters* **2015**, *6*, 343.

(208) Deb, S.; Weber, P. M. In *Annual Review of Physical Chemistry, Vol 62*; Leone, S. R., Cremer, P. S., Groves, J. T., Johnson, M. A., Eds. 2011; Vol. 62, p 19.

(209) Arruda, B. C.; Sension, R. J. *Physical Chemistry Chemical Physics* **2014**, *16*, 4439.

(210) Kobayashi, T.; Horio, T.; Suzuki, T. *Journal of Physical Chemistry A* **2015**, *119*, 9518.

Chapter 2. Experimental Set-Up

In this chapter, a general overview of the experimental procedure is presented. First, the method of producing the pulsed ion beam is discussed; the gaseous anions are produced by an electrospray ionisation source and passed into a vacuum chamber, where they are constrained by a ring electrode trap. The anions are then pulsed into a Wiley-McLaren time-of-flight mass spectrometer, allowing for mass selection of the relevant anions. The selected ions are then irradiated with a laser pulse, detaching electrons which are then detected by a velocity-map imaging apparatus coupled to an imaging detector. The PE *image is then processed by the Polar Onion Peeling algorithm in order to extract the* PE *spectrum.*

2.1 Gas-Phase Anion Photoelectron Spectroscopy

It is our aim to study the ultrafast dynamics of molecular anions via PE VMI. We must therefore consider the components required for the experiment: the production of an anion beam in vacuum, a means of producing pulses of radiation capable of ionising the anions of interest, a velocity-map imaging detector to extract the electrons and the methodology to reconstruct the PE from the experimental images. For this purpose, we employ a home-built femtosecond resolution PE imaging spectrometer, the construction of which has previously been described in detail.[1-3] The anion beam is produced by a time-of-flight mass spectrometer coupled to an electrospray ionisation source and is subsequently irradiated by pulses from either a nanosecond or femtosecond laser. The detached electrons are repelled onto a series of multichannel plates and a phosphor screen that function as a position sensitive detector. Finally, the experimental image is captured by a CCD camera and reconstructed by a polar-onion-peeling image reconstruction algorithm developed by the Verlet group.

2.2 Anion Beam Machine

2.2.1 Electrospray Ionisation Source

Electrospray ionisation (ESI) is a well-established, 'soft' ionisation technique commonly utilised in mass spectrometry for producing gaseous ions,[4-6] particularly large and fragile ions such as MCAs and biomolecules. In this set up, a syringe filled with a dilute solution (~ 1 mM) of the species of interest and typically a weak proton acceptor, such as ammonia, in order to promote the production of anions in solution. The solution is then pumped steadily (~ 200 μL/hr) by a syringe pump (World Precision Instrument, Aladdin 100) through a needle tip held at a high voltage (~–3 kV) to produce a Taylor cone of solution, which breaks down to form an aerosol spray of micro-droplets of solution, as described in section 1.3.2.

The needle tip is held ~ 10 mm from the tip of a steel capillary (held at ~–70 V) which serves as an entrance into the vacuum chamber. The high voltage on the ESI needle and a pinhole in the vacuum chamber (held at ~–45 V) forms a potential gradient, down which the anions are directed. This provides the passage for the anions from atmosphere to our time-of-flight mass spectrometer.

2.2.2 Vacuum Chamber

The schematic of the vacuum chamber is shown in Figure 2.1. The ions generated by ESI are passed into the vacuum chamber, which is divided into six differentially pumped regions. Region 1 is open to atmosphere through the steel capillary and serves as the entrance to the chamber. Region 2 contains the ion trap used to convert the continuous ESI ion source into pulsed ion packets. Region 3 contains the Wiley-McLaren type time-of-flight mass spectrometer electrodes,[7] while regions 4 and 5 each contain a set of *x-y* deflectors and an Einzel lens to guide the ion packets. The

final region, region 6, contains the VMI set-up and the ion detector for the mass spectrometer.

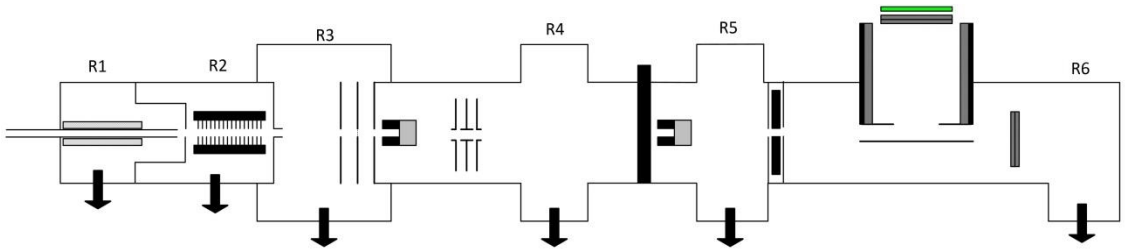

Figure 2.1 Design schematic of the mass spectrometer region of the experiment, with the six separate regions identified. Arrows indicate outlets to vacuum pumps. Adapted from reference 1.

The steel capillary (~25 cm) delivers the gaseous ions into region 1 (Pressure ≈ 1.2 torr). The end of the capillary is held ~4 mm from a metal plate held at ~–44 V. The metal plate has a pinhole, 1 mm in diameter, in the centre and serves as the passage between regions 1 and 2 (Pressure ≈ 10^{-3} torr). The capillary and the pinhole are slightly offset. This prevents the flow of neutral atmospheric molecules directly from atmosphere, through the machine and into the high vacuum region.

Attached to the opposite side of the pinhole is a radio-frequency ring-electrode ion trap. The trap consists of 33 steel electrodes spaced 2.5 mm apart, with a potential gradient applied between the first and penultimate electrodes. A radio-frequency voltage is also applied to the electrodes, phase-separated by a series of capacitors in order to prevent ions deviating from the path of travel. The final electrode is held at a higher voltage, creating a potential well in which the ions collect, losing kinetic energy through collisions with residual gas molecules. This ion trapping mechanism is based upon the Paul trapping phenomenon,[8] although our trap only constrains ions in the planes of the electrodes by this mechanism. The ions are constrained longitudinally by the ‘end cap’ voltage on the final electrode providing a potential barrier. To release the ions, the final electrode is switched to a higher voltage, to allow for the trapped ions to pass into the time-of-flight electrodes. The timing of this pulse is set relative to the time-of flight

electrodes. This switch reverses the potential gradient and allows the ions to proceed down the new potential gradient and out of the trap. The entrance between region 2 and 3 consists of 2 pinholes: one held at the voltage of the final electrode and one at ground. This arrangement forms a lens, collimating the ion packet into the time-of-flight electrodes. The voltages on and the timing of the trap are dependent upon the system of interest, but the trap is typically pulsed between 8 and 15 μs before firing the time-of-flight electrodes.

Regions 3-5 (~10^{-5}-10^{-8} torr) comprise the majority of the time-of-flight mass spectrometry region of the spectrometer. Region 3 contains 3 electrodes in an on-axis Wiley-McLaren arrangement.[7] The electrodes are steel rings and the first is held at ground to form the final point of the potential energy gradient from the ion trap. The second, the repeller, is held at –2.3 kV, 5 mm from the ground electrode. The third and final electrode, the accelerator, is held at –1.9 kV, 30 mm from the repeller electrode and with a high transmission (88 % optical transparency) steel mesh secured over the central hole. These electrodes are pulsed and timed to coincide with the arrival of the ion packet from region 2, whereupon the ions are accelerated through a pinhole to region 4 by the potential amplitude and gradient generated by the voltages on the electrodes.

Region 4 contains a set of *x*-*y* deflectors, where the *z* axis is defined by the direction of travel of the ion beam, onto which ±50 V can be applied in order to direct the ion beam through the machine and correct for any drift in the beam. These are followed by an Einzel lens, which consists of two grounded, tubular electrodes (30 mm inner diameter, 20 mm long) either side of a third electrode held at ~1.5 kV (30 mm inner diameter, 16 mm long). This acts as an electrostatic lens, the focal length of which can be adjusted by varying the voltage on the central electrode. Region 5 consists of a

time-of-flight tube, with an additional set of *x*-*y* deflectors and an Einzel lens in the same arrangement as in region 4. The purpose of the Einzel lens in this region is to tightly focus the ion beam into the interaction region in region 6.

The total time-of-flight length of the machine is 1.3 m. Region 4 and Region 5 are separated by both a pinhole and a pneumatic gatevalve, which, when closed, allows region 5 and 6, the high vacuum regions, to be isolated from the lower vacuum regions for maintenance.

Irradiation of the ion packets occurs in region 6 ($\sim 10^{-9}$ torr). Laser light enters the chamber through a CaF_2 window with the pulses timed to interact with the ion packet. The pulse exits the chamber through a second CaF_2 window, which is mounted at Brewster's angle in order to minimise reflections back into the chamber. The photodetached electrons produced are detected using a VMI set-up,[1,2,9] which is losely based upon the original design by Eppink and Parker[10] and shown in Figure 2.2. In this, the PEs are deflected into a resistive glass tube by a series of two electrodes held at a negative voltage. Both electrodes are held at the same voltage, but the bottom electrode is a solid plate, whereas the top electrode surrounds the resistive glass tube. This results in a slight gradient directed into the resistive glass tube and the spacing of the VMI electrodes has been chosen such that the electrons are focussed onto the micro-channel plates (MCP) of the detector by the electrostatic potentials. The opposite end of the resistive glass tube terminates with a pair of MCPs in a chevron arrangement to amplify the signal, and then onto a phosphor screen, the output of which is captured by a charge-coupled device. The resistive glass tube is grounded to create a potential gradient along the entirety of the VMI set-up.

In order to reduce noise in the experiment, the MCPs are pulsed and triggered to coincide with the irradiation of the ion packet. The main source of noise in the

instrument arises when the laser wavelength exceeds the work function of the steel of the instrument. Any scattered laser light that strikes the steel surface will then liberate a large number of PEs, which may be detected by the VMI set-up.

The VMI electrodes are made of mu-metal, which has very low magnetic permittivity, in order to minimise the effect of external magnetic fields on the imaging. The voltages on the electrodes varied significantly depending on the experiment, but a typical operating voltage was –500 V. The MCPs were typically operated at 0.7 kV across each and the phosphor screen was typically operated at 4.5 kV. The VMI detector is mounted perpendicularly to both the ion beam and the laser beam.

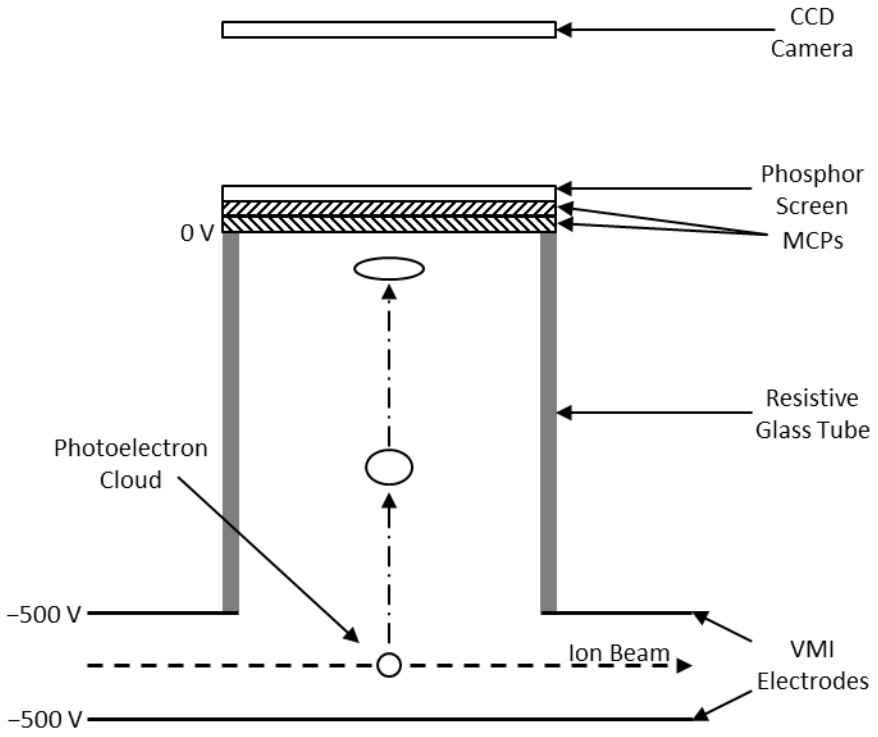

Figure 2.2 Schematic diagram of the VMI setup.

Finally, the ion detection MCP is mounted horizontally behind and in the opposing direction to the VMI spectrometer. This MCP is held at 2.2 kV and designed to optimise total signal output, as opposed to the imaging MCPs which are optimised for spatial resolution. The ion beam is directed onto this MCP by an electrode held at ~2

kV. The output is then passed to an oscilloscope triggered by the pulsing of the time-of-flight plates, which allows the mass spectrum of the ion beam to be recorded.

2.3 Calibration

The VMI set-up is calibrated by measurement of the well-known photodetachment spectrum of I^-. I^- is an atomic ion and so the peaks produced from photodetachment are extremely sharp and limited by the bandwidth of the detachment laser pulse. The detachment process can be summarised as:

$$I^-\left(^2S_0\right) + h\upsilon \rightarrow I\left(^2P_{3/2}\right) + e^- \qquad (2.1)$$

$$I^-\left(^2S_0\right) + h\upsilon \rightarrow I\left(^2P_{1/2}\right) + e^- \qquad (2.2)$$

$^2P_{3/2}$ and $^2P_{1/2}$ represent the two spin orbit states of atomic I. Both may be produced following photodetachment of I^- and are separated by 0.942648 eV due to spin-orbit splitting.[11] The $^2P_{3/2}$ is the lower energy configuration and has a vertical detachment energy of 3.059038 eV.[11-14] Therefore, a PE spectrum taken at a wavelength of less than 310 nm (4 eV) will yield a PE spectrum consisting of two peaks. The electron kinetic energy scales as R^2, where R is the number of pixels from the centre of the PE spectrum. The spectrum can then be fitted to two Gaussian distributions separated by the spin-orbit splitting of iodine in order to yield an energy scale of cR^2, where c is a calibration factor. From this, the resolution of the spectrometer has been determined to be $\Delta E/E$ = 5%.

2.4 Image Reconstruction

As the 3D electron cloud is 'flattened' onto the MCP plates to create 2D images, it is necessary to perform further analysis upon the collected images in order to extract the true PE momentum distribution. This is performed using the Polar Onion Peeling

algorithm (POP) developed by the Verlet group,[15] which is based upon 'onion-peeling'[16] and a basis-set expansion[17] in polar co-ordinates.

In our PE images, we collect the velocity vectors in the *x* and *y* plane. However, the PE velocities are described by vectors in the *x*, *y* and *z* axes. Hence at each point in our image we collect PEs with a certain velocity in the *xy* plane but are unable to determine the velocity in the *z* direction. We therefore wish to extract the *xy* plane of the PE cloud where the velocity in the *z* direction is zero and so the true velocity of the PE can be extracted from the image. The POP algorithm works on the assumption that this distribution is given by the outermost ring of the PE image. The image is converted into polar coordinates and the outermost ring is fitted to the equation:

$$I(\theta) = N\left(1 + \frac{\beta_2(3\cos^2\theta - 1)}{2}\right), \qquad (2.3)$$

where θ is the angle between the velocity vector of the outgoing PE and the polarisation vector of the light, $\boldsymbol{\varepsilon}$, which is the *y* axis in our experimental images, β_2 is an anisotropy parameter which spans from +2 to –1 for a $\cos^2\theta$ or $\sin^2\theta$ distribution, respectively, and *N* is a normalisation factor. This accounts for any PE anisotropy in the *xy* plane observed in the images. This 2D distribution is then used to recover the 3D distribution of the PE cloud (the basis-set expansion[17]), which is subsequently subtracted from the PE image. The process is then repeated for incrementally decreasing radii for the width of the PE image (onion-peeling[16]). The intensity of the PE image at each radial distance from the centre of the image gives the PE spectrum. An advantage of POP is that the program allows for negative intensity of PEs. Obviously, this is unphysical, but can be exploited for data analysis of time-resolved PE studies, as it can be used to indicate PE intensity from one feature feeding into a second. This will be discussed further in Chapter 3.

2.5 Ultrafast Laser Pulse Generation and Wavelength Variability

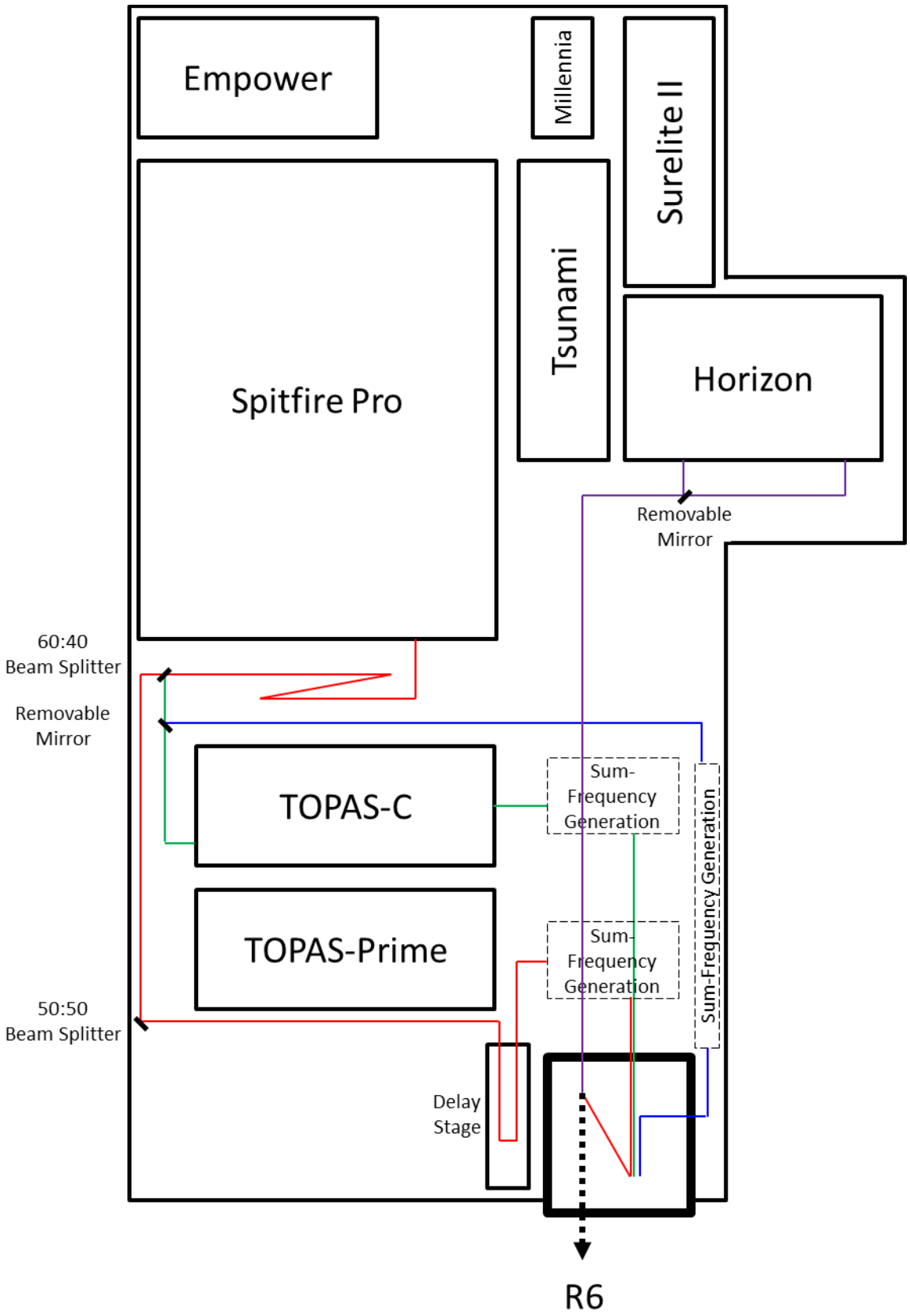

Figure 2.3 Schematic diagram of the Laser Table.

Over the course of this thesis, a variety of lasers, wavelengths and pulse durations were employed. A schematic diagram of our laser table, detailing the systems used and how the laser beam was directed into the interaction region of the anion beam machine, is presented in Figure 2.3. In order to investigate ultrafast dynamics on the femtosecond scale by PE spectroscopy, it is necessary to employ a laser system capable of operating on these timescales. For this purpose, we utilise a femtosecond Titanium:Sapphire oscillator coupled to a regenerative chirped pulse amplifier to generate pulses of 800 nm with a pulse width of ~35 fs duration.

The initial pulse is generated by a mode-locked Spectra Physics "Tsunami" Ti:Sapphire oscillator, which is pumped by the second harmonic (532 nm) of a 5 W Spectra Physics "Millennia" continuous wave Nd:YAG laser. This produces ~35 fs pulses of the Ti:Sapphire fundamental (800 nm) at a repetition rate of ~76 MHz with a power of 0.5 W. This output is then used to seed a Spectra Physics "Spitfire Pro XP" regenerative chirped pulse amplifier; a Ti:Sapphire crystal in the amplifier is pumped by the second harmonic (527 nm) of a 30 W Spectra Physics "Empower" pulsed Nd:YLF laser. A pulse from the seed laser is selected every millisecond by a series of Pockels' cells to stimulate emission from the crystal, enhancing the output power to 3W.

The output beam of the Spitfire XP Pro is initially split by a 60:40 beam splitter. 40% of the beam is used for one of two purposes: It may be used to pump a Light Conversion TOPAS-C optical parametric amplifier, which produces laser light of wavelengths between 1140 nm - 2600 nm. This may be achieved through non-linear splitting of a small percentage of the pump beam into two separate wavelengths. This can subsequently be used for sum frequency generation with the pump beam through use of a β-barium borate (BBO) crystal. Alternately, the 800 nm beam may be directed into the machine as a secondary harmonic generation line. The remaining 60% of the

output of the amplifier is passed through a second 50:50 beam splitter, where half of the output beam is removed for use in another experiment. This line is passed through a retroreflector mounted upon a Physik Instrumente delay stage, which is computer controlled and used to generate the various delays used in time-resolved experiments, and into a home-built harmonic generation stage. This stage can be used to produce wavelengths of 400 nm, 266 nm and 200 nm through harmonic generations in BBO crystals. Both lines converge on a raised stage where the beams are recombined through the use of dichroic mirrors. The combined pulse train is subsequently directed into region 6 of the anion beam machine through a CaF_2 window in order to interact with the ion packets and liberate PEs.

Additionally, we also employ a nanosecond system which may produce a wide range of wavelengths (190 nm - 2700 nm). In this, a "Continuum Surelite II" Q-switched Nd:YAG laser is coupled to a "Continuum Horizon" OPO. The OPO works on the same principle as TOPAS-C, in that part of the pump beam undergoes non-linear splitting to produce both a 'signal' and 'idler' beam (the sum of the two wavelengths will recover the wavelength of the pump beam), which can then be combined with the pump beam through sum-frequency generation. Through this, the system is capable of producing pulses of tunable wavelength of up to 50 mJ for UV wavelengths (190 nm – 400 nm) and 130 mJ for the signal/idler wavelengths (400 nm – 2700 nm) at peak efficiency. The pulses produced are ~ 6 ns in length, so cannot be usefully combined or used with the output of the femtosecond laser. The nanosecond laser is therefore primarily employed for single photon experiments.

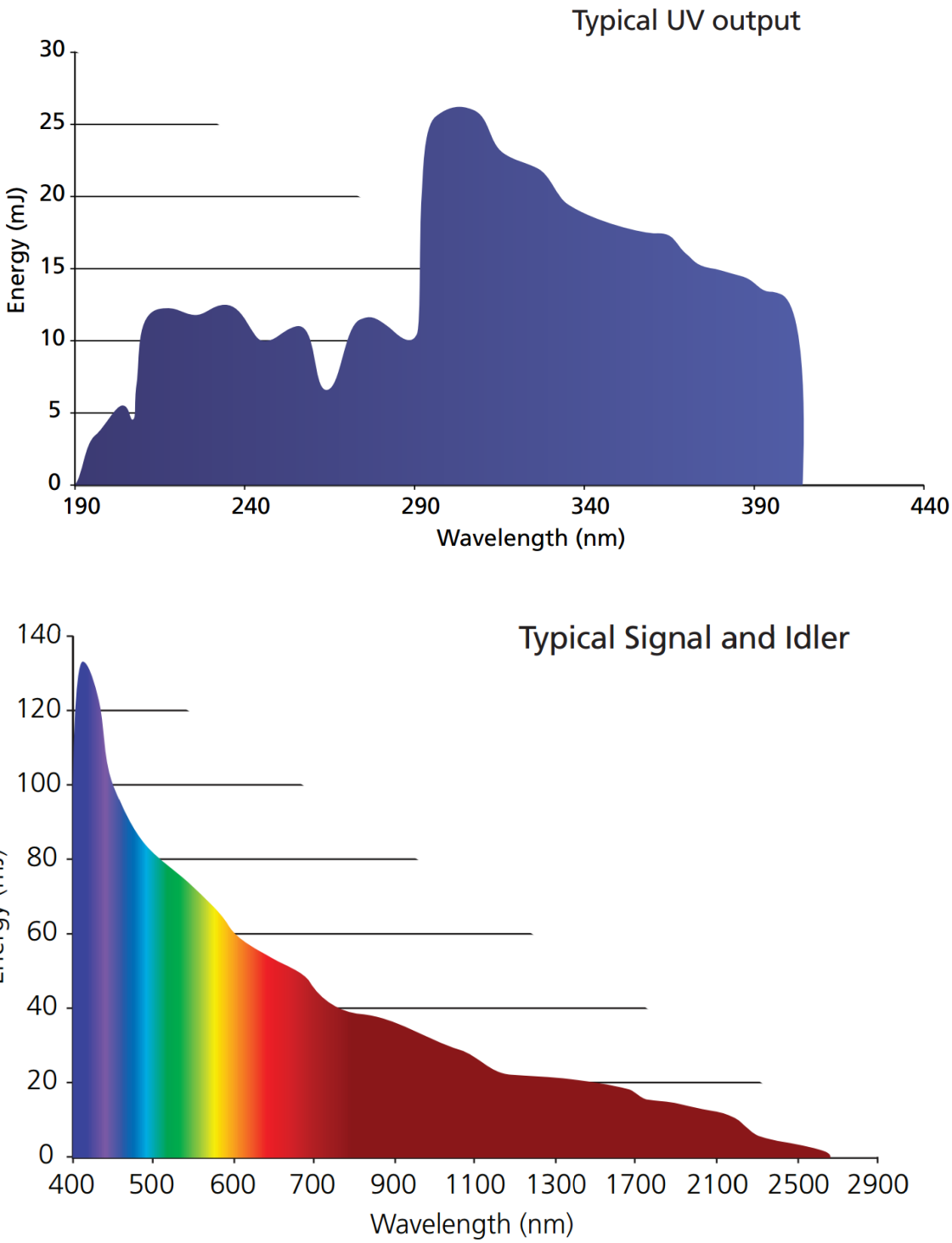

Figure 2.4 Typical performance of the Horizon OPO using a P800 pump laser. Reproduced from Continuumlasers.com.[18]

The OPO has two ports through which the laser pulse is emitted, one for the signal/idler wavelengths and another for the UV wavelengths. A prism is fixed in front of each port to direct the beam into a periscope and subsequently into the interaction

region in region 6. In order to maintain a single beam path into the interaction region, the prism in front of the UV port (the closest to the periscope) is mounted on a removable magnetic stage, so as not to block the beam path from the signal/idler port.

2.6 References

(1) Roberts, G. M. Development and Construction of an new photoelectron Imaging Spectrometer for Studying the Spectroscopy and Ultrafast Dynamics of Molecular Anions, PhD Thesis, Durham University, 2010.

(2) Lecointre, J.; Roberts, G. M.; Horke, D. A.; Verlet, J. R. R. *Journal of Physical Chemistry A* **2010**, *114*, 11216.

(3) Horke, D. A.; Verlet, J. R. R. *Physical Chemistry Chemical Physics* **2011**, *13*, 19546.

(4) Hines, R. L. *Journal of Applied Physics* **1966**, *37*, 2730.

(5) Fenn, J. B.; Mann, M.; Meng, C. K.; Wong, S. F.; Whitehouse, C. M. *Science* **1989**, *246*, 64.

(6) Fenn, J. B.; Mann, M.; Meng, C. K.; Wong, S. F.; Whitehouse, C. M. *Mass Spectrometry Reviews* **1990**, *9*, 37.

(7) Wiley, W. C.; McLaren, I. H. *Review of Scientific Instruments* **1955**, *26*, 1150.

(8) Paul, W.; Steinwedel, H. *Zeitschrift Fur Naturforschung Section a-a Journal of Physical Sciences* **1953**, *8*, 448.

(9) Horke, D. A.; Roberts, G. M.; Lecointre, J.; Verlet, J. R. R. *Review of Scientific Instruments* **2012**, *83*, 063101.

(10) Eppink, A.; Parker, D. H. *Review of Scientific Instruments* **1997**, *68*, 3477.

(11) Piani, G.; Becucci, M.; Bowen, M. S.; Oakman, J.; Hu, Q.; Continetti, R. E. *Physica Scripta* **2008**, *78*, 058110.

(12) Peláez, R. J.; Blondel, C.; Delsart, C.; Drag, D. *Journal of Physics B: Atomic, Molecular and Optical Physics* **2009**, *42*, 125001.

(13) Hanstorp, D.; Gustafsson, M. *Journal of Physics B: Atomic, Molecular and Optical Physics* **1992**, *25*, 1773.

(14) Berry, R. S.; Reimann, C. W. *Journal of Chemical Physics* **1963**, *38*, 1540.

(15) Roberts, G. M.; Nixon, J. L.; Lecointre, J.; Wrede, E.; Verlet, J. R. R. *Review of Scientific Instruments* **2009**, *80*, 053104.

(16) Zhao, K.; Colvin, T.; Hill, W. T.; Zhang, G. *Review of Scientific Instruments* **2002**, *75*, 3044.

(17) Garcia, G. A.; Nahon, L.; Powis, I. *Review of Scientific Instruments* **2004**, *75*, 4989.

(18) In *Horizon OPO Datasheet*,*http://www.continuumlasers.com/images/stories/products/specifications/Tunable_Lasers/Horizon_OPO_revF.pdf* 2015, (2015)

Chapter 3. Extracting Dynamical Information from Raw Velocity Map Images through Global Kinetic Fitting

In this chapter, an adaptaion of the global kinetic fit of a time-resolved PE *image series to a series of first order kinetic profiles convoluted with an Gaussian distribution is presented. The method performs a least-squared fit to the time-resolved* PE *velocity map images using physically modelled concentration profiles to describe the time-behaviour. The reconstruction of the central slice of the* PE *cloud is then performed on the fitted* PE *images for each species. In this fashion, the anisotropy of the* PE *features is conserved, allowing for the direct observation and fitting of time-resolved anisotropy. In order to test the fitting regime, real and simulated datasets are fitted by the new program and compared to the traditional global kinetic fit of the spectra. The global kinetic fit of a time-resolved* PE *image series is found to perform far better than the traditional fit to the spectra when dealing with low intensity datasets with overlapping features with differing anisotropies.*

3.1 Introduction

Since its inception,[1,2] VMI of the charged particles produced following irradiation of neutrals and ions by laser pulses has become a widely employed, efficient and accurate tool in investigating the electronic structure of molecules. In addition to a near 100% efficiency and the ability to detect particles emitted with 0 eV kinetic energy, VMI also allows for the detection of the photo-angular distribution of the emitted particles, providing further information about the electronic structure of the molecule and has therefore become a common detection method for PE spectroscopy.[3-20] The application of VMI to time-resolved pump-probe experiments was first demonstrated by Wang *et al.*[20] and has become a widespread, if not the norm,

detection method for charged particle excited state dynamics experiments in the gas phase.[3-5,13,18-21]

The data analysis procedure for recovering the dynamical information is fairly constant across the field: first, the central slice of the 3D cloud of charged particles projected onto the 2D detector is reconstructed. Numerous programs are available to perform this function, through either an inverse Abel transform,[22] such as employed by pBASEX,[23] or through polar onion-peeling.[24] This recovers the velocity distribution of the detected particles with respect to the radius of the detector. The time-resolved pump-probe signal is recovered by subtracting a background spectrum, typically a spectrum taken at a long negative time delay where no pump-probe signal can reasonably be expected, from the experimental spectra during this process. The resultant spectra are then analysed to extract the exponential decay lifetimes of the signal. Several methods of extracting these factors exist, but all depend on the assumption that the total integrated signal of the time-resolved spectra at any time delay can be described by a linear combination of a series of concentration profiles and that the contribution of each profile can be described by an exponential decay. Examples of such methods include fitting the total integrated signal to a series of exponent decays or principal component analysis or global kinetic fitting of the spectra, and the method chosen is strongly dependent upon the specific experiment. The order of this analysis, however, is the subject of almost no debate.

Although widespread, this procedure exhibits some drawbacks. For instance, through reconstructing the central slice of the charged particle cloud through POP,[24] the final analysis of the data considers only a fraction of the recorded hits on the detector. In addition, while the PE anisotropy parameters, β_2, may be extracted from the time-resolved images and fitted in a similar fashion to the PE spectra, only the overall

anisotropy of the image can be considered, rather than the anisotropy of the constituent features. It is almost impossible to extract information about the photo-angular distributions of the fitted concentration profiles. These issues are a result of the large amount of processing that the spectra must undergo before extracting the time constants. Most of these issues may be circumvented by simply performing the analysis on the VMI images before reconstruction of the central slice. It is therefore advantageous to develop a fitting technique that is capable of performing a global kinetic fit on a series of unprocessed VM images and to compare the results to a 'traditional' global fit of the extracted spectra.

3.2 Methodology

In a global kinetic fit, all points in *eKE* in the time-resolved spectra are simultaneously fitted to a series of time constants for a sum of *i* exponential decays:

$$S(eKE,t) = \sum_i S_i(eKE,t) = \sum_i G(t) \otimes k_i(eKE) e^{\frac{-(t-t_0)}{\tau_i}} \qquad (3.1)$$

where $k_i(eKE)$ is the decay associated spectrum (DAS) corresponding to the exponential decay with the lifetime τ_i, t_0 is the position of temporal overlap between the pump and probe pulses and $G(t)$ is the Gaussian instrument response function. In our previous data analysis,[25-28] the Levenberg-Marquardt algorithm was used to minimize the sum of the least squares between the experimental spectra and the fit, $S(eKE,t)$ in the MatLab optimization toolbox. It is facile to employ this algorithm in order to fit a series of images; one simply replaces the spectra with the experimental images. The difficulty arises from the size of the datasets. In order to fit a time-resolved spectrum, it is necessary to fit each individual lifetime to a DAS which is the length of the experimental spectrum. Therefore, in order to fit a series of images, it is necessary to fit each lifetime to a DAS with the same number of elements as the images. In our

experiment, the number of pixels in the images are 3 orders of magnitude larger than the number of elements in the spectra, resulting in the memory requirements for a nonlinear least-squares optimization becoming unfeasibly large due to the need to calculate a covarience matrix for a ~160000 parameter fit. In order to circumvent this issue, we removed the DAS from our fitting variables and instead only fit the time constants that define the decay curves. The DAS are determined through a *linear* least-squares solution of the matrix equation (equivalent to equation (3.1)):

$$\mathbf{E} = \mathbf{KC} \qquad (3.2)$$

where **E** is the known experimental time-resolved image series (each image compressed into a column), **K** is an unknown matrix with columns containing k_i, and **C** is the known trial decay curves (each curve as a row), determined by the fitting parameters. The solution to equation (3.2) is unambigous and quickly calculated.

In order to assess the applicability of our fitting procedure, we first compared the global kinetic fits on the time-resolved spectra and unprocessed images of the PE spectra of 2'-deoxyadenosine 5'-monophosphate (dAMP) taken using a pump wavelength of 4.66 eV (266 nm) and a probe wavelength of 3.10 eV (400 nm).[26] We then generated a series of datasets which featured overlapping features with differing anisotropies and lifetimes in extremely low count rates in order to simulate an extreme experimental dataset. Both the experimental spectra and DAS from the image fitting were generated by the Polar onion-peeling algorithm.[24]

3.3 Kinetic Fit of the dAMP⁻ Dataset

Figure 3.1 shows the results of the global kinetic fit of the time-resolved image series of dAMP⁻. The fitted integrated PE signal gives a reasonable fit to the experimental data and, crucially, is almost identical to the fits obtained from the global

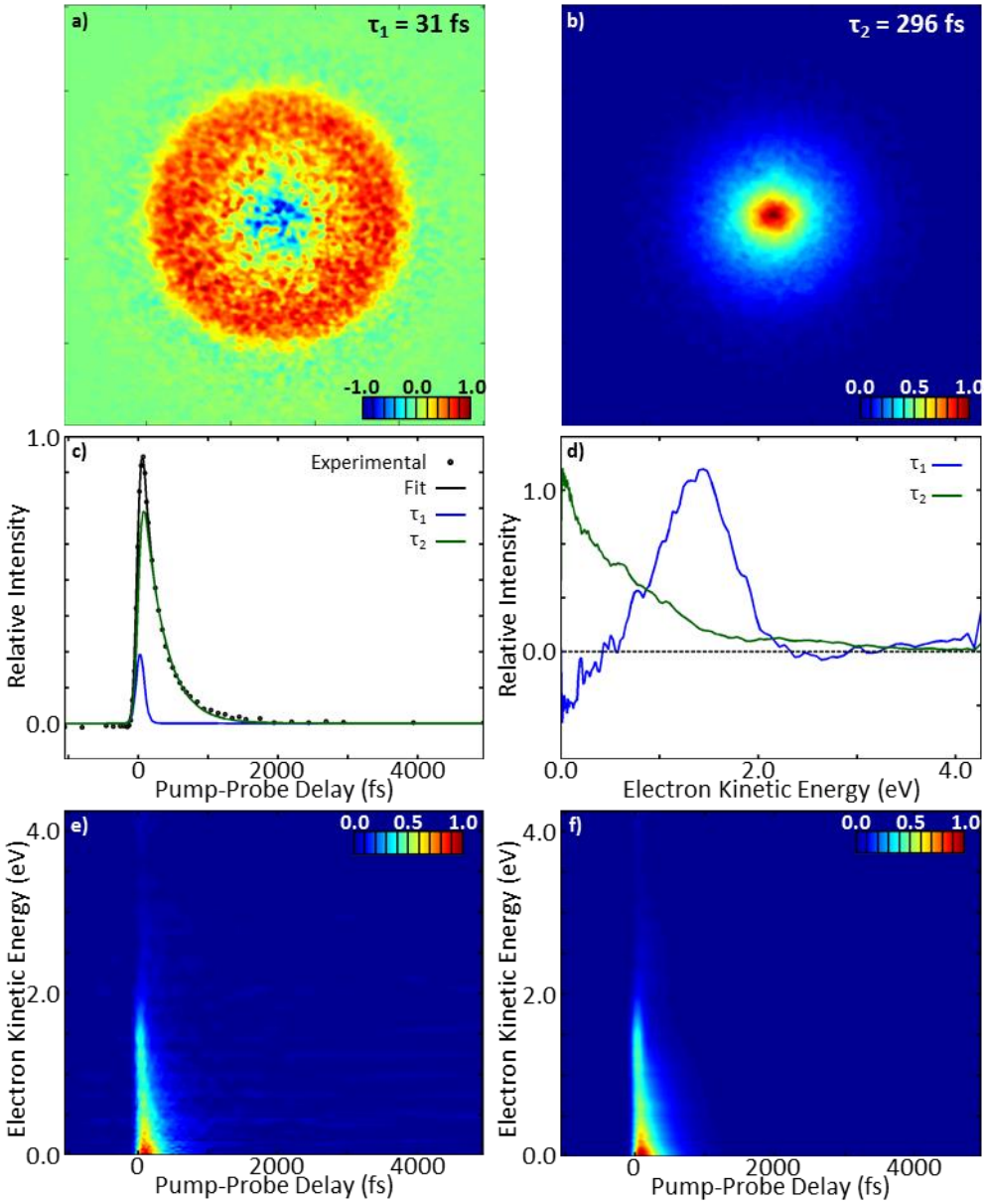

Figure 3.1 The results of the global kinetic fit of the time-resolved image series of $dAMP^-$. a-b) The normalised images associated with the decay lifetimes τ_1 = 31 fs and τ_2 = 296 fs respectively. c) The integrated time-resolved PE signal (black dots), the fit to the experimental data (black line) and the relative contributions from the decay lifetimes, $S_i(eKE, t)$. d) The decay associated spectra obtained from POP analysis of the decay associated images. e-f) The background subtracted and normalised time-resolved PE spectrum and the obtained fit to the spectrum respectively.

kinetic fit of the time-resolved spectrum. The values for τ_1 are 28 fs and 31 fs and for τ_2 are 288 fs and 296 fs for the global fit of the time-resolved spectra and images respectively, and are therefore well within the estimated ~40 fs time resolution for this

experiment, indicating that the image fitting model works at least equivalently well as the spectrum fitting model.

Of particular significance are the fitted time-resolved PE spectrum and the DAS; although the DAS in the global kinetic fit of the images are extracted from the decay associated images (DAI) by deconvolution via the POP program, the DAS are essentially identical to those obtained from the fit of the time-resolved spectra. This then allows for the reconstruction of the time-resolved PE spectrum to give a reasonable fit of the experimental data. This shows unequivocally that the program is able to resolve overlapping PE features with different lifetimes from the time-resolved images, which should allow us to resolve anisotropy within the DAI.

It is important to note that the DAS for τ_1 becomes negative at low *eKE*. We have previously assigned this to the population associated with τ_1 feeding into the population associated with τ_2. This means that the DAS cannot be directly assigned to features in the PE spectrum, as they describe concentrations at a point that can be reconstructed to form our fit, but which have no physical meaning. However, we can adjust our kinetic model to account for the consecutive dynamics:

$$S(eKE,t) = \left(G(t) \otimes k_1(eKE) \times e^{\frac{-(t-t_0)}{\tau_1}} \right) + \left(G(t) \otimes k_{2'}(eKE) \times \left(\frac{{\tau_1}^{-1}}{{\tau_2}^{-1} - {\tau_1}^{-1}} \times \left(e^{\frac{-(t-t_0)}{\tau_1}} - e^{\frac{-(t-t_0)}{\tau_2}} \right) \right) \right) \quad (3.3)$$

A fit to equation (3.3) should allow for the extraction of the PE features produced by photodetachment from the populations responsible for the observed lifetimes from the time-resolved PE signal. This is crucial for the efficacy of our global kinetic image fit of a time-resolved image series, as it allows us to directly deconstruct the PE images into the constituent spectra. The results of the fit are shown in Figure 3.2.

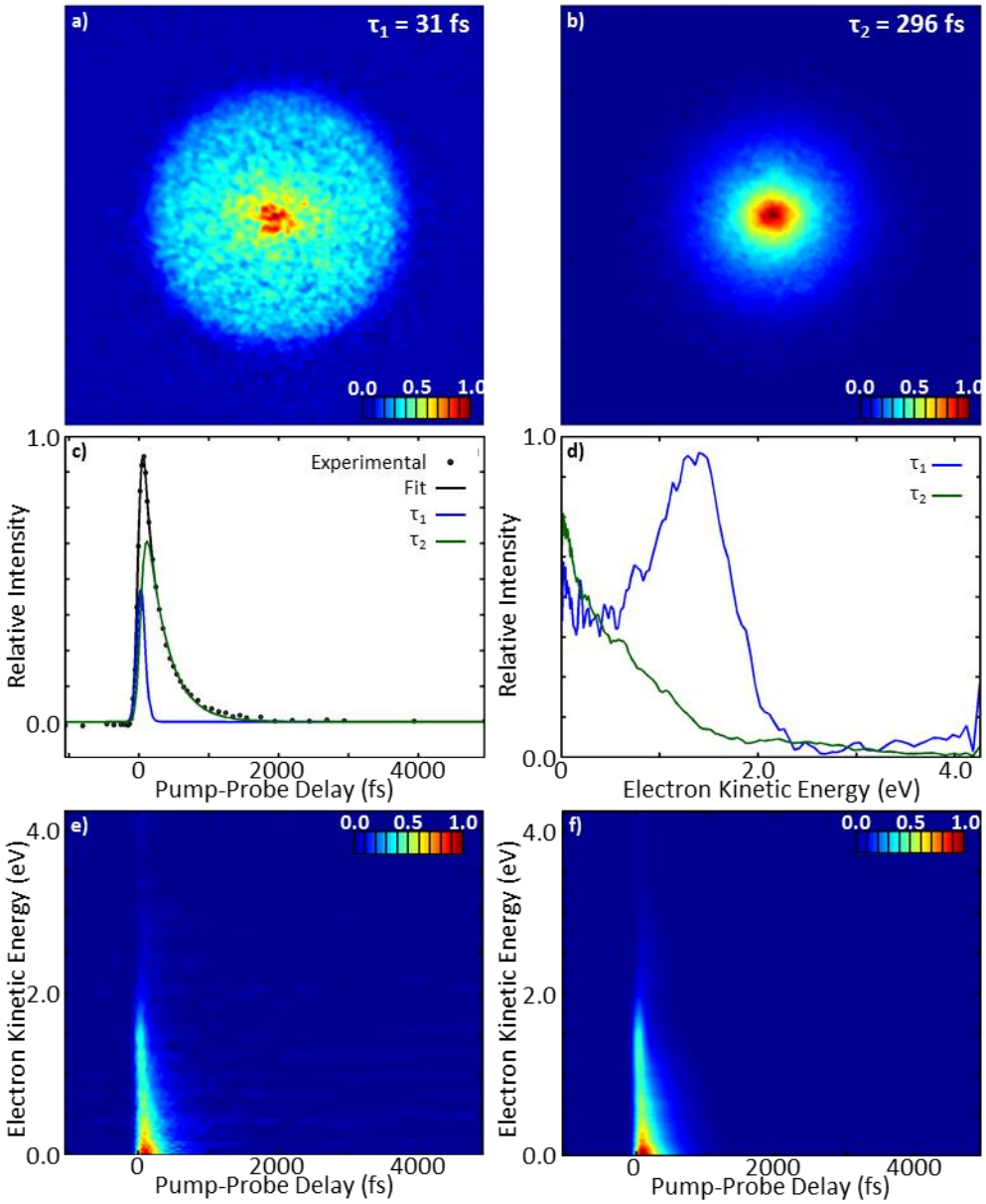

Figure 3.2 The results of the global kinetic fit of the time-resolved image series of $dAMP^-$ assuming sequential dynamics. a-b) The normalised images associated with the decay lifetimes τ_1 = 31 fs and τ_2 = 296 fs respectively. c) The integrated time-resolved PE signal (black dots), the fit to the experimental data (black line) and the relative contributions from the decay lifetimes, $S_i(eKE, t)$. d) The decay associated spectra obtained from POP analysis of the decay associated images. e-f) The background subtracted and normalised time-resolved PE spectrum and the obtained fit to the spectrum respectively.

The DAI for τ_1 has changed significantly; the DAS no longer becomes negative at low kinetic energy and instead shows a flat feature with approximately half the intensity of the peak. The contributions of the two lifetimes to the fit of the integrated total PE intensity have shifted so that the contribution of the τ_1 lifetime has increased

and the contribution from τ_2 has decreased and the peak of the curve has shifted slightly to a later time. This can be ascribed to the increase in the area of the DAS associated with τ_1 due to the loss of the negative region and the change in the kinetic model respectively. However, these appear to be the only effects of the change in the kinetic model used in the fit. The calculated lifetimes are identical to those calculated in the previous fit, as are the DAI for τ_2 and the fit to the time-resolved PE spectrum. This indicates that the results of the global kinetic fit are essentially unchanged but for the ability to extract physically meaningful images from the time-resolved image series.

3.4 Kinetic Fit of a Simulated Dataset

While the recovery of identical fitting parameters between the different fitting regimes is encouraging, the dataset is not particularly challenging to fit. In order to fully assess the relative efficacy of the differing regimes, we must consider a 'worst case scenario' dataset and attempt to recover the intrinsic dynamics. To this end, we have simulated a time-resolved PE images series with two overlapping and sequential PE features, each with a different lifetime and β_2 parameter and an extremely low PE count. We then attempted to fit the dataset using our global fitting programs and extract the orginal parameters.

The parameters chosen to generate the dataset are presented in Table 3.1. Two features, each described by a Gaussian distribution defined by the radius and σ in R space, are generated. The number of photoelectrons simulated for each feature is proportional to the amplitude, determined by the magnitude of the exponential decay curve at each time delay. Each simulated photoelectron hit on the detector is represented by a 'spot' of a given diameter in the simulated image.

Table 3.1 Parameters used in generating the simulated dataset.

Parameter	Feature 1	Feature 2
β_2	1	–0.5
Radius /Pixels	150	150
σ /Pixels	20	30
Amplitude	2000	2000
τ / fs	300	600
Instrument Response Function Full Width Half Maximum /fs		100
Spot Diameter /Pixels		5

The results of the global fit to the POP'ed time-resolved PE spectra are shown in Figure 3.3(a-b). The recovered lifetimes for τ_1 (247 fs) and τ_2 (631 fs) lie within the temporal resolution of the simulated lifetimes. The DAS for τ_2 shows a single, positive peak that appears similar to a Gaussian distribution. The DAS for τ_1, however, shows a single weak and negative feature that again can be approximated to a Gaussian distribution. This, as previously noted, can be ascribed to an exponential rise in this region of the PE spectrum. The DAS are notably noisy, which is most likely due to the poor quality of the dataset. Overall, the fit has recovered the simulated parameters reasonably well. Nevertheless, it is difficult to infer the existence of feature 1 from this fitting regime.

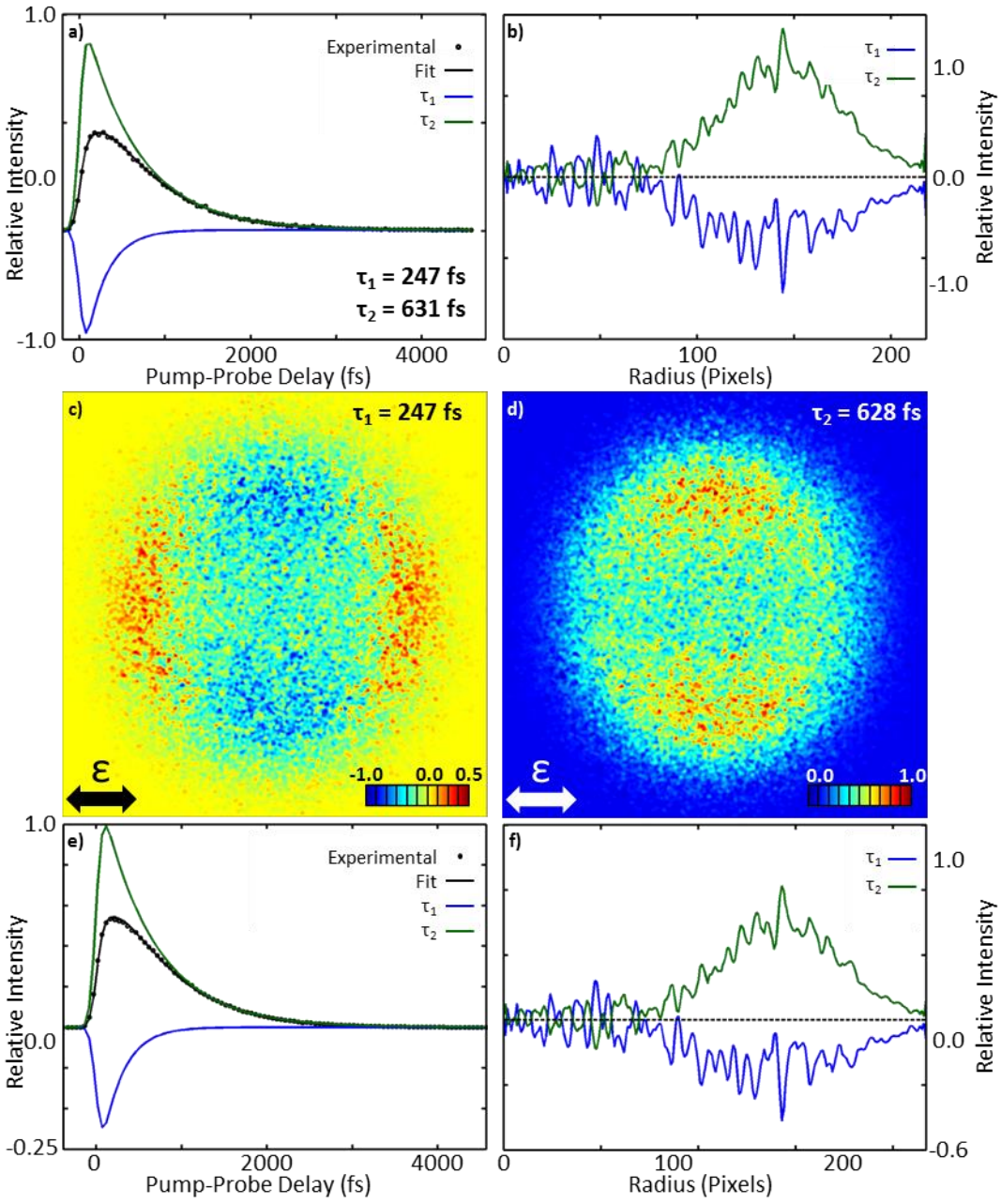

Figure 3.3 Results of the global kinetic fit to a-b) the time-resolved PE *spectra* and c-f) the time-resolved PE *images*. a) The integrated time-resolved PE signal (black circles), the fit to the simulated data (black line) and the relative contributions from the decay lifetimes, $S_i(eKE, t)$. b) The decay associated spectra. c-d) The normalised images associated with the decay lifetimes, τ_1 = 247 fs and τ_2 = 628 fs respectively. e) The integrated time-resolved PE signal (black dots), the fit to the simulated data (black line) and the relative contributions from the decay lifetimes. f) The decay associated spectra obtained from POP analysis of the decay associated images.

The results of the global fit to the time-resolved PE images are shown in Figure 3.3(c-f). It is clear from the DAI that we have been able to resolve two distinct features,

although the image associated with τ_1 shows two negative regions corresponding to the regions of maximum PE intensity in the image associated with τ_2, as we might expect to see from population from τ_1 feeding into τ_2 and reflected in the DAS as the negative region between 100-175 pixels. The DAS are almost identical to those extracted from the global kinetic fit to the POP'ed spectra. While regions of positive intenstiy are identifiable perpendicular to the negative regions and the laser polarisation, a clear positive photoelectron feature as observed in the image associated with τ_2 is not distinguishable in the decay associated image. This is likely due to the low signal levels and overlapped PE features, and we expect the image to become more resolved as we increase the number of datapoints in the spectrum. Nevertheless, one can clearly observe the existence of two PE features in the spectrum as opposed to a single PE feature exhibiting unusual dynamics. Both the extracted and set lifetimes for τ_1 (247 fs and 300 fs, respectively) and τ_2 (628 fs and 600 fs, respectively) lie within the temporal resolution of each other, and are extremely similar to the parameters extracted from the global fit to the POP'ed spectra. This implies that the program is capable of extracting the correct lifetimes and that the discrepancy between the values for τ_1 is a result of the low signal levels in the dataset and compounded by the overlapped PE features. This is to be expected; with so few 'PEs' in the images, it is likely that the experimental kinetic profiles will be incomplete, resulting in a noisy fit. This could be mitigated by smoothing the PE image series, for instance by applying a Gaussian distribution to each point. Despite these deficiencies, however, a global kinetic fit to a time-resolved image series is able to resolve overlapping features with differing time constants which cannot be resolved by a global kinetic fit of the time-resolved spectrum.

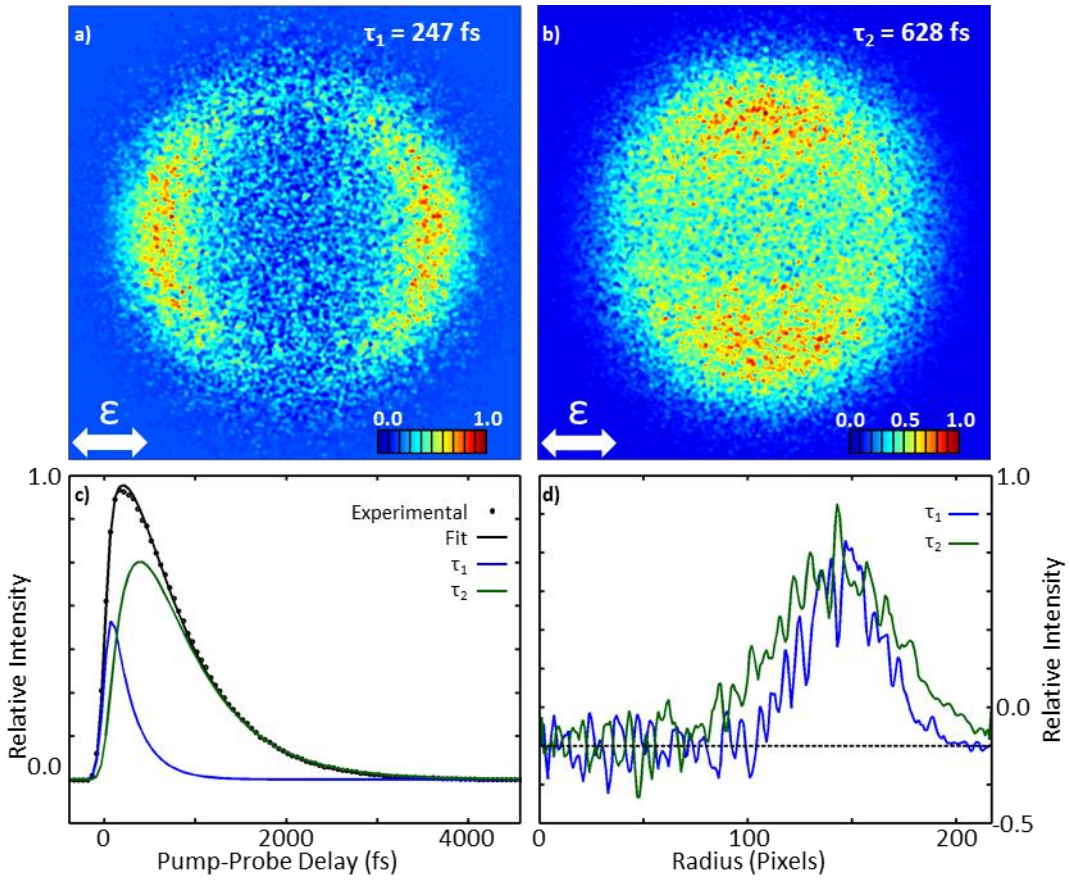

Figure 3.4 Results of the global kinetic fit to the time-resolved PE image series. a-b) The normalised images associated with the decay lifetimes, τ_1 = 247 fs and τ_2 = 628 fs respectively. c) The integrated time-resolved PE signal (black dots), the fit to the experimental data (black line) and the relative contributions from the decay lifetimes, $S_i(eKE,t)$. d) The decay associated spectra obtained from POP analysis of the decay associated images.

Figure 3.4 shows the result of a global kinetic fit of the time-resolved images assuming sequential dynamics. As demonstrated earlier, the extracted lifetimes, the DAI associated with τ_2, and the fit to the total integrated PE signal are identical to those extracted from the global kinetic fit assuming simultaneous dynamics. The DAI for τ_1 is significantly changed, however, with the loss of the pronounced negative regions corresponding to the maxima in the DAI for τ_2. However, these regions remain slightly negative and the expected positve regions corresponding to the major PE feature of the lifetime remain unresolved. Once again, we can ascribe this to the low signal level and

overlapped features. The loss of the pronounced negative regions is reflected in the relative contributions of the lifetimes to to fit of the total PE signal and in the DAS.

The relative contributions of both lifetimes to the overall fit are now both positive. The DAS are expected to be entirely positve, as, if the assignment of the negative regions in the DAI to an exponential rise in that region is correct, the change in the kinetic model is predicted to account for population from one lifetime shifting to another. The extracted DAI are indeed almost entirely positive (very few pixels show weak negative intensity, which we may assign to noise in the fit), which suggests that our previous assignments are indeed correct. The fit therefore appears to directly fit the PE features that contribute to the full time-resolved spectrum. Overall, the global fit is able to extract lifetimes of overlapping PE features in a time-resolved PE images series with reasonable accuracy and with far greater efficacy than for the time-resolved spectra.

Finally, we have generated a second simulated dataset with almost identical parameters to those in Table 3.1, but with the amplitude of the exponential decay for both features set to 100000000. The results of the global fit to the POP'ed time-resolved PE spectra and of a global kinetic fit of the time-resolved images assuming sequential dynamics are shown in Figure 3.5(a-b) and (c-f), respectively.

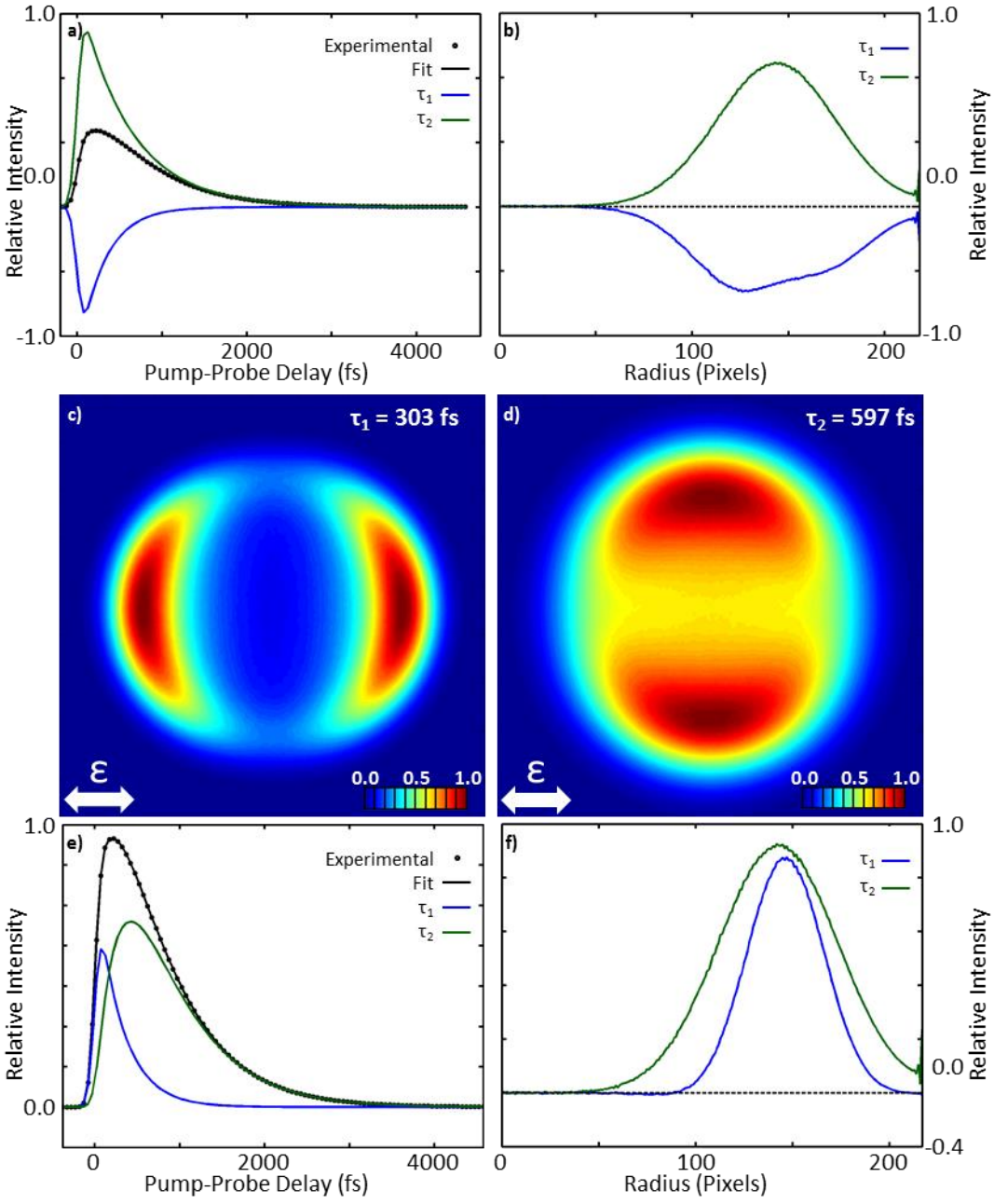

Figure 3.5 Results of the global kinetic fit to a-b) the time-resolved PE *spectra* and c-f) the time-resolved PE *images* assuming sequential dynamics. a) The integrated time-resolved PE signal (black dotss), the fit to the simulated data (black line) and the relative contributions from the decay lifetimes, $S_i(eKE, t)$. b) The decay associated spectra. c-d) The normalised images associated with the decay lifetimes, τ_1 = 303 fs and τ_2 = 597 fs respectively. e) The integrated time-resolved PE signal (black circles), the fit to the simulated data (black line) and the relative contributions from the decay lifetimes. f) The decay associated spectra obtained from POP analysis of the decay associated images.

Both global fitting regimes recovered τ_1 = 303 fs and τ_2 = 597 fs, in excellent agreement with the initial parameters. This supports our assertion that the two fitting

regimes work equally well when extracting lifetimes from high quality datasets. However, the difference between the regimes can be clearly observed in the DAS and the overall contribution of each lifetime to the overall fit. The DAS for τ_2 for both fitting regimes appear identical. For the fit to the POP'ed spectra, the DAS for τ_1 is entirely negative, which we can ascribe to an exponential rise of this feature. The contributions of both lifetimes to the overall fit are also far greater in magnitude than the overall fit and each appears to be cancelling the other out. In contrast, for the fit of the images, it is clear from the DAI that we are able to resolve the two overlapping features and recover the β_2 parameters. This is reflected in the DAS, in which we observe two large, mostly positive, Gaussian features, and in the contributions of the lifetimes to the overall fit. It is in this that the advantage of fitting to the images is highlighted; through a global kinetic fit to the images, it is possible to easily resolve overlapping photoelectron features with differing β_2 parameters and lifetimes that may not be extracted from a kinetic fit to the spectra.

3.5 Conclusions and Outlook

In conclusion, we have developed a global kinetic fitting routine that is able to fit directly to a series of time-resolved PE images. We have demonstrated this routine to be at least equivalent to a global kinetic fit to a series of time-resolved PE spectra from a good quality dataset with the additional benefit of extracting the decay associated images. We have extended this approach to account for sequential dynamics, which we have shown to give a fit that is at least equivalent to other methods and allows for the direct extraction of the contributing PE features. When tested on a poor quality dataset exhibiting overlapped PE features with differing lifetimes and β_2 parameters, the global fit of the time-resolved image series was found to return identical lifetimes to those

returned from the fit of the time-resolved spectra. However, the image fit was able to resolve highly anisotropic regions of positive intensity in the DAI for τ_1, whereas the fit of the time-resolved spectra was only able to resolve a large region of negative intensity in the DAS for τ_1. When the kinetic model to account for consecutive dynamics was introduced, it was possible to resolve the photoelectron features constituting the time-resolved spectra. The ability to retain the anisotropy in the DAI allows for the definitive identification of the photodetachment pathway associated with τ_1 that cannot be determined through a fit to the spectra and clearly demonstrates the advantages associated with retaining the angular distributions contained within the PE images when fitting the time-resolved data. These conclusions were supported by subsequent testing of the fitting regimes on a high quality dataset.

This method is applicable to any series of time-resolved velocity-map images and the challenges in the application of this method are mostly based on fitting the images to the correct dynamics. Although efforts have been made to ensure that the routine is as versatile as possible, it remains that the fitting program will need to be adapted for each image series presented to it. Additionally, the fitting routine cannot fit PE features that shift in electron kinetic energy since it violates the assumption that the experimental image can be expresssed as a linear combination of the images of a small number of species. This is a common feature of time-resoved PE spectroscopy and can significantly affect the results of a global kinetic fit, so accounting for shifting PE features can only increase the accuracy of the parameters extracted from fitting time-resolved PE spectra. Nevertheless, global kinetic fitting of time-resolved PE images remains a versatile and powerful method of extracting time constants and decay associated images from a time-resolved PE image series.

3.6 References

(1) Chandler, D. W.; Houston, P. L. *Journal of Chemical Physics* **1987**, *87*, 1445.

(2) Eppink, A. T. J. B.; Parker, D. H. *Review of Scientific Instruments* **1997**, *68*, 3477.

(3) Chatterley, A. S.; Horke, D. A.; Verlet, J. R. R. *Physical Chemistry Chemical Physics* **2014**, *16*, 489.

(4) Wang, L.-S. *Journal of Chemical Physics* **2015**, *143*, 040901.

(5) Wang, X. B.; Wang, L. S. In *Annual Review of Physical Chemistry*; Annual Reviews: Palo Alto, 2009; Vol. 60, p 105.

(6) Horke, D. A.; Roberts, G. M.; Lecointre, J.; Verlet, J. R. R. *Review of Scientific Instruments* **2012**, *83*, 063101.

(7) Eppink, A.; Parker, D. H. *Review of Scientific Instruments* **1997**, *68*, 3477.

(8) Eppink, A. T. J. B.; Parker, D. H. *Journal of Chemical Physics* **1999**, *110*, 832.

(9) Hock, C.; Kim, J. B.; Weichman, M. L.; Yacovitch, T. I.; Neumark, D. M. *Journal of Chemical Physics* **2012**, *137*, 244201.

(10) Kim, J. B.; Weichman, M. L.; Neumark, D. M. *Journal of the American Chemical Society* **2014**, *136*, 7159.

(11) Liu, Z.; Xie, H.; Qin, Z.; Fan, H.; Tang, Z. *Inorganic Chemistry* **2014**, *53*, 10909.

(12) Parker, D. H.; Eppink, A. T. J. B. *Journal of Chemical Physics* **1997**, *107*, 2357.

(13) Ashfold, M. N. R.; Nahler, N. H.; Orr-Ewing, A. J.; Vieuxmaire, O. P. J.; Toomes, R. L.; Kitsopoulos, T. N.; Garcia, I. A.; Chestakov, D. A.; Wu, S. M.; Parker, D. H. *Physical Chemistry Chemical Physics* **2006**, *8*, 26.

(14) Davies, J. A.; LeClaire, J. E.; Continetti, R. E.; Hayden, C. C. *Journal of Chemical Physics* **1999**, *111*, 1.

(15) Hayden, C. C.; Davies, J. A. *Abstracts of Papers of the American Chemical Society* **1999**, *218*, U315.

(16) Kammrath, A.; Griffin, G. B.; Verlet, J. R. R.; Young, R. M.; Neumark, D. M. *Journal of Chemical Physics* **2007**, *126*.

(17) Osterwalder, A.; Nee, M. J.; Zhou, J.; Neumark, D. M. *Journal of Chemical Physics* **2004**, *121*, 6317.

(18) Suzuki, T. *Annual Review of Physical Chemistry* **2006**, *57*, 555.

(19) Suzuki, T.; Wang, L.; Kohguchi, H. *Journal of Chemical Physics* **1999**, *111*, 4859.

(20) Wang, L.; Kohguchi, H.; Suzuki, T. *Faraday Discussions* **1999**, *113*, 37.

(21) Yandell, M. A.; King, S. B.; Neumark, D. M. *Journal of the American Chemical Society* **2013**, *135*, 2128.

(22) Whitaker, B. *Imaging in Molecular Dynamics: Technology and Applications*; Cambridge University Press: Cambridge, 2003.

(23) Garcia, G. A.; Nahon, L.; Powis, I. *Review of Scientific Instruments* **2004**, *75*, 4989.

(24) Roberts, G. M.; Nixon, J. L.; Lecointre, J.; Wrede, E.; Verlet, J. R. R. *Review of Scientific Instruments* **2009**, *80*, 053104.

(25) Chatterley, A. S.; Horke, D. A.; Verlet, J. R. R. *Physical Chemistry Chemical Physics* **2012**, *14*, 16155.

(26) Chatterley, A. S.; West, C. W.; Roberts, G. M.; Stavros, V. G.; Verlet, J. R. R. *Journal of Physical Chemistry Letters* **2014**, *5*, 843.

(27) Chatterley, A. S.; West, C. W.; Stavros, V. G.; Verlet, J. R. R. *Chemical Science* **2014**, *5*, 3963.

(28) Mooney, C. R. S.; Horke, D. A.; Chatterley, A. S.; Simperler, A.; Fielding, H. H.; Verlet, J. R. R. *Chemical Science* **2013**, *4*, 921.

Chapter 4. Exploring the Dynamics of the Model GFP Chromophore

The anionic, deprotonated form of p-hydroxybenzylidene-2,3-dimethylimidazolinone (HBDI, Figure 4.1) has been extensively employed as a model of the chromophore of the green fluorescence protein. The bright S_1 excited state of $HBDI^-$ has a measured lifetime of 1.4 ps in the gas-phase and is dominated by two non-radiative decay mechanisms: internal conversion and autodetachment into the neutral continuum. Higher excited states exist, but have not been as extensively studied. Notably, the S_2 and S_3 excited states lie ~3.7 eV and ~3.8 eV above the electronic ground state. Here, a combined frequency-, angle-, and time-resolved PE *spectroscopy study is used to unravel the excited state dynamics following photoexcitation. For the S_1 state, time-resolved* PE *spectroscopy has been used to determine the asymptotic yields of these two channels from which the lifetime for autodetachment was found to be ~30 ps. This remains approximately constant over an excitation range from 2.38 eV to 2.57 eV. Using two-photon absorption, additional evidence is provided for a decay channel corresponding to electron detachment from the S_0 ground state. Following UV excitation, the optically-bright S_3 state, which is populated for $h\nu > 3.7$ eV, is shown to decay predominantly by internal conversion to the S_2 state that in turn autodetaches to the neutral ground state. For $h\nu > 4.1$ eV, a new and favourable autodetachment channel from the S_2 state becomes available, which leads to the formation of the neutral in an excited state. The results indicate that the UV excited state dynamics of the GFP chromophore involve a number of strongly coupled excited states.*

This chapter is based upon 'Communication: Autodetachment versus Internal Conversion from the S_1 state of the isolated GFP Chromophore Anion', C. W. West, A. S. Hudson, S. L. Cobb and J. R. R. Verlet, *J. Chem. Phys.*, **139**, 071104 (2013) and 'Excited State Dynamics of the Isolated Green Fluorescent Protein Chromophore Anion

Following UV Excitation', C. W. West, J. N. Bull, A. S. Hudson, S. L. Cobb and J. R. R. Verlet, *J. Phys. Chem. B*, **119**, 3982 (2015)

4.1 Introduction

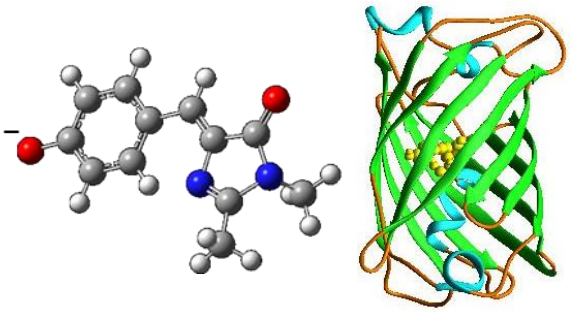

Figure 4.1 Left: structure of the *para*-hydroxybenzilidene-2,3-dimethylimidazolinone anionic model chromophore. Right: structure of the green fluorescent protein, showing the position of the chromophore (yellow). Reproduced with permission from Yang *et al.*[1]

The discovery of naturally occurring fluorescent proteins and their subsequent development into an *in vivo* biological fluorescent probe has revolutionised molecular biology over the past half-century. Specifically, the ability to insert the relevant allele into the genome of a target organism allows the organism to express the fluorescent probe both independently and incorporated onto another protein without impeding its biological function and gives rise to hitherto unparalleled locational specificity and sensitivity compared to traditional fluorescent probes.[1-7] Although several fluorescent proteins covering a broad spectral range have been discovered or developed,[6] the green fluorescent protein (GFP) was the first discovered and remains the most widely utilised. The impact of fluorescent proteins on the biological sciences was recognised by the award of the 2008 Nobel Prize in Chemistry to Shimomura, Chalfie and Tsien.[8] The molecular structure,[1] absorbance and fluorescence spectra[9-11] of GFP have been extensively studied and the origins of the remarkable optical properties traced to a chromophore enclosed deep within the β-barrel of the body of the protein, as shown in Figure 4.1.[1,12] However, due to the size of the protein shielding the chromophore

responsible for the fluorescent protein's remarkable optical properties, it has not been possible to study the chromophore directly. In order to study the chromophore, a model molecule with a similar structure must be used as a representative study.

In GFP, the chromophore is formed by an oxidative reaction between three amino acids, S65, Y66 and Y67, within the primary protein structure,[12] which is shown schematically in Figure 4.2. It is structurally similar to *para*-hydroxybenzylidene-2,3-dimethylimidazolinone and anchored within the protein by connecting groups on the imidazole subunit. Due to the importance of the chromophore to the properties of GFP and the inaccessibility of the chromophore in the protein, the photo-physical properties of HBDI have been investigated extensively.

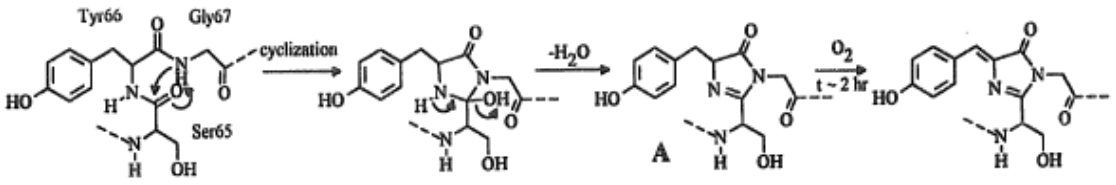

Figure 4.2 Proposed mechanism of the formation of the GFP chromophore within the primary protein structure. Adapted with permission from Cubitt *et al.*[2]

As the fluorescence of GFP has been attributed to the anionic form of the chromophore, formed by the deprotonation of a phenoxyl group,[7,9,10] most studies have focussed upon the analogous deprotonated form of the model chromophore, $HBDI^-$. There are some notable discrepancies between the properties of HBDI and the GFP chromophore; the absorption spectra of $HBDI^-$ and GFP in solution are dissimilar.[13] Additionally, in contrast to the GFP, $HBDI^-$ does not fluoresce appreciably in solution until cooled to below the glass transition temperature.[14] However, the exclusion of most solvent molecules from the environment of the chromophore by the β-barrel of the protein provides the chromophore in GFP with a pseudo-gas phase environment. As such, theoretical and experimental investigations of $HBDI^-$ have focussed upon isolated

ions. Both the absorption spectra and the $S_1 \leftarrow S_0$ transition of GFP have been found to be extremely similar to that of gas phase $HBDI^-$.[13,15] Bochenkova and Andersen have recently shown that several aspects of the $HBDI^-$ gas phase absorbance spectrum map directly onto that for the protein,[16] reaffirming the utility of $HBDI^-$ as a model chromophore. However, a recently obtained resonantly-enhanced multi-photon ionisation spectrum of the neutral form of HBDI has found that the absorption maximum is significantly blue-shifted by 0.5 eV.[17] This implies that the protein environment does have a significant impact on the electronic structure of the chromophore and that the lack of this environment can explain discrepancies between observations of the chromophore in the protein environment and of the isolated model chromophore.

Three groups have independently determined the vertical and adiabatic detachment energies (VDE and ADE, respectively) to be in the region of 2.8 eV and 2.6 eV respectively[18-20] and initially found to be higher than predicted by theoretical calculations.[21] However, recent calculations at higher levels of theory predict detachment energies consistent to those determined experimentally.[22] The excited state dynamics of $HBDI^-$ have previously been investigated by time resolved PE spectroscopy, yielding two lifetimes.[23] The first, a timescale of 300 fs has been assigned, following theoretical calculations,[23] to be motion on the excited state surface away from the Franck-Condon region and the fluorescent state geometry by a stretch along the central allyl bridge coordinate. The chromophore then undergoes a rotation about the central allyl bridge to form a twisted, non-luminescent intermediate,[23] which is inaccessible in the protein. This also explains the observed loss of fluorescence in $HBDI^-$ above the glass transition temperature.[14] The excited state then decays to the

ground state on a timescale of 1.4 ps,[23] in contrast to the long fluorescence lifetimes observed in the protein[5] but concurring with solution phase experiments.[24-26]

There are two possible pathways of decay from this excited state: PE loss to the D_0 state of the neutral species and internal conversion to a vibrationally excited S_0 state. Although the S_1 excited state is bound with respect to electron detachment, PEs may nevertheless be observed through vibrational autodetachment (AD).[18] In this process, a vibrational mode of the electronic excited allows the anion to access the geometry of the neutral molecule. In this orientation, the excited state becomes unbound, and the electron may detach and allow the molecule to form the ground state of the neutral. Bochenkova and Andersen have recently calculated the vibrational modes associated with each decay pathway and hence derived predictions of these lifetimes.[16] Previously, it has not been possible to experimentally distinguish the lifetimes of the individual decay pathways.

The decay channels by which the vibrationally excited ground electronic state may decay back to the ground state are a subject of some debate. Fragmentation of the parent ion by loss of a CH_3 radical and loss of energy by internal conversion are commonly observed and accepted. However, Horke *et al.* have also suggested thermionic electron emission from this state as a possible decay channel due to the observation of extremely low kinetic energy electrons,[20] although this assignment has been called into question.[18] Notably, the PE spectra of the two groups differ in that the 0 eV *eKE*, structured peak observed by Horke *et al.*[20] was absent in the spectra recorded by Toker *et al.*[18] Thermionic emission occurs on a far longer timescale than for most photodetachment processes (milliseconds as opposed to picoseconds),[27-31] which may explain the discrepancy. While the absorption spectra of the gas phase model chromophore and GFP may be similar, the absence of luminescence from the decay of

the excited state of $HBDI^-$ and the remarkable photostability of GFP would indicate that the decay channels of the excited states in the free chromophore and in the protein are disparate.

Forbes *et al.* have presented action spectra of $HBDI^-$ by monitoring the yield of both the parent ion and the product of the dominant fragmentation channel by mass spectrometry following excitation at various wavelengths.[32,33]The yield of the electron loss channel was inferred from the difference between the yields of the observed channels. This study showed that, while the PE and fragmentation yields were approximately equivalent for excitation wavelengths between 500 nm and 475 nm, the PE loss decay channel dominates at higher excitation energies. As fragmentation is associated with multiple photon absorption (as described in Chapter 1, page 13), this implies that excitation at these wavelengths produces a population of an excited state, from which a vibrationally hot population of the electronic ground state must be recovered. This is a pre-requisite for the observation of thermionic emission, supporting the assertions of Horke *et al.*[20]

Whilst the S_1 excited state has been the subject of the most interest, due to its contribution to the fluorescence of GFP, the higher lying excited states are far less well understood. Recently, Bochenkova *et al.* have calculated the positions and oscillator strengths of the first several excited states of $HBDI^-$ and subsequently recorded action spectra over the relevant spectral regions.[34] Although the S_2 state has an onset of ~3.7 eV, this state is has a very low oscillator strength and is therefore inaccessible by photoexcitation. The next optically-accessible excited state of the anion, which is formally the S_3 excited state, has been considered. The action spectrum of $HBDI^-$ suggests that the $S_3 \leftarrow S_0$ transition is almost as bright as the $S_1 \leftarrow S_0$ transition and has an onset of ~3.8 eV in the gas-phase.[34] Bochenkova *et al.* also highlight the potential

importance of these excited states in the photo-oxidation of GFP, as the absorption band of the S_3 state in the protein is quasi-resonant with the hydrated electron.[34] In isolation, the S_3 state is an anionic resonance and may be probed by PE spectroscopy. Mooney *et al.* have recently recorded three PE spectra with photon energies around the onset of the S_3 state, which indicate that the PE distribution broadens with increasing photon energy.[35] This spectral broadening was assigned to vibrational motion on the S_3 excited state surface, followed by autodetachment to a range of co-ordinates of the neutral D_0 state.[36]

In this work, we have employed frequency-, angle- and time-resolved PE spectroscopy in order to gain a more comprehensive understanding of the dynamics occurring both on the formally bound S_1 excited state surface and following excitation to the continuum of $HBDI^-$ around the S_3 state. We have been able to probe these dynamics in detail and hence: resolve the lifetime for electron autodetachment from the S_1 state; show that the primary dominant decay mechanism from the S_3 state is internal conversion to the S_2; and resolve the lifetimes of the S_3 and S_2 excited states following UV excitation.

4.2 Methodology

The experiments were performed as described in Chapter 2. HBDI, synthesised based broadly on published methods,[3] was provided by Alex Hudson and Dr Steven Cobb. Isolated deprotonated $HDBI^-$ anions were produced by electrospray ionisation of a ~1 mM solution of HBDI, reduced to pH 11 by the addition of NaOH or NH_3. In the frequency-resolved PE imaging experiments, laser pulses of ~6 ns duration with photon energies ranging between 2.38 eV (520 nm) to 4.39 eV (282 nm) were generated using the Horizon OPO. In the time-resolved experiments on the S_1 excited state, femtosecond

laser pulses at 2.57 eV (482 nm), 2.48 eV (500 nm) and 2.38 eV (519 nm) served as the pump and 1.55 eV (800 nm) femtosecond pulses probed the population from the S_1 excited state. In the time-resolved experiments on the S_3 and S_2 excited states, femtosecond pulses at 4.13 eV (300 nm) were used as the pump and 1.55 eV (800 nm) were used as the probe pulse. All time-resolved laser pulses were derived from a commercial femtosecond system. The 4.13 eV pump was generated by frequency doubling the 1.55 eV fundamental in a β-barium borate (BBO) crystal and combining this in a second BBO crystal with 1.03 eV (1200 nm) pulses produced by an optical parameter amplifier.

4.3 Frequency- and Angle-Resolved Photoelectron Imaging

The frequency-resolved PE spectra of $HBDI^-$ for photon energies between 2.39 eV (520 nm) and 4.39 eV (282 nm) are normalised to a maximum intensity of unity in order to highlight the changes in the PE spectra as a function of photon energy, and presented in Figure 4.3(a). However, the photo-induced detachment cross-section varies significantly over the range of photon energies. In order to highlight these variations, the action (absorption) spectra leading to "prompt" electron loss as reported in the recent study of Bochenkova *et al.*[34] is also included in Figure 4.3(a), together with their calculated energetics of relevant electronic states. In addition to the frequency-resolved PE spectra, the photoejection anisotropy parameter, β_2, which quantifies the PE angular distribution,[37] are plotted in Figure 4.3(b).

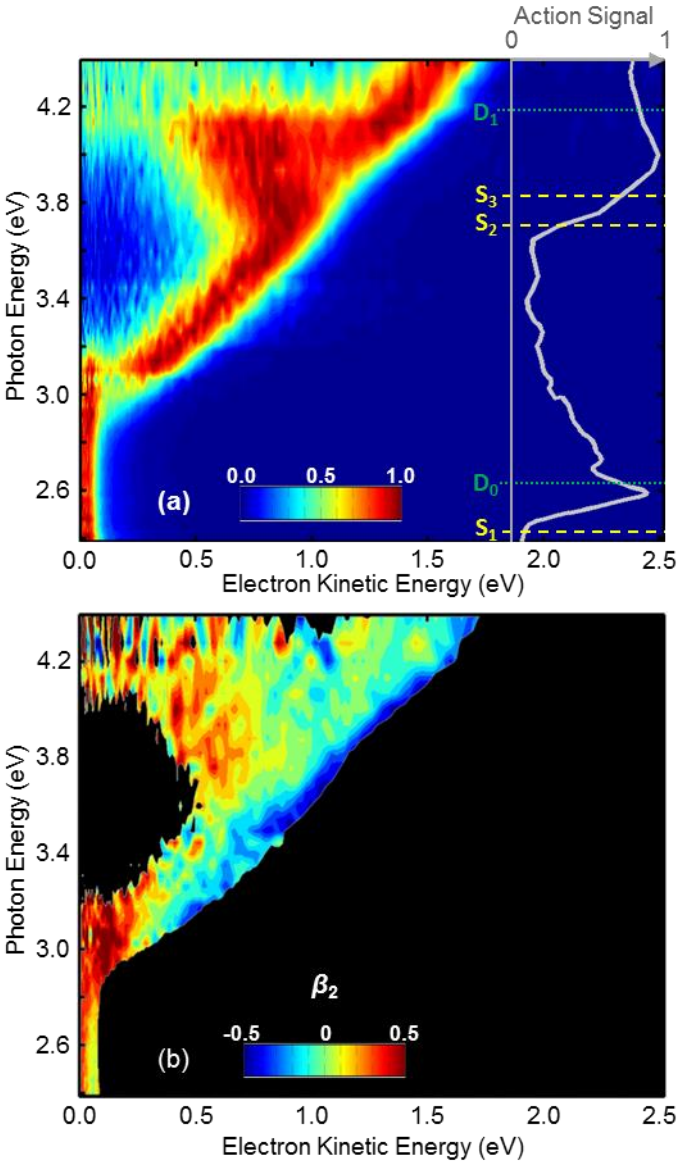

Figure 4.3 Frequency- and angle-resolved PE spectra of $HBDI^-$. The complete set of peak-normalised PE spectra is shown in (a), together with the action spectrum and calculated energies, taken from reference [34]. The PE anisotropy parameters are shown in (b).

4.4 Dynamics of the S_1 Excited State

The ADE of $HBDI^-$ has been determined by several groups to be 2.7 eV.[15,19,20,33] Despite this, PE signal was observed between 2.39 eV < $h\nu$ < 2.70 eV, although signal levels rapidly became very weak at the lower photon energies. The PE spectra in this range do not exhibit a change with photon energy and appear essentially identical; they

consist of a peak centred at *eKE* ~ 0.03 eV and a feature decaying exponentially from *eKE* = 0 eV. These features remain identifiable up to *hν* = 3.1 eV. This observation is consistent with both the action spectrum of Bochenkova *et al.*[34] and previous measurements of the PE spectra. The PE peak at *eKE* = 0.03 eV has previously been assigned to AD from the S_1 excited state[18] and the exponential tail decaying from *eKE* = 0 eV has been correlated with statistical (thermionic) electron emission.[20] This below-threshold contribution is facilitated by the ~300 K temperature of the anions in our experiment, which corresponds to an internal energy of ~ 310 meV. This excess internal energy allows some population of the S_1 excited state to be produced even at excitation energies below the onset of the S_1 state.

However, from *hν* = 2.8 eV, a new PE peak is observed at higher *eKE* that increases linearly with photon energy as might be expected for a direct (vertical) detachment process. Between 2.8 eV < *hν* < 3.1 eV the two processes are in competition and AD is dominant because the S_1 state is predominantly excited. This peak is the sole feature of the PE spectrum between 3.1 eV < *hν* < 3.6 eV, as the photoexcitation energy moves off resonance with the S_1 excited state and hence the AD channel is lost. The change in the dominant photodetachment channel is reflected in the β_2 parameters; the sole PE peak between 3.2 eV < *hν* < 3.6 eV has β_2 ~ 0 over the width of this constant binding energy peak, whereas at *hν* ~ 3 eV and between 0.1 eV < *eKE* < 0.2 eV, the PE anisotropy is β_2 ~ 0.4 indicating that the PEs are produced from different photodetachment channels.

In GFP, the major relaxation channel following photoexcitation is the eponymous fluorescence, whereas in $HBDI^-$ this channel is suppressed by a rotation about a central carbon bond.[23,25,38] As such, once excited to the S_1 state, $HBDI^-$ must decay to the ground state by alternative channels, primarily by internal conversion and

by AD. This has significant implications for dynamical studies of the S_1 excited state, as the observed lifetime of the excited state extracted from the experiment will contain contributions from both of the competing channels, by the well known kinetic relationship:

$$k_{\text{obs}} = \sum_i k_i \,, \qquad (4.1)$$

where i is the number of possible competing decay mechanisms. The dynamics of the S_1 excited state have recently been probed using time-resolved PE spectroscopy,[23] yielding an overall observed lifetime of 1.4 ps. However, it was not possible to deconvolute the individual contributions arising from internal conversion and autodetachment. Nevertheless, through careful measurements by time-resolved PE spectroscopy, it is possible to determine the lifetimes of both decay pathways.

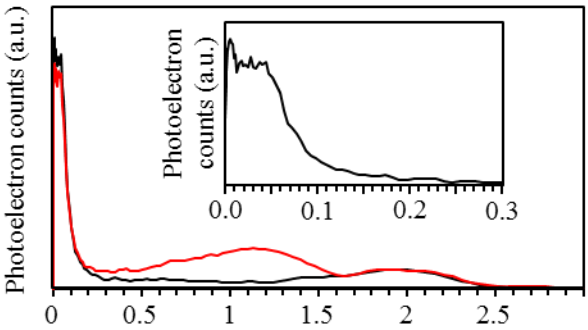

Figure 4.4 Time-resolved PE spectra taken with 2.48 eV (500 nm) pump and 1.55 eV (800 nm) probe pulses at delays of $t = -2$ ps (black) and $t = 0$ ps (red). Inset shows the first 300 meV of a PE spectrum taken at 2.48 eV at low VMI voltages.

Figure 4.4 presents the time-resolved PE spectra taken at 2.48 eV + 1.55 eV (500 nm + 800 nm) at delays of $t = -2$ ps and $t = 0$ ps. As the probe pulse has insufficient energy to detach an electron and is not resonant with any excited states, the PE spectra at $t = -2$ ps are virtually identical to those of the pump pulse. As with the frequency-resolved PE spectrum, the main feature of the PE spectra at 2.57 eV, 2.48 eV

and 2.38 eV is an intense peak at low electron kinetic energy, which is highlighted in the inset of Figure 4.4, for which the VMI voltage was reduced by a factor of ~4. The feature centred at 2 eV can be assigned to direct detachment from two photon absorption of the probe pulse.

The time-resolved PE spectrum at $t = 0$ shows a new feature, centred around *eKE* ~ 1.2 eV, which can be assigned to detachment by the 1.55 eV probe from the S_1 excited state. The evolution of this feature has been traced through time-resolved PE spectroscopy and is found to decay on a 1.4 ps timescale.[23] Notably, the low energy feature also exhibits a small decrease, although the total integrated area of this depletion is far smaller than the signal arising from photodetachment from the exited state.

As detachment from the S_1 state by the probe pulse is a direct measure of the excited state population, the integrated pump-probe feature is proportional to the excited state population, $[S_1]$. The rate of decay of $[S_1]$ is determined by competition between all possible decay mechanisms of the S_1, although internal conversion and AD are expected to dominate. As such, the observed rate constant for the decay of $[S_1]$ can be expressed as the sum of the rate constants for all possible decay mechanisms:

$$k_{obs} = \tau_{obs}^{-1} = \sum_i k_i = (1.4 \text{ ps})^{-1}. \qquad (4.2)$$

The low *eKE* feature is primarily a measure of the S_1 excited states that have undergone autodetachment. Therefore, the integrated depletion of the low *eKE* feature in Figure 4.4, [AD], is a measure of the population fraction of $[S_1]$ that has undergone autodetachment. The ratio of the rate constant for autodetachment, k_{AD}, to all other decay rates can be expressed as:

$$\frac{k_{AD}}{\sum_{i \neq AD} k_i} = \frac{[AD]}{[S_1] - [AD]} . \qquad (4.3)$$

Given that $k_{obs} = \sum_i k_i = k_{AD} + \sum_{i \neq AD} k_i$, we can now write that:

$$k_{AD} = \left(k_{obs} \frac{[AD]}{[S_1] - [AD]} \right) \left(1 + \frac{[AD]}{[S_1] - [AD]} \right)^{-1} \qquad (4.4)$$

where we have only considered autodetachment and internal conversion as the decay paths from the S_1 state. Taking $[S_1]$ as the integrated PE signal between 0.15 eV < *eKE* < 1.50 eV and [AD] as the integrated PE signal between 0 eV < *eKE* < 0.1 eV in Figure 4.4,[39] and using the previously determined[23] k_{obs} = (1.4 ps)$^{-1}$, the lifetimes for autodetachment and internal conversion can be calculated. At 2.57 eV, 2.48 eV and 2.38 eV, the autodetachment lifetime is 36 ps, 28 ps, and 33 ps, respectively. These are more than an order of magnitude longer than the observed lifetime so that the true internal conversion lifetime is only slightly longer than 1.4 ps (1.46 ps, 1.47 ps, and 1.46 ps at 2.57 eV (482 nm), 2.48 eV (500 nm) and 2.38 eV (519 nm), respectively). We note that there is a relatively large error associated with the τ_{AD} and τ_{IC} lifetimes. This is in part due to the increased noise generated during image reconstruction at low *eKE*.[40] More importantly, however, there is likely to be some overlap between the depleted signal and the $[S_1]$ signal. Finally, there are additional contributions to the low *eKE* feature as discussed below.

Bochenkova and Andersen have recently developed a model to explain the excited state behaviour of $HBDI^-$.[16] This work has identified several vibrational modes that are strongly coupled with specific decay mechanisms: numerous low-frequency modes associated with torsional motion were found to be coupled to the internal conversion pathway, whereas totally-symmetric higher frequency modes were correlated with promoting photodetachment into the continuum. Although the higher-frequency modes are the more Franck-Condon active, the interplay between the two modes results in a balance between the two decay mechanisms, from which the authors

were able to calculate statistical lifetimes for the IC and AD processes and the relative rates k_{AD}:k_{IC}.[16]

At 2.48 eV (500 nm), it was found that k_{AD}:k_{IC} ~ 0.1. This is in reasonable agreement with the ratio of k_{AD}:k_{IC} ~ 0.03 determined here. However, at higher excitation energies, the model predicts that the vibrational modes promoting autodetachment are more readily excited, resulting in a sharp increase in the rate of autodetachment; For example, at 2.57 eV (482 nm), the ratio k_{AD}:k_{IC} was expected to increase by a factor of 2.5.[16] Our results do not follow this trend. Within our experimental uncertainty, the lifetimes of all processes remains approximately the same over the 0.2 eV window probed here. In addition, we observe discrepancies between the calculated and experimentally observed lifetimes: while the calculated lifetime for IC is higher than the experimentally determined value and the calculated lifetime for AD is considerably lower than the experimentally determined value. However, the discrepancies in the ratios and the lifetimes can be ascribed to the small window probed and the inaccuracies in our experimental observations due to the small window over which we may observe depletion and contributions from other low eKE features. As such, we may state that our observations appear to be consistent with the calculations and that the model of Bochenkova and Andersen seems to have captured much of the underlying physics occurring on the S_1 excited state, but more accurate measurements may be needed.

We must also consider the action spectra obtained by the Jockusch group.[32,33] In this, the ratio of electrons formed to fragmentation is ~1:1 at 2.57 eV (482 nm). Fragmentation is a multiple photon process that is a direct consequence of internal conversion. If we take the fragmentation as a measure of k_{IC} and the electron loss channel as a measure of k_{AD}, then the ratio k_{AD}:k_{IC} must therefore be ~ 1 at 2.57 eV (482

nm), which is inconsistent with both our observations and the predictions of Bochenkova and Andersen.[16] This result could be explained by considering all electron detachment channels; $HBDI^-$ may undergo electron loss by both AD from the S_1 excited state and by thermionic emission, in which electrons are lost statistically from a vibrationally hot S_0 ground state.[27,29,30] Electrons emitted via thermionic emission are somewhat difficult to distinguish: the spectral peak appears as an exponential decay from a maximum at *eKE* = 0 eV and overlaps with the low *eKE* peak correlated with AD. We also are only able to recover a fraction of the thermionic emission peak – thermionic emission occurs with a lifetime on the order of microseconds, whereas our acquisition time is limited to ~100 ns by the velocity-map imaging arrangement. Additionally, the region at *eKE* = 0 eV suffers the greatest from noise from the image reconstruction program.

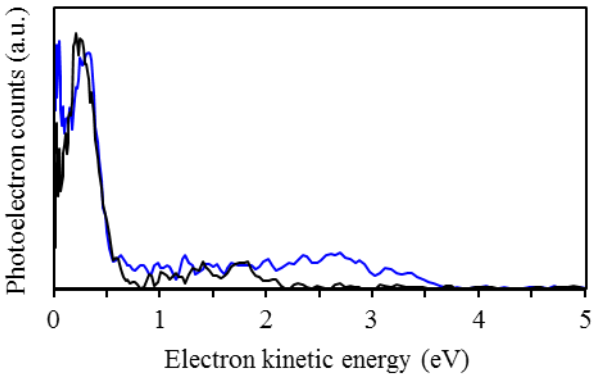

Figure 4.5 PE spectra taken at 3.10 eV (blue) and 1.55 eV (black). The feature at 0.3 eV is common to both spectra while at 3.10 eV a higher yield of thermionic emission is observed at very low kinetic energy. Features above 0.5 eV are due to 2-photon and 3-photon absorption at 3.10 eV and 1.55 eV, respectively.

Nevertheless, the contribution of thermionic emission may be clearly observed in Figure 4.5. Two PE spectra are presented: the first taken at *hv* = 3.10 eV (400 nm) and the second observed using a tightly focussed and therefore higher intensity pulse at *hv* = 1.55 eV (800 nm). While both excitation schemes give a total final energy of 3.10

eV, excitation at 1.55 eV requires a two-photon transition as the pump energy is insufficient to photodetach an electron. Disregarding the features above *eKE* = 1 eV, which are due to higher-order multiple photon transitions, the spectra appear similar with the notable exception of the peak at *eKE* = 0 eV, which is suppressed in the spectrum taken at 1.55 eV. This observation may be explained by the preferential population of modes that promote AD via the two-photon transition and clearly demonstrates the presence of thermionic emission in the spectrum. Interestingly, these slow electrons were not observed in the experiments of the Andersen group.[18]

The observation of this channel is significant in elucidating the dynamics of the S_1 excited state, in that it is almost impossible to distinguish between an electron that has been detached from either the S_1 state or the S_0 state. This difficulty is most apparent when considering the apparent discrepancies between the observations of the Jockusch and co-workers and our own. The $HDBI^-$ ions in the Jockusch experiments are constrained in an ion trap and irradiated over a far greater time period than in the current experiment, resulting in the time period over which electron loss channel may be measured being proportionally greater. As such, the Jockusch group observe a far greater contribution from thermionic emission to the electron loss channel which cannot be distinguished from the autodetachment channel,[32,33] resulting in the inflated k_{AD}:k_{IC} ratio.

As an attempt to reduce the effect of the overlapping features in our experiment, we have neglected to consider the depletion in the peak at < 10 meV. Its depletion at t = 0 is negligible compared to (and convoluted by) the depletion in the peak at 0.01 eV < *eKE* < 0.10 eV. The small depletion observed indicates that thermionic emission has a much longer lifetime than the vibrational autodetachment and internal conversion; as expected.[30,41,42] Therefore, if we were able to measure the PE spectrum across a far

greater timescale than currently possible, we would expect to see a far greater contribution of the thermionic emission peak to the PE spectrum.

4.5 Dynamics of Above-Threshold Resonances

While the dynamics of the S_1 excited state have been well studied, the dynamics of the higher lying excited states accessible through UV photoexcitation have received far less attention. However, these high lying excited states have been linked to redox pathways in the protein and a greater understanding of the intrinsic photodynamics is therefore desirable. Indeed, by inspection of the frequency-resolved spectrum in Figure 4.3(a), it is clear that substantial dynamics are occurring on an excited state surface following UV excitation. For $h\nu$ > 3.7 eV, the *eKE* distribution broadens with increasing photon energy, reaching a spectral width of *eKE* ~ 1 eV at $h\nu$ ~ 4.1 eV. The high energy edge of this PE feature remains linear with photon energy but the average *eKE* of the spectrum shifts to increasingly lower energy to yield a bimodal distribution. In fact, the low energy side of this bimodal distribution remains approximately constant in *eKE* with increasing $h\nu$. The maximum of the low energy peak is around *eKE* ~ 0.6 eV. For $h\nu$ > 4.1 eV, the progressively broadening feature abruptly collapses to a PE spectrum that has a feature consistent with direct detachment as well as a very broad and featureless distribution of electrons (0 eV < *eKE* < 1.3 eV). The relative intensity of this broad distribution is lower than the low energy peak observed for 3.7 eV < $h\nu$ < 4.1 eV, however, their integrated PE yields are approximately the same. The broadened feature contributes about 60% of the total PE yield, with the other 40% arising from the constant binding energy PE feature at high eKE.

The spectral broadening of the PE spectra over the 3.7 eV < $h\nu$ < 4.1 eV range suggests that excited state dynamics are occurring in competition with autodetachment.

This broadening was previously assigned to vibrational motion on the S_3 state.[36] However, the spectral broadening could also arise from internal conversion of the S_3 state to the lower-lying S_2 state followed by autodetachment. The S_2 state has a calculated energy that lies within 0.1 eV of the S_3 state[34] suggesting that pathways of coupling these two states may be present.

We must also consider the PE angular distributions over the spectral feature. These show that there is a small but consistent difference in $\beta_2(eKE)$ for the peak correlated with a direct detachment process and the feature at lower *eKE* in the 3.7 eV < $h\nu$ < 4.1 eV range. The β_2 parameter is negative on the high *eKE* edge, becomes 0 (indicating an isotropic image) over the centre of the feature before turning positive on the low *eKE* edge. As the anisotropy of the PE images is correlated to the symmetry of the excited states from which the electrons are detached, the change in β_2 is indicative that several excited states are involved in the detachment process to produce the observed PE feature.

In order to glean further insight into the decay mechanisms, the dynamics of the S_3 state were probed using time-resolved PE spectroscopy. In these experiments, the S_3 excited state was populated using femtosecond photoexcitation at 4.1 eV (300 nm), which was subsequently probed at 1.55 eV (800 nm). The excitation energy was chosen to energetically coincide with the spectral broadening observed in the 3.7 eV < $h\nu$ < 4.1 eV region of the frequency-resolved PE spectra as well as the local maximum in PE yield from the action spectra.

Figure 4.6(a) shows two representative pump-probe PE spectra recorded with the probe arriving before pump pulses (Δt = –525 fs) and near the temporal overlap of the two pulses (Δt = 25 fs). Both spectra show two peaks centred at ~0.25 eV and ~1.3 eV. The appearance of the PE spectrum between 0.5 eV < *eKE* < 1.5 eV is consistent

with the 4.1 eV (300 nm) PE spectrum obtained in the frequency-resolved experiments. The peak at *eKE* ~ 0.25 eV arises from a non-resonant two-photon detachment processes from the 1.55 eV probe; the PE spectrum at *eKE* < 0.5 eV is consistent with the PE spectrum recorded at 3.1 eV (400 nm).

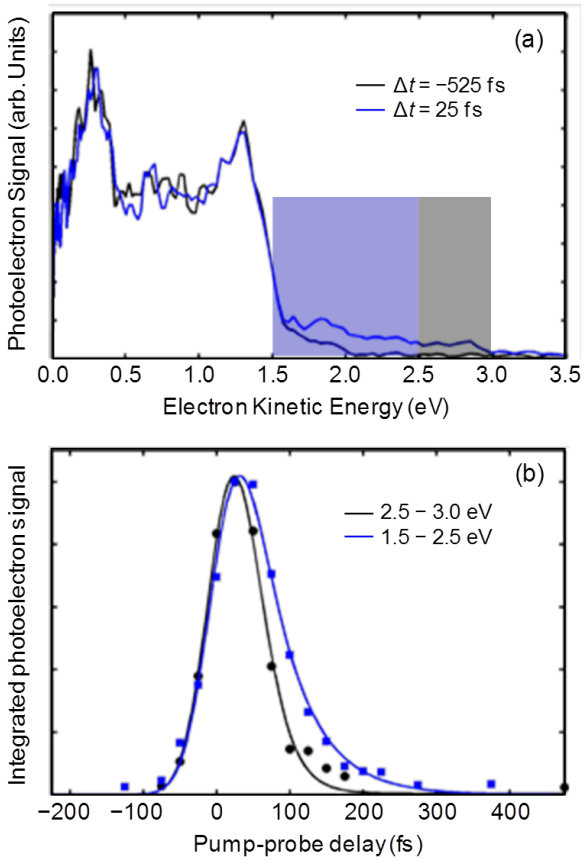

Figure 4.6 (a) Time-resolved PE spectra of $HBDI^-$ excited at 4.1 eV. (b) Decay dynamics of PE signal taken over the spectral windows shown in (a).

At Δt ~ 0, an additional PE feature between 1.5 eV < *eKE* < 3.0 eV is observed. This can be assigned to photodetachment from the excited state population; the PE spectrum of the time-dependent feature extends approximately an additional 1.55 eV beyond that of the pump-only PE spectrum. The breadth of the time-dependent PE feature suggests that it contains contributions from both excited state population leading to both prompt autodetachment (high *eKE* electrons) and delayed autodetachment (lower *eKE*).

To gain quantitative insight, the time-dependent PE feature can be divided into two spectral windows as shown in Figure 4.6(a). The 2.5 eV < *eKE* < 3.0 eV window probes population of the initially excited state and the 1.5 eV < *eKE* < 2.5 eV window probes population of the intermediate state to which the initial state has decayed. The time-varying integrated PE signals for each of these spectral windows are given in Figure 4.6(b) and were fitted to an exponential decay function;

$$f(t) = A\exp(-(t-t_0)/\tau) \qquad (4.5)$$

convoluted with the instrument response function (FWHM = 75 fs). The amplitude (A), lifetime (τ), and time-zero (t_0), were allowed to vary. The t_0 for both spectral windows were less than 5 fs apart and can be assumed to be essentially identical. The lifetime of the initially excited state was found to be 25 fs, which is less than our temporal resolution and so we may only quote this as < 40 fs. The lifetime of the intermediate state was found to be 55 fs, which is still extremely fast, although visibly slower than that of the initially excited state.

In the higher energy window, 3.2 eV < $h\nu$ < 3.7 eV, the cross-section for excitation to the S_1 sharply decreases and the PE signal may be dominated by direct detachment. The photoejection anisotropy is significantly more positive around $h\nu$ ~ 3.1 eV as shown in Figure 4.3(b). This might be a consequence of the interference between autodetachment and direct detachment into the continuum leading to a different β_2 value than for direct detachment only, which is dominant for 3.2 eV < $h\nu$ < 3.7 eV.

The frequency-resolved PE spectra combined with the prompt action-spectra from the Andersen group[34] show that for $h\nu$ > 3.7 eV higher-lying excited states are accessed, resulting in the observed broadening of the PE spectra. Using high-level calculations, Bochenkova *et al.* showed that the S_2 and S_3 are very close in energy at 3.7

eV and 3.8 eV, respectively, in the vertical Franck-Condon (FC) region (see Figure 4.3(a)).

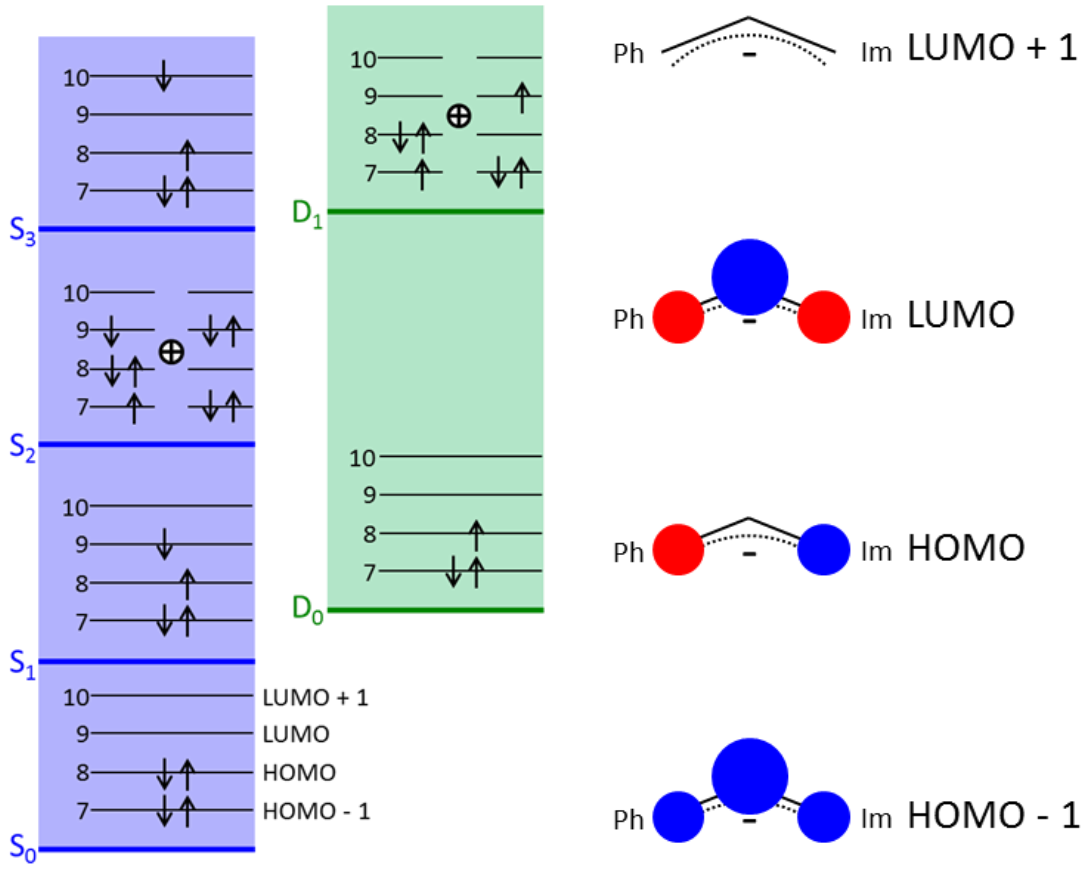

Figure 4.7 Left: Schematic representation of the electronic configuration of $HBDI^-$ showing the occupancy of the molecular orbitals at each excited state, as reported by Bochenkova *et al.*[34] Right: Schematic representation of the contributions of each orbital to the central allyl bridge that connects the phenol (Ph) with the imidazole (Im).

Figure 4.7 illustrates the configurations of the relevant electronic states and the occupancy of the molecular orbitals (MOs) of $HBDI^-$ and its neutral as calculated by Bochenkova *et al.*[34] It is useful to describe the MOs by the approximate localisation of the orbitals on the subunits and therefore in terms of the bonding character over the allyl bridge. We have considered the highest occupied molecular orbital (HOMO, MO(8)), the lowest unoccupied molecular orbital (LUMO, MO(9)) and the preceding and following molecular orbitals (HOMO – 1, MO(7), and LUMO + 1, MO(10), respectively). The HOMO is essentially non-bonding over the allyl bridge, whereas the

HOMO – 1 and LUMO exhibit π and π* character, respectively. The LUMO + 1 is localised almost entirely upon the phenoxy group and therefore does not contribute to the bonding on the allyl bridge.

We may now consider the behaviour of the excited state population in the FC region based on the change in the occupied orbitals. In the $S_2 \leftarrow S_0$ transition, either π bonding or non-bonding orbitals are replaced for antibonding orbitals over the allyl. Hence, the anti-bonding character of the S_2 state is increased relative to the S_0 state and the excited state population produced in the FC region following photoexcitation is likely to undergo rapid wave packet motion, leading to a stretching of the allyl bridge. The $S_1 \leftarrow S_0$ transition is similar in that it has π* character on the allyl bridge, although the anti-bonding character is expected to be less pronounced than that of the S_2 state, and initial wave packet dynamics of the allyl stretching mode on the S_1 state have been predicted to be on the order of 10 fs.[38,43] It is reasonable to assume that the wave packet dynamics on the S_2 will be similar to or faster than those on the S_1 state, due to the pronounced anti-bonding character. In contrast, the $S_3 \leftarrow S_0$ transition sees the promotion of an electron from the non-bonding MO(8) to MO(10), which is localised on the phenol-ring. As such, we might expect most major structural changes to be localised on the phenoxy sub-unit and any effects to the allyl bridge are likely to be far smaller than the changes observed on the S_1 and S_2 states. Finally, we consider the neutral states, D_0 and D_1. The ground D_0 state corresponds to loss of one electron from the MO(8), whereas the D_1 state corresponds either to the loss of an electron from MO(7) or the simultaneous loss of one electron from MO(8) and the promotion of one electron from MO(8) into MO(9). As MO(8) is essentially non-bonding on the allyl bridge, the structure of the allyl bridge is likely to be similar in the S_0 and D_0 minimum energy geometries. Indeed the PE feature for direct detachment is relatively sharp given

the molecular size of HBDI, indicating that little energy may be redistributed to vibrational modes in photodetachment.[20,44] We can now consider the allowed transitions in photodetachment. The S_3, S_1 and S_0 excited states are correlated with D_0 in a one electron Koopmans picture; that is, it is possible to produce the D_0 electronic configuration from these starting configurations by the detachment of a single electron. The S_3, S_1 and S_0 excited states are therefore shape resonances with respect to the D_0 state, which typically have very short autodetachment lifetimes (on the order of 10s fs). In contrast, the S_2 state requires an electronic transition in addition to photodetachment in order to access the electronic configuration of the D_0 state and therefore does not correlate with the D_0 state and is a Feshbach resonance with respect to this state. The S_2 is a shape resonance of the D_1 excited state of the neutral and the S_3, S_1 and S_0 excited states henceforth Feshbach resonances.

The spectral broadening in the 3.7 eV < $h\nu$ < 4.1 eV range suggests that, following excitation, wave packet motion may occur on the excited state surface before electron emission. The $S_3 \leftarrow S_0$ oscillator strength is significantly greater than that of the $S_2 \leftarrow S_0$ transition, hence, we may assume that the S_3 state is initially populated in this range. The observed broadening in the PE spectra could arise from vibrational dynamics on the S_3 state that precedes autodetachment, as suggested by Mooney *et al.*[36] Alternatively, because the S_2 state is in very close proximity to the S_3 state in the FC region, it is conceivable that there exists a strong coupling or conical intersection between these two states that can transfer population from S_3 to S_2 on a timescale faster than autodetachment. Such dynamics have indeed been observed in some quinone anions.[45-47]

The latter of the two scenarios above is more consistent with the experimental results. Firstly, we note that the PE angular distribution across the bimodal peak is not

constant. The anisotropy over the high energy component is slightly negative ($\beta_2 \sim -0.3$), changes to an isotropic distribution ($\beta_2 = 0$) over the centre of the peak and finally rises to a positive anisotropy ($\beta_2 \sim +0.2$) over the lower *eKE* portion. The observed PE angular distribution is intrinsically linked to the symmetry characteristics of the MO from which the electron is detached,[45] hence the change in anisotropy is indicative of a change in electronic state. This suggests that population from the S_3 state is indeed undergoing internal conversion to the S_2 state.

Additionally, from consideration of the occupied MOs, the S_3 and D_0 state minimum energy geometries are not expected to be dissimilar. As such, it is difficult to reconcile the large spectral red-shift observed with the expected range of energies accessible assuming vibrational motion occurring on a timescale of < 40 fs. In contrast, the strong π^* character on the allyl bridge on the S_2 state is expected to result in a minimum energy geometry far from the FC region. Therefore, one might expect that the S_2 and D_0 potential energy surfaces to diverge significantly along the allyl stretching coordinate, allowing for a greater range of detachment energies to be accessed than would be possible between the S_3 and D_0 states. Notably, the dynamics of the allyl stretch on the S_2 state have been found to occur on an extremely short timescale (10 fs),[38,43] well within the lifetime of the excited states observed by our time-resolved experiments. Any dynamics on the S_2 excited state surface would, by necessity, be in competition with autodetachment to the D_0 state (in the 3.7 eV < $h\nu$ < 4.1 eV range). However, as the S_2 state is a Feshbach resonance of the D_0 state, the $S_2 \rightarrow D_0$ autodetachment is a formally forbidden transition and the rate of this transition will therefore be slower than the $S_3 \rightarrow D_0$ transition, allowing for the vibrational wave packet to sample a larger area of the S_2 potential energy surface. This would in turn lead to a large spectral width in the PE emission, as observed.

Recent calculations by Bochenkova and Andersen may suggest that the spectral broadening is in fact a result of IVR.[48] In this, the S_3 and D_0 excited states are calculated to have almost identical shapes. As the excitation energy increases from the onset of the S_3 state, the number of accessible vibrational modes increases. Through conservation of vibrational quantum number ($\Delta v = 0$), the photoelectron spectra would take the form of a broad peak in which the lower *eKE* edge is constant in kinetic energy and the higher *eKE* edge is constant in electron binding energy (*eBE*). This is consistent with the assignment of Mooney *et al.*[49] and the S_2 state need not be involved in the excited state dynamics. This, however, does not explain the change in anisotropy observed over the peak, or the cut-off in PE intensity at the onset of the D_1 excited state onset.

The $S_3 \rightarrow S_2$ internal conversion can be associated with the first, sub-40 fs lifetime observed in the time-resolved PE spectrum. However, as with the dynamics of the S_1 state, the observed lifetime is a combination of the rates of internal conversion and autodetachment from the S_3 state to the D_0 state. We can gain insight into the dynamics occurring on the S_3 excited state surface by considering the high *eKE* feature that increases linearly with excitation energy in the frequency-resolved spectrum. Although this peak overlaps the expected position of the direct detachment feature, the observed PE feature is predominantly composed of PEs from the $S_3 \rightarrow D_0$ autodetachment channel. This is evidenced by the angle-resolved spectrum, in that the anisotropy of the feature increases markedly as the excitation energy exceeds the onset of the excited states, and that direct detachment into the continuum is a minor channel in this energy range[34] (see action spectrum in Figure 4.3(a)). By fitting the PE spectrum taken at $h\nu$ = 3.54 eV (i.e. a purely direct detachment spectrum) to the frequency-resolved spectra across the range 3.7 eV < $h\nu$ < 4.1 eV, it is possible to estimate the relative contributions of $S_3 \rightarrow D_0$ autodetachment to $S_2 \rightarrow D_0$ autodetachment. The

average PE yield due to $S_3 \rightarrow D_0$ autodetachment is ~40% of the total PE yield, with the remaining 60% arising from autodetachment from the S_2 state. Assuming that all population in the S_2 excited state is lost through autodetachment, we can therefore deduce through kinetic considerations that the $S_3 \rightarrow S_2$ internal conversion occurs on a <65 fs timescale while $S_3 \rightarrow D_0$ autodetachment is slower. The true lifetimes of these processes are likely to be considerably faster, but our observations are limited by the time resolution of the experiment. The spectral broadening observed over the 3.7 eV < $h\nu$ < 4.1 eV range can thus be assigned to vibrational dynamics on the S_2 state that leads to a broad PE spectrum in this range. The overall decay of this S_2 state feature is associated with the second lifetime observable in the time-resolved spectrum, 55 fs, and can be correlated to the $S_2 \rightarrow D_0$ autodetachment.

Perhaps the most striking feature of the frequency-resolved PE spectra is that at $h\nu$ > 4.1 eV, the PE spectra abruptly change from the bimodal distribution (between 3.7 eV < $h\nu$ < 4.1 eV) to a very broad distribution (see Figure 4.3(a)). This change is suggestive of a new decay pathway becoming available at this energy, and coincides with the calculated location of the D_1 excited state of the neutral in the FC region.[34] The D_1 state is a Feshbach resonance with respect to the S_3 state, hence detachment from the S_3 state to form the D_1 state is an unfavourable process. However, the S_2 state is a shape resonance of the D_1 state in a one electron Koopmans' interpretation (see Figure 4.7). Hence, we propose that, as the photon energy increases and becomes higher than the D_1 energy, autodetachment from the S_2 state becomes much faster by virtue of the favourable $S_2 \rightarrow D_1$ autodetachment channel. Indeed, it can be seen in the frequency-resolved PE spectra that the peak around *eKE* ~ 0.6 eV relative to the peak arising from $S_3 \rightarrow D_0$ autodetachment is decreasing with a concurrent rise in a new feature centred at lower *eKE*.

The observation of the shift in the composition of the PE spectra at the onset of the D_0 state has significant implications for the scenario where the S_2 state plays no part in the dynamics. In this case, all dynamics observed between 3.7 eV < $h\nu$ < 4.1 eV must occur on the S_3 excited state surface. The change in PE spectra at $h\nu$ = 4.1 eV therefore has two possible explanations: either a conical intersection with the S_2 state or the $S_3 \rightarrow D_1$ autodetachment channel becomes available at this energy. As we have stated, the S_3 state is not correlated with the D_1 state, hence, the channel is unfavourable and unlikely to be favourable. Additionally, in either case, one would expect that the PE yield in the $S_3 \rightarrow D_0$ autodetachment channel (peak at highest *eKE*) would transfer to a lower *eKE*, as observed in *para*-benzoquinone and discussed in Chapter 5,[45] and this is not experimentally observed. Instead, the contribution of the $S_3 \rightarrow D_0$ autodetachment channel to the total PE yield does not change between $h\nu$ = 3.9 eV and 4.3 eV. Rather, it is the feature at *eKE* ~ 0.6 eV, which we have associated with the excited state process responsible for the observed peak broadening, that donates the PE signal to form the feature at lower *eKE*. Therefore, we can state that only population that has first undergone internal conversion from the S_3 excited state is involved in detachment through the new channel; hence the evidence strongly suggests that there must be a process for the rapid conversion of population from the S_3 excited state to population on the S_2 excited state.

4.6 Summary

In summary, we have performed frequency-, angle- and time-resolved PE spectroscopy on the GFP model chromophore anion, $HBDI^-$, in an attempt to elucidate the dynamics of the excited state populations produced following photoexcitation. We have, through careful inspection of the depletion and concomitant rises in time-resolved

spectra taken at numerous wavelengths, been able to extract individual lifetimes for the relaxation mechanisms following excitation to the S_1 excited state: ~ 1.45 ps for internal conversion to the S_0 state and ~ 30 ps autodetachment to the D_0. The lifetime for autodetachment is consistent with the calculations by Bochenkova and Andersen.[50] However, we do not observe a lifetime dependence on the pump photon energy for autodetachment. We have also noted the importance of thermionic emission as an operative electron loss channel over long timescales.

Subsequently, we have assigned the dynamics following UV excitation to unbound anion resonances. Excitation with $h\nu$ > 3.7 eV leads to the population of the bright S_3 excited state that decays through a combination of autodetachment to the D_0 ground neutral state and internal conversion to the nearby S_2 excited state. We note that the relaxation mechanisms are competitive, with internal conversion being slightly dominant. The S_2 excited state population then undergoes rapid vibrational motion, which occurs in competition with autodetachment to the D_0 ground state. By increasing the photoexcitation energy over the onset of the D_1 excited neutral state, $h\nu \geq 4.1$ eV, a second decay pathway, the $S_2 \rightarrow D_1$ autodetachment channel, becomes available and is predicted to be favourable to the $S_2 \rightarrow D_0$ channel based on a Koopmans' interpretation.

4.7 References

(1) Yang, F.; Moss, L. G.; Phillips, G. N. *Nature Biotechnology* **1996**, *14*, 1246.

(2) Cubitt, A. B.; Heim, R.; Adams, S. R.; Boyd, A. E.; Gross, L. A.; Tsien, R. Y. *Trends in Biochemical Sciences* **1995**, *20*, 448.

(3) Kojima, S.; Ohkawa, H.; Hirano, T.; Maki, S.; Niwa, H.; Ohashi, M.; Inouye, S.; Tsuji, F. I. *Tetrahedron Letters* **1998**, *39*, 5239.

(4) Lippincott-Schwartz, J.; Patterson, G. H. *Science* **2003**, *300*, 87.

(5) Patterson, G. H.; Knobel, S. M.; Sharif, W. D.; Kain, S. R.; Piston, D. W. *Biophysical Journal* **1997**, *73*, 2782.

(6) Tsien, R. Y. *Annual Review of Biochemistry* **1998**, *67*, 509.

(7) Zimmer, M. *Chemical Reviews* **2002**, *102*, 759.

(8) In *"The Nobel Prize in Chemistry 2008",NobelPrize.org* NobelPrize.org 2008, (2013)

(9) Ward, W. W.; Prentice, H. J.; Roth, A. F.; Cody, C. W.; Reeves, S. C. *Photochemistry and Photobiology* **1982**, *35*, 803.

(10) Weber, W.; Helms, V.; McCammon, J. A.; Langhoff, P. W. *Proceedings of the National Academy of Sciences of the United States of America* **1999**, *96*, 6177.

(11) Bell, A. F.; He, X.; Wachter, R. M.; Tonge, P. J. *Biochemistry* **2000**, *39*, 4423.

(12) Cody, C. W.; Prasher, D. C.; Westler, W. M.; Prendergast, F. G.; Ward, W. W. *Biochemistry* **1993**, *32*, 1212.

(13) Nielsen, S. B.; Lapierre, A.; Andersen, J. U.; Pedersen, U. V.; Tomita, S.; Andersen, L. H. *Physical Review Letters* **2001**, *87*, 228102.

(14) Webber, N. M.; Litvinenko, K. L.; Meech, S. R. *Journal of Physical Chemistry B* **2001**, *105*, 8036.

(15) Rajput, J.; Rahbek, D. B.; Andersen, L. H.; Rocha-Rinza, T.; Christiansen, O.; Bravaya, K. B.; Erokhin, A. V.; Bochenkova, A. V.; Solntsev, K. M.; Dong, J.; Kowalik, J.; Tolbert, L. M.; Petersen, M. A.; Nielsen, M. B. *Physical Chemistry Chemical Physics* **2009**, *11*, 9996.

(16) Bochenkova, A.; Andersen, L. *Faraday Discussions* **2013**, *163*, 297.

(17) Greenwood, J. B.; Miles, J.; De Camillis, S.; Mulholland, P.; Zhang, L.; Parkes, M. A.; Hailes, H. C.; Fielding, H. H. *Journal of Physical Chemistry Letters* **2014**, *5*, 3588.

(18) Toker, Y.; Rahbek, D. B.; Klaerke, B.; Bochenkova, A. V.; Andersen, L. H. *Physical Review Letters* **2012**, *109*, 128101.

(19) Mooney, C. R. S.; Sanz, M. E.; McKay, A. R.; Fitzmaurice, R. J.; Aliev, A. E.; Caddick, S.; Fielding, H. H. *Journal of Physical Chemistry A* **2012**, *116*, 7943.

(20) Horke, D. A.; Verlet, J. R. R. *Physical Chemistry Chemical Physics* **2012**, *14*, 8511.

(21) Bravaya, K. B.; Khrenova, M. G.; Grigorenko, B. L.; Nemukhin, A. V.; Krylov, A. I. *Journal of Physical Chemistry B* **2011**, *115*, 8296.

(22) Bravaya, K. B.; Krylov, A. I. *Journal of Physical Chemistry A* **2013**, *117*, 11815.

(23) Mooney, C. R. S.; Horke, D. A.; Chatterley, A. S.; Simperler, A.; Fielding, H. H.; Verlet, J. R. R. *Chemical Science* **2013**, *4*, 921.

(24) Altoe, P.; Bernardi, F.; Garavelli, M.; Orlandi, G.; Negri, F. *Journal of the American Chemical Society* **2005**, *127*, 3952.

(25) Litvinenko, K. L.; Webber, N. M.; Meech, S. R. *Journal of Physical Chemistry A* **2003**, *107*, 2616.

(26) Mandal, D.; Tahara, T.; Webber, N. M.; Meech, S. R. *Chemical Physics Letters* **2002**, *358*, 495.

(27) Amrein, A.; Simpson, R.; Hackett, P. *Journal of Chemical Physics* **1991**, *95*, 1781.

(28) Andersen, J. U.; Bonderup, E.; Hansen, K. *Journal of Physics B-Atomic Molecular and Optical Physics* **2002**, *35*, R1.

(29) Baguenard, B.; Pinare, J. C.; Bordas, C.; Broyer, M. *Physical Review A* **2001**, *63*, 023204.

(30) Campbell, E. E. B.; Levine, R. D. *Annual Review of Physical Chemistry* **2000**, *51*, 65.

(31) Zhang, Y.; Stuke, M. *Physical Review Letters* **1993**, *70*, 3231.

(32) Forbes, M. W.; Jockusch, R. A. *Journal of the American Chemical Society* **2009**, *131*, 17038.

(33) Forbes, M. W.; Nagy, A. M.; Jockusch, R. A. *International Journal of Mass Spectrometry* **2011**, *308*, 155.

(34) Bochenkova, A. V.; Klaerke, B.; Rahbek, D. B.; Rajput, J.; Toker, Y.; Andersen, L. H. *Angewandte Chemie-International Edition* **2014**, *53*, 9797.

(35) Tang, R. Z.; Li, H. X.; Liu, Y. C.; Zhang, P.; Cao, X. Y.; Wang, W. F. *Acta Physico-Chimica Sinica* **2012**, *28*, 213.

(36) Mooney, C. R. S.; Parkes, M. A.; Zhang, L.; Hailes, H. C.; Simperler, A.; Bearpark, M. J.; Fielding, H. H. *Journal of Chemical Physics* **2014**, *140*, 205103.

(37) Reid, K. L. *Annual Review of Physical Chemistry* **2003**, *54*, 397.

(38) Martin, M. E.; Negri, F.; Olivucci, M. *Journal of the American Chemical Society* **2004**, *126*, 5452.

(39) Domcke, W.; Stock, G. *Advances in Chemical Physics D* **1997**, *100*, 1.

(40) Roberts, G. M.; Nixon, J. L.; Lecointre, J.; Wrede, E.; Verlet, J. R. R. *Review of Scientific Instruments* **2009**, *80*, 053104.

(41) Verlet, J. R. R.; Bragg, A. E.; Kammrath, A.; Cheshnovsky, O.; Neumark, D. M. *Journal of Chemical Physics* **2004**, *121*, 10015.

(42) Verlet, J. R. R.; Kammrath, A.; Griffin, G. B.; Neumark, D. M. *Journal of Chemical Physics* **2005**, *123*, 231102.

(43) Zhao, L.; Zhou, P.-W.; Li, B.; Gao, A.-H.; Han, K.-L. *Journal of Chemical Physics* **2014**, *141*, 235101.

(44) Deng, S. H. M.; Kong, X.-Y.; Zhang, G.; Yang, Y.; Zheng, W.-J.; Sun, Z.-R.; Zhang, D.-Q.; Wang, X.-B. *Journal of Physical Chemistry Letters* **2014**, *5*, 2155.

(45) West, C. W.; Bull, J. N.; Antonkov, E.; Verlet, J. R. R. *Journal of Physical Chemistry A* **2014**, *118*, 11346.

(46) Horke, D. A.; Li, Q.; Blancafort, L.; Verlet, J. R. R. *Nature Chemistry* **2013**, *5*, 711.

(47) Lezius, M. *International Journal of Mass Spectrometry* **2003**, *223*, 447.

(48) Bochenkova, A. V.,2015.

(49) Mooney, C. R. S.; Parkes, M. A.; Zhang, L.; Hailes, H. C.; Simperler, A.; Bearpark, M. J.; Fielding, H. H. *Journal of Chemical Physics* **2014**, *140*.

(50) Bochenkova, A. V.; Andersen, L. H. *Faraday Discussions* **2013**, *163*, 297.

Chapter 5. Dynamics of Electron Acceptors

The resonant attachment of a free electron to a closed shell neutral molecule, and the interplay between the following electron detachment and electronic relaxation channels represents a fundamental but common process throughout chemical and biochemical systems. Frequency- and angle-resolved PE *imaging is detailed and used to map-out molecular excited state dynamics of gas-phase para-benzoquinone, which is an electron accepting moiety in all biological electron-transfer chains. Three-dimensional spectra of excitation energy, electron kinetic energy and electron ejection anisotropy reveal clear fingerprints of excited and intermediate state dynamics. The results show that many of the excited states are strongly coupled, providing a route to forming the ground state radical anion, despite the fact that the electron is formally unbound in the excited states. The relation of our method to electron impact attachment studies and the key advantages, including the extension to time-resolved dynamics and to larger molecular systems is discussed.*

The interpretation of the PE spectra in this chapter is supported by multi-reference calculations performed by Dr James Bull. This chapter is based upon 'Anion Resonances of *para*-Benzoquinone Probed by Frequency-Resolved Photoelectron Imaging', C. W. West, J. N. Bull, E. Antonkov and J. R. R. Verlet, *J. Phys. Chem. A*, **118**, 11346 (2014).

5.1 Introduction

Electron transfer is amongst the most fundamental chemical reactions and features prominently in all branches of chemistry. Quinones are often encountered as part of the active site in electron transfer reactions in nature;[1-4] for example, plastoquinone and ubiquinone are key electron acceptors in the electron transport chains of photosynthesis[5]

and respiration,[6] respectively. Inspired by their widespread use in nature, quinones have also been commonly used in synthetic electron transport chains in order to create simple prototypes that model the electron acceptor dynamics of these biological reaction centers.[7] Of the various quinone derivatives, the *para*-benzoquinone (pBQ, Figure 5.1) moiety is that most common in nature. From a rudimentary perspective, electron transfer to a closed shell neutral molecule such as pBQ can be viewed as the electron attachment through resonances of its radical anion. From this point-of-view, electron attachment and transmission studies on pBQ have attracted considerable interest over the last few decades.[8-14] Such studies have provided detailed insight into the available temporary anion resonances of pBQ, although dynamical information is typically difficult to extract because nascent excited state resonances can have lifetimes on a sub-picosecond timescale. Horke *et al.* have recently shown that a PE spectrum of $pBQ^{\bullet-}$ contains signatures of such ultrafast dynamics and that time-resolved PE spectroscopy can be used to follow these dynamics in real-time.[15] These time-resolved experiments considered excitation dynamics at a single photon energy.

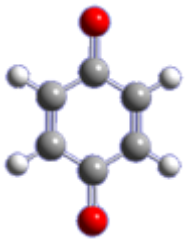

Figure 5.1 Structure of *para*-benzoquinone.

Here, we present a comprehensive study of $pBQ^{\bullet-}$ by frequency- and angle-resolved PE imaging, as introduced in Chapter 4. Through this, we demonstrate that both the PE spectral trends and the angular distributions extracted from the PE images may be used to identify the location of excited state resonances, and that these show clear evidence for above-threshold dynamics involving several excited states of $pBQ^{\bullet-}$.

The experimental methodology provides complementary and new information concerning the analogous electron attachment processes. Moreover, frequency-resolved PE imaging can be readily scaled up to much larger and more complex systems through the use of an appropriate radical anion source, paving the way to studying the above-threshold dynamics of a range of important molecular systems.

The excited states of $pBQ^{\bullet-}$ have been the subject of a number of gas-phase [8-11,13-21] and computational[16,21-26] studies. It is well-established that both the radical anion and neutral pBQ have planar D_{2h} ground state geometries with $^2B_{2g}$ and ^1A_g electronic symmetry, respectively. Anion photodetachment experiments have determined the adiabatic electron affinity of pBQ to be 1.860 ± 0.005 eV.[16] By varying the photon energy, Schiedt and Weinkauf identified a number of vibrationally-resolved above-threshold resonances of jet-cooled $pBQ^{\bullet-}$.[16] Notably, a broad and intense peak at 2.50 eV above the anionic ground state was assigned to the ^2A_u excited state with predominantly shape resonance character. A series of weaker sharp resonances were assigned to vibrational states of the lower lying $^2B_{2u}$ and $^2B_{3g}$ states. Both of these are formally optically dark Feshbach resonances with predominantly $n\pi^*$ character, but they gain some oscillator strength due to Herzberg-Teller coupling with the ^2A_u state. Additionally, Schiedt and Weinkauf showed that the PE spectra at different excitation energies resonant with the ^2A_u state changed due to varying Franck-Condon factors following autodetachment. In another study, Wang and co-workers have reported PE spectra of $pBQ^{\bullet-}$ at ~70 K using 355 nm (3.496 eV) and 266 nm (4.661 eV) photons identifying no apparent vibrational structure for photon energies less than 4 eV, however at least two sharp spectral features with vibrational structure emerge at $h\nu$ ~ 4.2 eV.[21] Finally, Brauman and co-workers have reported low resolution *total* photodetachment cross sections with photon energies up to ~4.6 eV, identifying two

broad maxima centered at ~3.0 eV and ~4.1 eV, as well as the onset of an intense band starting at ~4.4 eV.[26-28]

pBQ has also been the subject of a number of electron attachment and transmission studies, which have identified at least three resonances centered at 0.7 eV, 1.4 eV and ~2.0 eV above the ground state of the neutral, with the latter producing radical anions that survive for at least several microseconds.[8,12-14] Although some vibrational structure could be discerned in these experiments, on the whole, the bands are very broad and overlapping. In a number of other molecular systems, systematic electron attachment measurements have illustrated vibrationally-resolved two-dimensional electron attachment, which can be considered as analogous to the frequency-resolved methodology presented in this work.[29-31]

The experiments of Schiedt and Weinkauf demonstrated the sensitivity of PE spectroscopy to investigate excited state electron detachment processes of pBQ, although were limited to a narrow spectral range around the ^2A_u resonance and only changes in the vibrational structure were observed in the PE spectra. For the experiments presented here, we trade off the energetic resolution of the excitation pulse for the range of wavelengths accessible. We present PE spectra obtained at a variety of excitation wavelengths between 2.48 eV < $h\nu$ < 4.59 eV, thus probing up to 2.73 eV into the electron detachment continuum of $pBQ^{\bullet-}$. The use of a VMI detector allows for the simultaneous detction of the angle-resolved PE spectrum, which provides additional rich insight into resonances in the continuum. Through comparison of the frequency- and angle-resolved anion PE spectra with neutral electron attachment and transmission spectra, combined with high-level *ab initio* calculations on the energetics for appropriate geometries, a comprehensive deconvolution of electron detachment dynamics can be gained.

5.2 Methodology

The experiments were performed as described in Chapter 2. Briefly, $pBQ^{\bullet-}$ radical anions were produced by electrospray of ~1 mM of pBQ (97%, Sigma Aldrich) in methanol, and trapped in a radio frequency ring-electrode ion trap operating at ambient temperature. The ion trap was unloaded at a 10 Hz repetition rate. For the $pBQ^{\bullet-}$ experiments, laser pulses of ~6 ns duration with photon energies from 2.48 eV (500 nm) to 4.59 eV (270 nm) in 10 nm increments were generated using the Horizon OPO. For the naphthoquinone experiments, laser pulses of ~6 ns duration with photon energies from 1.77 eV (700 nm) to 4.13 eV (300 nm) in 10 nm increments were generated using the Horizon OPO. PE spectra and PADs were extracted from the raw images using a polar onion peeling algorithm.[32] The PE spectra were calibrated using the known spectrum of I^- and have a resolution of ~5 %.

5.2.1 Theoretical Methods

Ab initio calculations were performed by Dr James Bull using the GAMESS-US (May 2013 release)[33] and Gaussian 09 computational packages.[34] All calculations used the aug-cc-pVTZ basis set to described the carbon and oxygen atoms, although the most diffuse set of *f* functions were omitted from this basis set.[35] The hydrogen atoms were described using the cc-pVTZ basis set.[36] The final molecular basis set should provide an accurate account of valence shells for shape or core-excited Feshbach resonances without excess diffuse mixing.[37] Following Weber *et al.*,[23] CASSCF reference wave functions with (16,12) and (17,12) active spaces for neutral and anion states, respectively, and were used for all geometrical optimizations and frequency calculations. All relevant zero-point energy corrections assumed harmonic values scaled

with factor 0.98.[38] Dynamical electron correlation was added with MRMP2 theory, within the more general multi-state XMCQDPT framework.[39] The occurrence of intruder states in single state multi-reference calculations was checked by inspecting the weight of the reference function and applying denominator level shifting. In some instances multistate calculations were performed to ensure level shifting was sufficient to remove any small intruder state contributions. Calculated ground state energetics (experimental values in parentheses) are AEA = 1.96 (1.86)[16] eV, VEA = 1.57 (1.5 ± 0.1)[14] eV, and VDE = 2.03 (2.0 ± 0.1)[21] eV, where AEA is the adiabatic electron affinity of pBQ, VEA is the vertical electron affinity of pBQ, and VDE is the vertical detachment energy of $pBQ^{\bullet-}$. For comparison, CCSD(T) theory[40] considering the same molecular basis set gives AEA = 1.85 eV, VEA = 1.63 eV, and VDE = 1.98 eV.

5.3 Frequency- and Angle-Resolved Photoelectron Spectroscopy

Figure 5.2 shows three representative PE spectra taken at photon energies of: (a) 2.48 eV (500 nm); (b) 3.10 eV (400 nm); and (c) 4.13 eV (300 nm). The central slices through the respective reconstructed images are inset, where both the experimental (left) and Legendre polynomial fits (from equation (2.3)) are retained (right). The PE spectrum at 2.48 eV shows a main feature centered around an electron kinetic energy of 0.4 eV. The maximum of this feature is consistent with that for a direct detachment process based on the 3.496 eV spectrum from the Wang group;[21] however, at *eKE* = 0 eV, an additional feature is observed that exponentially decays with increasing *eKE*. The PE spectrum at 3.10 eV is clearly more complicated. The feature centered at *eKE* ~ 0.9 eV is consistent with a direct detachment feature, but an additional feature can be seen around *eKE* ~ 0.4 eV as well as a peak at *eKE* = 0 eV. On initial inspection, the additional feature at *eKE* ~ 0.4 eV has the appearance of the PE spectrum recorded at

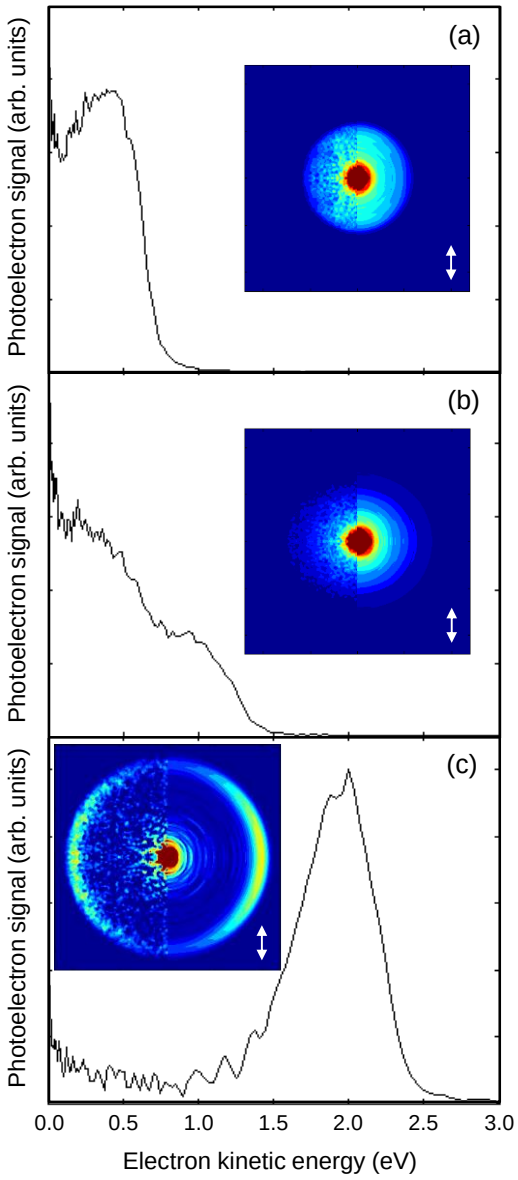

Figure 5.2 PE spectra acquired at photon energies of (a) 2.48 eV, (b) 3.10 eV, and (c) 4.13 eV. Inset in each plot are the central slices through the corresponding PE velocity-map image; the left semicircle is the experimental data retained in polar onion peeling and the right semicircle is the fitted Legendre polynomials.

2.48 eV, but does not have the expected shift in *eKE* commensurate with the increase in photon energy for direct detachment – this trend becomes obvious in the two-dimensional spectrum. The 3.10 eV PE spectrum is essentially identical to the earlier spectrum acquired by Horke *et al.* with laser pulses of ~40 fs duration,[15] implying that we are observing single photon processes despite the increase in the duration of the laser

pulse to ~6 ns. The PE spectrum at 4.13 eV shows predominantly a single PE feature at high *eKE*, which is consistent with direct detachment and the additional feature observed in the 3.10 eV spectrum has essentially disappeared. A small peak at *eKE* = 0 eV can still be identified, although this is much weaker compared to the spectra at the other two photon energies.

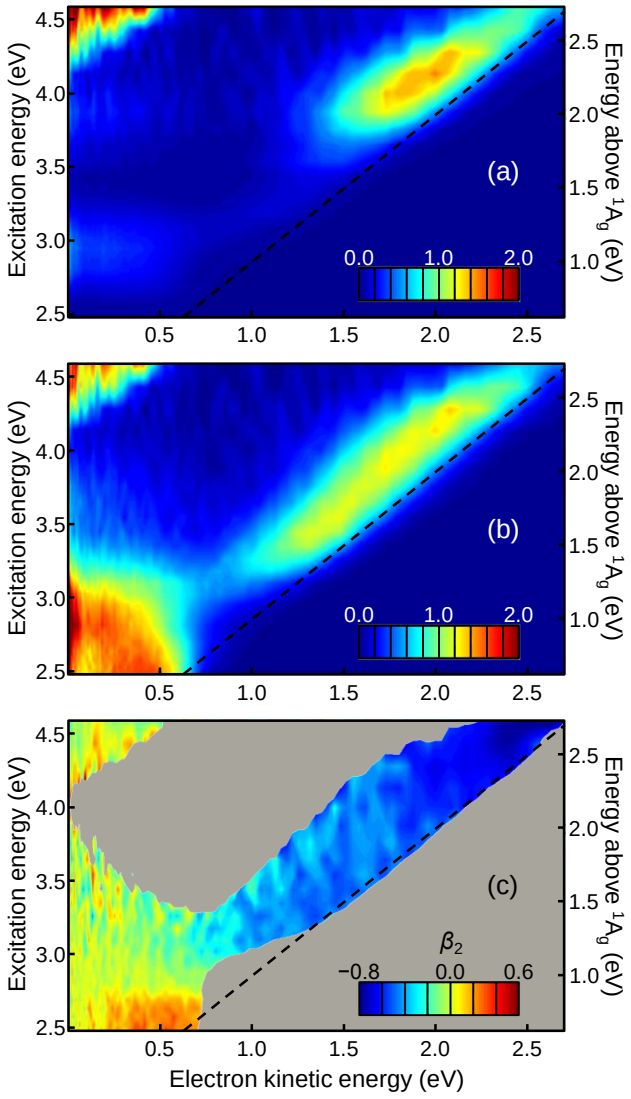

Figure 5.3 (a) Frequency-resolved PE spectra normalized to the total detachment cross section; (b) same as (a), although normalized to the total integrated PE signal in each spectrum; and (c) β_2 anisotropy parameter spectra as a function of excitation energy, where the shaded areas indicate regions with a normalized PE intensity of less than 0.375 a. u. The dashed line indicates the maximum PE kinetic energy available and the right-hand side axes indicate the energy above threshold.

To provide a complete overview for photon energies from 2.48 eV to 4.59 eV, the PE spectra are plotted in Figure 5.3(a) and (b) in false-color. In Figure 5.3(a), each PE spectrum has been normalized to the relative total PE cross sections of Brauman and co-workers.[27] The total integrated cross section increases rapidly for hv > 3.8 eV as evidenced by the prominence of the feature at high *eKE* in Figure 5.3(a). The cross section for direct detachment as a function of *eKE* is expected to be a smoothly increasing function and the sharp increase observed suggests that a resonance is accessed at these photon energies. At hv > 4.2 eV, a new feature emerges at low *eKE* which has been correlated with the excitation of excited states in the neutral following detachment.[21] The high *eKE* feature in this range scales linearly with photon energy as may be expected for a direct detachment PE feature. For hv < 3.3 eV, the PE spectra change quite dramatically indicative of processes occurring in the detachment continuum and therefore again pointing to resonances at these photon energies. However, the cross section in this energy range is significantly smaller than at higher photon energies.

To accentuate the spectral changes as a function of photon energy, in Figure 5.3(b), each PE spectrum has been normalized to the total area of that spectrum. This procedure illustrates that the *relative* intensities of PE features vary quite dramatically with excitation energy and clearly shows the changes in the PE spectra for hv < 3.3 eV. Specifically, at *eKE* < 0.1 eV, a maximum is observed for hv ~ 2.9 eV, and a second feature is observed in the 2.5 eV < hv < 3.3 eV spectra that on first inspection seems to have a decreasing *eKE* with increasing photon energy. Finally, no resolvable vibrational structure was observed in any of these PE spectra.

In addition to the spectral changes observed as a function of excitation energy, clear changes can be observed in the PADs. The PADs are quantified by the anisotropy

parameter (β_2) defined by equation (1.25). The β_2 spectra in Figure 5.3(c) include a five-point moving average. Regions for which the PE signal is below 0.375 (area normalized intensity units), at which level the uncertainty in determining the PADs becomes very large, have been shaded out. The dashed diagonal line in Figure 5.3 indicates the maximum *eKE* expected based on the known adiabatic electron affinity (AEA) of 1.86 eV.

5.4 Discussion

The PE signal in the lowest *eKE* window (< 0.1 eV) can be assigned to thermionic emission, as described in section 1.3.3. A broad peak centered around *eKE* ~0.4 eV is observed in all spectra with photon energies 2.5 eV < *hv* < 3.3 eV, although a small red-shift to *eKE* ~ 0.2 eV is observed around *hv* ~ 2.9 eV. Schiedt and Weinkauf have shown that at *hv* = 2.5 eV, the cross section to excitation of the ^2A_u shape resonance is significantly greater than direct detachment into the continuum. Hence, the feature at *eKE* ~ 0.4 eV can be assigned to autodetachment processes primarily from the ^2A_u shape resonance, with possible small contributions from the lower lying $^2B_{2u}$ Feshbach resonance. This is consistent with the observations of Stockett and Nielsen.[26] The calculated VDEs for autodetachment from the ^2A_u state to the ^1A_g state are 0.78 eV and 0.56 eV, considering $^2B_{2g}$ (anion ground state) and ^2A_u geometries, respectively – calculated energy levels are summarized in Figure 5.4. Detachment processes to higher vibrationally excited ^1A_g would shift these detachment distributions to lower *eKE*. However, there have been no reports of resolved vibrational structure in this PE band, even at 70 K.[21] Additionally, the presence of a thermionic emission feature at *eKE* = 0 eV suggests that the anion ground state can be recovered following excitation to the ^2A_u state. An intermediate strength conical intersection between the ^2A_u and the slightly

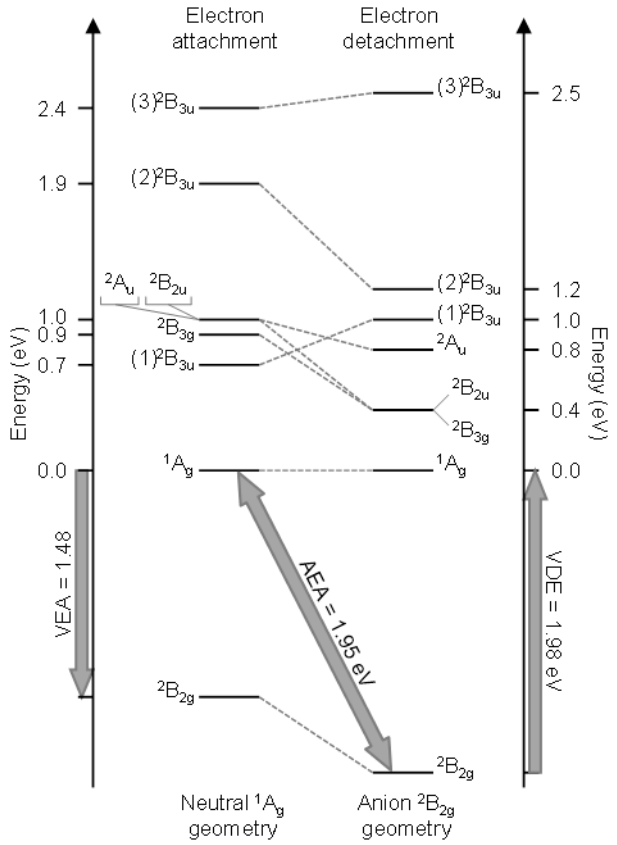

Figure 5.4 Calculated energy level diagram provided by Dr James Bull assuming ^1A_g neutral (left) and $^2B_{2g}$ anion (right) geometries. Energies given as vertical values with respect to the initial ground state; for the PE case, the photon energy is given by adding the electron affinity.

lower energy $^2B_{2u}$ state has been previously calculated,[15] which provides an internal conversion route between the two states. The small relative PE signal in the thermionic emission feature compared to the autodetachment peak (see Figure 5.3(b)) suggest, however, that the time-scale for internal conversion is longer. This would be in line with the fact that the ^2A_u state is a shape resonance and can thus be expected to lead to very fast autodetachment. Nevertheless, internal conversion can clearly compete as evidenced by the thermionic emission. In this process, the $^2B_{2u}$ (and possibly the $^2B_{3g}$) could be populated as an intermediate, which may also undergo autodetachment and could therefore contribute to the PE spectra around $h\nu$ = 2.5 eV. The calculated VDE for the $^2B_{2u}$ state is 0.23 eV and 0.57 eV, assuming the $^2B_{2g}$ and ^2A_u geometries,

respectively. Interestingly, the $^2B_{2u}$ Feshbach resonance in its equilibrium geometry is *bound* by around 0.52 eV. In fact, the calculated ADE is also slightly negative at 0.06 eV, although this includes zero within the estimated ± 0.1 eV error inherent in these calculations.

The spectral features associated with the ^2A_u state persist for photon energies up to $h\nu \sim 3.3$ eV, which are no longer resonant with the ^2A_u state. Indeed, the width of the ^2A_u state has previously been calculated to be 0.013 eV,[25] which is consistent with the width of the resonant peak in the photodetachment spectrum of Schiedt and Weinkauf.[16] The width of the excitation in our experiment is expected to be larger due to the ~ 300 K temperature of the anions in our experiment. Nevertheless, the range over which the spectral features are observed remains anomalously large. However, for 2.75 eV < $h\nu$ < 3.2 eV the *eKE* distribution shifts towards slightly lower *eKE* and is accompanied with a relative increase in the thermionic emission peak at *eKE* = 0 eV. The PADs clearly show that a new channel opens up at $h\nu$ = 2.75 eV. When $h\nu$ < 2.75 eV, β_2 = + 0.2 between 0.2 eV < *eKE* < 0.5 eV. This abruptly changes to β_2 = 0.0 between 2.75 eV < $h\nu$ < 3.2 eV over the same *eKE* range, while for *eKE* > 0.5 eV, β_2 is slightly negative. For a direct detachment process, gradual changes in anisotropy may be expected as partial waves with differing angular momentum interfere. Abrupt changes, as those observed here, point to sudden changes in the detachment process. At $h\nu$ = 2.5 eV, the excitation of the ^2A_u state leads to an alignment of the excited state ensemble, which may then undergo autodetachment on a timescale much faster than molecular rotation. The combination of alignment and the anisotropy expected for the autodetachment from the ^2A_u defines the observed PAD. This process persists up to $h\nu$ = 2.75 eV, where the anisotropy changes.

At $h\nu$ = 3.1 eV (400 nm), previous experiments and CASPT2 calculations have shown that the $(2)^2B_{3u}$ Feshbach resonance is excited and undergoes an internal conversion to the ^2A_u state on a ~20 fs timescale.[15] This assignment is consistent with the spectra in Figure 5.2(a) and (b), which both show autodetachment at *eKE* ~ 0.4 eV. Hence, a large part of the PE spectrum between 2.75 eV < $h\nu$ < 3.3 eV contains autodetachment from the ^2A_u state. The observation that the *eKE* of this autodetachment peak does not steadily increase with increasing photon energy suggests that the internal energy content of the ^2A_u (and $^2B_{2u}$) state is approximately conserved upon autodetachment into the $^1A_g + e^-$ continuum. Similar observations of non-shifting *eKE* features with $h\nu$ can be seen in the vibrational autodetachment from other anions[41,42] and in polyanions.[43-45] At first glance however, the abrupt change to β_2 = 0.0 for 2.75 eV < $h\nu$ < 3.2 eV is not consistent with the assignment of this peak to autodetachment from the ^2A_u state, as the same process is observed for $h\nu$ < 2.75 eV. However, the initially excited state for 2.75 eV < $h\nu$ < 3.2 eV is the $(2)^2B_{3u}$ state instead of the ^2A_u which is excited at $h\nu$ < 2.75 eV. This has a direct consequence as the transition dipole moments for excitation from the $^2B_{2g}$ ground state to the $(2)^2B_{3u}$ state and the ^2A_u state are orthogonal to each other. Hence, the initial $(2)^2B_{3u}$ excited state ensemble is aligned differently and, given that the internal conversion is much faster (~20 fs) compared to rotation, the autodetachment from the sequential ^2A_u state has a different laboratory-frame alignment. The abrupt changes in PADs around $h\nu$ = 2.75 eV might therefore be expected. At *eKE* > 0.5 eV, the anisotropy is negative and points to the fact that the higher energy peak of the PE spectrum (Figure 5.2(b)) corresponds to a different electronic state ($(2)^2B_{3u}$) than the peak around 0.4 eV (^2A_u), which provides additional support for our assignments.

In Figure 5.3(b), a maximum in the relative contribution of the thermionic emission peak (*eKE* = 0 eV) can be observed at *hv* ~ 2.9 eV. This maximum is concomitant with a minimum in direct detachment and suggests that the internal conversion at this energy is most efficient; the thermionic peak must result from internal conversion to the $^2B_{2g}$ electronic ground state of the radical anion. This maximum also coincides with the first broad peak in the total relative detachment cross sections measured by Brauman and co-workers. The observed increase in thermionic emission following excitation of the $(2)^2B_{3u}$ excited state relative to that following direct excitation of the ^2A_u state could occur through two mechanisms: (i) the $(2)^2B_{3u}$ state may undergo internal conversion directly to vibrationally hot $^2B_{2g}$ ground state; or (ii) the $(2)^2B_{3u}$ state may undergo internal conversion to a vibrationally excited ^2A_u, which in turn is able to undergo internal conversion (*via* the $^2B_{2u}$ state) to the $^2B_{2g}$ ground state more efficiently than the ^2A_u states produced by direct excitation. Calculations have identified a conical intersection that could funnel population directly into the $^2B_{2g}$ state. However, in order to access this intersection, a large out-of-plane motion is required. It is unlikely that this geometry could be accessed within the lifetime of the excited state based on the ~20 fs timescale of the internal conversion that was measured in time-resolved PE experiments.[15] The second mechanism, in which internal conversion to the ground state may be accelerated *via* internal conversion to the ^2A_u and $^2B_{2u}$ states, may thus be more likely. This latter mechanism would be promoted if the vibrational mode(s) coupling internal conversion out of the ^2A_u or $^2B_{2u}$ states are selectively excited following internal conversion from the $(2)^2B_{3u}$ state through the first conical intersection. Our calculations indicate that the $(2)^2B_{3u}$ geometry is more similar to the $^2B_{2u}$ state, while the $^2B_{2g}$ geometry is more similar to the ^2A_u state. Indeed, the PE spectrum following autodetachment for the two processes shows differences in the *eKE*

distribution, as the local maximum shifts from 0.2 eV to 0.4 eV following preparation of the $^2A_u/^2B_{2u}$ state by internal conversion from the $(2)^2B_{3u}$ state or optical excitation, respectively (see Figure 5.3(b)). It should also be noted that an additional conical intersection, also involving large out-of-plane motion, was identified between the ^2A_u and the $^2B_{2g}$ ground state that may only be accessible when large amounts of internal energy in the ^2A_u state are available and this may also explain the enhanced re-population of the ground state to produce the thermionic emission peak.[15] Finally, we have also calculated a slightly lower-lying $(1)^2B_{3u}$ state, which has predominantly shape resonance character but it has a negligible oscillator strength. In previous calculations, the ordering of these two $^2B_{3u}$ states was reversed because of the diffuse nature of the orbitals involved. As this $(1)^2B_{3u}$ state may be close in energy to the optically prepared $(2)^2B_{3u}$ state and of the same symmetry, it is not unreasonable to expect that this state may also play some role in the internal conversion dynamics from the excited $(2)^2B_{3u}$ state.

At 3.3 eV < *hv* < 4.2 eV, Figure 5.3(b) shows the relative intensity of the constant *eKE* feature compared to the higher *eKE* features quickly diminishes with increasing photon energy. The higher *eKE* features shift with increasing photon energy as might be expected from a direct detachment process. However, the increase in total cross section in Figure 5.3(a) for *hv* > 3.5 eV suggest an additional resonance in this energy range, which correlates with the broad shoulder centered at ~4 eV in the Brauman and co-workers photodetachment spectrum. The highest *eKE* feature does show evidence of a trend discontinuity at this energy, where the maximum of the peak has shifted to slightly lower *eKE*. Further, there remains a small thermionic contribution to the PE spectra, all implying either a broad absorption spectrum of the lowest $(2)^2B_{3u}$ Feshbach resonance or the appearance of a new channels correlating with the higher

energy resonance. Finally, for $h\nu \sim 3.9$ eV, PE features can be discerned in Figure 5.3(a) with $eKE < 0.5$ eV that appear similar to those observed at lower excitation energy that were assigned to autodetachment from the ^2A_u state.

The most likely candidate for the observed increase in cross section at $h\nu > 3.5$ eV is an optically bright $(3)^2B_{3u}$ state. No other states with appreciable oscillator strength are located between this state and the $(2)^2B_{3u}$ state. The $(3)^2B_{3u}$ state has predominantly shape resonance character, which suggests that autodetachment is likely to be fast from this state. Nevertheless, one would anticipate some changes in the Franck-Condon envelope to the neutral ground state, as observed by Schiedt and Weinkauf following ^2A_u autodetachment, which would account for the slight deviations in vertical binding energy of this peak around $h\nu \sim 4$ eV. Additionally, there is evidence for internal conversion to form intermediate states and the presence of thermionic emission at $eKE = 0$ eV. The relatively low yield of low energy electrons may be because of fast autodetachment or because internal conversion is not as efficient. The latter can be consolidated by the large energetic gap between the $(3)^2B_{3u}$ and lower excited states.

The PADs in the 3.5 eV $< h\nu <$ 4.2 eV vary monotonically from $\beta_2 = -0.5$ to -0.6, although the negative anisotropy is already evident at $h\nu = 3.0$ eV associated with autodetachment from the $(2)^2B_{3u}$ state. Given that the autodetachment is from a state of the same symmetry, it is not unreasonable to anticipate similar PADs for these two processes. Smooth variations with eKE are expected as the weighting of different partial waves are kinetic energy dependent.

At $h\nu = 4.2$ eV, new channels open that lead to the formation of neutral excited states. A number of states that these could correspond to have been identified and include the lowest lying $^3B_{1g}$, ^3A_u and $^1B_{1g}$, ^1A_u states.[37] Some of these states may be

accessed directly from the ground state or may be formed following autodetachment from the $(3)^2B_{3u}$ state. In addition to the formation of excited neutral pBQ, there is evidence of thermionic emission reappearing for $h\nu$ > 4.2 eV. However, it is difficult to disentangle this from the intense features at low *eKE*. Our PE spectra do not show clear evidence for peaks that would identify intermediate states in this internal conversion process, although again, some of this may be obscured by the emergence of PE peaks leading to several different neutral excited states. The presence of the high *eKE* peak diminishes for $h\nu$ > 4.2 eV, relative to the lower *eKE* peaks suggesting that the excitation is no longer resonant with the $(3)^2B_{3u}$ state at these energies. However, the cross section data of Brauman and co-workers indicates that an additional sharp increase in cross section is observed for higher photon energies. Experimentally, it becomes difficult to measure high-quality PE spectra for photon energies above ~5 eV (~250 nm) in the current set-up because laser flux from our OPO system rapidly decreases at shorter wavelengths and noise associated with the UV light increases.

The frequency-resolved PE energetics and interpretations can also be compared with literature electron transmission and attachment spectra.[46] The primary difference between these two techniques, aside from the two processes not complying to exactly the same selection rules,[47,48] is that they probe different initial geometries; PE spectroscopy initially prepares excited states assuming the geometry of the ground state anion, while electron attachment probes anion resonances from the neutral geometry. Moreover, it is generally observed in electron attachment experiments that shape resonances exhibit attachment cross sections up to several-fold larger than similar Feshbach resonances, which might be intuitively expected within the framework of Koopmans' theorem.[48] Similarly, autodetachment lifetimes for shape resonances are typically much faster than those of Feshbach resonances. In the limit of the anion and

neutral geometries being similar (*i.e.* VEA ~VDE), the energetics produced from these two techniques should be comparable. For pBQ, the VEA and VDE differ by ~0.5 eV and our calculations indicate there are also changes in the relative energetics of several of the active resonances. Figure 5.4 summarises all calculated energies assuming the ^1A_g ground state neutral and $^2B_{2g}$ ground state anion equilibrium geometries, respectively.

Electron attachment spectra have indicated three low-energy resonances centred around 0.7 eV, 1.4 eV, and ~2.0 eV.[12-14] Of particular interest are the detailed experiments of Allan, identifying a number of specific vibrational excitations associated with several of these bands.[8,9] The electronic symmetry assignments of these three electron attachment resonances have been the subject of some controversy between different authors, primarily because assignments considered (erroneous) Koopmans' theorem energetics. Dr Bull's calculations indicate that the 0.7 eV band probably corresponds to a $(1)^2B_{3u}$ shape resonance calculated at 0.68 eV; the 1.4 eV band to the ^2A_u shape resonance calculated at 1.01 eV (and to some extent the $^2B_{2u}$ Feshbach resonance calculated at 1.03 eV); and the ~2.0 eV (weakest) band to the $(2)^2B_{3u}$ Feshbach resonance calculated to lie at 1.86 eV. The latter band may also have some contribution from the $(3)^2B_{3u}$ shape resonance, calculated at 2.4 eV.

In general, the electron attachment resonances are considerably broader than those from photoexcitation and detachment. Energetic agreement between the second 1.4 eV band and *ab initio* calculations is not ideal considering the very good agreement between all other calculated and experimental energies, and may indicate the involvement of some other processes. Of note, configuration interaction (SAC) calculations of Nakatsuji and co-workers,[22] which have been considered as theoretical references in a number of experimental studies, have assignments of the $(1)^2B_{3u}$ and

$(2)^2B_{3u}$ states reversed; overall the energetics calculated in this work are in significantly better agreement with experiment.

The electron attachment energetics can be compared with those for the associated PE experiments (Figure 5.4), with the most important change being the convergence of the two lowest $^2B_{3u}$ states within 0.2 eV of each other assuming the anion geometry. Optically, the $(1)^2B_{3u}$ is not directly accessible, although its participation in the dynamics *via* internal conversion cannot be ruled out. The large separation in energy between the $(2)^2B_{3u}$ and $(3)^2B_{3u}$ states in the anion geometry is observed in Figure 5.3(a) as a region where direct detachment probably dominates the PE spectra. It is somewhat fortuitous that the PE spectra of the Wang group were collected at 3.496 eV and 4.661 eV, where the former lies within this gap such that the PE spectrum probably represents that without significant perturbations of autodetachment processes from resonances.

Finally, the time-resolved electron-energy-loss spectra of Allan assuming electron impact energies resonant with the band at ~2.0 eV or the $(2)^2B_{3u}$ Feshbach resonance, identified two detachment channels; a fast channel limited by the experimental resolution, and a much slower thermionic or so-called 'non-specific' vibrational excitation channel. These observations are in agreement with our earlier time-resolved PE measurements and the spectra recorded in this work, in that efficient internal conversion and energy redistribution can produce a population of ground state anions that statistically detaches to the neutral. The fast channel can be correlated with autodetachment from the excited states. Similar to our PE spectra, the thermionic signal was also observed by Allan when the electron energy was tuned over the lower lying resonances, although this apparently occurred on shorter statistical detachment timescales than for the higher ~2.0 eV band. Further, Allan noted strong excitation of a

few specific vibrations over the three resonances, which usually indicate a large change of equilibrium geometry. Apart from the lowest-lying $(1)^2B_{3u}$ shape resonance, it is indeed the case that for the $(2)^2B_{3u}$ Feshbach and ^2A_u shape resonances, the $^2B_{2g}$ anion geometry is closer to their equilibrium geometry than the ^1A_g neutral equilibrium geometry. It may therefore be that the lack of vibrational structure in our PE spectra compared with the electron attachment spectra is, in part, reflective of varying Frank-Condon factors. It is possible that the internal temperature of our anions obscures the vibrational structure, although we again note that vibrational structure was not observed in PE spectra obtained at 70 K.[21]

In summary, the electron attachment spectra broadly agree with our frequency-resolved PE spectra, although the number of accessible states, and ultrafast dynamical timescales mean that detailed comparisons are difficult. The primary advantage of frequency-resolved PE imaging presented here is that the dynamics occurring on the excited states can be clearly identified through changes in the PE spectra as a function of excitation energy. In some respects, our methodology is analogous to two-dimensional electron impact studies, which to the best of our knowledge has only been demonstrated for electron attachment to N_2, CO_2 and C_3H_3N.[29-31] The additional dimension provided by the angular distributions in frequency resolved PE imaging offers even greater insight. As demonstrated here, the PADs can be very sensitive to changes in the symmetry of the resonances involved. Currently, only a qualitative discussion was offered. However, it should be possible to more formally calculate the differential electron ejection probability. This can be done by using, for example, the Dyson orbital approach, which works well for resonances in which only a single excitation dominates.[49,50] However, the calculation of PADs for more complex Feshbach resonance processes and autodetachment processes in general requires further

theoretical input. The extension of anion PE imaging to the time-domain using femtosecond lasers allows the dynamics of very short-lived temporary negative ions to be studied in real-time and, combined with high-level *ab initio* calculations, ultimately provides the most detailed understanding of the dynamics. Finally, an important advantage of the frequency-resolved PE imaging approach presented here is that the range of systems that can be studied is almost infinite. We have demonstrated that electrospray can be a very useful method for the generation of radical anions. As such, the technique can be scaled up to larger systems and subsequently used to probe the anionic resonances of the closed-shell neutral species.[51]

5.5 Summary

Frequency-dependent PE imaging to map-out resonances in the radical anion continuum can reveal excited state dynamics through both trends in the PE spectra and *via* anisotropies in the electron angular distributions. Changes in the PE spectra following the excitation of a resonance can be assigned to autodetachment from the prepared state that leads to changes in the Franck-Condon window to the final neutral states or internal conversion to lower lying states that subsequently autodetach. The additional information obtained through the PADs clearly identifies the involvement of resonances; similar changes in PADs have been observed in vibrational autodetachment of anions.[41,42] In principle, PADs can be calculated using, for example, the relevant Dyson orbitals.[49,50] However, when autodetachment occurs from resonances and interference can occur with direct detachment channels, these methods become more difficult to apply and additional development on the theoretical front is required to capture changes in the PADs.

The methodology presented in this chapter can, in general, be applied to any system with a sufficiently positive adiabatic electron affinity to electrospray in good yield. Such processes are comparable with inelastic electron impact experiments and provide complementary information that enable the identification of above-threshold dynamics and the appearance of resonances. Electronic structure calculations and/or theoretical models are necessary to fully exploit the information provided by the frequency-resolved PE imaging, and this is particularly the case when there is a significant geometrical change between the ground states of the neutral and anion. As a final summary, frequency-resolved PE imaging has several key advantages over conventional electron attachment or transmission experiments: (i) the identification of intermediate electronic states with higher confidence; (ii) the addition of the angular electron ejection information; (iii) the ability to extend to the time-domain using femtosecond laser sources allowing the dynamics to be probed in real-time; and (iv) anion preparation using electrospray can be easily applied to larger molecular systems that would be otherwise difficult to produce in the gas phase in abundant and stable number densities.

5.6 References

(1) El-Najjar, N.; Gali-Muhtasib, H.; Ketola, R. A.; Vuorela, P.; Urtti, A.; Vuorela, H. *Phytochemistry Reviews* **2011**, *10*, 353.

(2) Nohl, H.; Jordan, W.; Youngman, R. J. *Advances in Free Radical Biology and Medicine* **1986**, *2*, 211.

(3) Brunmark, A.; Cadenas, E. *Free Radical Biology and Medicine* **1989**, *7*, 435.

(4) Closs, G. L.; Miller, J. R. *Science* **1988**, *240*, 440.

(5) Kurisu, G.; Zhang, H.; Smith, J. L.; Cramer, W. A. *Science* **2003**, *302*, 1009.

(6) Iverson, T. M.; Luna-Chavez, C.; Cecchini, G.; Rees, D. C. *Science* **1999**, *284*, 1961.

(7) Fukuzumi, S. *Bulletin of the Chemical Society of Japan* **2006**, *79*, 177.

(8) Allan, M. *Chemical Physics* **1983**, *81*, 235.

(9) Allan, M. *Chemical Physics* **1984**, *84*, 311.

(10) Modelli, A.; Burrow, P. D. *Journal of Physical Chemistry* **1984**, *88*, 3550.

(11) Strode, K. S.; Grimsrud, E. P. *Chemical Physics Letters* **1994**, *229*, 551.
(12) Christophorou, L. G.; Carter, J. G.; Christodoulides, A. A. *Chemical Physics Letters* **1969**, *3*, 237.
(13) Collins, P. M.; Christophorou, L. G.; Chaney, E. L.; Carter, J. G. *Chemical Physics Letters* **1970**, *4*, 646.
(14) Cooper, C. D.; Naff, W. T.; Compton, R. N. *Journal of Chemical Physics* **1975**, *63*, 2752.
(15) Horke, D. A.; Li, Q.; Blancafort, L.; Verlet, J. R. R. *Nature Chemistry* **2013**, *5*, 711.
(16) Schiedt, J.; Weinkauf, R. *Journal of Chemical Physics* **1999**, *110*, 304.
(17) Pshenichnyuk, S. A.; Asfandiarov, N. L.; Fal'ko, V. S.; Lukin, V. G. *International Journal of Mass Spectrometry* **2003**, *227*, 281.
(18) Asfandiarov, N. L.; Pshenichnyuk, S. A.; Fokin, A. I.; Nafikova, E. P. *Chemical Physics* **2004**, *298*, 263.
(19) El Ghazaly, M. O. A.; Svendsen, A.; Bluhme, H.; Nielsen, S. B.; Andersen, L. H. *Chemical Physics Letters* **2005**, *405*, 278.
(20) Siegert, S.; Vogeler, F.; Weinkauf, R. *Zeitschrift Fur Physikalische Chemie-International Journal of Research in Physical Chemistry & Chemical Physics* **2011**, *225*, 507.
(21) Fu, Q.; Yang, J.; Wang, X.-B. *Journal of Physical Chemistry A* **2011**, *115*, 3201.
(22) Honda, Y.; Hada, M.; Ehara, M.; Nakatsuji, H. *Journal of Physical Chemistry A* **2002**, *106*, 3838.
(23) Weber, J.; Malsch, K.; Hohlneicher, G. *Chemical Physics* **2001**, *264*, 275.
(24) Pou-Amerigo, R.; Serrano-Andres, L.; Merchan, M.; Orti, E.; Forsberg, N. *Journal of the American Chemical Society* **2000**, *122*, 6067.
(25) Kunitsa, A. A.; Bravaya, K. B. *Journal of Physical Chemistry Letters* **2015**, *6*, 1053.
(26) Stockett, M. H.; Nielsen, S. B. *Physical Chemistry Chemical Physics* **2015**, *Accepted*.
(27) Comita, P. B.; Brauman, J. I. *Journal of the American Chemical Society* **1987**, *109*, 7591.
(28) Marks, J.; Comita, P. B.; Brauman, J. I. *Journal of the American Chemical Society* **1985**, *107*, 3718.
(29) Regeta, K.; Allan, M. *Physical Review Letters* **2013**, *110*, 203201.
(30) Currell, F.; Comer, J. *Physical Review Letters* **1995**, *74*, 1319.
(31) Reddish, T.; Currell, F.; Comer, J. *Journal of Physics E-Scientific Instruments* **1988**, *21*, 203.
(32) Roberts, G. M.; Nixon, J. L.; Lecointre, J.; Wrede, E.; Verlet, J. R. R. *Review of Scientific Instruments* **2009**, *80*, 053104.
(33) Schmidt, M. W.; Baldridge, K. K.; Boatz, J. A.; Elbert, S. T.; Gordon, M. S.; Jensen, J. H.; Koseki, S.; Matsunaga, N.; Nguyen, K. A.; Su, S. J.; Windus, T. L.; Dupuis, M.; Montgomery, J. A. *Journal of Computational Chemistry* **1993**, *14*, 1347.
(34) Frisch, M. J.; Trucks, G. W.; Schlegel, H. B.; Scuseria, G. E.; Robb, M. A.; Cheeseman, J. R.; Scalmani, G.; Barone, V.; Mennucci, B.; Petersson, G. A.; Nakatsuji, H.; Caricato, M.; Li, X.; Hratchian, H. P.; Izmaylov, A. F.; Bloino, J.; Zheng, G.; Sonnenberg, J. L.; Hada, M.; Ehara, M.; Toyota, K.; Fukuda, R.; Hasegawa, J.; Ishida, M.; Nakajima, T.; Honda, Y.; Kitao, O.; Nakai, H.; Vreven, T.; Montgomery Jr., J. A.; Peralta, J. E.; Ogliaro, F.; Bearpark, M. J.; Heyd, J.; Brothers, E. N.; Kudin, K. N.;

Staroverov, V. N.; Kobayashi, R.; Normand, J.; Raghavachari, K.; Rendell, A. P.; Burant, J. C.; Iyengar, S. S.; Tomasi, J.; Cossi, M.; Rega, N.; Millam, N. J.; Klene, M.; Knox, J. E.; Cross, J. B.; Bakken, V.; Adamo, C.; Jaramillo, J.; Gomperts, R.; Stratmann, R. E.; Yazyev, O.; Austin, A. J.; Cammi, R.; Pomelli, C.; Ochterski, J. W.; Martin, R. L.; Morokuma, K.; Zakrzewski, V. G.; Voth, G. A.; Salvador, P.; Dannenberg, J. J.; Dapprich, S.; Daniels, A. D.; Farkas, Ö.; Foresman, J. B.; Ortiz, J. V.; Cioslowski, J.; Fox, D. J.; Gaussian, Inc.: Wallingford, CT, USA, 2009.

(35) Kendall, R. A.; Dunning Jr., T. H.; Harrison, R. J. *Journal of Chemical Physics* **1992**, *96*, 6796.

(36) Dunning Jr., T. H. *Journal of Chemical Physics* **1989**, *90*, 1007.

(37) Schreiber, M.; Silva-Junior, M. R.; Sauer, S. P. A.; Thiel, W. *Journal of Chemical Physics* **2008**, *128*, 134110.

(38) Merrick, J. P.; Moran, D.; Radom, L. *Journal of Physical Chemistry A* **2007**, *111*, 11683.

(39) Granovsky, A. A. *Journal of Chemical Physics* **2011**, *134*, 214113.

(40) Pople, J. A.; Head-Gordon, M.; Raghavachari, K. *Journal of Chemical Physics* **1987**, *87*, 5968.

(41) Schneider, H.; Vogelhuber, K. M.; Schinle, F.; Stanton, J. F.; Weber, J. M. *Journal of Physical Chemistry A* **2008**, *112*, 7498.

(42) Mbaiwa, F.; Wei, J.; Van Duzor, M.; Mabbs, R. *Journal of Chemical Physics* **2010**, *132*, 134304.

(43) Xing, X.-P.; Wang, X.-B.; Wang, L.-S. *Journal of Physical Chemistry A* **2010**, *114*, 4524.

(44) Butcher, C. P. G.; Johnson, B. F. G.; McIndoe, J. S.; Yang, X.; Wang, X.-B.; Wang, L.-S. *Journal of Chemical Physics* **2002**, *116*, 6560.

(45) Horke, D. A.; Chatterley, A. S.; Verlet, J. R. R. *Journal of Chemical Physics* **2013**, *139*, 084302.

(46) Jordan, K. D.; Burrow, P. D. *Chemical Reviews* **1987**, *87*, 557.

(47) Goddard III, W. A.; Huestis, D. L.; Cartwright, D. C.; Trajmar, S. *Chemical Physics Letters* **1971**, *11*, 329.

(48) Allan, M. *Helvetica Chimica Acta* **1982**, *65*, 2008.

(49) Oana, C. M.; Krylov, A. I. *Journal of Chemical Physics* **2007**, *127*, 234106.

(50) Oana, C. M.; Krylov, A. I. *Journal of Chemical Physics* **2009**, *131*, 124114.

(51) Bull, J. N.; West, C. W.; Verlet, J. R. R. *Chemical Science* **2015**, *6*, 1578.

Chapter 6. Photoelectron Spectroscopy of Carboxylic Acids

In this chapter, the PE spectra of a number of carboxylic acids, concentrating on; phenylcarboxylic acids with varying lengths of aliphatic and conjugated carbon chains; systems with π-conjugation chains; and biologically relevant molecules, are presented. In the saturated phenyl carboxylic acids, the PE spectra at 4.13 eV appears similar to equivalent spectra of a simple organic aliphatic chain carboxylic acid. However, a PE feature at low eKE *with a magnitude that increased with the length of the carbon chain linking the phenyl group and the carboxylic acid was observed. This was assigned to the interaction between the carboxylic acid group and the hydrogen in the* para *position on the phenyl, which becomes stronger as the carbon chain length increases. For the unsaturated carboxylic acids, the spectra were dominated by a statistical emission peak at low eKE. This was ascribed to initial photoexcitation of a π* ← π transition, followed by efficient internal conversion to the ground electronic state. As the lifetime of the internal conversion process is likely to be considerably shorter than the duration of the laser pulse, the vibrationally excited electronic ground state produced can then lose an electron by thermionic emission, or absorb additional photons and decay back to the ground state, leading to thermionic emission and/or unimolecular dissociation.*

An anomalous sharp peak was observed in the PE spectrum of octatrienoic acid and assigned to photodetachment of hydride. H^- ions were directly observed via velocity-map imaging, and the mechanism of H^- loss was assigned to a statistical process on the ground state. The PE spectra of tryptophan and tyrosine were found to differ significantly, which was assigned to differences in the relative cross-section for direct photodetachment between the molecules.

The interpretation of the PE spectra in this chapter is supported by DFT calculations performed by Dr James Bull.

6.1 Introduction

The carboxylic acid is the proto-typical example of a weak acid and has been employed in a vast array of applications.[1,2] The ready deprotonation of the carboxyl group to form the carboxylate anion in water and other polar solvents has led to widespread use of carboxylic acids in applications such as surfactants, dyes, flavourings[1,2] and the development of large water soluable carbon nanomaterials, such as graphene,[3,4] buckminsterfullerenes[5,6] and nanotubes.[7,8] In nature, examples of carboxylic acids are extremely widespread and, most notably, include amino acids, the 'building blocks' of proteins.[9] From a gas-phase spectroscopic view, however, it can provide an efficient and non-destructive pathway from the solution phase to the gas phase.[10-13]

A variety of mass-spectroscopic methods have been employed in order to produce a number of gaseous molecules and ions for study by a variety of analytical techniques.[10-12,14-16] PE spectroscopy is a useful gas phase technique for studying the electronic properties of charged particles and neutrals, which can also be easily extended to time-resolved PE spectroscopy. TRPES is a powerful tool for probing the dynamics of excited states in real time and is particularly useful in the study of anions; the lower ionisation potentials involved in studying anions allows for probing of the ground electronic state at lower photoexcitation energies. A great variety of systems have been studied by this method, as discussed in Chapter 1. Nevertheless, the impetus on the gas phase community has been to attempt to generate and study ever larger molecules, in particular biological molecules such as proteins. Many traditional techniques, such as laser ablation and heating,[10] create harsh environments for the

molecules and often lead to fragmentation of the target molecule.[10] Electrospray ionisation is notable for being a 'soft' technique, that can produce gas phase molecules with minimal fragmentation[11-13,17] and has been extensively coupled with PE spectroscopy.[18-20] However, the method requires an ionic species of interest. Carboxylic acids are therefore of interest, as they may often be fairly easily attached to a molecule and, particularly in biomolecules, are often an intrinsic part of the molecule itself.[9,21,22]

For the addition of a carboxylic acid group to serve as an efficient labiliser for large, complex molecules to the gas phase, we must first ensure that the carboxyl group does not affect the excited state structure of the chromophore and merely serves as a spectator anion to lower the ionisation energy of the neutral chromophore.[23] However, no systematic studies have been performed in order to investigate the interaction between a charged group and the electronic structure of a chromophore. As the size of the systems studied increases and particularly in systems where carboxylic acids are widespread (such as proteins), it is necessary to understand the influence of the carboxylic acid on the excited states of the molecule. In this chapter, we present a series of PE spectra of deprotonated carboxylic acids attached to a series of saturated and unsaturated carbon chains and a phenyl group to act as a chromophore. These systems are then compared to biologically relevant anions: the amino acids tryptophan and tyrosine, which both contain a CO_2^- moiety and an indole group or a phenol group respectively, and to all-*trans*-retinoic acid (ATRA), which is an unsaturated carbon chain conjugated to a terminal CO_2^-. A TRPES study of the excited state dynamics of ATRA is then presented.

A number of gas phase PE studies of carboxylic acids have been previously reported in the literature.[24-37] As discussed, electrospray ionisation is the method of choice for the production of the gaseous ions, due to the ready depronation of

carboxylic acids in basic solution.[13] By far the most comprehensive study on carboxylic acids was performed by the Wang group and focussed on dicarboxylic acid dianions.[25-28,30-34] In this, it was shown that the repulsive Coulomb barrier as measured by PE spectroscopy may be used as an intramolecular ruler,[25,26] that the PE angular anisotropy is dependent upon the geometry of the repulsive Coulomb barrier[31-33] (as shall be discussed in greater depth in Chapter 8) and to demonstrate the interplay between intramolecular charge repulsion, intramolecular strain and solvation.[28] While it must be noted that the carboxylic acid is not a necessity to labilise species, as evidenced by similar PE imaging studies on sulfonate dianions,[38-40] the observations of the Wang group were wide ranging and included measurements of several mono-carboxylic acids and indications of dynamics occuring following photoexcitation.

6.2 Experimental Details

The experiment was performed as described in Chapter 2. All chemicals were purchased from Sigma Aldrich and used without further purification. Isolated deprotonated anions were produced by ESI (~1 mM in MeOH, adjusted to pH ~11 by the addition of 2 M NH_3 in MeOH). The ion packet was pulsed out of the trap at 10 Hz, mass selected by time-of-flight, and subsequently irradiated at the centre of a velocity-map-imaging PE spectrometer. All PE spectra were collected via irradiation by nanosecond laser pulses generated by the Horizon OPO operating at 10 Hz and delivering ~5 ns pulses at 4.13 eV (300 nm) and 4.66 eV (266 nm). Above 4.13 eV, a considerable amount of PE noise is observed and so an additional PE image is collected, in which the laser, but not the ions, is fired through the spectrometer. The resultant image is then subtracted from the PE image colected with ions in order to recover the PE distribution. The experimental images were deconvoluted using the polar-onion

peeling algorithm[41] in order to extract the PE spectra. The spectral resolution of the PE spectrometer is ~ 5% and has been calibrated using the PE spectrum of I^-.

In addition to experiments, DFT calculations were performed by Dr James Bull to explore the minimum energy structures and relative energetics between isomers of molecules, as discussed below. For this we have employed CAM-B3LYP//aug-cc-pVDZ level of theory using Gaussian 09.

6.3 Phenyl-Carboxylic Acids

6.3.1 Results

Presented in the bottom panel of Figure 6.1 are the PE spectra of the range of phenyl-carboxylic acids of the form $C_6H_5(CH_2)_nCO_2^-$ (where n = 1 – 5, 7), varying by the length of the carbon chain between the carboxylic acid and the phenyl group, taken at photoexcitation energies of 4.13 eV (300 nm) and 4.66 eV (266 nm). The range has been chosen so that the carboxylic acid group is not expected to be conjugated to the π system located on the phenyl. For comparison, three additional PE spectra are presented: the 4.13 eV (300 nm) and 4.66 eV (266 nm) spectra of benzoic acid (n = 0), where the carboxylic acid is conjugated to the phenyl group, and the 4.13 eV spectrum of butyric acid, which provides an example of a PE spectrum of an organic carboxylic acid with no interacting groups. The PE spectra are fairly uniform across the range n = 1-5,7, although a peak at low *eKE* is observed to increase with n.

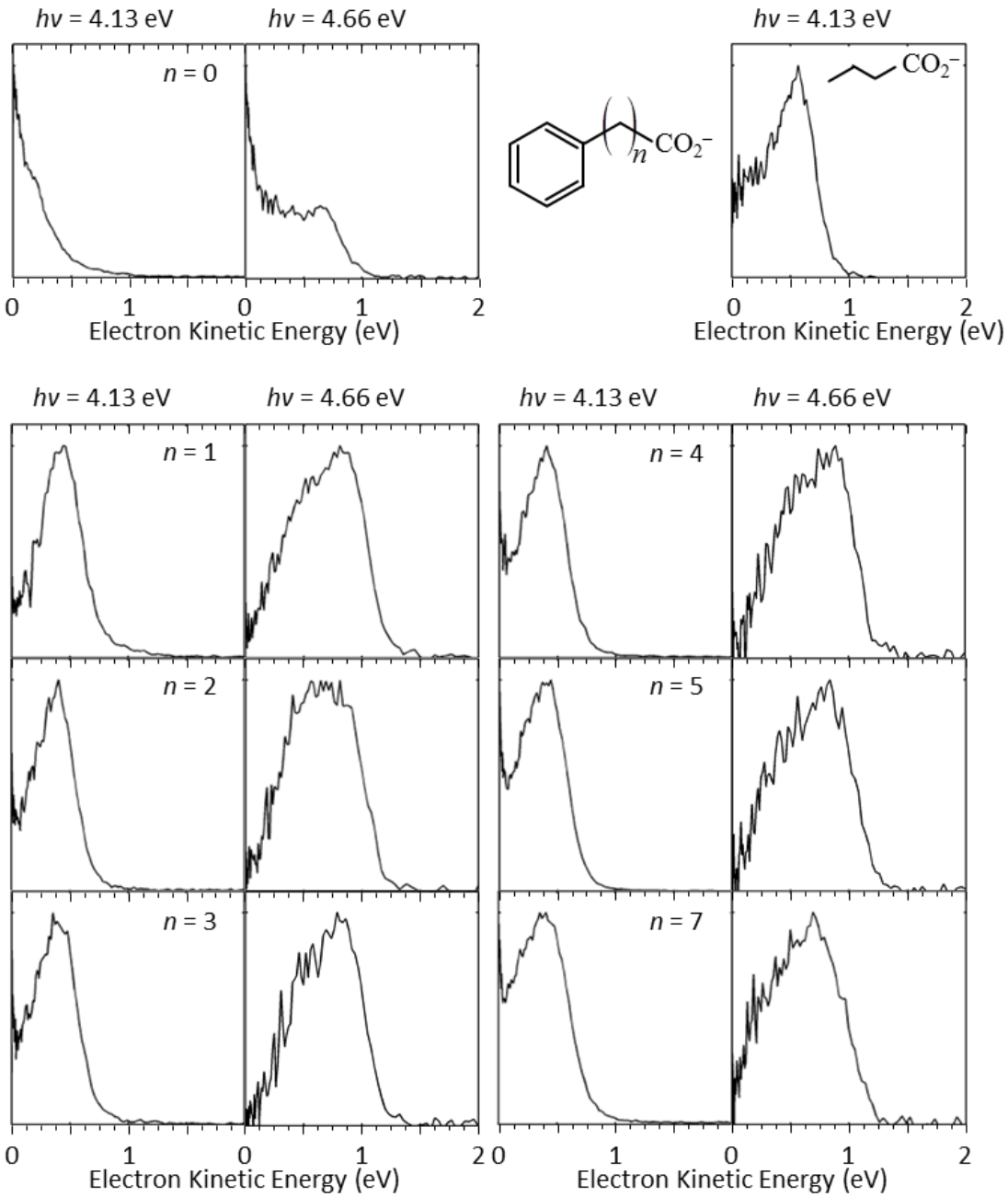

Figure 6.1 Normalised PE spectra of butyric acid at 4.13 eV (300 nm) and a range of phenyl-carboxylic acids at 4.13 eV (300 nm) and 4.66 eV (266 nm). The number of linker CH_2 groups between the phenyl group and the carboxylic acid group is given by *n*, where *n* = 0-5, 7.

6.3.2 Discussion

Figure 6.1 presents the PE spectra for butyric acid, which acts as a representative, isolated in terms of π-conjugation, CO_2^- group in an organic molecule, and a series of carboxylic acids of the form $C_6H_5(CH_2)_nCO_2^-$, where *n* = 0-5, 7. For $n \geq$

1, the PE spectral profiles at both photoexcitation wavelengths are extremely similar and the 4.13 eV (300 nm) spectra are broadly consistent with the spectral profile of butyric acid at this wavelength. The major peak in the spectra can be assigned to direct detachment into the continuum of an electron from the highest lying molecular orbital, which is localised on the CO_2^- group.[29] The detachment energetics are slightly shifted in the phenyl-carboxylic acids comparative to butyric acid; the adiabatic detachment energy (ADE) of $C_6H_5(CH_2)_1CO_2^-$ is determined to be 3.37 ± 0.10 eV, whereas the ADE of butyric acid is measured as 3.25 ± 0.10 eV. The ADE for butyric acid is in excellent agreement with the value determined for the acetoxyl radical at 3.250 ± 0.010 eV.[29]

The PE spectra at 4.66 eV (266 nm) exhibit a single peak with a bimodal distribution, consistent with the observations of the detachment spectra of similar molecules.[20,21,24] The high energy peak of the bimodal distribution in the PE feature is consistent with photodetachment to produce the ground and first electronic excited states of the radical neutral molecule, which are separated by 0.17 eV in the acetoxyl radical. The lower energy peak corresponds to photodetachment to the second electronic excited state of the radical, which is calculated to lie 0.7 eV above the ground state.[29] The photoexcitation energy at 4.13 eV is insufficient for vertical detachment to the second excited state of the radical for the phenyl-carboxylic acids, although the second peak is observed in the butyric acid spectrum as the detachment energy is slightly lower. As such, the 4.13 eV spectra are dominated by the feature corresponding to direct detachment. With increasing *n*, the direct detachment peak in the 4.13 eV spectra exhibits slight broadening towards the low *eKE* side and a new feature, with a maximum at *eKE* = 0 eV, is observed at $n \geq 2$. This feature increases in intensity relative to the direct detachment peak as *n* increases. Neither the broadening of the

corresponding direct detachment peak nor the low *eKE* feature are observed in the corresponding 4.66 eV spectra. By delaying the timing of the MCP gate by tens of nanoseconds, hence delaying the time at which the PE image is acquired, it was observed that the low *eKE* peak completely disappears. This indicates that the low *eKE* peak is not a result of thermionic emission.

A possible explanation for the observation of electrons at *eKE* = 0 eV is that we are accessing a resonance of the π-system following photoexcitation at 4.13 eV. The excited state population produced may then undergo some above-threshold dynamics, leading to delayed emission of low *eKE* electrons.[16,45,46] However, the onset of the $\pi^* \leftarrow \pi$ transition on the phenyl group accessed lies at 4.6 eV in benzene[42] and at 4.5 eV in phenylacetic acid.[43] Not only is it unlikely that these resonances are accessible at 4.13 eV, even with the intrinsic thermal energy of the ions (~0.3 eV), but photoexcitation at 4.66 eV is expected to be resonant with this transition. As such, if the peak at *eKE* = 0 eV is a result of dynamics on the π* state, a larger effect might be expected following excitation at 4.66 eV than at 4.13 eV, which is not the case.

In an attempt to quantitatively describe the trend in the low *eKE* peak of the 4.13 eV spectra, we have performed a fit of the normalised spectra at all *n*. First, the spectra were fitted to two Gaussian peaks over the energy range 0.04 eV < *eKE* < 0.75 eV in order to avoid the peak at 0 eV. The fit was then expanded to include an exponential decay over the energy range 0 eV < *eKE* < 0.75 eV, keeping the parameters for the Gaussians constant. An example of each fitting procedure for *n* = 4 is shown in Figure 6.2. The spectral profiles are recovered well by both fitting regimes within the selected energy ranges for all *n*. The fitting parameters, such as the centre and width of the Gaussians, are reasonably similar across the PE spectra, with two significant exceptions:

first, the amplitude of the low energy Gaussian and hence the relative contribution of this peak to the area of the overall spectrum increases with *n*, as shown in Figure 6.2(e).

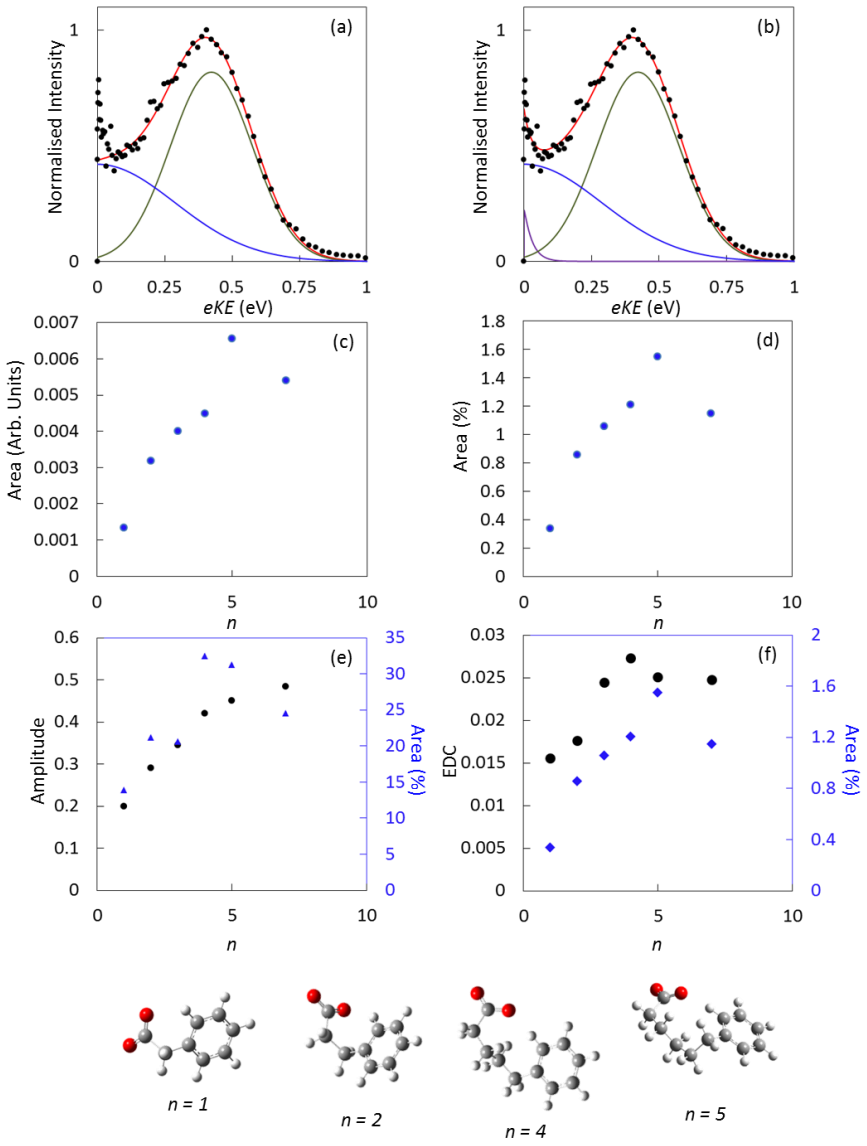

Figure 6.2 Examples of the (a) 2 Gaussian and (b) 2 Gaussian and an exponential decay fit of the 4.13 eV spectrum of n = 4. Total sum of (c) the integrated PE signal in the range 0 eV < *eKE* < 0.04 eV of the experimental PE spectrum less the 2 Gaussian fit and (d) the integrated area of the exponential decay from the second fit, as a percentage of the overall fit. (e) amplitudes of the lower energy Gaussian, (f) lifetimes of the exponential decay and relative contributions of each function to the overall area of the fit. Bottom: Minimum energy geometries of selected phenyl-carboxylic acids.

Additionally, the exponential decay constant (EDC) of the exponential decay initially increase with n before reaching a stable plateau, as shown in Figure 6.2(f). This

reflects the increase in the size of the low energy peak with increasing *n*. The integrated area of the spectra in the range 0 eV < *eKE* < 0.04 eV, minus the 2 Gaussian fit and the contribution of the exponential function to the total fit, increase with *n*. This reflects the increase in the contribution of the low *eKE* peak to the spectrum with increasing *n*. The increase in the contribution of the low *eKE* Gaussian reflects the observed peak broadening with increasing *n*.

By inspection of the PE spectra of butyric acid and $C_6H_5(CH_2)_1CO_2^-$, aside from the shift in *eBE*, the CO_2^- group appears to be uninfluenced by the phenyl ring. However, spectral broadening is observed with increasing *n*, implying both that the phenyl group and CO_2^- group do in fact interact and that the magnitude of the interaction is dependent upon *n*. Given the innate ability of aliphatic hydrocarbon chains to rotate about the sp^3 hybridised carbons,[23,25] as *n* increases the hydrocarbon chain length increases and becomes increasingly flexible. This flexibility allows the CO_2^- group to interact with the phenyl group more readily.

In order to explore the feasibility of this mechanism, DFT calculations of the energy differences between the straight chain conformer of $C_6H_5(CH_2)_nCO_2^-$ and a conformation where the chain is bent so that the CO_2^- group may interact with the phenyl group were performed by Dr James Bull. The minimum energy structural isomers are presented in Figure 6.2. Crucially, an oxygen in the CO_2^- group forms a weak hydrogen bond with the hydrogen on the *ortho* position of the phenyl group even at $n = 1$. The energy differences between the two conformers and the bond distance between the interacting O in the CO_2^- group and the phenylic hydrogen for $1 < n < 5$ are tabulated in Table 6.1.

$Ph(CH_2)_nCO_2^-$	n = 1	n = 2	n = 3	n = 4	n = 5
ΔE (eV)	–	–0.05	–0.11	–0.13	–0.17
R (Å)	2.350	2.238	2.190	2.094	2.065

Table 6.1 Energy difference between the lowest energy (bent) isomer and straight isomer for $Ph(CH_2)_nCO_2^-$ and distance between terminal O atom on CO_2^- group to the phenyl H atom in the para position (R). Both are given as a function of chain length, *n*, and show a decreasing trend.

As *n* increases, the energy of the bent conformer decreases relative to the straight chain conformer and the hydrogen bond distance clearly decreases. These trends are clearly consistent with the observed broadening of the major feature in the PE spectra at 4.13 eV, as shown in Figure 6.2(e-f). Experimentally, however, we will expect to sample a range of conformers as our ions are thermalized to ~300 K, and the number of potential conformers increases factorially with *n*. Despite this, it is clear that the probability of the molecule adopting a configuration in which the CO_2^- group may interact with the phenyl group increases with *n*. We therefore assign the observed peak broadening to the interaction between the HOMO located on the CO_2^- group with the phenyl group, although we note that the VDE does not exhibit any significant trend with *n*.

Additionally, the trends are also consistent with the overall increase in the feature at *eKE* = 0 eV with increasing *n*, as shown in Figure 6.2(c-d), which suggests that this feature is also linked to the CO_2^--phenylic hydrogen interaction. We must note that our analysis in this region is subject to a significant error due to the processing method of the raw velocity map images. Nevertheless, the increase in this feature with *n* is clearly observed. As the cross-section for photodetachment at threshold (*eKE* = 0 eV) is 0 by the Wigner threshold laws,[44] zero-energy PEs are not expected to be observed by direct photodetachment of anions;[44,45] this suggests that the low energy feature arises from an indirect process.

As the presence of the phenyl group appears to induce the mechanism, we must consider the possibility that the phenyl group acts as an electron acceptor and results in

a degree of charge-transfer from the CO_2^- group to the phenyl ring. In this, the phenyl would accept an electron into a π^* orbital and subsequently undergo dynamics, resulting in delayed autodetachment leading to the low energy electrons observed. However, this requires the production of PEs with kinetic energies resonant with the π^* orbital; isolated benzene has a negative electron affinity of –1.12 eV,[46] hence electrons of ~1 eV would in principle be required to access the necessary orbital. The emitted electrons at 4.13 eV have *eKE* < 0.8 eV and are therefore outside of the requisite range. The emitted electrons at 4.66 eV do have sufficient energy, however, and the absence of the low energy peak at this photoexcitation energy provides further evidence against this mechanism.

Conversely, the electron affinity of deprotonated benzene is positive at + 1.10 eV.[47] As such, the π^* orbital could in principle be accessed by the PEs liberated following photoexcitation at 4.13 eV. In order to access this, an excited state proton transfer from the *para* position on the phenyl ring to the carboxylic acid group could occur, and has been postulated for the model GFP chromophore dimer anion by the Andersen group.[48] This would also explain the absence of evidence of any indirect processes in the 4.66 eV spectra; the PE spectra are essentially identical with the exception of n = 7, which does exhibit some broadening. No low energy PEs are observed, despite the production of PEs with kinetic energies comparable to those produced by photodetachment at 4.13 eV. This suggests that the mechanism is initiated following excitation by a photon in a specific energy range, which in turn implies that the mechanism involves excitation to a specific resonance. However, the *ab initio* calculations required to confirm the plausibility of this mechanism are beyond the scope of this thesis and the postulated mechanism remains speculation.

6.4 π-Conjugated Carboxylic Acids

6.4.1 Results

Figure 6.3 presents the PE spectra recorded at 4.13 eV (300 nm) and 4.66 eV (266 nm) for 2,4-hexadienoic acid, 2,4,6-octatrienoic acid, benzoic acid and 4-phenylbut-2-enoic acid (*trans*-cinnamic acid). In these, a delocalised π-system is conjugated to the carboxylic acid group. 2,4-Hexadienoic acid and 2,4,6-octatrienoic acid provide a π-system along a straight carbon chain, whereas benzoic acid and *trans*-cinnamic acid provide examples where the carboxylic acid is conjugated directly to the phenyl group. All spectra have the general appearance of an exponential decay peaking at *eKE* = 0 eV, with additional features at higher *eKE*. The features below ~1 eV can be ascribed to direct detachment processes, whereas those with higher energy almost certainly arise from multiple photon transitions. In order to highlight these features, each PE spectrum is cut off at a intensity of 10% of the maximum PE intensity and presented inset to the relevant PE spectra.

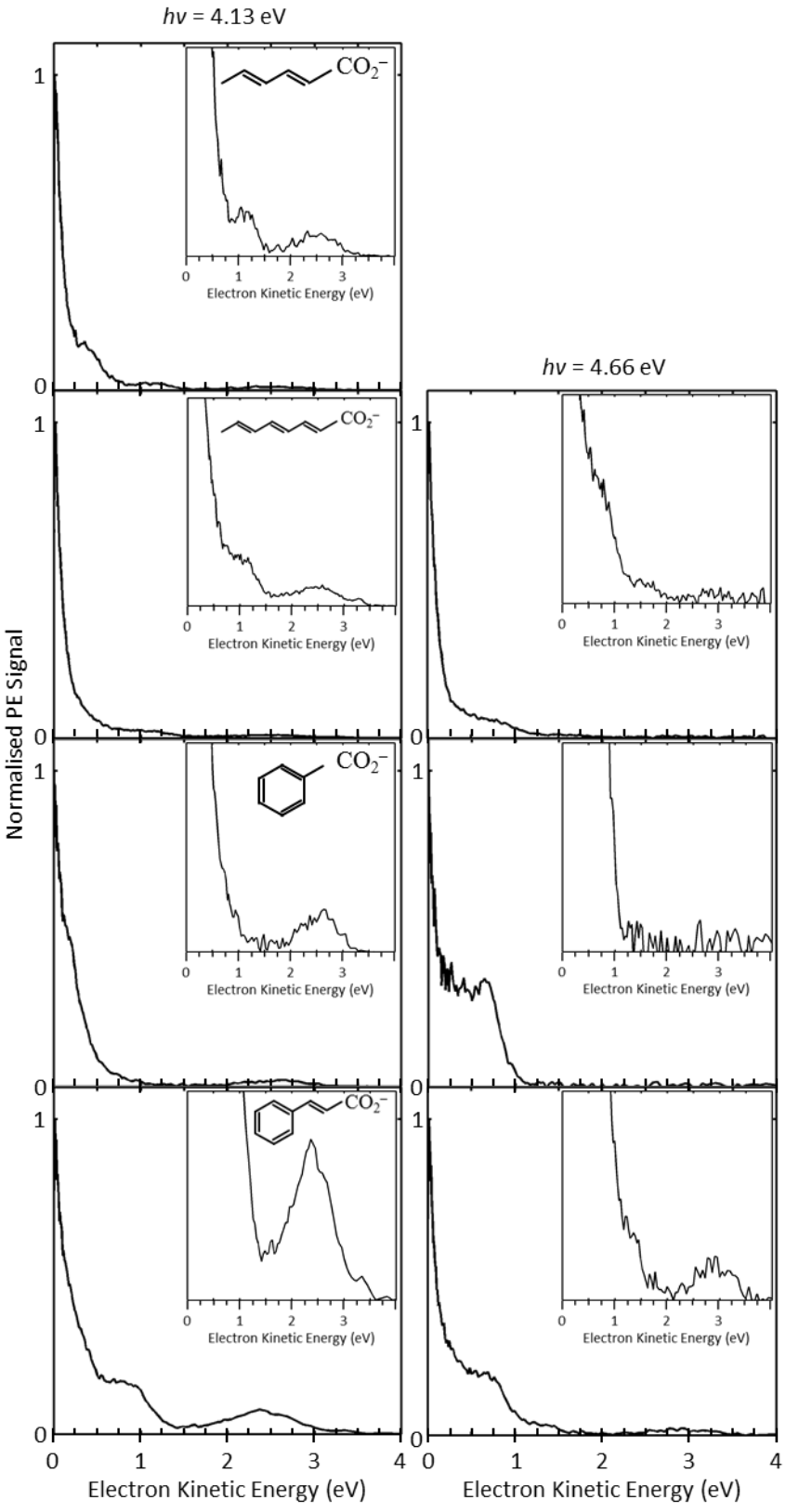

Figure 6.3 Normalised PE spectra of (in descending order) hexadienoic acid, octatrienoic acid, benzoic acid and *trans*-cinnamic acid at 4.13 eV (300 nm) and 4.66 eV (266 nm). Inset to each spectrum is the lowest 10% of the spectrum in order to highlight the high energy peaks in the spectra.

6.4.2 Discussion

The PE spectra of all measured π-conjugated carboxylic acids taken at both 4.13 eV (300 nm) and 4.66 eV (266 nm) are dominated by a peak at *eKE* = 0 eV, as is shown in Figure 6.3. The observation of this low energy peak, as with the low energy peak observed in the phenylcarboxylic acids, implies the involvement of an indirect electron detachment process. It is likely that at both photoexcitation energies, the photon is resonant with the $\pi^* \leftarrow \pi$ transition in the extended π-system, which is expected for all systems except for deprotonated benzoate, as the onset of the solution phase absorption spectrum occurs at ~ 4.1 eV.[49] No gas phase absorption spectrum is available for benzoate, but the assumption that the solution phase absorption spectrum is blue shifted from that in the gas phase is not unreasonable. In general, the spectra appear to have the form of an exponential decay from 0 eV with a shoulder visible at higher *eKE* that is blue-shifted as the photoexcitation energy increases. An exception is *trans*-cinnamic acid, in which the shoulder appears to red-shift with increasing photoexcitation energy. This is likely due to overlapping features in the PE spectrum, potentially from multiple photon processes, combining to produce an artificially high peak following excitation at 4.13 eV. Indeed, the exponential feature appears more prominent at higher *eKE*s, which would blue-shift the observed shoulder. The exponential decay is consistent with the spectral form of statistical emission, indicating that the excited states involved in the detachment process are extremely short lived. This also raises the possibility that multiple photons are absorbed over the duration of the laser pulse.

The additional feature observed in the spectra at higher *eKE* is consistent with a direct detachment feature, given the increase in *eKE* as the photoexcitation energy increases. However, the peaks of the direct detachment features are generally consistent with those observed in Figure 6.1. A notable exception to this is the detachment peak of

benzoate. Nevertheless, the consistency implies that the presence of a π-system does not exert a significant influence on the HOMO despite the conjugation of the π-system to the carboxylic acid, although the same does not appear to hold for a conjugated phenyl group.

The observation of a direct detachment feature coupled with the involvement of excited states in the photoemission spectrum is significant, as both excitation energies exceed the vertical detachment energy (~3.5 eV) of the carboxylic acid group determined from the unconjugated phenyl-carboxylic acids. As such, the initially excited states would be able to undergo autodetachment. Fast autodetachment could feasibly contribute a considerable proportion of the PE intensity to the peak previously assigned to direct detachment. However, the size of the low energy peak relative to the intensity of the higher *eKE* feature suggests that fast internal conversion is the dominant decay pathway of the excited state, which has previously been observed in gas phase polyenes.[73,74]

Presented inset to the PE spectra in Figure 6.3 are the PE curtailed in intensity to highlight the weak PE features above *eKE* ~ 1 eV, which must arise from almost simultaneous multiple photon absorption. These indicate that the initial photoexcitation energies are resonant with an excited state. No similar resonance is observed for the $C_6H_5(CH_2)_nCO_2^-$ systems, indicating that the resonance arises from the presence of the π-system. Notably, the multiple-photon peak, whilst present in all 4.13 eV spectra, is absent from some 4.66 eV spectra. This may be due to the increased noise present in the 4.66 eV obscuring the signal, or the decrease in the fluence of the pulses (the 4.13 eV pulses are ~ 5 times more powerful than those at 4.66 eV).

6.5 Photodissociation of Octatrienoic Acid to yield H^-

6.5.1 Results

In addition to the predominant electron loss channel observed in all conjugated carboxylic acids leading to slow electrons, octatrienoic acid exhibits another, somewhat unexpected relaxation mechanism. In the PE spectrum at 4.13 eV (300 nm), a weak feature (~1% of the height of the maximum peak in the spectrum) is observed at *eKE* = 3.4 eV. Despite the small size of the peak, the feature is very sharp and the width of the feature is essentially limited by the resolution of the spectrometer. This is surprising for a molecule as large as octatrienoic acid, as features so sharp are typically observed in atomic anions. In contrast to the isotropic distributions observed in all of the PE images of the conjugated acids, the feature corresponding to this peak exhibits extremely strong positive anisotropy parallel to the polarisation axis ($\beta_2 \sim 2$). This again is uncommon for molecules without a large degree of symmetry and is a typical feature of atomic anions, which suggests that, following photoexcitation at 4.13 eV, the octatrienoic acid is undergoing fragmentation to produce an atomic anion. Octatrienoic acid consists of only three elements, so we can readily assign the PE feature to photodetachment of H^- at 4.13 eV.[50] The electron affinity of H is 0.754195(19) eV[51] and, as photodetachment corresponds to the loss of an s electron, the symmetry of the outgoing electron must be a p-wave ($l = 1$),[52,53] which would result in a strongly anisotropic PE image as we have observed.

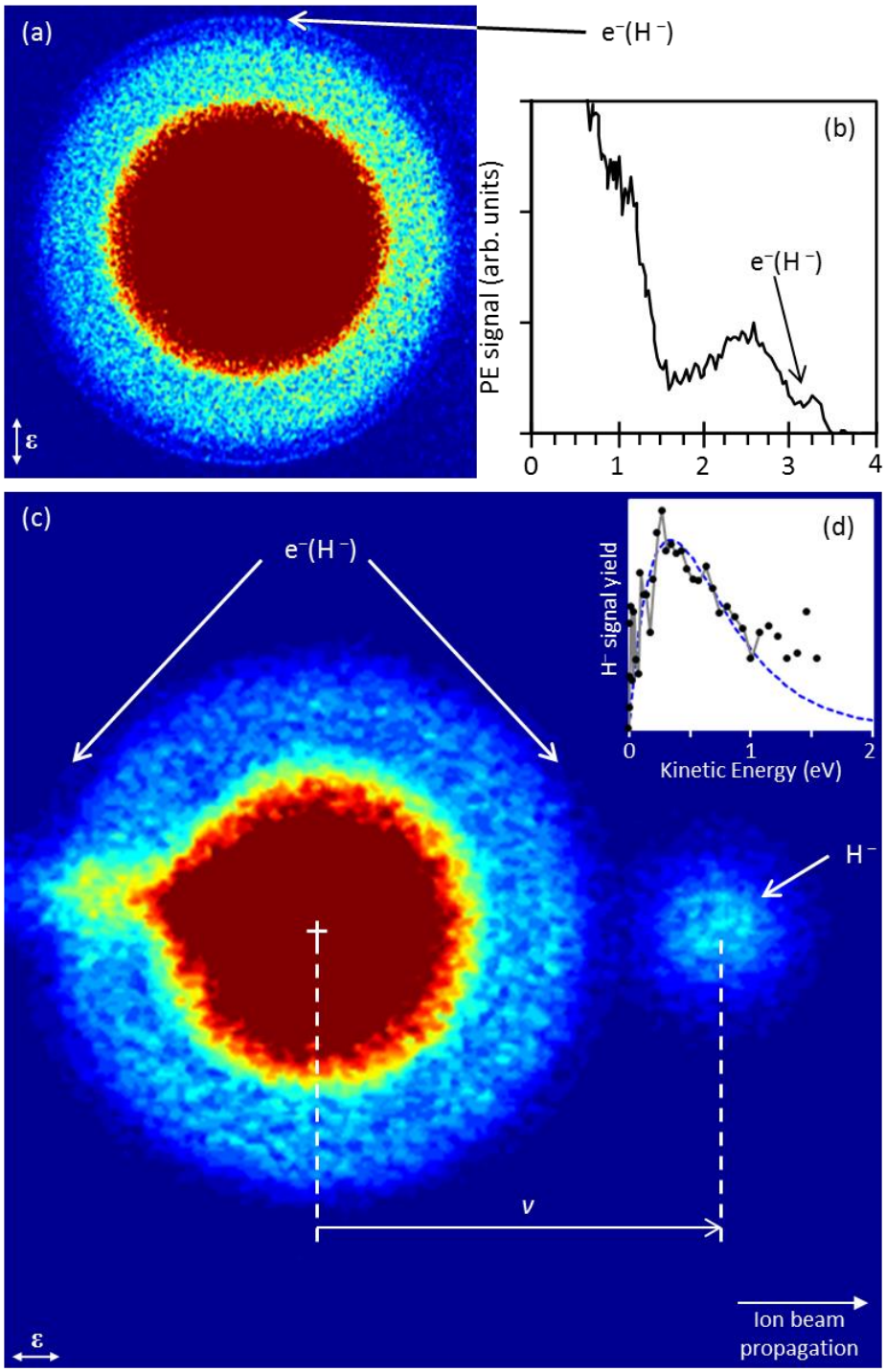

Figure 6.4 (a) The 4.13 eV (300 nm) PE image of deprotonated octatrienoic acid, scaled to highlight the anisotropic PE feature due to H^- photodetachment. The laser polarisation axis, **ε**, is indicated by an arrow. (b) PE spectrum obtained from (a), scaled to highlight the peak from H^-. (c) Velocity map image obtained at a higher VMI voltage and a longer MCP gate in order to observe the H^- fragment in addition to the PE spectrum at 4.13 eV, where the cross marks the centre of the electron image and *v* is the velocity of the parent ion beam, whose propagation axis is shown. (d) Kinetic energy release spectrum of H^- derived from (c), where the dashed line is a simulated Boltzmann distribution as a guide to the eye.

6.5.2 Discussion

Hydride loss is an unexpected channel as it is typically not thermodynamically favoured; that is, following photoexcitation at 4.13 eV and internal conversion to a vibrationally hot state, unimolecular fragmentation to produce H^- is not expected to occur on a timescale sufficient to compete with internal vibrational energy redistribution, dissociation of CO_2 or H and thermionic emission. Moreover, in order to observe photodetachment from H^-, the fragmentation process must occur on a timescale faster than the laser pulse duration (~ 5 ns).

We must therefore consider the possibility that the H^- loss channel is occurring on an excited state surface. The most compelling evidence is the fact that we do not observe a corresponding feature in the 4.66 eV PE spectrum, which suggests that the hydride loss channel is an excited state process accessed through photoexcitation to a resonance. However, the 4.66 eV PE spectrum is significantly noisier than that at 4.13 eV and it is possible that the noise simply obscures the spectrum. However, should the dissociation occur on the ground electronic state surface, H^- would most likely be liberated by a statistical mechanism, as internal vibrational energy redistribution typically occurs on a picosecond timescale. The kinetic energy available to the H^- in this case would be expected to be small and have a Boltzmann distribution.[54] Additionally, the angular distribution of emission would be isotropic with respect to the laser polarisation. In contrast, should fragmentation be an excited state process, one might expect to see a significant release of kinetic energy to the H^- in a non-Boltzmann distribution. The angular distribution of emission could also feasibly be anisotropic. This behaviour has been seen for excited state H atom dissociation.[55] We must therefore attempt to measure the distribution of emitted H^- following photoexcitation.

Although the experiment has not been designed to probe fragments, our velocity-map imaging detector can in principle detect any charged particle and is limited only by the voltages applied. As such, H^- may be observed on the detector, offset from the centre of the electron image along the propagation axis of the ion beam due to the difference in the time-of-flight along the VMI apparatus between an electron and H^-.

In order to observe H^-, it was necessary to both extend the gate on the MCP (to 1000 ns from 200 ns for the PE images) and increase the initial repelling voltage (to 1500 V from 500 V for the PE images) to account for the extended time-of-flight of H^- compared to an electron. The resultant PE image at 4.13 eV (300 nm) is presented in Figure 6.4(c). The PE image is similar to that obtained by using the original VMI settings with two new features observed in the image: a line of increased PE signal on the left of the PE image and a second spot to the right of the PE image. The feature to the left arises from thermionic emission of PEs on a timescale on the order of at least hundreds of nanoseconds. Our ion packet is not stationary, but moving with ~ 1.3 keV of kinetic energy and so passes out of the region where the velocity-map imaging condition is maintained approximately 100 ns following photoexcitation. The presence of this feature therefore confirms our observation of thermionic emission and ground state recovery following photoexcitation: thermionic emission typically occurs on a μs timescale,[56,57] resulting in slow electrons being liberated from the ion packet outside of the region where the VMI condition holds. These electrons are then repelled backwards relative to the direction of propagation of the ion beam and result in the characteristic line observed in our image. This has also been observed in SIMION simulations of our VMI spectrometer. The second spot arises from H^- impacting onto the MCP detector. The offset of the centre of the H^- image from the centre of the PE image provides a direct calibration for the kinetic energy of the H^-; the initial velocity of both H^-,

assuming no release of kinetic energy to the fragment, is the same as the velocity of the ion beam, which we have determined to be 4.8×10^4 m s^{-1} for octatrienoic acid. The offset in pixels between the centres of the PE and H^- images is therefore proportional to this velocity (assuming that the centre of the PE image is the true v = 0 m s^{-1} centre of the VMI apparatus) and can therefore be used to calibrate the kinetic energy release spectrum of H^-.

We have re-centred the image onto the centre of the H^- image and performed the image deconvolution routine in order to extract the kinetic energy release spectrum of H^-, which is shown in Figure 6.4(d). The spectrum is broad, devoid of fine structure and appears to follow a Boltzmann distribution. Given that the H^- angular distribution is entirely isotropic, these observations suggest that H^- loss is a statistical process occurring on the ground state. This is consistent with the observation of thermionic emission and ground state recovery observed in the PE spectra. Unfortunately, we cannot discern any information about the mechanism of H^- elimination by our current experiment, beyond our assignment that it is a ground state process.

6.6 Amino Acids: Tryptophan and Tyrosine

Finally, in Figure 6.5, the PE spectra of two deprotonated biological chromophores, the amino acids tryptophan and tyrosine, at 4.13 eV (300 nm) and 4.66 eV (266 nm) are shown. The excited state dynamics of these molecules have been of considerable interest, as both exhibit fluorescence following UV excitation and can therefore be used as an *in situ* fluorescent probe in order to study protein structure.[58] While both amino acids have a π-conjugated chromophore (an indole group in tryptophan and a phenoxy group in tyrosine), the chromophore is not conjugated to the carboxylic acid group in either species. Nevertheless, the PE spectrum of tryptophan is

remarkably similar to those of the π-conjugated acids in Figure 6.3, in particular those of deprotonated benzoate and *trans*-cinnamic acid, implying some degree of interaction between the carboxylic acid and the π-system on the indole group.

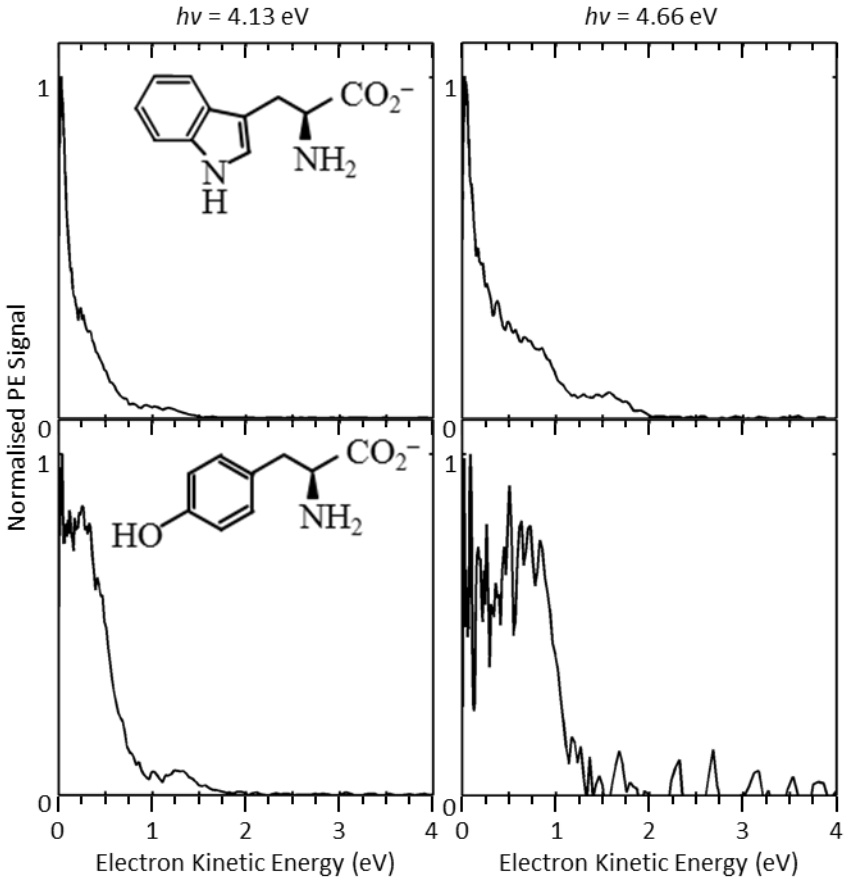

Figure 6.5: PE spectra of Tryptophan (top row) and Tyrosine (bottom row) at 4.13 eV (left column) and 4.66 eV (right column).

The solution phase absorption spectrum of deprotonated tryptophan has an onset at ~ 4.1 eV and a maximum at 4.43 eV,[21] corresponding to excitation of the π* ← π transitions of indole. Although the absorption and fluorescence spectra of tryptophan are red shifted in the gas phase,[59] indicating a change in the electronic structure of the gaseous molecule from the solution phase, we might expect both photoexcitation energies used to be resonant with an excitation on the tryptophan chromophore, which, crucially, lies above the adiabatic electron affinity of the carboxylic acid group and is hence unbound with respect to electron detachment. The similarity of the spectra to the

conjugated carboxylic acids therefore has two possible explanations: that the carboxylic acid group can couple to the excited state of the indole group and subsequently undergo electron loss, or that the resonance on the indole group provides an efficient pathway through internal conversion back to the ground electronic state of the anion. The ground state produced would retain some energy as vibrational excitation and could absorb additional photons and relax down to the ground electronic, but vibrationally hot state numerous times until the system either undergoes dissociation or thermionic emission of an electron, resulting in the statistical emission feature observed in the PE spectra of tryptophan and in Figure 6.3.

The spectroscopy of deprotonated tyrosine is complicated by the presence of an additional deprotonation site on the phenoxy group. However, the obtained PE spectra would seem to indicate that the carboxylic acid is deprotonated preferentially to the phenoxy group; the vertical binding energy (ADE) of the phenoxy anion is 2.37 eV,[47] which is considerably lower than the observed ADE of 3.48 eV from the 4.66 eV (266 nm) PE spectrum in Figure 6.5. Indeed, no PE features corresponding to photodetachment from the phenoxy anion are observed in either of the PE spectra of tyrosine. The observed PE spectra are consistent with the previously measured spectrum by Tian *et al.*[22] and are broadly consistent with the PE spectra of photodetachment of a carboxylate group as observed in Figure 6.1 and in Figure 6.3. The 4.13 eV spectrum clearly shows that the both the direct detachment peak and the low *eKE* peak expected from photodetachment from a carboxylate group, although the spectrum at 4.66 eV shows a considerable reduction in the contribution from the low *eKE* peak. Tian *et al.* determined through calculations and mass spectrometric measurements that deprotonated tyrosine produced via electrospray ionisation exists in a ratio of 30:70 of carboxylate anions to phenoxide anions.[22] Assuming that our instrument produces the

anions in a similar ratio, the absence of phenoxide in our PE spectra indicates that the photodetachment cross-section of the carboxylate group is far higher than the phenoxy group, which is again consistent with the observations of Tian *et al.*[22]

The PE spectra of deprotonated tryptophan and tyrosine initially appear quite dissimilar; the PE spectra of tryptophan resembles those where the carboxylic acid is conjugated to an extended π-system (Figure 6.3), whereas the spectra of tyrosine resemble those of the unconjugated carboxylic acids (Figure 6.1) more closely. This could be related to the resonant excitation of the $\pi^* \leftarrow \pi$ transition on the indole group in tryptophan. However, the absorption spectrum of tyrosine has an onset of ~ 4.3 eV and an absorption maximum between 4.4-4.5 eV,[60] corresponding to the $\pi^* \leftarrow \pi$ transition of phenol, hence we might expect excitation at 4.66 eV to be resonant with this transisiton. Despite this, the PE spectrum at 4.66 eV of tyrosine indicates that the predominant channel is direct detachment from the carboxylate group. Alternatively, as the excited state is unbound with respect to electron detachment, the resonance may undergo extremely fast autodetachment with very little energy redistribution on the excited state surface, leading to the direct detachment-like PE spectrum.

Nevertheless, the differences between the PE spectra of the two species might be explained by the difference in the relative cross-section of the direct detachment process. Assuming that the major feature in the PE spectra of tryptophan arises from statistical emission, one may then fit and subtract an exponential decay to the spectrum, as shown in Figure 6.6. The resultant PE feature is extremely similar to the spectra of tyrosine and to the unsaturated phenylcarboxylic acids at both wavelengths. This suggests that the difference in the spectra arises from the presence of an efficient decay mechanism from the $^1\pi\pi^*$ excited state located on the indole group of tryptophan to the ground state that is preferentially excited compared to the direct detachment channel.

The PE spectrum of tyrosine is dominated by direct detachment from the electronic ground state or possibly fast autodetchment from the excited state accesed by photoexcitation of the $\pi^* \leftarrow \pi$ transition of phenol.

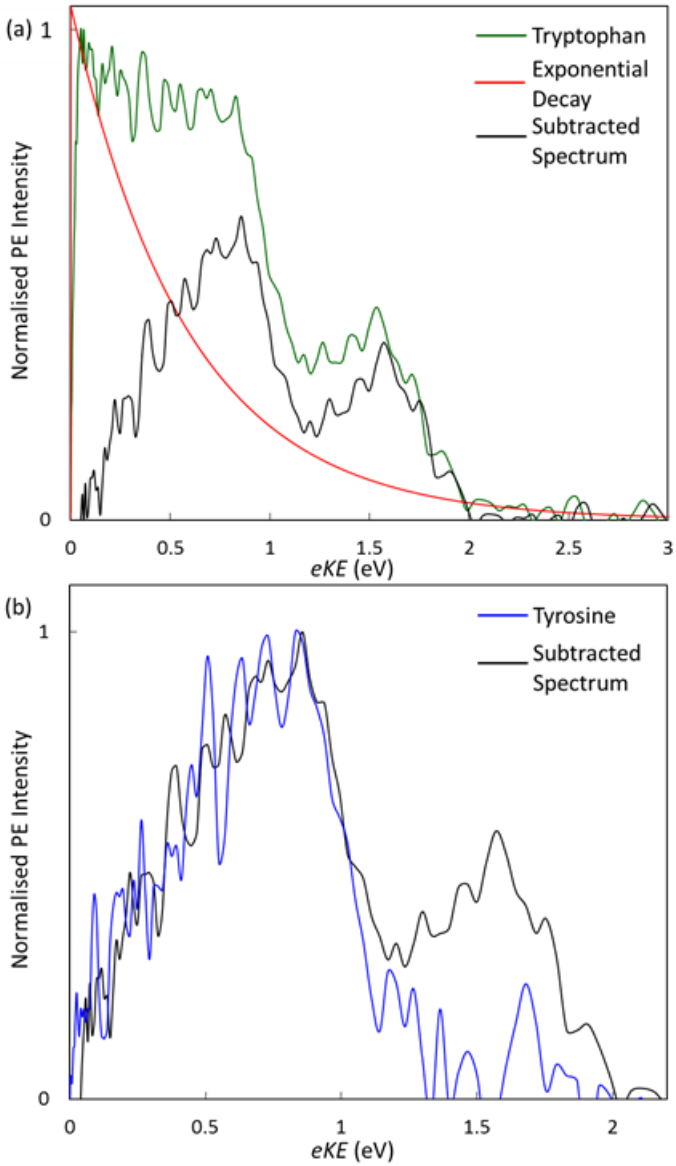

Figure 6.6 (a) (Green) PE spectrum of tryptophan and (black) the spectrum with an exponential decay (shown in red) subtracted. (b) PE spectrum of tyrosine (blue) and the subtracted tryptophan spectrum (black).

6.7 Summary

In conclusion, we have acquired PE spectra of a number of carboxylic acids, concentrating on phenylcarboxylic acids with varying lengths of aliphatic and

conjugated carbon chains, systems with π-conjugation chains and biologically relevant molecules. In the phenyl carboxylic acids, the PE spectra at 4.13 eV (300 nm) appeared similar to equivalent spectra of a simple organic aliphatic chain carboxylic acid, with an increase in signal at low *eKE* that increased concurrently with chain length. This was assigned to an interaction between the carboxylic acid group and the hydrogen in the *para-* position on the phenyl, which becomes stronger as the carbon chain length of the phenylcarboxylic acid increases. We have postulated that excited state charge transfer reaction involving the transfer of a proton from the phenyl to the carboxylic acid group, accessed through resonant photoexcitation at 4.13 eV, is involved, although the calculations involved to support this mechanism are beyond the scope of this project.

For a series of unsaturated carboxylic acids, the spectra were dominated by a statistical emission peak at low *eKE*. This was ascribed to initial photoexcitation of a π* ← π transition, followed by efficient internal conversion to the ground electronic state. The vibrationally excited electronic ground state produced can then lose an electron by thermionic emission, or absorb additional photons and decay back to the ground state, as the lifetime of the internal conversion process is likely to be considerably faster than the duration of the laser pulse. In the PE spectrum of octatrienoic acid, an anomalous sharp peak was observed and assigned to photodetachment of hydride. Through manipulation of the electron velocity-map imaging apparatus, we were able to directly observe hydride and extract the kinetic release spectrum. We have assigned the H^- loss mechanism to a statistical process on the ground state. PE spectra of the biological amino acids tryptophan and tyrosine were recorded and found to differ significantly; while the tyrosine spectra appeared similar to the the PE spectra of the unsaturated phenylcarboxylic acids, the tryptophan spectra were dominated by a statistical emission peak at low *eKE* typical of the unsaturated carboxylic acids, despite the carboxylic acid

group not being conjugated to the indole group. This discrepancy was assigned to the presence of an efficient decay mechanism to the electronic ground state following photoexcitation to an excited state resonance located predominantly on the indole group, allowing for repeated photoexcitation and eventually thermionic emission of an electron, leading to the observed statistical emission peak. While we might expect to see a similar resonance in the π-system of the phenoxy group, the PE spectrum of tyrosine is dominated by direct detachment.

→

6.8 References

(1) Clayden, J.; Greeves, N.; Warren, S.; Wothers, P. *Organic Chemistry*; Oxford University Press: Oxford, 2001.

(2) Patai, S. *Carboxylic Acids and Esters*; John Wiley & Sons, Ltd.: New York, 1969.

(3) Li, D.; Müller, M. B.; Gilje, S.; Kaner, R. B.; Wallace, G. G. *Nature Nanotechnology* **2008**, *3*, 101.

(4) Si, Y.; Samulski, E. T. *Nano Letters* **2008**, *8*, 1679.

(5) Nakamura, E.; Isobe, H. *Accounts of Chemical Research* **2003**, *36*, 807.

(6) Lamparth, I.; Hirsch, A. *Journal of the Chemical Society-Chemical Communications* **1994**, *14*, 1727.

(7) Kosynkin, D. V.; Higginbotham, A. L.; Sinitskii, A.; Lomeda, J. R.; Dimiev, A.; Price, B. K.; Tour, J. M. *Nature* **2008**, *458*, 872.

(8) Peng, H.; Alemany, L. B.; Margrave, J. L.; Khabashesku, V. N. *Journal of the American Chemical Society* **2003**, *125*, 15174.

(9) Barrett, G. C.; Elmore, D. T. *Amino Acids and Peptides*; Cambridge University Press: Cambridge, 1998.

(10) El-Aneed, A.; Cohen, A.; Banoub, J. *Applied Spectroscopy Reviews* **2009**, *44*, 210.

(11) Fenn, J. B.; Mann, M.; Meng, C. K.; Wong, S. F.; Whitehouse, C. M. *Mass Spectrometry Reviews* **1990**, *9*, 37.

(12) Fenn, J. B.; Mann, M.; Meng, C. K.; Wong, S. F.; Whitehouse, C. M. *Science* **1989**, *246*, 64.

(13) Fenn, J. B. *Angewandte Chemie-International Edition* **2003**, *42*, 3871.

(14) Marcus, R. K. *Glow Discharge Spectroscopies*; Plenum Press: New York, 1993.

(15) Märk, T. D.; Dunn, G. H. *Electron Impact Ionization*; Springer-Verlag/Wien: Austria, 1985.

(16) Adams, F.; Gijbels, R.; Van Grieken, R. *Inorganic Mass Spectrometry*; John Wiley & Sons, Ltd.: New York, 1988.

(17) Kebarle, P.; Peschke, M. *Analytica Chimica Acta* **2000**, *406*, 11.

(18) Wang, L.-S. *Journal of Chemical Physics* **2015**, *143*, 040901.

(19) Wang, L. S.; Ding, C. F.; Wang, X. B.; Barlow, S. E. *Review of Scientific Instruments* **1999**, *70*, 1957.

(20) Wang, X. B.; Wang, L. S. In *Annual Review of Physical Chemistry*; Annual Reviews: Palo Alto, 2009; Vol. 60, p 105.

(21) McLean, D. J.; Giese, A. C. *Journal of Biological Chemistry* **1950**, *187*, 537.

(22) Tian, Z.; Wang, X.-B.; Wang, L.-S.; Kass, S. R. *Journal of the American Chemical Society* **2009**, *131*, 1174.

(23) Chatterley, A. S.; Johns, A. S.; Stavros, V. G.; Verlet, J. R. R. *Journal of Physical Chemistry A* **2013**, *117*, 5299.

(24) Kim, E. H.; Bradforth, S. E.; Arnold, D. W.; Metz, R. B.; Neumark, D. M. *Journal of Chemical Physics* **1995**, *103*, 7801.

(25) Wang, L. S.; Ding, C. F.; Wang, X. B.; Nicholas, J. B.; Nicholas, B. *Physical Review Letters* **1998**, *81*, 2667.

(26) Wang, X. B.; Ding, C. F.; Wang, L. S. *Physical Review Letters* **1998**, *81*, 3351.

(27) Skurski, P.; Simons, J.; Wang, X. B.; Wang, L. S. *Journal of the American Chemical Society* **2000**, *122*, 4499.

(28) Yang, X.; Fu, Y. J.; Wang, X. B.; Slavicek, P.; Mucha, M.; Jungwirth, P.; Wang, L. S. *Journal of the American Chemical Society* **2004**, *126*, 876.

(29) Wang, X. B.; Woo, H. K.; Wang, L. S.; Minofar, B.; Jungwirth, P. *Journal of Physical Chemistry A* **2006**, *110*, 5047.

(30) Wang, X.-B.; Yang, J.; Wang, L.-S. *Journal of Physical Chemistry A* **2008**, *112*, 172.

(31) Xing, X.-P.; Wang, X.-B.; Wang, L.-S. *Physical Review Letters* **2008**, *101*, 083003.

(32) Xing, X.-P.; Wang, X.-B.; Wang, L.-S. *Journal of Chemical Physics* **2009**, *130*, 074301.

(33) Xing, X.-P.; Wang, X.-B.; Wang, L.-S. *Journal of Physical Chemistry A* **2009**, *113*, 945.

(34) Xing, X.-P.; Wang, X.-B.; Wang, L.-S. *Journal of Physical Chemistry A* **2010**, *114*, 4524.

(35) Brunet, C.; Antoine, R.; Dugourd, P.; Canon, F.; Giuliani, A.; Nahon, L. *Journal of the American Society for Mass Spectrometry* **2012**, *23*, 274.

(36) Lu, Z.; Continetti, R. E. *Journal of Physical Chemistry A* **2004**, *108*, 9962.

(37) Horke, D. A.; Chatterley, A. S.; Verlet, J. R. R. *Physical Review Letters* **2012**, *108*, 083003.

(38) Chatterley, A. S.; Horke, D. A.; Verlet, J. R. R. *Physical Chemistry Chemical Physics* **2014**, *16*, 489.

(39) Horke, D. A.; Chatterley, A. S.; Verlet, J. R. R. *Journal of Chemical Physics* **2013**, *139*, 084302.

(40) Horke, D. A.; Chatterley, A. S.; Verlet, J. R. R. *Journal of Physical Chemistry Letters* **2012**, *3*, 834.

(41) Roberts, G. M.; Nixon, J. L.; Lecointre, J.; Wrede, E.; Verlet, J. R. R. *Review of Scientific Instruments* **2009**, *80*, 053104.

(42) Inagaki, T. *Journal of Chemical Physics* **1972**, *57*, 2526.

(43) Buckles, R. E.; Bremer, K. G. *Journal of the American Chemical Society* **1955**, *77*, 805.

(44) Wigner, E. P. *Physical Review* **1948**, *73*, 1002.

(45) Bragg, A. E.; Verlet, J. R. R.; Kammrath, A.; Cheshnovsky, O.; Neumark, D. M. *Science* **2004**, *306*, 669.

(46) Burrow, P. D.; Michejda, J. A.; Jordan, K. D. *Journal of Chemical Physics* **1987**, *86*, 9.

(47) Gunion, R. F.; Gilles, M. K.; Polak, M. L.; Lineberger, W. C. *International Journal of Mass Spectrometry and Ion Processes* **1992**, *117*, 601.

(48) Kiefer, H. V.; Lattouf, E.; Persen, N. W.; Bochenkova, A. V.; Andersen, L. H. *Physical Chemistry Chemical Physics* **2015**, *17*, 20056.

(49) Baum, J. C.; McClure, D. S. *Journal of the American Chemical Society* **1979**, *101*, 2335.

(50) Andersen, T. *Physics Reports-Review Section of Physics Letters* **2004**, *394*, 157.

(51) Lykke, K. R.; Murray, K. K.; Lineberger, W. C. *Physical Review A* **1991**, *43*, 6104.

(52) Reichle, R.; Helm, H.; Kiyan, I. Y. *Physical Review A* **2003**, *68*, 063404.

(53) Mabbs, R.; Grumbling, E. R.; Pichugin, K.; Sanov, A. *Chemical Society Reviews* **2009**, *38*, 2169.

(54) Ashfold, M. N. R.; Nahler, N. H.; Orr-Ewing, A. J.; Vieuxmaire, O. P. J.; Toomes, R. L.; Kitsopoulos, T. N.; Garcia, I. A.; Chestakov, D. A.; Wu, S. M.; Parker, D. H. *Physical Chemistry Chemical Physics* **2006**, *8*, 26.

(55) Roberts, G. M.; Stavros, V. G. *Chemical Science* **2014**, *5*, 1698.

(56) Andersen, J. U.; Bonderup, E.; Hansen, K. *Journal of Physics B-Atomic Molecular and Optical Physics* **2002**, *35*, R1.

(57) Campbell, E. E. B.; Levine, R. D. *Annual Review of Physical Chemistry* **2000**, *51*, 65.

(58) Suelter, C. H.; Eftink, M. R. *Fluorescence Techniques for Studying Protein Structure*; Jon Wiley & Sons: New York City, 2006.

(59) Rizzo, T. R.; Park, Y. D.; Levy, D. H. *Journal of Chemical Physics* **1986**, *85*, 6945.

(60) Lapinskaya, E. M.; Khenokh, M. A. *Doklady Akademii Nauk S. S. S. R.* **1954**, *94*, 109.

Chapter 7. Photoelectron Spectroscopy of All-*trans*-Retinoic Acid

*One photon photoelectron spectra of the isolated, anionic, biologically relevant chromophore all-*trans*-Retinoic acid are presented. From this, the ADE is determined. Subsequently, a time-resolved photoelectron study of the excited state energetics is reported. In this, the dynamics of the initially excited S_3 state are traced by photoionisation. Two different pump-probe excitation schemes are employed in order to maximise the temporal resolution of the experiment and the range of internal energies over which the anion may be ionised by the probe pulse. A minimum of 2 sequential lifetimes are confidently observed. We assign the first, ultrafast lifetime to decay of the initially excited S_3 state to the S_2 and subsequently the S_1 states. The second lifetime is then assigned to a* trans-cis *isomerisation through internal conversion from the S_1 state to the S_0 state.*

7.1 Introduction

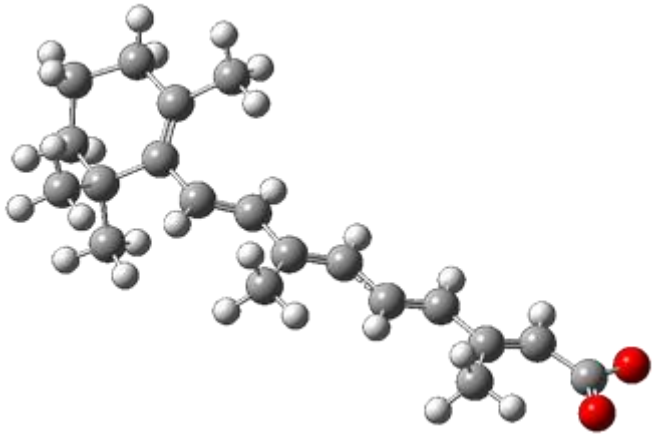

Figure 7.1 Structure of all-*trans*-retinoic acid.

In order to attempt to explore the effect of a carboxylate group on the excited state dynamics of a system, we have performed a TRPES study on the biological chromophore ATRA. Much of the biological activity of Vitamin A (retinol), such as growth and embryonic development, is mediated by a metabolite of Vitamin A,[1-4]

ATRA, although the application of Vitamin A as a visual pigment requires retinaldehyde (retinal). The presence of retinol as a visual pigment has led to considerable interest in the optical activity of retinol and its derivatives. The carboxylic acid derivative of vitamin A, ATRA, is therefore a textbook example of a biologically relevant carboxylic acid that exhibits excited state dynamics. Like tryptophan and tyrosine, deprotonated ATRA is an example of an anionic biological chromophore. However, while the amino acids feature chromophores that are not conjugated to the carboxylic acid group, $ATRA^-$ features an extended π-system that may interact with the carboxylic acid group.

Of the three major retinoid compounds, the optical properties of retinal have been the most extensively investigated.[5-10] The first optically bright singlet excited state is the $^1B_u^+$ state, which lies above the optically dark $^1A_g^-(\pi\pi^*)$ and $^1n\pi^*$ states.[8,9] However, these three excited states are close in energy and have been shown to be involved in the ultrafast excited state dynamics of all-*trans* retinal (ATR). The relative ordering of the excited states and hence the quantum yields of intersystem crossing, as impacted by, for instance, solvent dependence, have previously been shown to have a great effect on the dynamics of the system.[6,11] However, the energy level ordering is unaffected by the polarity of the solvent.[10]

Similarly, investigations of ATRA in solution and bound to a TiO_2 nanoparticle have concluded that three low-lying excited states (S_3, S_2 and S_1) exist in the singlet manifold, which may be assigned as the $^1B_u^+$, $^1n\pi^*$ and $^1A_g^-(\pi\pi^*)$ states respectively.[12-15] The level ordering of the $^1A_g^-(\pi\pi^*)$ and $n\pi^*$ states is reversed from ATR due to the effect of the inclusion of the hydroxyl group.

Additionally, a triplet state, T_1, has been observed in both ATR and ATRA.[8,12,15] As intersystem crossing to the T_1 state is more efficient from a $n\pi^*$ state than from a $\pi\pi^*$

state,[16] the relative population of the T_1 state produced following photo-excitation has been used to assign the lowest lying singlet state: $n\pi^*$ in ATR[8] and $\pi\pi^*$ in ATRA.[12] The relative ordering of the excited states in ATR is not affected by the polarity of the solvent.[10]

Ultrafast time-resolved spectroscopy, specifically fluorescence up-conversion and transient absorption measurements, has proved invaluable in elucidating the mechanisms of the excited state dynamics of both ATR and ATRA. The dynamics of ATR were initially measured in hexane by the time-resolved fluorescence up-conversion technique,[8] determining that the fluorescence decay contained three components: an ultrafast (λ_{max} = 430 nm and τ = 30 ± 15 fs), a fast (λ_{max} = 440 nm and τ = 370 ± 20 fs) and a slower (λ_{max} = 560 nm and τ = 33.5 ps) component, which were assigned to emission from the $^1B_u^+$, $^1A_g^-(\pi\pi^*)$ and $^1n\pi^*$ states respectively. Further femtosecond time-resolved transient visible absorption measurements in cyclohexane identified four absorption bands, which can be assigned to the first three singlet states and the first triplet state.[10]

ATRA has recently been studied by both transient absorption spectroscopy[12] and the time-resolved fluorescence up-conversion technique in a number of solvents.[16] Analogous to ATR, the decay profiles observed through the transient absorption experiment were fitted to three exponential decays, with lifetimes of 110 fs, 2.2 ps and 30 ps. These components were assigned to the decay of the $^1B_u^+$, $^1n\pi^*$ and $^1A_g^-(\pi\pi^*)$ states respectively.[12] In the fluorescence up-conversion experiment, three lifetimes were again observed: in ethanol, an ultrafast (λ_{max} = 460 nm and τ = 80 fs), an intermediate (λ_{max} = 545 nm and τ = 2.2 ps) and a weak, slow (λ_{max} = 540 and τ = 10 ps) component was observed.[16] However, it was not possible to observe emission from the $^1n\pi^*$ state. The ultrafast component was assigned to emission from the $^1B_u^+$ state, which decays by

an ultrafast internal conversion process to the $^1n\pi^*$ and $^1A_g^-(\pi\pi^*)$ states. The intermediate and slow lifetimes were assigned to emission from the $^1A_g^-(\pi\pi^*)$ state. The intermediate component was found to be strongly dependent upon the viscosity of the solvent and was ascribed to a *trans-cis* isomerisation in this state, resulting in a non-radiative decay process to the ground electronic state. The slow lifetime was assigned to the forbidden transition from the $^1A_g^-(\pi\pi^*)$ state to the ground ^1A_g state.

In the gas phase, the majority of studies on ATRA have been theoretical.[17-19] However, the gas phase PE spectrum of neutral ATRA has been observed by Jericevic *et al.*,[20] and Katsumata and Ikehata.[21] In both experiments, ATRA was vaporised in a furnace, passed into an ionisation chamber and irradiated with light from a HeI lamp. PE spectra were then collected by use of a hemispherical electrostatic analyser. The subsequent simulations by Abyar and Farrokhpour[19] have revealed that the spectrum contains overlapping contributions from several conformers, indicating the presence of several stable conformers in the gas phase. Katsuma and Ikehata also observed the presence of peaks assigned to decomposition products of ATRA produced through the vaporisation process,[21] indicating the need for a soft vapourisation process in obtaining PE spectra.

7.2 Experimental Details

The experiment was performed as described in Chapter 2. ATRA was purchased from Sigma Aldrich and used without further purification. Isolated deprotonated anions were produced by ESI (~1 mM in MeOH, adjusted to pH ~11 by the addition of 2 M NH_3 in MeOH). The ion packet was pulsed out of the trap at 50 Hz, mass selected by time-of-flight, and subsequently irradiated at the centre of a velocity-map-imaging PE spectrometer. For one colour PE spectra, the isolated $ATRA^-$ ions were irradiated by

femtosecond laser pulses of 3.10 eV (400 nm) and 4.66 eV (266 nm), generated by the second and third harmonic respectively of a commercial femtosecond Ti:Sapphire oscillator coupled to a regenerative amplifier (SpectraPhysics Tsunami/Spitfire Pro). For time-resolved PE spectra, the $ATRA^-$ ions are promoted to the S_3 excited state with a 3.10 eV (400 nm) femtosecond pump laser pulse. The excited state population is then promoted into the photodetachment continuum after a delay *t* using a probe pulse of 1.55 eV (800 nm) or 2.49 eV (500 nm). Pulses at 2.49 eV are generated by sum-frequency mixing of the fundamental with the signal output from an optical parametric amplifier (Light Conversion TOPAS-C). Above 4.13 eV, a considerable amount of PE noise is observed and so an additional PE image is collected, in which the laser, but not the ions, is fired through the spectrometer. The resultant image is then subtracted from the PE image colected with ions in order to recover the PE distribution. The experimental images were deconvoluted using the polar-onion peeling algorithm[22] in order to extract the PE spectra. The spectral resolution of the PE spectrometer is ~ 5% and has been calibrated using the PE spectrum of I^-. The temporal resolutions of the time-resolved experiments are on the order of 70 fs and 120 fs for the 3.10 eV + 1.55 eV (400 nm + 800 nm) and 3.10 eV + 2.49 eV (400 nm + 500 nm) pump-probe schemes respectively.

7.3 Electronic Structure of ATRA

Figure 7.4 shows PE spectra of $ATRA^-$ collected at 4.66 eV and 3.10 eV. From the 4.66 eV spectrum, through linear extrapolation of the falling edge, we may estimate the ADE to be 3.5 ± 0.1 eV. At an excitation energy of 3.1 eV, we are below the detachment threshold and therefore do not expect to see PEs from single photon absorption. The PE spectrum observed at this photon energy is therefore a result of a

1+1 resonance-enhanced multi-photon ionisation scheme, where $ATRA^-$ is initially excited to the S_3 excited state before absorption of the second photon. The available photon energy in this spectrum is therefore 6.2 eV. In contrast to the spectrum at 4.66 eV, we estimate the ADE from linear extrapolation of the falling edge to be 3.6 ± 0.1 eV. This shows good agreement with the ADE determined from the 4.66 eV spectrum.

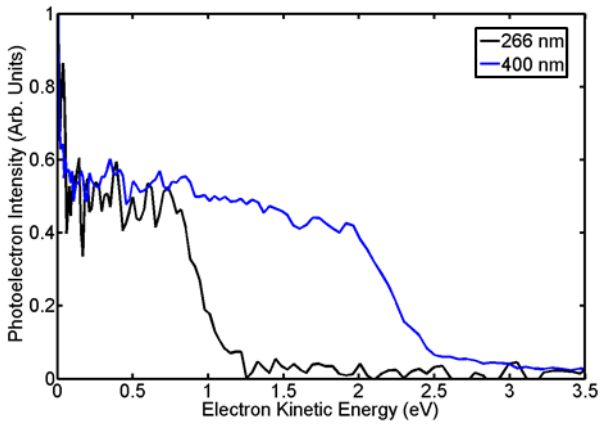

Figure 7.2 Normalised PE spectra of ATRA taken using probe photons at 4.66 eV (266nm) and 3.10 eV (400 nm). While the 4.66 eV photon has sufficient energy to detach an electron, the photon at 3.10 eV does not. Hence, the spectrum at 3.10 eV is observed due to a 1+1 resonance-enhanced multiple-photon ionisation scheme. As such, the available ionisation energy is 6.20 eV.

The appearance of the PE spectra is notable for two reasons: there is a peak at eKE = 0 eV and the body of the spectra are almost flat over a range of approximately 0.8 eV and 2 eV for the 4.66 eV (266 nm) and 3.10 eV (400 nm) spectra respectively, with no clearly discernable peaks. As previously discussed, the Wigner threshold law states that the photodetachment cross-section of an anion at threshold is zero,[23] hence the peak at eKE = 0 eV cannot be observed through direct detachment processes. As such, the provenance of this peak is uncertain. At 3.10 eV, we are both resonant with the $S_3 \leftarrow S_0$ transition and observing a two-photon process. As initial electronic relaxation from the S_3 state has been observed in ATRA on timescales of $\tau \leq 80$ fs when in solution[12,16] and bound to a TiO_2 nanoparticle,[12] and considering our excitation pulse temporal width of ~60 fs, it is reasonable to assume that some population has undergone

electronic relaxation and that we are sampling population from excited states produced subsequent to the initial excitation. This ultrafast conversion of energy would indicate that the molecule is suitable for investigation by TRPEI. However, at 4.66 eV there is a local minimum in the absorption spectrum,[24] so we do not expect to be resonant with an optically bright excited state at this energy. It is possible that, due to the conjugated nature of the molecule, a number of resonance structures of the neutral molecule may be available following photodetachment at an variety of internal energies, resulting in a wide range of electron kinetic energies being observed and the 'blurring' of the PE spectrum. Nevertheless, there is still absorption at this wavelength, hence the appearance of the PE spectrum could be explained by motion on an electronic excited state surface.

Finally, we note that the appearance of the spectra in Figure 7.4 are similar to those of deprotonated benzoate and *trans*-cinnamic acid in Figure 6.3. In addition, the feature that we have assigned to direct detachment in all spectra appears far more dominant in the $ATRA^-$ spectra. This could be explained by a change in the relative dominance of different detachment channels between the molecules, resulting in an increase in the prevalence of the direct detachment channel in ATRA. On the other hand, if we assume that the peak at low energy in the $ATRA^-$ spectra has the form of an exponential decay and arises from a similar detachment channel as those in the deprotonated conjugated phenylcarboxylic acids, then the difference in the forms of the spectra could be explained by the different excitation lasers used; the $ATRA^-$ spectra were obtained using a femtosecond laser as opposed to a nanosecond system. As such, if this channel is linked to multiple-photon absorption, the low energy peak is expected to be far less dominant than seen in the deprotonated conjugated phenylcarboxylic acids.

7.4 Excited State Dynamics of ATRA

7.4.1 Results

Time-resolved PE spectra taken using the pump-probe schemes 3.10 eV + 1.55 eV (400 nm + 800 nm) and 3.10 eV + 2.49 eV (400 nm + 500 nm) are shown in Figure 7.3(a) and (b), respectively. To extract only the excited state PE spectra, a spectrum taken at a large negative Δt (comprising only of the pump-only and probe-only PE spectra) has been subtracted from the pump-probe spectra. At short time delays (0 fs < Δt < 100 fs), a large, flat feature in the range of 0.1 eV < *eKE* < 0.9 eV and 0.1 eV < *eKE* < 1.7 eV for the 3.10 eV + 1.55 eV and 3.10 eV + 2.49 eV spectra, respectively, is observed in addition to the peak at 0 eV < *eKE* < 0.1 eV. As the pump-probe delay increases, the intensity of the flat PE feature decreases as the location of the falling edge shifts to lower kinetic energy, with the intensity falling to zero within 500 fs. This is accompanied by a concomitant increase in the intensity of the peak at 0 eV < *eKE* < 0.1 eV, which then falls to zero as Δt increases further. No pump probe signal is observed beyond Δt ~ 1000 fs.

Figure 7.4 shows the PE spectrum taken at 4.66 eV (266 nm) and the background subtracted PE spectrum taken at 3.10 eV + 1.55 eV (400 nm + 800 nm) at Δt ~0 fs. The two spectra are almost identical, although the pump-probe spectrum has a greater contribution from the peak at 0 eV < *eKE* < 0.1 eV. Below 1 eV, the two spectra are comparable: discrepancies include an increased dominance and broadening of the low energy peak in the time-resolved spectrum. This suggests that the detachment processes leading to PE emission following excitation by the two excitation schemes are similar.

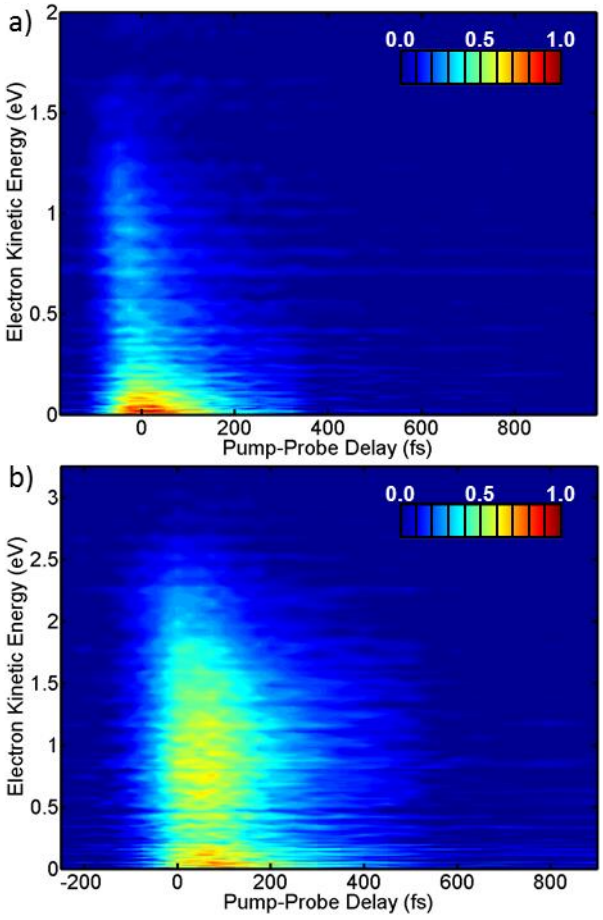

Figure 7.3 The background subtracted time-resolved PE spectrum of ATRA, acquired using a a) 3.10 eV pump pulse and a 1.55 eV probe pulse and b) a 3.10 eV pump pulse and a 2.49 eV probe pulse.

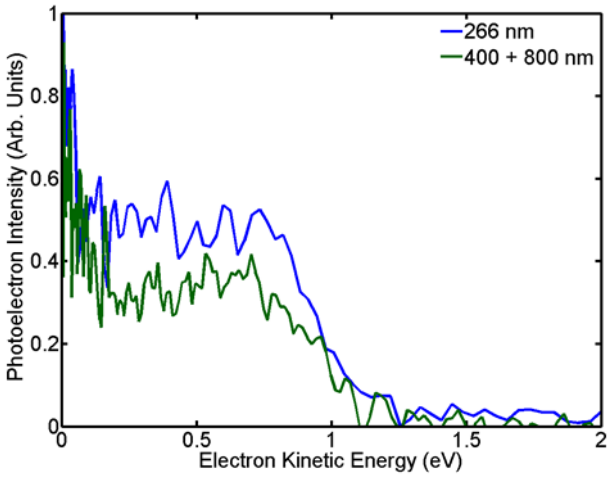

Figure 7.4 Normalised PE spectra of ATRA taken using 4.66 eV (blue) and the background subtracted normalised PE spectrum taken using 3.10 eV + 1.55 eV laser pulses at a ~0 fs pump-probe delay.

The presence and subsequent loss of the peak at 0 eV < *eKE* < 0.1 eV in the time-resolved spectrum is significant. The peak appears structurally similar to the peak

in the same spectral region that appears in the one photon spectra, as can be seen in Figure 7.4. The peak appears to be both slightly broadened and increased in relative spectral intensity to the higher *eKE* feature in the two photon spectra, which implies that there are two separate detachment channels leading to the features at high and low *eKE* that are accessed disproportionately by the different excitation schemes. The low *eKE* peak can be fitted to an exponential decay, which is consistent with thermionic emission of electrons from a vibrationally 'hot' ground state.[25-27] However, thermionic emission occurs on a timescale on the order of milliseconds,[27] whereas the peak observed in the time resolved spectra decays on the order of hundreds of femtoseconds. The fact that the peak is constant in *eKE* with respect to excitation energy suggests that the low energy peak is the result of vibrational autodetachment from an excited state. Another possibility is that the detached electron is able to access the π^* orbital of the conjugated π on either the ATRA molecule from which it was detached or on another molecule, where it may undergo rapid vibrational energy redistribution before the electron is detached again with a lower *eKE*. The calculations required to assess the plausibility of these mechanisms are beyond the scope of this thesis, hence the origins of the low *eKE* peak remain uncertain.

7.4.2 Analysis

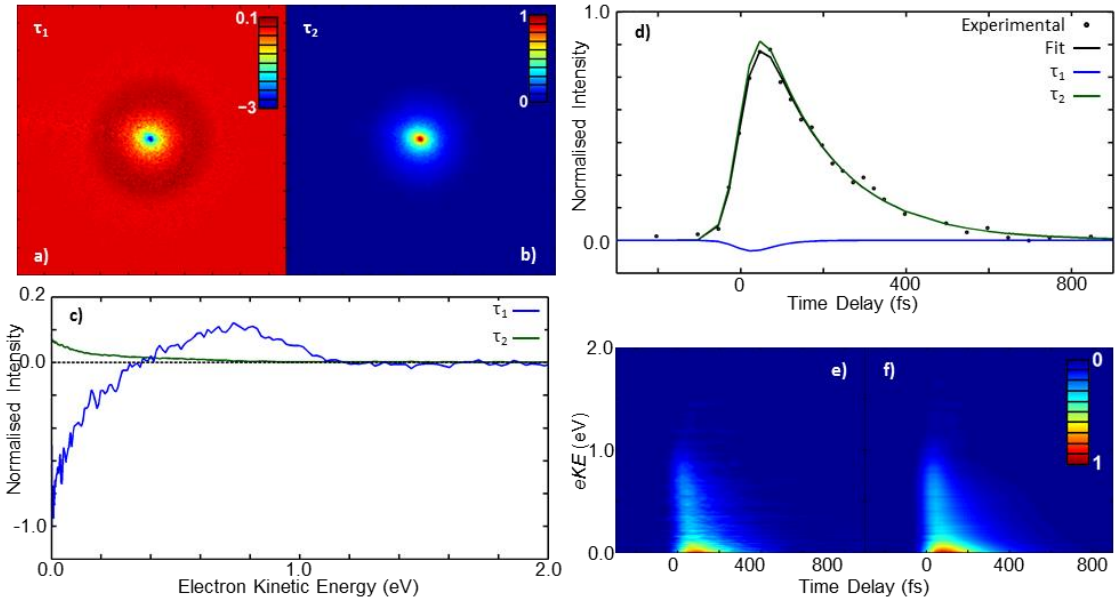

Figure 7.5 Results of the global kinetic fitting to a two lifetime model on the 3.10 eV + 1.55 eV pump-probe experiments. Presented are; the decay associated images extracted from the fitting program for a) τ_1, b) τ_2 and c) the deconvoluted images to extract the PE distribution; d) integrated PE signal and the calculated fit as a function of pump-probe delay; Background subtracted TRPES data of ATRA from e) experiment and f) simulation, presented as a false colour plot.

The observed dynamics were fitted by the global kinetic image fit described in Chapter 3 and the results shown in Figure 7.5 - Figure 7.7: Figure 7.5 shows the global kinetic fit of the 3.10 eV + 1.55 eV (400 nm + 800 nm) time-resolved spectra assuming independent lifetimes and the results of the global fit assuming sequential lifetimes for the 3.10 eV + 1.55 eV and 3.10 eV + 2.49 eV (400 nm + 500 nm) spectra are shown in Figure 7.6 and Figure 7.7, respectively. For the 3.10 eV + 1.55 eV spectra, two τ_i lifetimes were observed from both fitting procedures: τ_1 = 48 fs and τ_2 = 171 fs. For the 3.10 eV + 2.49 eV spectra, two τ_i lifetimes were also observed: τ_1 = 144 fs and τ_2 = 143 fs. The time resolutions of our experiments were 60 fs and 140 fs for 3.10 eV + 1.55 eV and 3.10 eV + 2.49 eV, respectively. We can confidently assert our lifetime for τ_2 from the 3.10 eV + 1.55 eV spectra, although the lifetimes obtained for the 3.10 eV + 2.49 eV

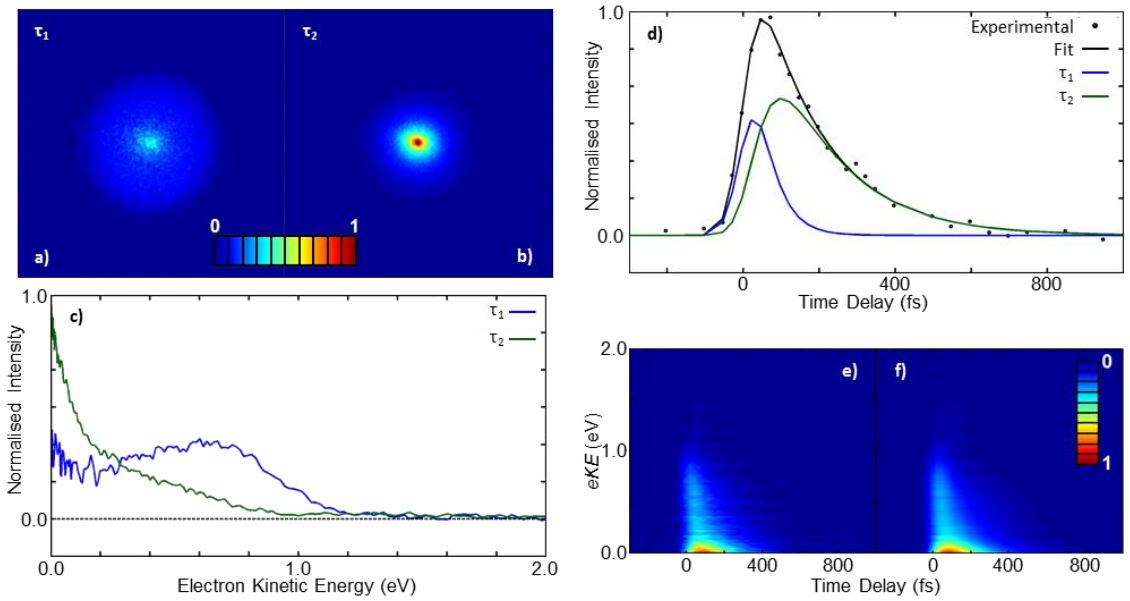

Figure 7.6 Results of the global kinetic fitting to a two lifetime model, assuming population from the first lifetime directly feeds into the population that decays by the second lifetime, on the 3.10 eV + 1.55 eV pump-probe experiments. Presented are; the decay associated images extracted from the fitting program for a) τ_1, b) τ_2 and c) the deconvoluted images to extract the PE distribution; d) integrated PE signal and the calculated fit as a function of pump-probe delay; Background subtracted TRPES data of ATRA from e) experiment and f) simulation, presented as a false colour plot.

spectra are close to the temporal resolution for the experiment. The actual lifetimes for the components are therefore likely to be obscured by the instrument response function.

The decay associated image (DAI) and the decay associated spectrum (DAS) of τ_1 for the initial fit of the 3.10 eV + 1.55 eV spectra (Figure 7.5) shows a positive and a negative region at 0.4 eV < *eKE* < 1.2 eV and 0 eV < *eKE* < 0.4 eV, respectively. The DAI and DAS of τ_2 has a similar spectral profile to that of τ_1, although with a larger amplitude and opposite sign. As negative amplitudes indicate a concurrent exponential rise, this implies that signal initially contributing to the higher energy feature is decaying into the low energy feature, hence the dynamics are sequential.

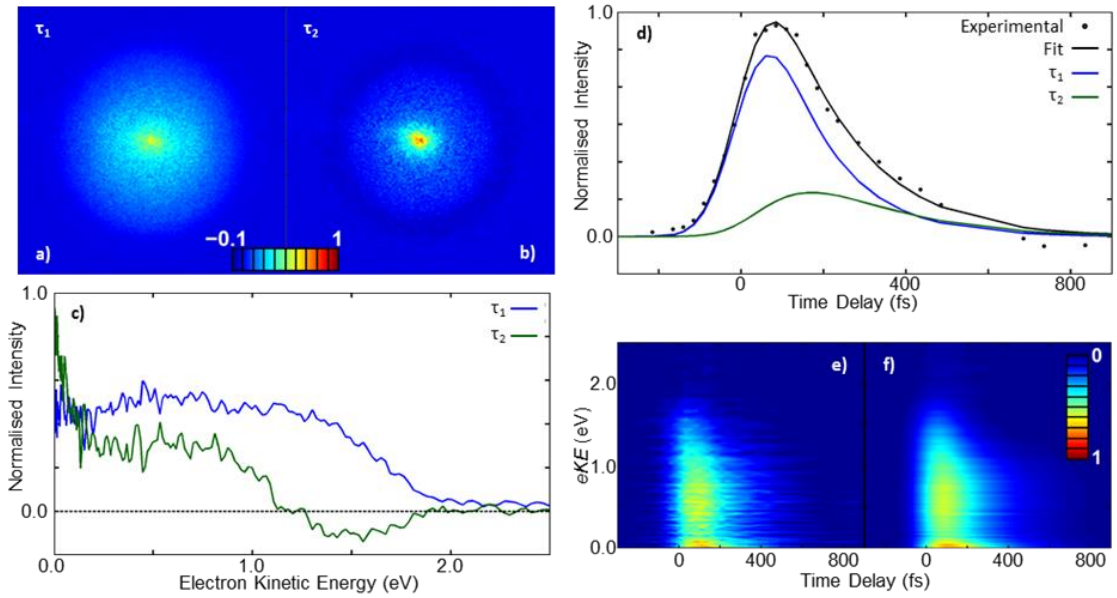

Figure 7.7 Results of the global kinetic fitting to a two lifetime model, assuming population from the first lifetime directly feeds into the population that decays by the second lifetime, on the 3.10 eV + 2.49 eV pump-probe experiments. Presented are; the decay associated images extracted from the fitting program for a) τ_1, b) τ_2 and c) the deconvoluted images to extract the PE distribution; d) integrated PE signal and the calculated fit as a function of pump-probe delay; Background subtracted TRPES data of ATRA from e) experiment and f) simulation, presented as a false colour plot.

The DAI and DAS for both lifetimes from the fit to the sequential dynamics kinetic model for the 3.10 eV + 1.55 eV (400 nm + 800 nm) spectra (Figure 7.6) are entirely positive, indicating that we have extracted realistic DAS from the TRPES. This confirms our previous assignment from the initial kinetic fitting model that the dynamics are sequential. The DAS for τ_1 again shows PE intensity at high *eKE* and appears as a broad peak across the length of the spectrum, 0 eV < *eKE* < 1.2 eV, centred at *eKE* ~ 0.7 eV. A slight increase in intensity at *eKE* = 0 eV is observed. The DAS for τ_2 appears identical to the DAS for τ_2 obtained by the independent lifetime kinetic fit shown in Figure 7.5.

The DAI and DAS for both lifetimes from the fit to the sequential dynamics kinetic model for the 3.10 eV + 2.49 eV (400 nm + 500 nm) spectra (Figure 7.7) show similar features. The DAS for τ_1 shows PE intensity across the entire length of the

spectrum, 0 eV < *eKE* < 2 eV. The DAS does not show a similar increase in intensity at *eKE* = 0 to that observed in the DAS for τ_1 in the 3.10 eV + 1.55 eV spectra. However, the DAS for τ_1 in the 3.10 eV + 2.49 eV spectra appears as a relatively flat feature, hence, the discrepancy may described as the absence of the decrease in the PE intensity at low (~0.2) *eKE*. The DAS for τ_2 shows a peak at *eKE* = 0 eV, a region of relatively flat PE intensity at 0.2 < *eKE* < 1.1 eV and a negative region of PE intensity at 1.1 eV < *eKE* < 1.8 eV. We do not expect to see negative regions in the DAI or DAS using the sequential dynamics kinetic fitting routine. This negative amplitude indicates an exponential rise in this region, which overlaps with the high *eKE* region of the DAS for τ_1.

This may be explained by considering the time resolution of the pump-probe scheme, 140 fs. This is extremely close to the extracted lifetimes for τ_1 and τ_2, 144 fs and 143 fs, respectively. We may therefore state that the true dynamics of the system are obscured by the time resolution of the experiment. Additionally, from the 3.10 eV + 1.55 eV experiments, we expect τ_1 < 60 fs, which is well within the time resolution of the experiment. The DAI and DAS are therefore likely to be inaccurate, reflecting the inaccuracy of the lifetimes that we may extract from the fit.

As an additional exercise, the decay profiles of both time-resolved spectra and the simulated PE spectra from the global kinetic fit were analysed through fitting to three lifetimes via fitting the total PE signal and by a global kinetic fit. The values for τ_2 and τ_3 obtained for each spectrum were similar and well within the time resolution of the experiments. This implies that the spectra have been over-fitted and that two lifetimes are sufficient to analyse the decay profiles.

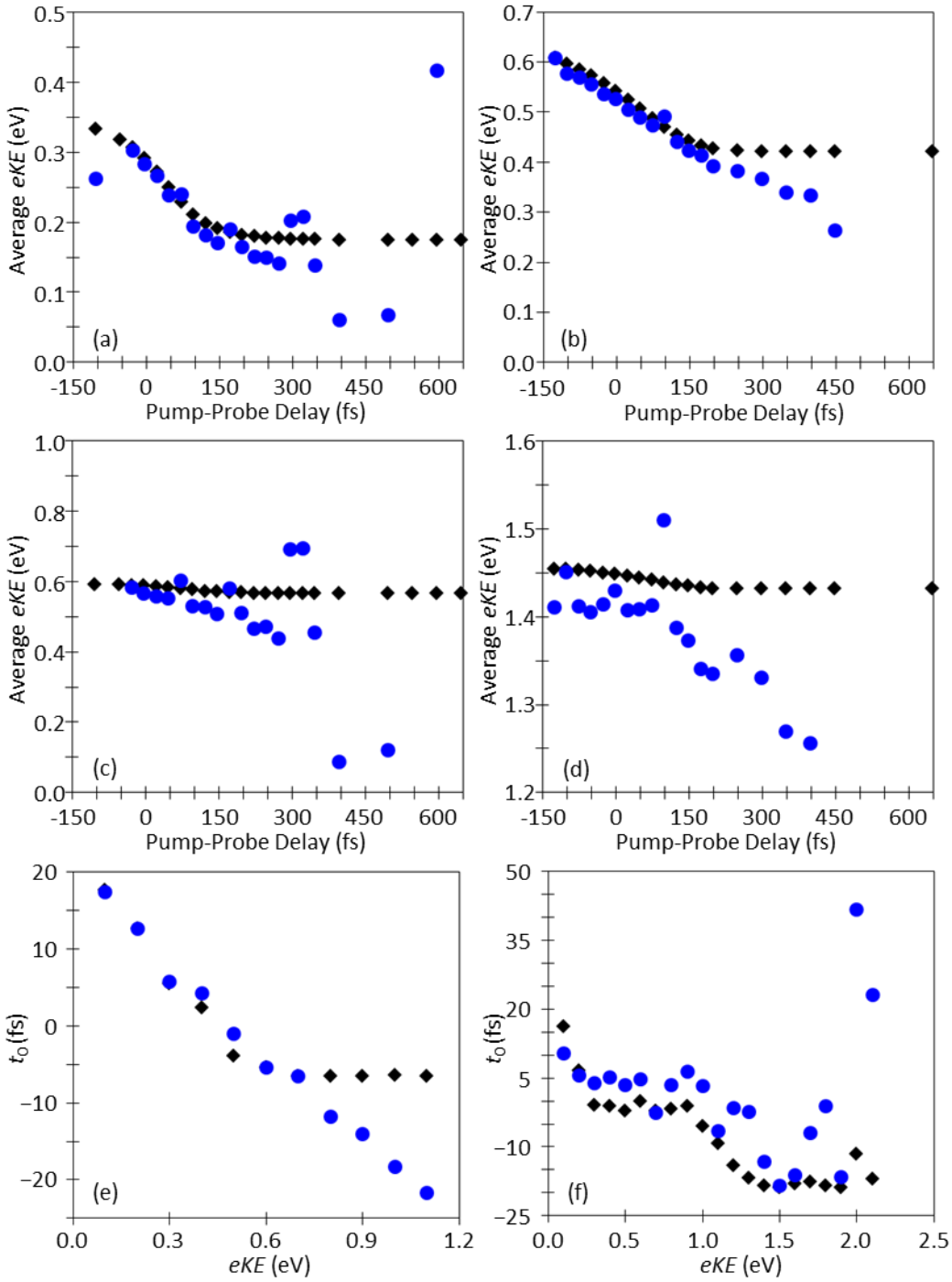

Figure 7.8 (a-b) Average *eKE* of the spectrum taken at each pump-probe delay (blue circles) and of the fitted TRPES obtained from the global kinetic fit of the experimental data (black diamonds), obtained at photoexcitation energies of (a) 3.10 eV + 1.55 eV and (b) 3.10 eV + 2.49 eV. (c-d) As for the top figures, but with the low energy peak (< 0.2 eV and < 1.0 eV respectively) excluded from the calculation of the average kinetic energy for photoexcitation energies of (c) 3.10 eV + 1.55 eV and (d) 3.10 eV + 2.49 eV. (e-f) The shift in t_0 of the total PE intensity of a 0.1 eV wide bin of the time-resolved spectrum fitted to a single exponential decay as compared to the total PE intensity of the overall time-resolved spectrum, obtained at (e) 3.10 eV + 1.55 eV and (f) 3.10 eV + 2.49 eV.

The fitting process was unduly arduous and recovers worse fits for similar PE intensity in the spectrum than those obtained in Chapter 3. As previously noted, a global kinetic fit assumes that the PE features in the time-resolved spectra are stationary in *eKE*. In order to test the validity of this assumption for this data set, we have measured the average kinetic energy of the spectrum obtained at each pump-probe delay in the time-resolved spectrum for both excitation schemes and then presented in Figure 7.8(a-b). Additionally, we have fitted the total integrated PE intensity of the TRPES to a single exponential decay convoluted with a Gaussian, and subsequently repeated the process for the total integrated PE intensity of a 0.1 eV wide bin of the each PE spectrum for the width of the TRPES. The change in t_0 (a measure of the onset of the fit) from the fit of the total spectrum is then recorded and presented in Figure 7.8(c-d).

As shown in Figure 7.8(a-b), the average *eKE* decreases linearly with the pump-probe delay for both excitation schemes. Additionally, the rate of decrease is not constant; both plots exhibit two clear gradients. As indicated by the global kinetic fit, there are at least two major spectral components with different lifetimes. The overall trends observed in the average *eKE* are consistent with two PE features, constant in *eKE*, decaying on different timescales. The changing contributions of the features to the overall spectrum with time, in particular the reduction of the contribution of the ultrafast component to zero, would cause the sudden change in gradient. However, also shown are the average *eKE*s of the fitted TRPES obtained by the global kinetic fitting model described in Chapter 3, which are constructed by the sum of two PE features with constant *eKE*. The contribution of each feature to the PE spectrum at a given time delay is described by an exponential decay convoluted with a Gaussian. The average *eKE* shows good agreement between the experimental and simulated datasets at short pump-probe delays. Above ~ 200 fs, however, the average *eKE* reaches a plateau for the fitted

datasets and continues to decrease for the experimental dataset. This is clear evidence that features in the TRPES are shifting in kinetic energy with time.

Further evidence of this shift can be seen in Figure 7.8(c-d). In each figure, the average *eKE* has been calculated the spectral range *eKE* > 0.1 eV. This range has been selected in order to exclude the low *eKE* peak, hence preserving only the peak at high kinetic energy. As the pump-probe delay varies, the average *eKE* of the fit remains approximately constant at ~0.6 eV and ~1.45 eV. However, the average *eKE* of the experimental data shows a significant decrease as the pump-probe delay increases, unequivocably demonstrating that the PE feature is not constant in *eKE* with respect to time.

A dependence of t_0 on the kinetic energy of the spectrum is observed in Figure 7.8(e-f), where the relative shifts of the t_0 of the experimental and simulated TRPES in a spectral region 0.1 eV wide are presented. For the 3.10 eV + 1.55 eV data, the t_0 of the fits of the binned experimental data shift to more negative values (early in time) than the t_0 values extracted by the binned simulated data at high *eKE*, indicating that the high *eKE* peak is not constant with respect with *eKE*. This shift in t_0 could indicate either that spectral features in the TRPES are shifting in *eKE* with time, or that the PE features in the spectrum have different onsets in time. We do not observe a similar shift in the 3.10 eV + 2.49 eV, which appears to follow the same pattern as the simulated dataset. However, the fitted parameters are considerably noisier than that of the 3.10 eV + 1.55 eV dataset, which could obscure any underlying trends.

7.5 Discussion

Previous studies of ATRA have determined that, following excitation at 3.10 eV (400 nm), the S_3 ($^1B_u^+$) excited state is populated.[12,15,16] Time-resolved experiments

have concluded that this initial excited state population may then cascade sequentially through the S_2 ($n\pi^*$) and S_1 ($^1A_g^-(\pi\pi^*)$) states, before relaxing to the ground electronic state.[12,16] In the S_1 state, the molecule may undergo a *trans-cis* isomerisation, which may then decay by a radiationless process to the ground state.[16] Additionally, some population may undergo intersystem crossing to the T_1 state.[15]

Although the shifts in the *eKE* of the spectral features will undermine the accuracy of the global kinetic fit, we may still use the results of the fit as a guide to further discussion. Through global kinetic fitting, we are able to fit the TRPES to two sequential lifetimes, indicating that the population that decays on the timescale τ_1 undergoes a decay pathway that directly produces the population that decays on the timescale τ_2. The observation of two components in the excited state decay is in qualitative disagreement with the observations of Zhang *et al.*[12] and Presiado *et al.*[16] There are numerous explanations for the discrepancy: firstly, the ordering of the excited states may have changed between the solution and gas phases so that the $^1B_u^+$ state energetically lies below the $n\pi^*$ state, i.e. the S_3 and S_2 states are reversed. This situation is not unfeasible (this ordering of the excited states is equivalent to that in ATR[8,9]) and, as the initially excited state is the second excited state, we might expect to observe two lifetimes in the dynamics. However, an alternate explanation is that the $S_2 \leftarrow S_3$ and $S_1 \leftarrow S_2$ transitions are sufficiently fast that we simply cannot differentiate the two lifetimes within our time resolution. Given that the observed lifetimes at both excitation schemes are within the time resolution of our experiment, it is unsurprising that we would be unable to resolve two separate lifetimes. We also note from inspection of the DAS of the global fits that the spectral feature associated with this lifetime spans much of the width of the entire spectrum, which suggests that two excited states contributing PE intensity to the spectral feature would not be an unreasonable suggestion. As we are

unable to ascertain the excited state ordering from our experiment, we therefore tentatively assign τ_1 <60 fs to the ultrafast internal conversion of the S_3 state to the S_2 state and subsequently the S_1 state.

We now turn our attention to the assignment of τ_2. By process of elimination, we can assign this lifetime to the decay of the S_1 excited state. While triplet states have been observed, the lifetime is too fast to consider that this decay corresponds to a population of triplet states. Presiado *et al.* observed a long lived, viscosity dependent lifetime (0.9-4 ps)[16] which was assigned to the forbidden transition between the $^1A_g^-$ ($\pi\pi^*$) state and the ground state via a conical intersection accessible through a *trans-cis* isomerisation. In the gas phase, this transition is unencumbered by solvent steric effects and hence we expect the lifetime of this process to be reduced significantly. Crucially, previous observations of *cis-trans* isomerisation in retinal derivatives have shown that, as the geometry of the molecule changes, the energetics of the orbitals change;[7,28,29] in our experiment, we would expect to observe this as a feature shifting in *eKE* with time. This is clearly observed in the average *eKE* and in the relative change in t_0 of the fits of our binned TRPES shown in Figure 7.8(e-f). As such, we can assign the longer second lifetime of < 200 fs, τ_2, to a *trans-cis* isomerisation through internal conversion from the S_1 state to the S_0 state. This is consistent with previous measurements of the *cis-trans* isomerisation in the structurally similar rhodopsin.[30-33] The lifetime is, however, considerably shorter than previous lifetime measurements of ATRA,[12,16] which we assign to the absence of steric hiderance from the solution phase.

We must consider the possibility that the sub-200 fs lifetime does not describe the loss of the S_1 state to the S_0 state. Alternatively, as the molecule undergoes IVR, the internal energy along the reaction coordinate may drop sufficiently low that we are unable to observe the $S_0 \leftarrow S_1$ transition by photoionisation at the energies used in our

excitation schemes; the $S_n - D_0$ gap increases to an energy greater than that of the probe pulse. At 3.10 eV + 2.49 eV (400 nm + 500 nm), there is a ~ 1 eV window above the S_0 in which we are unable to probe. However, this assumes that the energetics of the excited states are constant between the Franck-Condon geometry and the geometry accessed through IVR, which is unlikely to be the case, so the un-probable window could be considerably smaller or wider. We are unable to comment on the feasibility of this mechanism without high-level *ab initio* calculations, however. Nevertheless, we note that, for this mechanism to be feasible, a large geometric change might be expected that would be unlikely on the observed timescale[34] and again stress that the lifetime of τ_2 is consistent with the *cis-trans* isomerisation observed in rhodopsin.[30,31]

A schematic representation of the potential dynamics following photoexcitation at 3.10 eV (400 nm) is presented in Figure 7.9. This assignment is in good accord with previous studies of the excited state dynamics of ATRA,[12,13,16] although the observed dynamics occur on timescales that are orders of magnitude faster than previously observed. This implies that the solvent environment has a significant effect on the excited state dynamics of ATRA. Given the importance of the *trans-cis* isomerisation in the excited state decay, it is reasonable to assume that the solvent environment sterically hinders the isomerisation, which is consistent with the observation of a viscosity dependent lifetime by Presiado *et al.*[16] As the dynamics of the S_3 and S_2 excited states are similarly affected by the solvent environment, it may therefore follow that excitation to these excited states is followed by a significant geometric change, although this might have been expected to have been observed by Presiado *et al.*[16] The change in the dynamics of these states could otherwise be explained by shifting of the energetic positions of the electronic excited states induced by solvation.

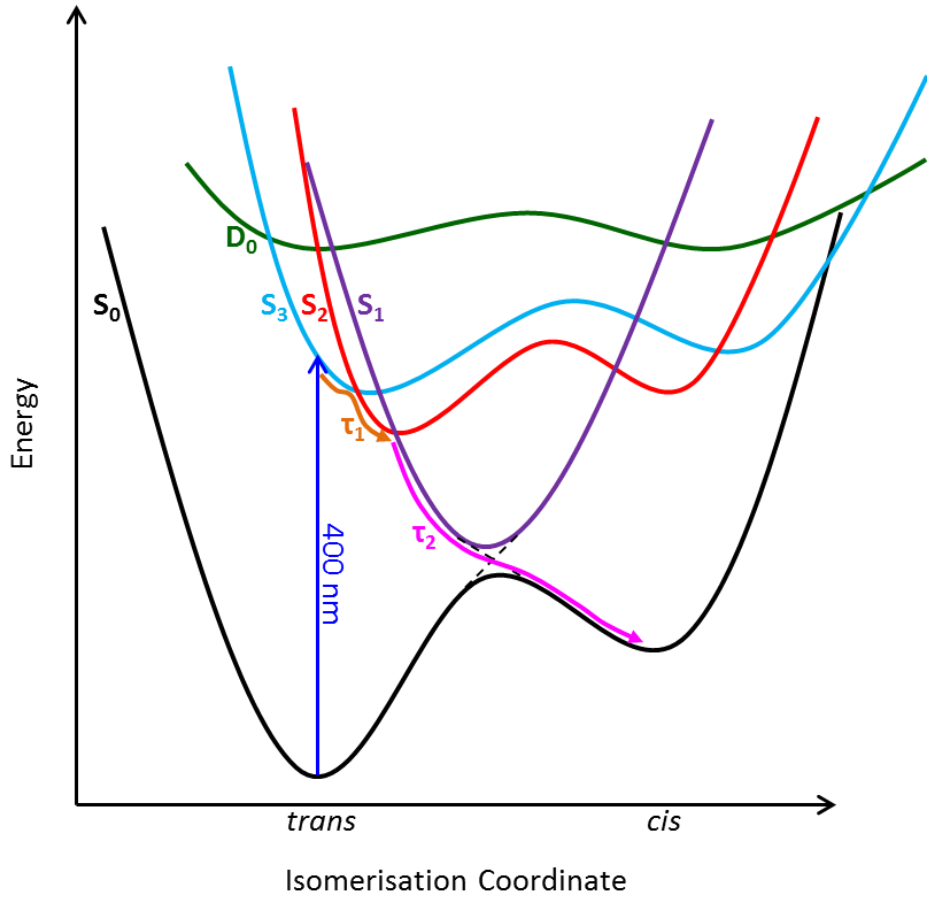

Figure 7.9 Schematic energy level diagram representing the possible decay pathway of ATRA in the 3.10 eV + 1.55 eV (400 nm + 800 nm) time-resolved experiment.

In apparent contradiction to numerous other observations,[12,14,15] we do not observe formation of triplet states following photoexcitation. It has previously been noted that the intersystem crossing from the $^1A_g^-(\pi\pi^*)$ state to the T_1 state is inefficient[16] and the previously observed lifetimes of the $^1A_g^-(\pi\pi^*)$ state in solution are considerably longer than our present observations, due to the loss of the constrictive solution-phase environment. It is therefore reasonable to assume that the formation of the triplet state is sufficiently slow compared to the loss of the $^1A_g^-(\pi\pi^*)$ state through the *trans-cis* isomerisation that the ground electronic state is the dominant product and the triplet state population is essentially nil. However, we cannot rule out the possibility that we are simply unable to observe the T_1 state under our photoexcitation schemes, as the

probe pulse has insufficient energy to ionise the ground state. Ideally, a pump-probe excitation scheme of 3.1 eV + 4.66 eV (400 nm + 266 nm) would be used in order to allow us to probe ground state recovery – unfortunately, the pump-probe signal for this excitation scheme is effectively zero when this excitation scheme is employed using our current set-up.

7.6 Summary

In summary, we have identified the detachment energetics of all-*trans*-retinoic acid and probed the excited state dynamics following photoexcitation at 3.10 eV through time-resolved PE spectroscopy. We observe a minimum of 2 sequential lifetimes and note that the spectral features are not constant in *eKE* with time. We assign the first, ultrafast lifetime to decay of the initially excited S_3 state to the S_2 and subsequently the S_1 states. The second lifetime is then assigned to the subsequent decay of the S_1 excited state population to the S_0 state via a conical intersection accessible *via* a *trans-cis* isomerisation. The lifetime of this process is consistent with previous measurements of the *cis-trans* isomerisation in rhodopsin.

7.7 References

(1) Maden, M. *Nature Reviews Neuroscience* **2007**, *8*, 755.
(2) Giguere, V. *Endocrine Reviews* **1994**, *15*, 61.
(3) Niederreither, K.; Dolle, P. *Nature Reviews Genetics* **2008**, *9*, 541.
(4) Curley, R. W.; Fowble, J. W. *Photochemistry and Photobiology* **1988**, *47*, 831.
(5) Christen R. L.; Kohler, B. E. *Photochemistry and Photobiology* **1974**, *19*, 401.
(6) Fisher, M. M.; Weiss, K. *Photochemistry and Photobiology* **1974**, *20*, 423.
(7) Polli, D.; Altoe, P.; Weingart, O.; Spillane, K. M.; Manzoni, C.; Brida, D.; Tomasello, G.; Orlandi, G.; Kukura, P.; Mathies, R. A.; Garavelli, M.; Cerullo, G. *Nature* **2010**, *467*, 440.
(8) Takeuchi, S.; Tahara, T. *Journal of Physical Chemistry A* **1997**, *101*, 3052.

(9) Tallent, J. R.; Birge, J. R.; Zhang, C. F.; Wenderholm, E.; Birge, R. R. *Photochemistry and Photobiology* **1992**, *56*, 935.

(10) Yamaguchi, S.; Hamaguchi, H. *Journal of Physical Chemistry A* **2000**, *104*, 4272.

(11) Takemura, T.; Das, P. K.; Hug, G.; Becker, R. S. *Journal of the American Chemical Society* **1978**, *100*, 2626.

(12) Zhang, L.; Yang, J.; Wang, L.; Yang, G. Z.; Weng, Y. X. *Journal of Physical Chemistry B* **2003**, *107*, 13688.

(13) Sahyun, M. R. V.; Serpone, N. *Journal of Photochemistry and Photobiology a-Chemistry* **1998**, *115*, 231.

(14) Weng, Y. X.; Xu, J. Z.; Pan, J.; Lin, K. L.; Wang, L.; Yang, G. Z. *Acta Botanica Sinica* **2000**, *42*, 1215.

(15) Xiang, J. F.; Rondonuwu, F. S.; Kakitani, Y.; Fujii, R.; Watanabe, Y.; Koyama, Y.; Nagae, H.; Yamano, Y.; Ito, M. *Journal of Physical Chemistry B* **2005**, *109*, 17066.

(16) Presiado, I.; Shomer, S.; Erez, Y.; Gepshtein, R.; Amdursky, N.; Huppert, D. *Journal of Photochemistry and Photobiology a-Chemistry* **2013**, *258*, 30.

(17) Fu, Z.; Li, X.; Merz, K. M., Jr. *Journal of Chemical Theory and Computation* **2012**, *8*, 1436.

(18) Ruiz-Anchondo, T.; Flores-Holguin, N.; Glossman-Mitnik, D. *Molecules* **2010**, *15*, 4490.

(19) Abyar, F.; Farrokhpour, H. *RSC Advances* **2014**, *4*, 35975

(20) Jericevic, Z.; Klasinc, L.; Kovac, B.; Novak, I. *Kemija u Industiji* **1980**, *29*, 117.

(21) Katsumata, S.; Ikehata, N. *Journal of Electron Spectroscopy and Related Phenomena* **2000**, *107*, 139.

(22) Roberts, G. M.; Nixon, J. L.; Lecointre, J.; Wrede, E.; Verlet, J. R. R. *Review of Scientific Instruments* **2009**, *80*, 053104.

(23) Wigner, E. P. *Physical Review* **1948**, *73*, 1002.

(24) Furr, H. C. *Journal of Nutrition* **2004**, *134*, 281S.

(25) Amrein, A.; Simpson, R.; Hackett, P. *Journal of Chemical Physics* **1991**, *95*, 1781.

(26) Baguenard, B.; Pinare, J. C.; Bordas, C.; Broyer, M. *Physical Review A* **2001**, *63*.

(27) Campbell, E. E. B.; Levine, R. D. *Annual Review of Physical Chemistry* **2000**, *51*, 65.

(28) Migani, A.; Sinicropi, A.; Ferré, N.; Cembran, A.; Garavelli, M.; Olivucci, M. *Faraday Discussions* **2004**, *127*, 179.

(29) Gai, F.; Hasson, K. C.; McDonald, J. C.; Anfinrud, P. A. *Science* **1998**, *279*, 1886.

(30) Mathies, R. A.; Cruz, C. H. B.; Pollard, W. T.; Shank, C. V. *Science* **1988**, *240*, 777.

(31) Schoenlein, R. W.; Peteanu, L. A.; Mathies, R. A.; Shank, C. V. *Science* **1991**, *254*, 412.

(32) Kandori, H.; Katsuta, Y.; Ito, M.; Sasabe, H. *Journal of the American Chemical Society* **1995**, *117*, 2669.

(33) Kim, J. E.; Tauber, M. J.; Mathies, R. A. *Biochemistry* **2001**, *40*, 13774.

(34) Gilbert, A.; Baggott, J. *Essentials of Molecular Photochemistry*; Blackwell Scientific Publications: Great Britain, 1991.

Chapter 8. Spectroscopy of the Antimony Tartrate Dianion

Gaseous multiply charged anions (MCAs) have been the subject of considerable interest due to the presence of the repulsive Coulomb barrier (RCB) and its effects on the electronic structure of the molecule and the corresponding photoelectron (PE) spectra. Here, we present a PE *imaging study of a highly symmetric dianion, antimony tartrate, in order to investigate the effect of the geometry of the RCB on the outgoing PE angular distribution. We report the detachment energetics (vertical detachment energy = 2.5 ± 0.1 eV) and the minimum height of the RCB (0.9 ± 0.1 eV), and note that the spectra exhibit strong anisotropy parallel to the laser polarisation. In order to describe the effect of the RCB on the observed PE angular distribution, we present classical electron dynamical simulations and show that, overall, the anisotropy can be predominantly described by these simulations once the molecular and lab frames have been reconciled.*

The interpretation of the PE spectra in this chapter is supported by DFT calculations performed by Dr James Bull. This chapter is based upon 'Photoelectron Imaging of the Isolated Antimony Tartrate Dianion', C. W. West, J. N. Bull, D. A. Woods and J. R. R. Verlet, *Chem. Phys. Lett.*, **645**, 138 (2016)

8.1 Introduction

MCAs are both common and facile to produce in the solution and solid phase. In contrast, in the gas phase, the lack of a stabilising influence through solvation and other electrostatic interactions, coupled with the strong Coulomb repulsion between the negative charges, tends to destabilise MCAs. Nevertheless, the strong Coulomb repulsion also leads to dynamic stability of MCAs.[1-5] Specifically, the loss of an electron (or anionic fragment) is inhibited by the presence of the so-called repulsive Coulomb barrier (RCB),[6,7] which arises from the long-range repulsion between the

electron (fragment) and remaining anion. This dynamic stability can be sufficient to enable the observation of MCAs with a negative electron affinity,[8] in which the ground state lies above that of the detachment threshold. The nature of the RCB can be conveniently probed by PE spectroscopy.[1,4,6] Only electrons with sufficient kinetic energy to overcome the RCB can be ejected, leading to a characteristic cut-off in the PE spectra of MCAs at low energy. Additionally, because the outgoing electron is sensitive to the RCB at long-range, the angular distribution of PEs can be shaped to reflect the RCB. Because velocity-map imaging records both the electron kinetic energy and the PE angular distribution, PE imaging is ideally suited to studying dianion RCB characteristics.[1,9,10] Highly symmetric molecular MCAs are of particular interest from the perspective since they can exhibit strong RCB-induced anisotropy. More generally, there has been considerable interest in studying MCAs in the gas phase,[4] due to the absence of external influences on the molecules allowing the intrinsic electronic structure to be probed. Here, a PE imaging study of antimony tartrate dianion (AT^{2-}, Figure 8.1) which is a text-book inorganic dianion salt with high-symmetry (D_2) and a relatively high charge-density, is presented together with simulations of the outgoing PE distribution. Additionally, the PE spectroscopy of its potassium salt anion ($[AT+K]^-$) is presented.

Antimony potassium tartrate has been employed in a variety of applications: as a fixing agent for dyes in the tanning and textile industries[11] (although this use is becoming increasingly uncommon with the advent of other, safer techniques),[12] in the production of V-Sb-O catalysts for the production of acrylonitrile,[13] and as a colorimetric test for phosphate in water.[14] However, the vast majority of historical applications are based around the well-documented toxicity of antimony potassium tartrate and medicinal use.[15-17] Antimony, in a number of different complexes, has been

employed by physicians for millennia; the Ebers Papyrus,[18] written in approximately 1550 BCE, details several antimony-containing treatments for complaints such as eye infections and gonorrhoea. Despite their long history, widespread use of antimonyl treatments began in the late 1500s BCE due to the teachings of Paracelsus[19] and the publication of 'The Triumphant Chariot of Antimony'.[†] [20] APT, also known as tartar emetic, was first described by Mynsicht in 1631,[21] although the compound was known to and used by Paracelsus.[19] Although small doses (<50 mg) induce sweating and vomiting, and larger doses are fatal,[22] antimony potassium tartrate has been used as a treatment for parasitic infections such as Leishmaniasis[23] and Schistosomiasis,[24] which are still in use today, although antimony containing treatments have been historically prescribed for a vast and wide ranging number of ailments,[18,21,22] such as depression,[21] rheumatism and alcoholism.[22] This last use has been remarkably persistent, with antimony potassium tartrate being legally sold for this purpose in the US until the 1940s[25] and reported as recently as 2010.[26]

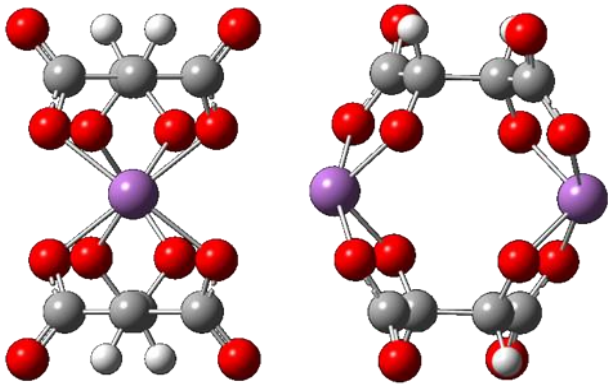

Figure 8.1 Top (left) and side (right) view of the structure of the Antimony Tartrate dianion (AT^{2-}), which adopts a D_2 symmetric equilibrium geometry.

[†] The provenance of this text is somewhat fantastical – Basilius Valentinus, a 15th century alchemist and Canon of the Benedictine Priory of Saint Peter in Erfurt, Germany, studied the properties of Antimony and secreted his work in a pillar in the priory. The work was lost for years after his death, until the pillar was split by a bolt of lightning, the work rediscovered and subsequently published. The veracity of the story was called into question in the 18th century, as no record of the monk existed in either Rome or Germany. The work has since been attributed, at least in part, to a 16th century salt manufacturer, Johann Thölde.

The vast majority of scientific studies on antimony potassium tartrate have been concerned with its interactions with and effects on biological systems.[27-29] The use of optical enantiomerically pure antimony potassium tartrate as a counter ion in order to precipitate enantiomerically pure chiral complexes from solution is also a well-documented separation method.[30,31] However, in the realms of physical chemistry and particularly in the gas phase, antimony potassium tartrate has attracted far less attention. As might be expected, almost all of studies in this area are concerned with the accurate determination of antimony in environmental samples.[14,32-36] An extremely wide range of techniques have been employed to this end, both individually and coupled,[31,33-35,37] including electrospray mass spectrometry,[38,39] high-performance liquid chromatography,[38,40] capillary electrophoresis interfaced to a plasma mass spectrometer[41] and molecular gas phase absorption spectroscopy.[42-44] In this work, we have isolated AT^{2-} and $[AT+K]^{-}$ in the gas phase and recorded their PE spectra at a variety of wavelengths. From these data, we have determined the electron detachment energetics and the effective height of the RCB in the dianion, and we present classical electron dynamical simulations to describe how the RCB guides the outgoing PE emission, which in turn provides insight into the detachment process.

As a representative high-symmetry dianion, AT^{2-} exhibits highly anisotropic PE images. We present classical electron dynamical simulations to describe how the RCB guides the outgoing PE emission, which in turn provides insight into the detachment process. Overall, our results show that the PE angular distribution can be described by classical dynamics provided a suitable connection between the laboratory and molecular reference frames. For AT^{2-} the connection is the differential detachment cross section.

8.2 Methodology

The experiment was performed as described in Chapter 2. Antimony potassium tartrate (Aldrich, 99+ %) was used without further purification. Isolated AT^{2-} were produced by electrospray ionisation (~1 mM in MeOH), introduced into vacuum and trapped by a radio frequency ring-electrode ion trap. The ion packet was pulsed out of the trap at 10 Hz. The isolated AT^{2-} or $[AT+K]^-$ ions were irradiated by nanosecond laser pulses ranging between 3.49 eV (355 nm) and 5.13 eV (240 nm), generated by the Horizon OPO. The experimental PE images were collected outside the vacuum by monitoring with a CCD camera the electron impacts on a dual multichannel-plate detector that was coupled to phosphor screen. Raw PE images were deconvoluted using the polar-onion peeling algorithm[45] in order to extract the PE spectra and angular anisotropies. PE spectra were calibrated from the atomic I^- spectrum and the resolution was ~5%.

Supporting density functional theory calculations to characterise geometries and electron detachment energetics were performed by Dr James Bull at the M06-2X//GEN and M11//GEN levels of theory using the Gaussian 09 software package.[46-48] Briefly, the GEN basis set includes the aug-cc-pVTZ basis set excluding the most diffuse *f* and *d* sets of functions for carbon and oxygen atoms, and excluding the most diffuse *d* functions for hydrogen atoms. Antimony was treated with the aug-cc-pVTZ-PP effective core potential basis set.[49] Optimized geometries were confirmed to represent geometrical minima through computation of harmonic vibrational frequencies, which also provided zero-point energy corrections.

8.3 Photoelectron Spectra

The minimum energy structure of the dianion has D_2 point symmetry. Despite the deficiencies of DFT for this system, Mulliken or natural bond order (NBO) population analysis[50] indicates that each antimony atom in the dianion equilibrium geometry has a charge of +0.9 or +1.9, respectively. The excess negative charge is distributed across the four carboxylic acid groups and hence AT^{2-} may be treated as a main group ionic complex.

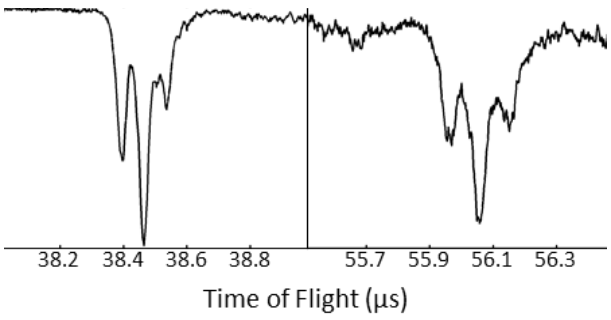

Figure 8.2 Negative ion Time of Flight mass spectrum of potassium antimony tartrate, showing the AT^{2-} (top) and $[AT+K]^-$ (bottom) anions and the characteristic isotopic distribution of Sb.

The time-of-flight mass spectrum, shown in Figure 8.2, contains two major peaks, each split into triplets with a ratio of approximately 2:3:1, centred at m/z = 268 and 575. The isotopic distribution leading to the observed triplets arises from the natural abundance of Sb. For two Sb ions with ^{121}Sb:^{123}Sb ~ 57:43,[51] the resulting distribution is expected to have a ratio of 1.8:2.6:1, in good agreement with experiment. The two peaks at m/z = 268 and 575 can thus be confidently assigned to AT^{2-} and $AT+K^-$, respectively.

Figure 8.3 shows the PE spectra of the AT^{2-} dianion collected at 3.49 eV (355 nm), 4.25 eV (290 nm), 4.74 eV (260 nm), and 5.17 eV (240 nm). The insets show the reconstructed central slices of the 3D PE distribution, where the top section shows the experimental slice and the bottom section shows the fit to equation (2.3).[52,53] The anisotropy can be quantified using the β_2 parameter (for a single photon process), which spans from +2 to –1 for a $\cos^2\theta$ or $\sin^2\theta$ distribution, respectively.

All spectra show a single peak centred at an electron binding energy (*eBE*) of ~2.5 eV, which broadens on the low kinetic energy side with increasing photon energy. The vertical detachment energy (VDE) can be determined to be 2.5 ± 0.1 eV. The adiabatic detachment energy (ADE) can be estimated by extrapolation of the low *eBE* edge towards the *eBE* axis to the value of ADE = 2.1 ± 0.1 eV.

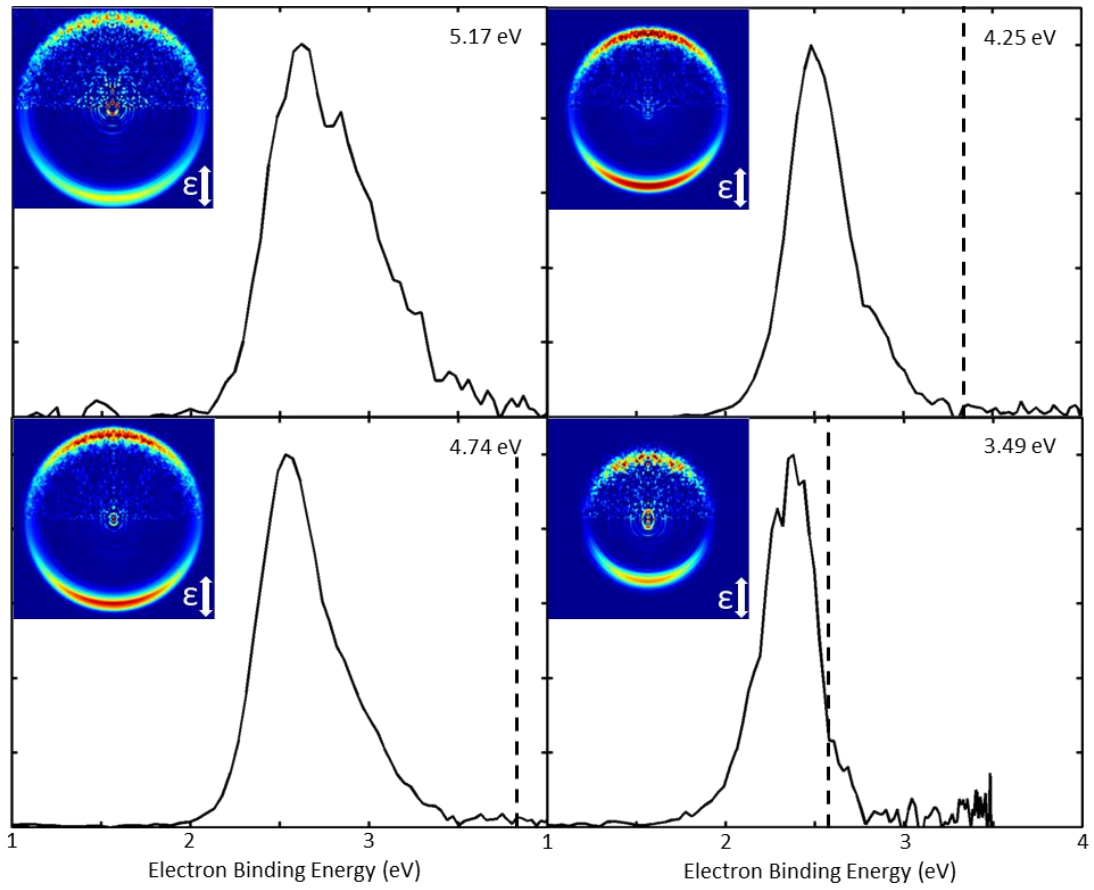

Figure 8.3 PE spectra recorded at 5.17 eV (240 nm), 4.74 eV (260 nm), 4.25 eV (290 nm) and 3.49 eV (355 nm). Inset in each plot is the central slice through the experimental (left) and simulated (right) velocity-map image. The position of the repulsive coulomb barrier at each binding energy is indicated by a vertical dashed line.

From the DFT calculations, the VDE is calculated at 2.78 eV (M06-2X functional) or 3.05 eV (M11 functional), while the ADE was calculated at 2.63 eV (M06-2X) and 2.84 eV (M11). In both cases the computed values are above those determined experimentally. Several calculations varying the amount of global Hartree-Fock exchange in the M06 suite of functionals shows the VDE to change between 2.11

eV and 3.91 eV, for 27% and 100% exchange, respectively. This simply reflects the inadequacies in DFT and functional parameterization to correctly describe systems of this type. Of note, M06-2X has 54% Hartree-Fock exchange, while M11 is a range-separated functional in which there is 43% local and 100% non-local Hartree-Fock exchange. Despite these variations in electron affinities, population analysis of the charge localization showed a reasonable insensitivity to the specific functional parameterization.

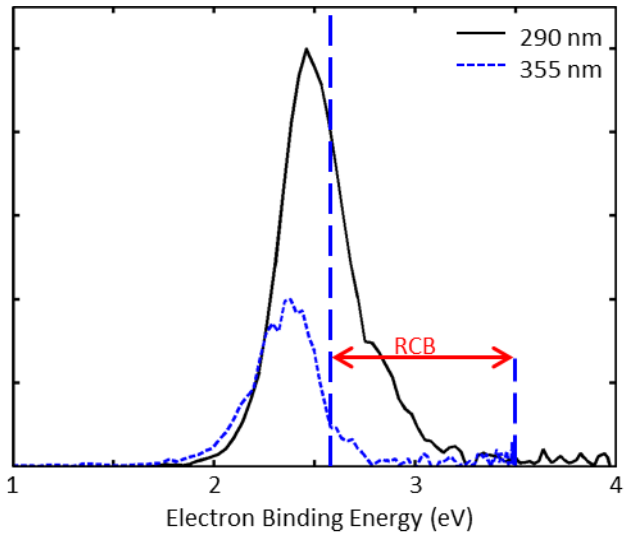

Figure 8.4 Overlaid PE spectra recorded at 290 nm (black) and 355 nm (blue dotted), and the position of the ends of the repulsive coulomb barrier at 355 nm (blue dashed).

The PE spectrum at 355 nm was excluded from the determination of photodetachment energetics as the observed signal levels were orders of magnitude lower due to the close proximity to the top of the RCB.[4,54] Briefly, the RCB presents a barrier to photodetachment of MCAs, produced through the competition between short range attraction of the liberated PE and the resultant AT^- anion, and long range repulsion between the PE and the AT^- anion.[1,4] Classically, only PEs with sufficient kinetic energy to surmount the RCB can be detected using PE spectroscopy.[4] Quantum mechanically, excitation near the top of the RCB may lead to electron tunnelling, thus leading to PE signal below the RCB cut-off. This contribution becomes particularly

pronounced if excitation accesses a dianion excited state that is situated above the detachment threshold but below the RCB.[1,10,55-58] In AT^{2-}, there are no excited states near 3.5 eV. The proximity of the RCB, however, means that the true VDE is never sampled in the 3.49 eV PE spectrum and therefore, this spectrum shows a spectral maximum that is 0.15 eV less than the spectra at higher photon energies, as is clearly shown in Figure 8.4. However, this spectrum does enable an accurate determination of the RCB height by extrapolating the falling edge at the high binding energy side of the peak. This yields an RCB height of 0.9 ± 0.1 eV for AT^{2-}. The position of the RCB has been included in all of the relevant PE spectra in Figure 8.3.

It is apparent from the PE images that photodetached electrons have strong ejection anisotropy that is predominantly parallel to the polarisation of the light, **ε**, as indicated in the inset PE images. The β_2 parameters for the PE peak averaged between 2.3 eV < *eBE* < 2.7 eV are +1.32, +1.16 and +0.97 at the excitation energies of 4.28 eV (290 nm), 4.77 eV (260 nm), and 5.17 eV (240 nm), respectively.

8.4 Elucidating the Effect of the RCB on the Photoelectron Anisotropy

For a singly-charged anion, the PE ejection anisotropy is predominantly dictated by the quantum interference between outgoing partial waves of the PE.[52,53] While some qualitative insight can be gained through symmetry considerations,[59] the quantitative prediction of the PE angular distribution for large molecular systems remains very difficult.[60,61] In contrast, the PE emission from a dianion is dominated by the long-range RCB effects; inherent quantum mechanical anisotropy influences are usually less important.[1,9,62] In accord, in a first approximation, photoemission from a dianion can be viewed as a classical electron moving on the RCB of the system. Within this zeroth order picture the observed anisotropy can be modelled using classical trajectories.

The classical dynamics requires knowledge of the molecular RCB surface, $V(x, y, z)$, which can be calculated using *ab initio* electronic structure methods.[63-65] However, given the known deficiencies of DFT for this system, we approximate $V(x, y, z)$ as the repulsion between an electron and AT^{-} defined as a series of point charges with magnitude as either the Mulliken or NBO charges[50] of AT^{-}. Because electron emission is essentially instantaneous with respect to molecular vibrations, we take AT^{-} to be in the equilibrium geometry of the dianion. Mulliken or NBO populations indicates that each antimony atom has a charge of +0.9 or +1.9, respectively. The excess negative charge is predominantly distributed across the four carboxylic acid groups (see Figure 8.1). The aim of the model here is not to achieve quantitative agreement, rather to determine if a simple classical picture can capture the observed dynamics and trends. The point-charge model will almost certainly not reproduce the true shape of the RCB at short-range, but should perform better at long-range. It is also important to recognise that the model ignores polarization of AT^{-} by the outgoing electron.

Figure 8.5 shows $V(x, y = 0, z)$ and $V(x = 0, y, z)$ on the left and right panes, respectively, calculated using NBO charges. The shape of $V(x, y, z)$ has two characteristics that are important in determining the observed PE anisotropy. Firstly, there is a large repulsive barrier in the xy plane around the molecule which roughly coincides with the location of the tartrate subunits; and secondly, two large attractive wells surround the antimony atoms as these are predominantly cationic in nature. The antimony ions lower the potential so that the lowest RCB (maximum along the saddle point) lies along the z axis. Electrons will require less energy to overcome these valleys and therefore, we anticipate that the electron will leave along the z axis at low photon energies.

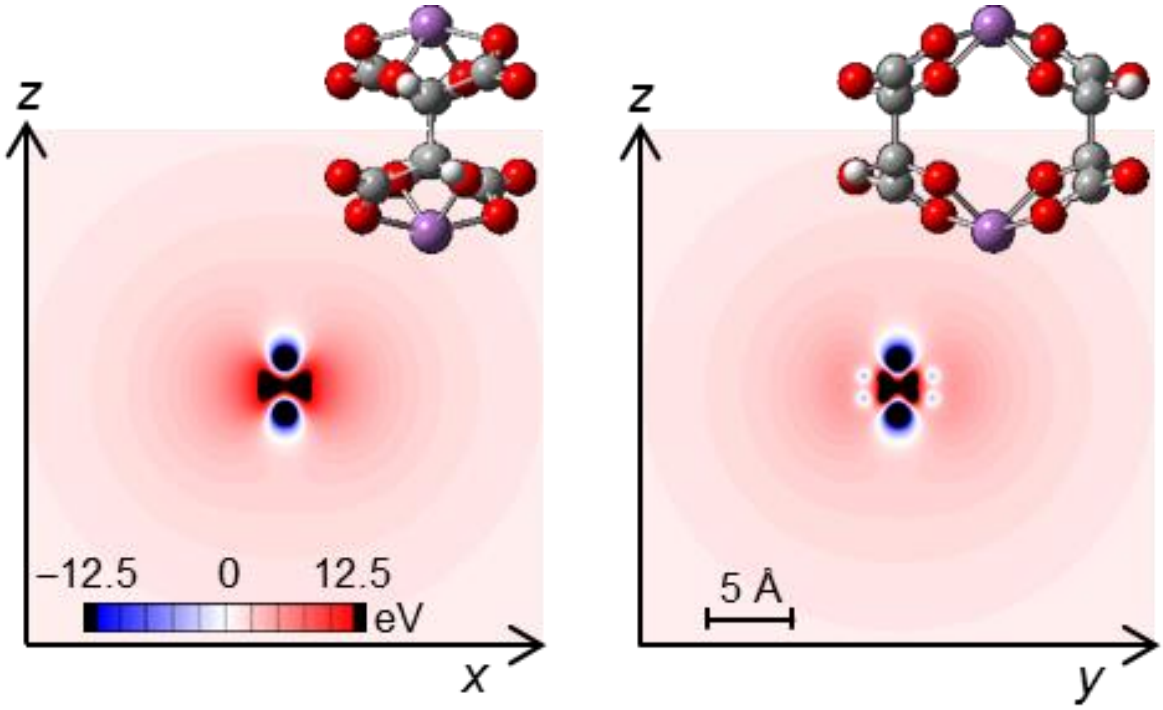

Figure 8.5 The electrostatic potential energy surface of an electron and the AT^- anion in the *xz* (left) and *yz* (right) planes. Repulsion is indicated by positive energy. Regions where the electrostatic interactions are greater than ±12.5 eV are indicated by black. The positions of the antimony cations are clearly identifiable by the large attractive (blue) potential wells.

The minimum energy barrier (RCB) along the *z* direction was calculated to be 1.1 eV (1.4 eV using Mulliken charges). This compares reasonably well with the 0.9 eV RCB determined from the experiment, given the approximations and the limitations of the DFT calculations.

To more completely examine the effect of the RCB on the observed PE anisotropy, we have simulated the PE images using the electrostatic potential, $V(x, y, z)$. In order to do this, we have invoked an approximation in which electron detachment can be considered equivalent to electron attachment. That is, to model the PE trajectories, we begin with a PE at some constant distance from the AT^- and that is allowed to propagate towards the AT^-. If the incoming PE has sufficient kinetic energy to overcome any part of the $V(x, y, z)$, then there is some probability that this electron trajectory could have been accessed in photodetachment of AT^{2-}. In a simple physical

picture, the electrons that contribute to the PE spectrum are those with trajectories that lead to a bound dianion – *i.e.* when $V(x, y, z) < 0$. To implement this, a series of random starting positions on a sphere of radius 1000 Å (Coulomb repulsion ~ 0.014 eV) from the centre of the molecule is chosen. From these positions, electrons with a given kinetic energy are directed towards the centre. The electrostatic force on the electron at each point was calculated and the electron progresses according to Newton's equations of motion using the Verlet algorithm.[66,67] A time step (proportional to the inverse square root of the force) was chosen to be sufficiently small ($5*10^{-20}$ s at 2.4 Å from the centre of the molecule) to sample the dynamics accurately. The trajectories are continued until either the electron returns to a long distance or when the electron reaches a region at which $V(x, y, z) < 0$. We consider that the former do not contribute to the PE emission while the latter do. In order to fully replicate photodetachment, we have generated the initial molecular frame distribution by collating several runs of the simulation at a single kinetic energy whilst varying the point towards which we direct our electrons by up to ±2 Å on an *x*, *y* and *z* raster.

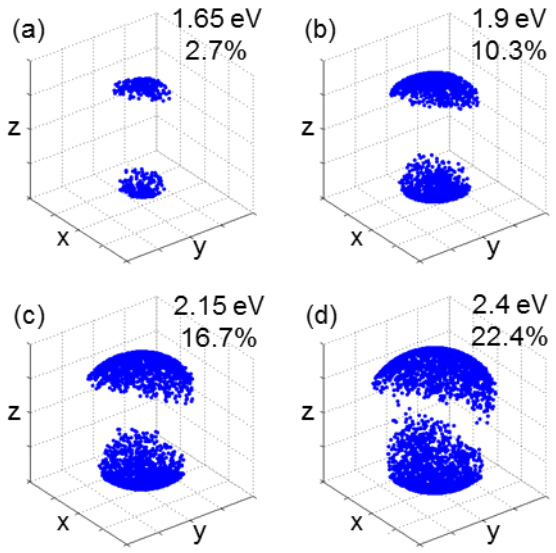

Figure 8.6 Plots showing the initial starting positions of the simulated electrons at various initial kinetic energies on a sphere with a radius of 1000 Å. The starting positions of electrons that surpass the RCB are shown in blue. The percentage of trajectories that surpass the RCB is also given.

In order to relate the simulation to the PE images, we record the initial velocities of the trajectories that may surpass the RCB, as the velocities are measured in VMI. In Figure 8.6, the initial velocities are plotted on a sphere representing those trajectories that contribute to the PE emission, calculated using the Mulliken point charges. Each panel represents a different initial kinetic energy of the electron as shown and each simulation consists of 15360 trajectories.

From Figure 8.6, it is clear that the initial positions of trajectories of electrons that surpass the RCB are clustered about the *z*-axis, which is in agreement with the expected result based on the shape of $V(x, y, z)$ shown in Figure 8.5. Figure 8.6 (a) shows the results for energies of 0.25 eV above the RCB. Only a tiny fraction (2.7%) of the trajectories contributes to the PE emission, which forms an almost symmetric circle around the *z*-axis. As the kinetic energy is increased, the fraction of trajectories increases to 22.4% for kinetic energies of 1 eV in excess of the RCB (Figure 8.6 (d)). As the electron kinetic energy increases, the distribution of trajectories that contribute to the PE emission also broadens. This broadening is caused by two factors: (i) the area over which the RCB can be overcome increases because the RCB is a saddle point; and (ii) the effect of $V(x, y, z)$ on the trajectory of the incoming (outgoing) electron becomes less as the relative excess kinetic energy increases. Additionally, the anisotropy in $V(x, y, z)$ becomes clearly apparent as the distribution of PE emission is no longer a symmetric circle around the *z*-axis. This is a direct effect of the geometry of the molecule; the distribution widens over the *x* axis, whereas the tartrate subunits are located over the *y* axis. The presence of the tartrate subunits results in a far higher repulsion of the electron from the *y* direction than the *x* axis, resulting in a lower RCB on the *xz* plane than the *yz* plane, as can be observed in Figure 8.6. Experimentally, of course, this anisotropy is not measured.

The anisotropy plotted in Figure 8.6 is not directly comparable with a single-photon PE spectroscopy experiment because the simulations present a molecular-frame (MF) PE emission for a laboratory-frame (LF) fixed molecule. In the experiment, a LF distribution of the PE emission is measured from a randomly distributed ensemble of dianions. In order to relate the simulated distributions to the experimentally observed β_2 parameters, the random orientation of AT^{2-} relative to $\boldsymbol{\varepsilon}$ must be accounted for.

If the differential cross section for photodetachment relative to $\boldsymbol{\varepsilon}$ was isotropic, then for a random initial distribution of AT^{2-}, one would expect a perfectly isotropic PE distribution with $\beta_2 \equiv 0$, regardless of any RCB anisotropy.[1] Experimentally, a large positive β_2 was observed, instead suggesting a differential cross section peaking along the molecular *z*-axis. To generate a laboratory-frame distribution, we convolute our simulated molecular-frame distribution with the differential cross section to photodetachment, where the angle θ is defined between $\boldsymbol{\varepsilon}$ and *z*. Because rotation about the *z* axis does not change θ, convolution with a uniform distribution about a 2π rotation in the *xy* plane is sufficient. In contrast, rotation about the *x* and *y* axes does affect θ. The limiting distributions are a $\cos^2\theta$ or $\sin^2\theta$ distribution, which correspond to the differential cross section peaking parallel and perpendicular to the molecular z axis, respectively, and would therefore lead to the maximal and minimal experimental β_2 parameters, respectively. These transformations should allow direct comparisons with the experimental velocity-map images. For such comparisons, we consider a 1% slice of the initial sphere about the *yz* plane of the simulated distribution from which the β_2 parameters are extracted by fitting the angular intensity to equation (2.3).

The convolution with a $\cos^2\theta$ distribution yields large, positive β_2 parameters, as observed experimentally, suggesting a differential detachment cross section that is predominantly parallel to the laser polarisation. We convolute the laboratory-frame PE

distribution with equation (2.3) where β_2 now becomes the anisotropy parameter of the differential detachment cross section, which we label as β_2'. Using this procedure, we find that β_2' = 2 provides good quantitative agreement with experiment. The results of these simulations using both the NBO and Mulliken charges are shown in Figure 8.7 together with the β_2 parameters extracted from the experiment. To aid comparison between experiment and simulation, the β_2 parameters are plotted as a function of the electron's kinetic energy in excess of the RCB. The experimental β_2 parameters are shown at a number of energies across the peak (where PE signal is greater than half of the peak – see Figure 8.3) for the four different photon energies.

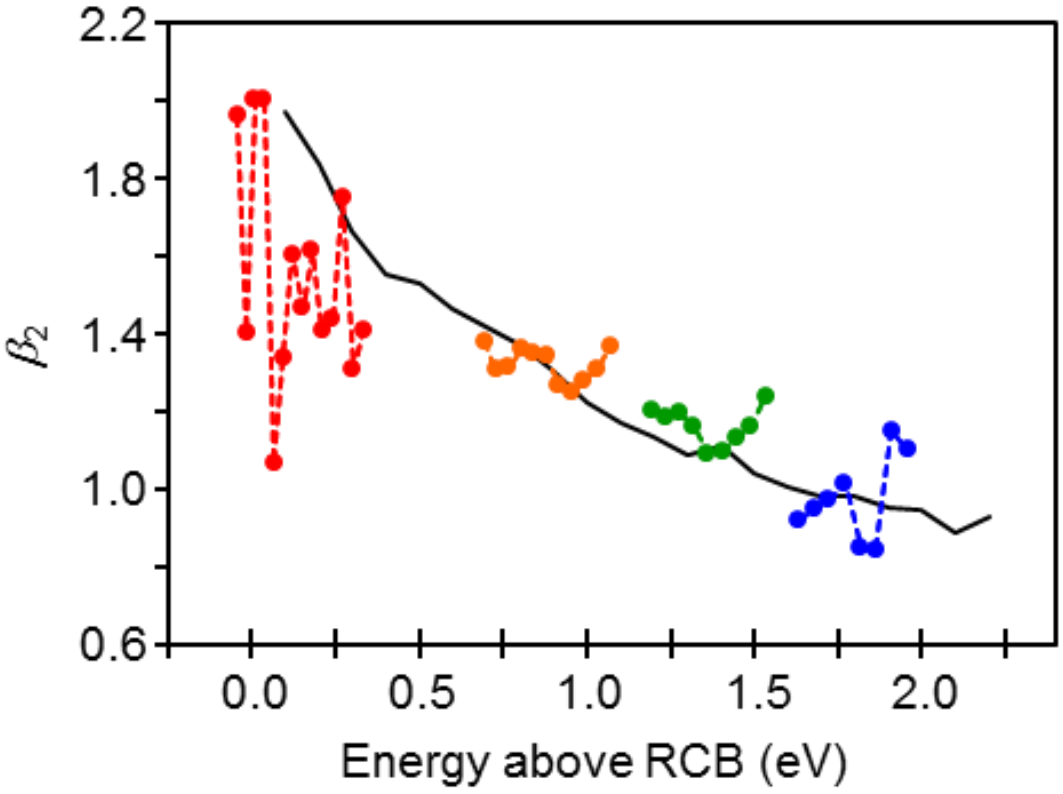

Figure 8.7 Comparison between β_2 parameters obtained by fitting the central plane of an electron distribution extracted from the simulation (black line) using the Mulliken charges and their associated error (grey line) and the β_2 parameters extracted from the PE images (circles, dashed line) taken at 3.49 eV (red), 4.28 eV (orange), 4.77 eV (green) and 5.17 eV (blue).

At the lowest photon energy, the β_2 data is very noisy and reflects the close proximity to the RCB cut-off where the signal levels were very low. Similarly, at the highest photon energy (5.17 eV), noise increases because of the increase in background electrons in our experiment.

The simulation results for the Mulliken and NBO charges were essentially identical, although the simulations using the NBO charges tend to predict lower β_2 parameters. This suggests that, even though the localised partial charges vary between both methods, the overall shape of the Coulomb potential is very similar, although the absolute RCB heights differ by ~0.3 eV. Any differences in the calculated electron trajectories due to the differences in the point charges between the two charge models and the different gradients of the potential energy surfaces that result should be more pronounced at short-range. Thus, the similarity of the final PE angular distributions for both methods supports the contention that the experimental PE distributions are dominated by long-range Coulomb interactions. That the experimental β_2 values decrease with increasing excess kinetic energy is reproduced in the simulations. Furthermore, the rate of decrease in β_2 with increasing energy above the RCB is also reproduced reasonably well, suggesting that the simple classical model has captured the underlying physics.

The model has numerous limitations and approximations, for instance the simplistic point charge potential. Since the charges are localised fractional point charges, the potential at these sites are singularities and probably have potential gradients that are too steep in the immediate proximity of the charge sites; lower photon energies are unable to create electrons that have trajectories that sample such immediate vicinities. In addition, polarisation of AT^- by the incoming electron may have some influence on the charge distribution and thus gradient of β_2 as a function of energy.

Again, polarization effects have not been considered. Finally, we have assumed a constant β_2' value across the energy range, although β_2' might have a modest energy dependence. We note that if neutral excited states were to become available with increasing photon energy, sudden in β_2' might be expected, although is not the case here. Despite these assumptions, which cannot be trivially accounted for or measured, and despite the simple classical dynamics approach and point-charge potential energy surface, there is overall good agreement between theory and experiment.

In summary, the results support the contention that classical dynamics dominate the PE angular distributions of dianions by virtue of the long-range interaction of the outgoing electron and the remaining anion.[1,9,62] Through comparison with simulations, we have characterized a possible differential cross section for detachment from AT^{2-}, which we emphasise is needed to connect the experimental (imaging) LF and simulation MF. Without a suitable transformation, experimental PE anisotropy can be difficult to interpret. A possible method to allow more direct comparisons would be molecular pre-alignment before photodetachment, for example, using resonant excitation if the dianion supports a bound electronic excited state.[62,68] However, even in this case, the differential cross section for photodetachment should be taken into account and this is in general not known *a priori*.

Finally, we consider the effect of the addition of a counter ion on the PE spectrum. The mass-spectrum (Figure 8.2(b)) also contained a peak distribution corresponding to AT^{2-} coordinated to a potassium cation: $[AT+K]^-$. The reduction from a dianion to a mono-anion is expected to have a significant effect on the PE spectrum; reducing the overall charge of the molecule will remove the RCB which, as we have previously shown, has significant influence over the distribution of detached electrons.

The PE spectrum taken at 300 nm is shown in Figure 8.8 and compared to the spectrum of AT^{2-} at 290 nm.

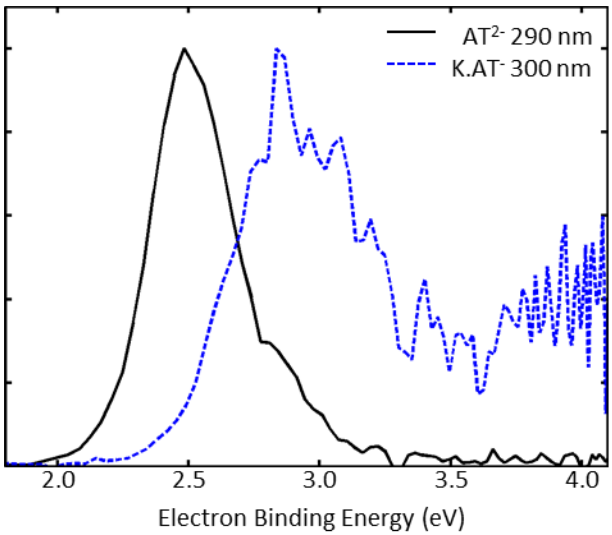

Figure 8.8 Normalised PE spectra of the AT^{2-} dianion, taken at 290 nm (black), and the $AT\text{-}K^-$ complex (blue dashed), taken at 300 nm.

Immediately apparent is the shift in binding energy. We have determined the VDE to be 2.8 ± 0.1 eV and the ADE to be 2.4 ± 0.1 eV; a shift of ~0.3 eV from AT^{2-}. While the direction of the shift is to be expected, as mono-anions do not experience the Coulomb repulsion between the charges as MCAs do, the magnitude is far smaller than might be expected. For reference, assuming that the charges are localised each on a single oxygen atom in AT^{2-} at the furthest possible distance from each other and no confounding influences, the Coulomb repulsion between the two charges is ~3 eV. Obviously this is mitigated by other factors such as shielding by the other atoms and orbital binding energies, but it still implies that we should expect to observe a much greater shift in binding energies following the loss of this intramolecular repulsion. This may imply that the electronic structure of the AT^{2-} is not significantly affected by the addition of the K^+ cation.

The shape of the PE spectrum of $[AT+K]^-$ between 2.2 eV < *eBE* < 3.2 eV exhibits a large, asymmetric peak that exhibits broadening to the high *eBE* side and tails

off to a plateau of high binding energy electrons. This is considerably broader than the peak observed for AT^{2-} and indicates that the detachment process has been altered. It is feasible that the addition of the K^+ cation has caused a greater number of vibrational modes in the neutral to be accessible following photodetachment, resulting in a wider range of electron energies being produced and hence the peak broadening and the observed plateau. The most significant change in the PE spectrum, the observation of the low energy electrons, could be explained by the loss of the RCB and a wider range of vibrational modes being available following photodetachment. The *ab initio* calculations required to explore the plausibility of this mechanism are beyond the scope of this thesis. However, these observations do not indicate a significant shift in the electronic structure of the AT^{2-} subunit, indicating again that the presence of the K^+ cation leaves the AT^{2-} relatively unperturbed.

Finally, we consider the anisotropy. While the dianion exhibits strong positive anisotropy, the PE image of the K^+ coordinated complex is completely isotropic. As the anisotropy in the AT^{2-} images are a direct result of the shape of the RCB, the addition of K^+ and the subsequent loss of the RCB, as also indicated by the observation of low kinetic energy electrons, has resulted in the completely isotropic observed image. This is expected, because there is no long range repulsion between the photoelectron and the neutral molecule. Therefore, the RCB and the associated anisotropy are absent.

8.5 Summary

A PE imaging study of the text-book antimony tartrate dianion ionic complex has been presented at a number of wavelengths. The VDE and ADE were determined to be 2.5 ± 0.1 and 2.1 ± 0.2 eV, respectively. The PE spectra show the expected cut-off due to the RCB, from which the height has been determined to be 0.9 ± 0.1 eV. All PE

images are highly anisotropic. DFT calculations provided the equilibrium structure of AT^{2-} and partial charges on each atom in AT^{-} as either Mulliken or NBO populations. The full RCB potential energy surface was then calculated using a simple model of an electron in the electrostatic field of AT^{-} point charges assuming the AT^{2-} geometry. The surface indicates that the RCB is highly anisotropic and would result in electron emission predominantly along the Sb–Sb axis (*z*-axis). The PE images were simulated using classical dynamics of an electron on the RCB surface and compared to experiment. This showed that good agreement was attainable assuming a differential cross section predominantly peaking along the *z*-axis. The simulations broadly reproduced the observed changes of PE anisotropy as a function of the electron's kinetic energy. The agreement between experiment and this simple model reflects that the PE angular distributions of a dianion are likely dominated by the long-range Coulomb interaction of the outgoing electron and the remaining anion. The results also highlight that knowledge of the relationship between laboratory and molecular frames is essential to correctly characterize such effects. Finally, we have recorded PE spectra of the $[AT+K]^{-}$ complex. Due to the loss of the RCB, the PE image is isotropic. The peak in the spectrum is found to have shifted in binding energy and low kinetic energy electrons are observed, which are ascribed to the presence of the K^{+} cation. The magnitude of the shift in binding energy is far less than expected.

8.6 References

(1) Chatterley, A. S.; Horke, D. A.; Verlet, J. R. R. *Physical Chemistry Chemical Physics* **2014**, *16*, 489.

(2) Dreuw, A.; Cederbaum, L. S. *Chemical Reviews* **2002**, *102*, 181.

(3) Scheller, M. K.; Compton, R. N.; Cederbaum, L. S. *Science* **1995**, *270*, 1160.

(4) Wang, X.-B.; Wang, L.-S. In *Annual Review of Physical Chemistry*; Annual Reviews: Palo Alto, 2009; Vol. 60, p 105.

(5) Wang, L.-S. *Journal of Chemical Physics* **2015**, *143*, 040901.

(6) Wang, X.-B.; Ding, C.-F.; Wang, L.-S. *Physical Review Letters* **1998**, *81*, 3351.
(7) Simons, J.; Skurski, P.; Barrios, R. *Journal of the American Chemical Society* **2000**, *122*, 11893.
(8) Wang, X.-B.; Wang, L.-S. *Nature* **1999**, *400*, 245.
(9) Xing, X.-P.; Wang, X.-B.; Wang, L.-S. *Physical Review Letters* **2008**, *101*, 083003.
(10) Horke, D. A.; Chatterley, A. S.; Verlet, J. R. R. *Journal of Physical Chemistry Letters* **2012**, *3*, 834.
(11) Burkinshaw, S. M. *Chemical Principles of Synthetic Fibre Dyeing*; Chapman and Hall: Glasgow, 1995.
(12) Burkinshaw, S. M.; Kumar, N. *Dyes and Pigments* **2008**, *79*, 48.
(13) Guerrero-Pérez, M. O.; Fierro, J. L. G.; Bañares, M. A. *Topics in Catalysis* **2006**, *41*, 43.
(14) Tiong, S. M. I. *Pertanika* **1987**, *10*, 27.
(15) Winship, K. A. *Adverse Drug Reactions and Acute Poisoning Reviews* **1987**, *6*, 67.
(16) Sundar, S.; Chakravarty, J. *International Journal of Environmental Research and Public Health* **2010**, *7*, 4267.
(17) Winslow, F. *The Journal of Psychological Medicine and Mental Pathology* **1857**, *10*, 1.
(18) trans. Ebbell, B. *The Papyrus Ebers*; Oxford University Press: London, 1937.
(19) Paracelsus *Opera omnia medico-chemico-chirurgica* Genevae, 1658.
(20) Valentinus, B.; Thölde, J. *Triumph Wagen Antimonii fratris Basilii Valentini ... allen so den Grund suchen der uhralten Medicin, auch zu der hermetischen Philosophy beliebnis tragen zu gut publiciret und an Tag geben*; in Verlegung Jacob Apels: Leipzig, 1611.
(21) von Mynsicht, A. *Thesaurus et Armamentarium Medico-Chymicum*; Schernwebel/Schmalherz: Lübeck, 1631.
(22) McCallum, R. I. *Antimony in Medical History*; The Pentland Press: Durham, 1999.
(23) Low, G. C. *Transactions of the Royal Society of Tropical Medicine and Hygine* **1916**, *10*, 37.
(24) Christopherson, J. B. *The Lancet* **1918**, *192*, 325.
(25) In *United States v. 11 1/4 Dozen Packages Labeled in Part 'Mrs. Moffat's Shoo Fly Powders for Drunkenness'*; Dist. Court, WD New York: 1941; Vol. 40, p 208.
(26) Konstantopolous, W. M.; Ewald, M. B.; Pratt, D. S. *The New England Journal of Medicine* **2012**, *367*, 259.
(27) *Biological Chemistry of Arsenic, Antimony and Bismuth*; 1st ed.; John Wiley & Sons Ltd: Chichester, 2011.
(28) Gebel, T. *Chemico-Biological Interations* **1997**, *107*, 131.
(29) Leonard, A.; Gerber, G. B. *Mutation Research/Reviews in Genetic Toxicology* **1996**, *366*, 1.
(30) Ward, T. J. *Analytical Chemistry* **2002**, *74*, 2863.
(31) Wijeratne, A. B.; Schug, K. A. *Journal of Separation Science* **2009**, *32*, 1537.
(32) Filella, M.; Belzile, N.; Chen, Y.-W. *Earth Science Reviews* **2002**, *57*, 125.

(33) Kumar, A. R.; Riyazuddin, P. *International Journal of Environmental Analytical Chemistry* **2007**, *87*, 469.

(34) Smichowski, P. *Talanta* **2008**, *75*, 2.

(35) Smichowski, P.; Madrid, Y.; Camara, C. *Fresenius' Journal of Analytical Chemistry* **1998**, *1998*, 623.

(36) Wilson, S. C.; Lockwood, P. V.; Ashley, P. M.; Tighe, M. *Environmental Pollution* **2010**, *158*, 1169.

(37) Miravet, R.; Hernández-Nataren, E.; Sahuuquillo, A.; Rubio, R.; López-Sánchez, J. F. *TrAC Trends in Analytical Chemistry* **2010**, *29*, 28.

(38) Lintschinger, J.; Schramel, O.; Kettrup, A. *Fresenius' Journal of Analytical Chemistry* **1998**, *361*, 96.

(39) Zheng, J.; Takeda, A.; Furuta, N. *Journal of Analytical Atomic Spectrometry* **2000**, *16*, 62.

(40) Lintschinger, J.; Koch, I.; Serves, S.; Feldmann, J.; Cullen, W. R. *Fresenius' Journal of Analytical Chemistry* **1997**, *359*, 484.

(41) Michalke, B. *Journal of Chromatography A* **1999**, *834*, 341.

(42) Cabredo, S.; Galban, J.; Sanz, J. *Talanta* **1998**, *46*, 631.

(43) Gallignani, M.; Ayala, C.; Brunetto, M. R.; Burguera, M.; Burguera, J. L. *Talanta* **2003**, *59*, 923.

(44) Gallignani, M.; Ovalles, F.; Brunetto, M. R.; Burguera, M.; Burguera, J. L. *Talanta* **2005**, *68*, 365.

(45) Roberts, G. M.; Nixon, J. L.; Lecointre, J.; Wrede, E.; Verlet, J. R. R. *Review of Scientific Instruments* **2009**, *80*, 053104.

(46) Kendall, R. A.; Dunning Jr., T. H.; Harrison, R. J. *Journal of Chemical Physics* **1992**, *96*, 6796.

(47) Frisch, M. J.; Trucks, G. W.; Schlegel, H. B.; Scuseria, G. E.; Robb, M. A.; Cheeseman, J. R.; Scalmani, G.; Barone, V.; Mennucci, B.; Petersson, G. A.; Nakatsuji, H.; Caricato, M.; Li, X.; Hratchian, H. P.; Izmaylov, A. F.; Bloino, J.; Zheng, G.; Sonnenberg, J. L.; Hada, M.; Ehara, M.; Toyota, K.; Fukuda, R.; Hasegawa, J.; Ishida, M.; Nakajima, T.; Honda, Y.; Kitao, O.; Nakai, H.; Vreven, T.; Montgomery Jr., J. A.; Peralta, J. E.; Ogliaro, F.; Bearpark, M. J.; Heyd, J.; Brothers, E. N.; Kudin, K. N.; Staroverov, V. N.; Kobayashi, R.; Normand, J.; Raghavachari, K.; Rendell, A. P.; Burant, J. C.; Iyengar, S. S.; Tomasi, J.; Cossi, M.; Rega, N.; Millam, N. J.; Klene, M.; Knox, J. E.; Cross, J. B.; Bakken, V.; Adamo, C.; Jaramillo, J.; Gomperts, R.; Stratmann, R. E.; Yazyev, O.; Austin, A. J.; Cammi, R.; Pomelli, C.; Ochterski, J. W.; Martin, R. L.; Morokuma, K.; Zakrzewski, V. G.; Voth, G. A.; Salvador, P.; Dannenberg, J. J.; Dapprich, S.; Daniels, A. D.; Farkas, Ö.; Foresman, J. B.; Ortiz, J. V.; Cioslowski, J.; Fox, D. J.; Gaussian, Inc.: Wallingford, CT, USA, 2009.

(48) Peverati, R.; Truhlar, D. G. *Journal of Physical Chemistry Letters* **2011**, *2*, 2810.

(49) Peterson, K. A. *Journal of Chemical Physics* **2003**, *119*, 11099.

(50) Reed, A. E.; Curtiss, L. A.; Weinhold *Chemical Reviews* **1988**, *88*, 899.

(51) Haynes, W. M.; Lide, D. R. *CRC Handbook of Chemistry and Physics: A Ready-Reference Book of Chemical and Physical Data*; 94 ed.; Fla: CRC: Boca Raton, 2010.

(52) Zare, R. N. *Molecular Photochemistry* **1972**, *4*, 1.

(53) Reid, K. L. *Annual Review of Physical Chemistry* **2003**, *54*, 397.

(54) Simons, J. *Journal of Physical Chemistry C* **2013**, *117*, 22314.

(55) Chatterley, A. S.; Horke, D. A.; Verlet, J. R. R. *Physical Chemistry Chemical Physics* **2012**, *14*, 16155.

(56) Horke, D. A.; Chatterley, A. S.; Verlet, J. R. R. *Physical Review Letters* **2012**, *108*, 083003.

(57) Dau, P. D.; H.-T., L.; Yang, J.-P.; Winghart, M.-O.; Wolf, T. J. A.; Unterreiner, A. N.; Weis, P.; Miao, Y.-R.; Ning, C.-G.; Kappes, M. M.; Wang, L.-S. *Physical Review A* **2012**, *85*, 064503.

(58) Winghart, M.-O.; Yang, J.-P.; Kuehn, M.; Unterreiner, A.-N.; Wolf, T. J. A.; Dau, P. D.; Liu, H.-T.; Huang, D.-L.; Klopper, W.; Wang, L.-S.; Kappes, M. M. *Physical Chemistry Chemical Physics* **2013**, *15*, 6726.

(59) Sanov, A. *Annual Review of Physical Chemistry* **2014**, *65*, 341.

(60) Oana, C. M.; Krylov, A. I. *Journal of Chemical Physics* **2009**, *131*, 124114.

(61) Liu, Y.; Ning, C. *Journal of Chemical Physics* **2015**, *143*, 144310.

(62) Mooney, C. R. S.; Horke, D. A.; Chatterley, A. S.; Simperler, A.; Fielding, H. H.; Verlet, J. R. R. *Chemical Science* **2013**, *4*, 921.

(63) Horke, D. A.; Chatterley, A. S.; Verlet, J. R. R. *Journal of Chemical Physics* **2013**, *139*, 084302.

(64) Dreuw, A.; Cederbaum, L. S. *Physical Review A* **2001**, *63*, 049904.

(65) Ning, C.-G.; Dau, P. D.; Wang, L.-S. *Physical Review Letters* **2010**, *105*, 263001.

(66) Verlet, L. *Physical Review* **1967**, *159*, 98.

(67) Verlet, L. *Physical Review* **1968**, *165*, 201.

(68) Horke, D. A.; Chatterley, A. S.; Bull, J. N.; Verlet, J. R. R. *Journal of Physical Chemistry Letters* **2015**, *6*, 189.

Chapter 9. Concluding Remarks

A brief summary of the major conclusions of the Thesis is presented alongside a discussion of future extensions of the work described previously.

9.1 Summary of Main Results

The first chapter of this thesis was devoted to a general overview of the expansive field of gas-phase femtochemistry. A short discussion of the fundamental concepts underlying the physical processes investigated preceeded a brief discussion of the experimental methods available to femto chemists. PE spectroscopy and its extension into the time domain by pump-probe spectroscopy, time-resolved PE spectroscopy, were discussed. Finally, a short discussion of the recent application of PE spectroscopy to the study of the dynamics of a variety of molecular systems was presented.

The second chapter was given to describing the PE spectrometer. The details of the pulsed anion beam machine and the production of femtosecond pulses were discussed, along with the principles of electrospray ionisation. The underlying principles of the VMI detector were discussed.

The third chapter presented an adaptaion of the global kinetic fit of a time-resolved PE spectrum to a series of exponential decays convoluted with an Gaussian distribution. The method fits the intensity of every pixel in a range of time-resolved PE velocity map images to an exponential decay convoluted with a Gaussian distribution. This fit is applied before the reconstruction of the central slice of the PE cloud from the images in order to extract the PE images. In this fashion, the anisotropy of the PE features is conserved, allowing for the direct observation and fitting of time-resolved anisotropy. This fitting program was found to perform far better than the traditional

global kinetic fit to the spectra when dealing with low intensity datasets with overlapping features with differing anisotropies.

The fourth chapter concerns the dynamics of the first three excited states of the isolated model chromophore of GFP, $HBDI^-$. For the S_1 state, time-resolved PE spectroscopy has been used to determine the relative lifetimes of internal conversion and electron autodetachment, from which the lifetime for autodetachment was found to be ~ 30 ps. This remains approximately constant over an excitation range from 2.38 eV to 2.57 eV. Following UV excitation, the optically-bright S_3 state, which is populated for $h\nu$ > 3.7 eV, is shown to decay predominantly by internal conversion to the S_2 state that in turn autodetaches to the neutral ground state. For $h\nu$ > 4.1 eV, a new and favourable autodetachment channel from the S_2 state becomes available, which leads to the formation of the first excited state of the neutral. The results indicate that the UV excited state dynamics of the GFP chromophore involve a number of strongly coupled excited states.

The fifth chapter details the application of anion frequency- and angle- resolved PE imaging in order to map-out molecular excited state dynamics of the biologically important moiety *para*-benzoquinone in the gas phase. Three-dimensional spectra of excitation energy, electron kinetic energy and electron ejection anisotropy were recorded and reveal clear fingerprints of excited and intermediate state dynamics. The results show that many of the excited states are strongly coupled, providing a route to forming the ground state radical anion, despite the fact that the electron is formally unbound in the excited states. The conclusions drawn here cannot be compared directly with electron impact attachment studies, mostly due to the differing Franck-Condon factors and the differences between the geometry in the neutral and anionic ground state. However, despite these caveats, frequency- and angle-resolved PE imaging can be

utilised to efficiently explore anionic resonances and can be easily extended to time-resolved experiments and to larger molecular systems.

The sixth chapter begins by presenting the PE spectra of a number of carboxylic acids, concentrating on phenylcarboxylic acids with varying lengths of aliphatic and conjugated carbon chains, systems with π-conjugation chains and biologically relevant molecules. In the saturated phenyl carboxylic acids, a PE feature at low eKE with a magnitude that increased with the length of the carbon chain linking the phenyl group and the carboxylic acid was observed. This was assigned to the interaction between the carboxylic acid group and the hydrogen in the *para* position on the phenyl, which becomes stronger as the carbon chain length increases. For the unsaturated carboxylic acids, the spectra were dominated by a statistical emission peak at low eKE, which was ascribed to initial photoexcitation of a $\pi^* \leftarrow \pi$ transition, followed by efficient internal conversion to the ground electronic state. An anomalous sharp peak was observed in the PE spectrum of octatrienoic acid and assigned to photodetachment of hydride. H^- ions were directly observed via velocity-map imaging, and the mechanism of H^- loss was assigned to a statistical process on the ground state. This was followed by the discussion of the PE spectra of biologically relevant molecules. The PE spectra of tryptophan and tyrosine were reported and found to differ significantly, which was assigned to differences in the relative cross-section for direct photodetachment between the molecules.

The seventh chapter presents a TRPES study of a biologically relevant chromophore, all-*trans*-retinoic acid. The adiabatic detachment energy and excited state energetics of are reported. Following photoexcitation to the S_3 state, a minimum of two sequential lifetimes are confidently observed. We assign the first, ultrafast lifetime to decay of the initially excited S_3 state to the S_2 and subsequently the S_1 states. The

second lifetime is then assigned to a trans-cis isomerisation on the S_1 excited state and the subsequent decay of the S_1 excited state population to the S_0 state via a conical intersection accessible in the cis state geometry.

Finally, the eighth chapter was devoted to a PE imaging study of a highly symmetric dianion, antimony tartrate, in order to investigate the effect of the geometry of the RCB on the outgoing PE angular distribution. We report the detachment energetics and the minimum height of the RCB. The spectra exhibit strong anisotropy parallel to the laser polarisation, which is a result of the geometry of the RCB potential energy surface. In order to describe this effect, we present classical electron dynamical simulations and show that, overall, the anisotropy can be predominantly described by these simulations once the molecular and lab frames have been reconciled.

9.2 Research Outlook

Some major themes in the work of this laboratory are the study of biologically relevant systems and 'building up' to larger and more complex molecular systems. Often, these goals are intertwined, as with a recent study of adenosine mononucleotide, dinucleotide and trinucleotide.[1] The monoanion of adenosine has an *m*/*z* of almost 1000 and has been shown to form a long-lived π-stacked excimer in the solution phase following photoexcitation.[2-6] However, this was not observed in our work. We assigned this observation to the excimer being more stable in the solution phase than the gas phase; indeed, the Bowers group showed that only 65% of $d(A)_2^-$ was in the π-stacked conformation in the gas phase at 80 K.[7] We estimate the temperature of the ions in the ion trap to be approximately 300 K, which would explain the absence of excimers in our spectra. If it were possible to cool the ions by use of a cryogenic ion trap, then we might expect to observe π-stacking. In addition, obtaining PE spectra of vibrationally cold

molecules allows for the resolution of vibrational bands, that are often smeared out in room temperature PE spectra.[8]

To this end, a new cryogenic ion trap is being installed on the machine at the time of writing.[9] The ability to generate cryogenically cooled molecules and solvent clusters of systems of interest cannot be understated. It is not unreasonable to suggest that we might wish to repeat almost every experiment that we have reported over the past several years. As cryogenic cooling 'locks' the molecule in a conformer, it is desireable to repeat experiments where we have observed changes in geometry; namely, excitation to the S_1 state of $HBDI^-$,[10] short chain DNA oligomers[1] and the excited state decay of ATRA (Chapter 7). It is also desireable to produce solvent clusters of our previously studied biologically relevant molecules such as $HBDI^-$,[10-13] DNA[1,14,15] and electron acceptors.[16-19]

The PE spectra of $HBDI^-$ could potentially provide a wealth of insight into the excited state dynamics. First and foremost, the ability to obtain vibrationally resolved PE spectra from cold anions is a great advantage when considering vibrational autodetachment from the S_1 excited state. Bochenkova and Andersen have calculated[20] that two high lying vibrational modes are responsible for mapping the geometry of the anion onto the geometry of the neutral, which is integral to the observation of below threshold threshold PEs through vibration autodetachment. If we are able to obtain a vibrationally resolved PE spectrum, it may be possible to experimentally identify these vibrational modes.

Additionally, isolated $HBDI^-$ does not exhibit fluorescence. However, when constrained in a matrix that is below the glass transition temperature, it is possible to observe the fluorescence.[21,22] This observation has previously been assigned to a rotation about the central allyl bridge following photoexcitation, resulting in a twisted

geometry that is unable to fluoresce.[10] When the molecule is constrained by a matrix, this geometry is inaccessible, hence the molecule may fluoresce. It may be possible to identify the prescence or absence of a barrier to rotation on the excited state surface through the use of careful TRPES measurements; by varying the pump pulse energy, we necessarily vary the initial vibrational energy on the S_1 excited state. If there is sufficient energy to surpass a barrier to rotation, then the observed dynamics will be identical to the observations of Mooney *et al.*[10] If there is insufficient energy, then the molecule will be 'trapped' in the fluorescent geometry. The excited state decay is then expected to be orders of magnitude slower. Therefore, by measuring the lifetime of the isolated anion, it should be possible to identify both the existence and height of a barrier to rotation.

Moving forward, we wish to expand our work on the methodology of FAT-PI, in particular for the application of this methodology to explore the resonances of electron acceptors. We have recently expanded the work detailed in Chapter 4 to a number of quinone systems. There are a variety of molecules that are suitable for study by FAT-PI. We have also begun to explore the excited state structure and dynamics of molecules found in the interstellar medium, such as polyaromatic hydrocarbons and $C_{2n}H^-$. However, an aim of the group for a number of years has been to study buckminsterfullerene, C_{60}. The ability of C_{60} to act as an electron acceptor has attracted significant interest and considerable effort has been applied in order to understand the anionic excited state structure, through electron attachment[23-29] and absorption[30] experiments and theoretical investigations.[31-35] The electron attachment spectrum recorded by Elhamidi *et al.* is extremely broad, with C_{60}^- produced at incident electron energies of at least 10 eV, highlighting C_{60}'s exceptional ability as an electron acceptor. Also present are a series of resonances, indicating the presence of above-threshold

anionic excited states and again suggesting that the Buckminsterfullerene anion is a suitable candidate for FAT-PI.

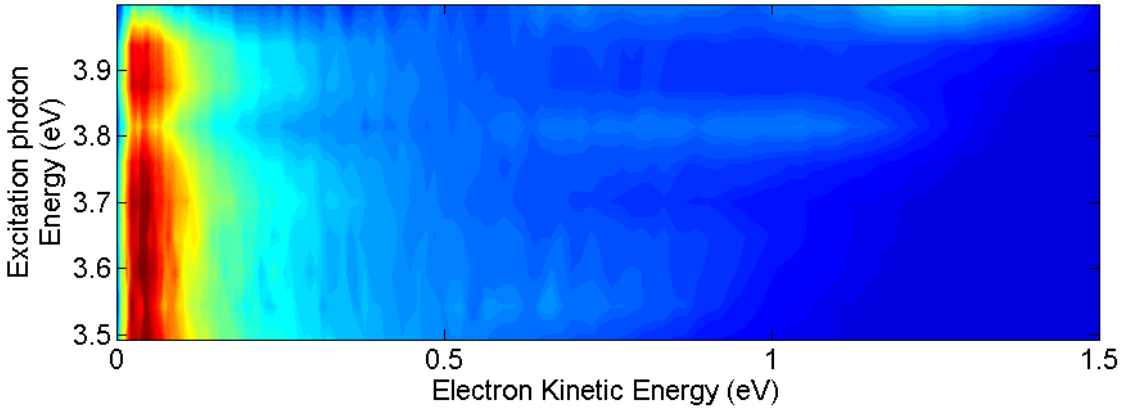

Figure 9.1 Area-normalised frequency resolved spectra of C_{60}^-.

Preliminary spectra for C_{60}, which have been obtained at excitation photon wavelengths of 310 nm - 355 nm in increments of 5 nm and are normalised to the area of the spectrum, are presented in Figure 9.1. There are two major peaks in the spectrum: an peak at low kinetic energy which has the appearance of an exponential decay and a peak at higher kinetic energy from direct detachment. The relative intensities of these peaks vary sharply between the spectra and several are dominated by the low energy peak. This is most likely due to multiple photon cycling; the molecule absorbs the excitation radiation to form an excited state, which subsequently decays to produce a vibrationally excited ground electronic state. This state can again absorb the incident radiation and relax, accumulating energy until an electron is lost through thermionic emission, giving rise to the low energy peak observed in the spectra. This peak may then obscure the spectral features from single photon processes, hindering assignment. Nevertheless, the presence of optically accessible resonances in the frequency-resolved spectrum can be clearly observed. We therefore plan to repeat the experiment over a much broader range of wavelengths, using far smaller increments in excitation energy and carefully selecting the detection settings in order to minimise the detection of

electrons detached from multiple photon processes in order to fully map the anionic excited states of the C_{60} anion.

The ordering and number of the bound anionic states of C_{60} are also uncertain.[31-36] Of particular interest is a correlation-bound s-type state, which is bound by 120 meV and has 91% of the charge density located outside of the C_{60} cage.[32,33] We wish to attempt to locate these excited states through photoelectron spectroscopy, although this is no longer straightforward; C_{60}^- has a vertical electron affinity of 2.689 eV[8], yet the first excited state is predicted to lie at 1.33 eV above the ground state.[31] We therefore have two options open to us: we can focus the nanosecond laser pulse into the chamber and attempt two-photon ionisation, or we can combine the nanosecond pulse with our femtosecond system and employ a pump-probe scheme.

Finally, we wish to perform time-resolved experiments to determine the dynamics of the excited state decay mechanisms of the determined excited states. Through this work, we aim to increase the understanding of both the anionic excited state structure and the mechanisms of electron attachment to C_{60}.

9.3 References

(1) Chatterley, A. S.; West, C. W.; Roberts, G. M.; Stavros, V. G.; Verlet, J. R. R. *Journal of Physical Chemistry Letters* **2014**, *5*, 843.

(2) Middleton, C. T.; de La Harpe, K.; Su, C.; Law, Y. K.; Crespo-Hernandez, C. E.; Kohler, B. In *Annual Review of Physical Chemistry*; Annual Reviews: Palo Alto, 2009; Vol. 60, p 217.

(3) Crespo-Hernandez, C. E.; Cohen, B.; Kohler, B. *Nature* **2005**, *436*, 1141.

(4) Crespo-Hernandez, C. E.; Cohen, B.; Hare, P. M.; Kohler, B. *Chemical Reviews* **2004**, *104*, 1977.

(5) Su, C.; Middleton, C. T.; Kohler, B. *Journal of Physical Chemistry B* **2012**, *116*, 10266.

(6) Olaso-Gonzalez, G.; Merchan, M.; Serrano-Andres, L. *Journal of the American Chemical Society* **2009**, *131*, 4368.

(7) Gidden, J.; Bowers, M. T. *European Physical Journal D* **2002**, *20*, 409.

(8) Wang, X. B.; Woo, H. K.; Wang, L. S. *Journal of Chemical Physics* **2005**, *123*, 051106.

(9) Stanley, L. H., *Personal Communication*,2015.

(10) Mooney, C. R. S.; Horke, D. A.; Chatterley, A. S.; Simperler, A.; Fielding, H. H.; Verlet, J. R. R. *Chemical Science* **2013**, *4*, 921.

(11) Horke, D. A.; Verlet, J. R. R. *Physical Chemistry Chemical Physics* **2012**, *14*, 8511.

(12) West, C. W.; Hudson, A. S.; Cobb, S. L.; Verlet, J. R. R. *Journal of Chemical Physics* **2013**, *139*, 071104.

(13) West, C. W.; Bull, J. N. H., A. S.; Cobb, S. L.; Verlet, J. R. R. *Journal of Physical Chemistry B* **2015**, *119*, 3982.

(14) Chatterley, A. S.; Johns, A. S.; Stavros, V. G.; Verlet, J. R. R. *Journal of Physical Chemistry A* **2013**, *117*, 5299.

(15) Chatterley, A. S.; West, C. W.; Stavros, V. G.; Verlet, J. R. R. *Chemical Science* **2014**, *5*, 3963.

(16) Bull, J. N.; West, C. W.; Verlet, J. R. R. *Chemical Science* **2015**, *6*, 1578.

(17) Horke, D. A.; Li, Q.; Blancafort, L.; Verlet, J. R. R. *Nature Chemistry* **2013**, *5*, 711.

(18) Horke, D. A.; Roberts, G. M.; Verlet, J. R. R. *Journal of Physical Chemistry A* **2011**, *115*, 8369.

(19) West, C. W.; Bull, J. N.; Antonkov, E.; Verlet, J. R. R. *Journal of Physical Chemistry A* **2014**, *118*, 11346.

(20) Bochenkova, A. V.; Andersen, L. H. *Faraday Discussions* **2013**, *163*, 297.

(21) Litvinenko, K. L.; Webber, N. M.; Meech, S. R. *Journal of Physical Chemistry A* **2003**, *107*, 2616.

(22) Webber, N. M.; Litvinenko, K. L.; Meech, S. R. *Journal of Physical Chemistry B* **2001**, *105*, 8036.

(23) Smith, D.; Spanel, P. *Journal of Physics B-Atomic Molecular and Optical Physics* **1996**, *29*, 5199.

(24) Kasperovich, V.; Tikhonov, G.; Kresin, V. V. *Chemical Physics Letters* **2001**, *337*, 55.

(25) Wang, S.; Trajmar, S.; Khakoo, M. A. *Journal of Physics B-Atomic Molecular and Optical Physics* **1993**, *26*, 3639.

(26) Prabhudesai, V. S.; Nandi, D.; Krishnakumar, E. *European Physical Journal D* **2005**, *35*, 261.

(27) Elhamidi, O.; Pommier, J.; Abouaf, R. *Journal of Physics B-Atomic Molecular and Optical Physics* **1997**, *30*, 4633.

(28) Huang, J.; Carman, H. S.; Compton, R. N. *Journal of Physical Chemistry* **1995**, *99*, 1719.

(29) Ptasinska, S.; Echt, O.; Denifl, S.; Stano, M.; Sulzer, P.; Zappa, F.; Stamatovic, A.; Scheier, P.; Mark, T. D. *The Journal of Physical Chemistry A* **2006**, *110*, 8451.

(30) Kato, T. *Laser Chemistry* **1994**, *14*, 155.

(31) Klaiman, S.; Gromov, E. V.; Cederbaum, L. S. *Journal of Physical Chemistry Letters* **2013**, *4*, 3319.

(32) Klaiman, S.; Gromov, E. V.; Cederbaum, L. S. *Physical Chemistry Chemical Physics* **2014**, *16*, 13287.

(33) Voora, V. K.; Cederbaum, L. S.; Jordan, K. D. *Journal of Physical Chemistry Letters* **2013**, *4*, 849.

(34) Negri, F.; Orlandi, G.; Zerbetto, F. *Journal of the American Chemical Society* **1992**, *114*, 2909.

(35) Zakrzewski, V. G.; Dolgunitcheva, O.; Ortiz, J. V. *Journal of Physical Chemistry A* **2014**, *118*, 7424.
(36) Mignolet, B.; Johansson, J. O.; Campbell, E. E. B.; Remacle, F. *Chemphyschem* **2013**, *14*, 3332.

Chapter 10. Appendices

10.1 Global Kinetic Fit to a Time-Resolved Images Series

```
function [Input,Control,Output] = Global_Image_Fit(Input,Control)
%%      ~~Global Image Fit to a Kinetic Model~~
%
% This code fits a series of velocity map images to a series of exponential
% decays. To begin, enter 'Global_Image_Fit;' into the Command Window. You
% will then be asked to define a number of variables required for the
% fitting program.
%
% Starting in this fashion will fit the time resolved data to a series of
% independent exponential decays convoluted by a Gaussian (the Instrument
% Response Function), in addition to a constant background image. The
% program will then plot the decay associated images, the experimental and
% fitted decay curves, the POP'ed background and decay associated spectra
% and, finally, the time-resolved experimental data and fit.
%
% After your first fit, we recommend that you subsequently enter
% '[Output,Control,Input] = Global_Image_Fit(Input,Control);' to avoid
% re-entering values and to give you greater control of the output of the
% program and the schemes that the data is fitted to. In particular, the
% program is able to fit to decay curves assuming 2 and 3 sequential
% lifetimes (Population 1 flows into population 2, and so on). The beta
% parameters of the decay associated images and the time-resolved data may
% also be extracted.
```

```
%
% Good luck!
% CWW, ASC, DAW


%%              ~~INPUTS~~
%
%  Input = Structured matrix containing all inputs.
%    Input.directory = Base directory of image files.
%    Input.tau = Row vector of initial lifetime estimates. Number of
%        inputs defines number of lifetimes in the fit.
%            (Default = 1, 2 and 3 lifetimes dependent
%            upon fitting regime used)
%    Input.IRF = Estimate of instrument response function.
%            (Default = 100 fs)
%    Input.ImCentre = Input for cropping images. [xcentre, ycentre,
%        radius] - When finding the image centre,
%        column number gives x.
%            (Default = [250 250 200])
%    Input.eKE = Calibration factor.
%            (Default = 1)
%    Input.t0 = t0
%            (Default = 0)
%    Input.Limits = Sets eKE and time limits.
%        [eKEmin eKEmax; tMin tMax]
%            (Default = [0 0; 0 0])
```

```
%              If eKEmin = eKEmax, limits are set to
%              minimum and maximum of the working scales
% Control = Controls functionality of code. Input blank variable for
%    default settings.
%    Fitting Controls
%     Control.Fitting_Proc = Controls fitting procedure.
%       1 = Runs fitting loop
%       0 = Skips to output
%          (Default = 1)
%     Control.Decay_Curves = Controls decay curves used.
%       1 = Assumes all lifetimes are independent.
%       2 = Assumes two lifetimes, with population from Tau(1)
%         feeding into population for Tau(2).
%       3 = Assumes three lifetimes, with population from
%         Tau(1) cascading into population for all other
%         lifetimes.
%          (Default = 1)
%    Plotting Controls
%       1 = On
%       0 = Off
%     Control.Plot_DAI = Plot DAI.
%                (Default = 1)
%     Control.Plot_Decay_Curves = Plot Decay Curves and
%                Integrals.
%                (Default = 1)
```

```
%       Control.POP_Output  = POP output experimental and fit
%               data.
%                   (Default  = 1)
%       Control.Plot_DAS  = Plot Background and DAS.
%                   (Default  = 1)
%       Control.TR_Data  = Plot all Time Resolved Data.
%                   (Default  = 1)
%       Control.TR_Beta  = Plot Time Resolved Beta(2)
%              Parameters.
%                   (Default  = 0)
%       Control.Figures  = Plotting for Figures.
%                   (Default  = 0)

%%              ~~OUTPUTS~~
%
% Output = Structured matrix containing all inputs
%   Output.tau  = Row vector of final lifetimes.
%   Output.IRF  = Fit of instrument response function.
%   Output.eKE  = eKE Vector used.
%            (Set POP_Output On)
%   Output.t0  = t0
%   Output.Limits  = Outputs the eKE and time lits used.
%            (Set POP_Output On)
%   Output.DAI  = Matrix of decay associated images.  1st column is the
%         background image,  2nd:end columns are the images
```

```
%       associated with Tau(1:end).
%   Output.delay_curves = Exponential decays that the TRPEI is fitted
%           to.
%   Output.shape = Original shape of the input images - use with
%       reshape to manually extract the decay associated
%       images from DAI.
%   Output.TR_Int = Row vector of the total intensity of the input
%       images at each time delay.
%         (Set Plot_Decay_Curves On)
%   Output.DAI_Int = Matrix of the total intensity of the decay
%       associated images at each time delay convoluted
%       with the associated delay curve - essentially the
%       contribution of each decay associated image to the
%       image at each time delay.
%       DAI_Int(1,:) = Background image
%       DAI_Int(2:end-1,:) = image associated with
%               Tau(1:end-1)
%       DAI_Int(end,:) = Sum of Lifetime contributions
%         (Set Plot_Decay_Curves On)
%   Output.TD = Time delays used in the experiment adjusted for t0.
%   Output.POPcomponents = Deconvoluted radial spectra of the decay
%         associated images extracted through POP.
%         (Set POP_Output On)
%   Output.DAIBeta2 = Beta(2) parameters of the decay associated images
%       extracted through POP.
```

```
%           (Set POP_Output On)
%   Output.DAIBeta4  = Beta(4) parameters of the decay associated images
%           extracted through POP.
%           (Set POP_Output On)
%   Output.ExTRPES  = Experimental TR photoelectron spectrum.
%           (Set POP_Output On)
%   Output.TRBeta2  = Beta(2) parameters of the decay associated images
%           extracted through POP.
%           (Set POP_Output On)
%   Output.TRBeta4  = Beta(4) parameters of the decay associated images
%           extracted through POP.
%           (Set POP_Output On)
%   Output.FitTRPES  = TR photoelectron spectrum from the fit.
%           (Set POP_Output On)
%   Output.BKGSubEx  = Background subtracted Experimental TR
%           photoelectron spectrum.
%           (Set POP_Output On)
%   Output.BKGSubFit  = Background subtracted fitted TR photoelectron
%           spectrum.
%           (Set POP_Output On)
% Control = Control Matrix.
% Input = Input Matrix.

%%          ~~TROUBLESHOOTING~~
%
```

% Q: The program is not extracting the time delays from the file names.

% A: This program was designed for use on our anion photoelectron

% spectrometer, which gives file names of the type

% '1_~1000_RA_400+800nm_200V_TR_r2.asc'. The program splits the

% filename into segments indicated by '_' and constructs the time

% delay vector by taking the 2nd part of the file name. You may

% either construct your filenames in a similar fashion or adjust the

% program - Go to the Extract_Images function and change the

% indicated value on line 506.

% Q: What is POP and why doesn't the code run without it?

% A: The program uses the Polar Onion Peeling algorithm to analyse

% the input images. The Matlab code was produced by Adi Natan and can

% be found at http://uk.mathworks.com/matlabcentral/fileexchange/41064-polar-onion-peeling

% Q: The program ends before a reasonable fit is found.

% A: Increase the 'MaxFunEvals' (FC1, line 697) or the 'MaxIter'

% (FC2, line 698) values.

% Q: The program gives an insufficiently accurate fit.

% A: Reduce the 'TolFun' (FC3, line 699) and 'TolX' (FC4, line 700)

% values.

% Q: My supervisor dislikes the colours of the line plots.

% A: You can adjust the colour scheme used to plot the decay curves

% and decay associated spectra by adjusting the 'Colours' colourmap

% on line 908. The other half of the issue, I can't help with.

%% ~~THE CODE~~

%% ~~CONTENTS~~

%

```
% Fitting Controls - 914
% Fitting Program - 920
% Construct Output matrix - 1043
% Extract Data - 1053
%  POP Output - 1074
%  Define Colour palette for plotting - 1181
%  Output fitting parameters - 1189
% Plot Results - 1215
% Extract DAI and residuals - 1217
% Plot Decay Curves and Integrals - 1249
% Plot Background and DAS - 1364
% Plot all Time Resolved Data - 1420
% Plot Time Resolved Beta(2) and Beta(4) Parameters - 1475
% Plotting for figures - 1576

%% Check Control and Input Matricies
% Check Input Variables
if ~exist('Input','var') || isempty(Input)
 Input = 0;
end

if isfield(Input,'Working_Directory')
 directory = Input.Working_Directory;
else
 disp('Please define the directory where your data is stored')
```

```
 directory = uigetdir('C:\');
 Input.Working_Directory = directory;
end

if ~exist('Control','var') || isempty(Control)
 Control = 0;
end

% Check Control structure exists
if ~isfield(Control,'Fitting_Proc')
 Control.Fitting_Proc = 1;
end
if ~isfield(Control,'Decay_Curves')
 disp('1 = Independent Lifetimes')
 disp('2 = 2 Sequential Lifetimes')
 disp('3 = 3 Sequential Lifetimes')
 disp('4 = 2 Sequential Lifetimes and additional independent lifetimes')
 disp('5 = 3 Lifetime Fit, 2 lifetimes simultaneously and sequentially')
 disp(' following from the first.')
 disp('6 = 3 Sequential Lifetimes and additional independent lifetimes')
 prompt = 'Which fitting proceedure would you like to use? ';
 x = input(prompt);
 Control.Decay_Curves = x;
end
if ~isfield(Control,'POP_Output')
```

```
  Control.POP_Output  = 1;
end
if ~isfield(Control,'Plot_DAI')
  Control.Plot_DAI  = 1;
end
if ~isfield(Control,'Plot_Decay_Curves')
  Control.Plot_Decay_Curves  = 1;
end
if ~isfield(Control,'Plot_DAS')
  Control.Plot_DAS  = 1;
end
if ~isfield(Control,'TR_Data')
  Control.TR_Data  = 1;
end
if ~isfield(Control,'TR_Beta')
  Control.TR_Beta  = 0;
end
if ~isfield(Control,'Figures')
  Control.Figures  = 0;
end

% Check Input structure exists
if ~isfield(Input,'tau')
  if isfield(Control,'Plot_Decay_Curves')
    switch Control.Decay_Curves
```

```
case 1
  prompt = 'How many lifetimes would you like to fit to? ';
  x = input(prompt);
  if x < 1
    prompt = 'How many lifetimes would you like to fit to? ';
    disp('Please enter a positive integer')
    x = input(prompt);
  end
  Input.tau = ones(1,x)*500;
case 2
  Input.tau = [100 500];
case 3
  Input.tau = [100 500 1000];
case 4
  disp('This fitting proceedure fits to two seqential')
  disp('lifetimes and a number of additional lifetimes.')
  prompt = 'How many additional lifetimes would you like to fit to? ';
  x = input(prompt);
  if x < 1
    prompt = 'How many lifetimes would you like to fit to? ';
    disp('Please enter a positive integer')
    x = input(prompt);
  end
  Input.tau = ones(1,(x+2))*500;
case 5
```

```
      Input.tau  = [100 250 500];
    case 6
      disp('This  fitting  proceedure fits to three seqential')
      disp('lifetimes  and a number  of additional  lifetimes.')
      prompt = 'How many  additional  lifetimes  would you like to fit to? ';
      x = input(prompt);
      if x < 1
        prompt = 'How many  lifetimes  would you like to fit  to? ';
        disp('Please  enter a positive  integer')
        x = input(prompt);
      end
      Input.tau  = ones(1,(x+3))*500;
   end
  end
end
if ~isfield(Input,'IRF')
  Input.IRF  = 100;
end
if ~isfield(Input,'ImCentre')
  prompt = 'Do you know the image  centre? Y/N  ';
  str = input(prompt,'s');
  if str == 'Y' || str == 'y'
    prompt = 'What is x (the column  number)?  ';
    x = input(prompt);
    prompt = 'What is y (the row number)?  ';
```

```
    y = input(prompt);
    prompt = 'What radius would you like to use?  ';
    r = input(prompt);
    Input.ImCentre  = [x y r];
  elseif  str == 'N' || str == 'n'
    disp('The  centre is set to default')
    disp('POP_Output  has been supressed')
    Input.ImCentre  = [250 250 200];
    Control.POP_Output  = 0;
  end
end

if ~isfield(Input,'eKE')
  prompt = 'Do you know the eKE scale? Y/N  ';
  str = input(prompt,'s');
  if str == 'Y' || str == 'y'
    prompt = 'What is the Calibration  factor?  ';
    x = input(prompt);
    Input.eKE  = x;
  elseif  str == 'N' || str == 'n'
  disp('The  eKE scale has been set to default')
  Input.eKE  = 1;
  end
end
```

```
if ~isfield(Input,'t0')
  Input.t0  = 0;
end

if ~isfield(Input,'Limits')
  Input.Limits  = [0 0; 0 0];
end

% Check Inputs
if length(Input.ImCentre)  ~= 3;
  disp('Overwriting  ImCentre  - Check Input')
  Input.ImCentre  = [250 250 200];
end

tauDim  = size(Input.tau);
if tauDim(1)  ~= 1
  if tauDim(2)  == 1
    Input.tau  = Input.tau';
  else
    msg = 'Input.tau  must  be a row vector';
    error(msg);
  end
end

if size(Input.IRF)  ~= 1
```

```
  disp('Input.IRF  must  be a 1x1 matrix  - overwritten')
  Input.IRF  = 100;
end
if size(Input.eKE)  ~= 1
  eKEtest = size(Input.eKE);
  if eKEtest(1)*eKEtest(2)  == eKEtest(1) && Input.eKE(1)  == 0
    disp('Assuming  eKE input  is a full  scale')
    disp('Input.eKE  must  be the calibration  factor')
    disp('Taking  2nd value  as calibration  factor')
    Input.eKE  = Input.eKE(2);
  elseif  eKEtest(1)*eKEtest(2)  == eKEtest(2)  && Input.eKE(1)  == 0
    disp('Assuming  eKE input  is a full  scale')
    disp('Input.eKE  must  be the calibration  factor')
    disp('Taking  2nd value  as calibration  factor')
    Input.eKE  = Input.eKE(2);
  end
  msg  = 'Input.eKE  must  be a 1x1 matrix';
  error(msg);
end
if size(Input.t0)  ~= 1
  disp('Input.t0  must  be a 1x1 matrix  - overwritten')
  Input.t0  = 0;
end
if size(Input.Limits)  ~= [2 2]
  disp('Input.Limits  must  be a 2x2 matrix  - overwritten')
```

```
 Input.Limits  = [0 0; 0 0];
end

% Clear Output File
Output = 0;

% Check Control Inputs
if Control.Fitting_Proc  == 0
 disp('Extracting  Fit at Input  Values')
elseif  Control.Fitting_Proc  == 1
 disp('Beginning  Fitting  Proceedure')
else
 msg = 'Check Fitting_Proc';
 error(msg);
end

if Control.Decay_Curves  == 1
 fprintf('Assuming  %0.0f Independent  Lifetimes\n',length(Input.tau))
elseif  Control.Decay_Curves  == 2
 if length(Input.tau)  == 2
  disp('Assuming  2 Consecutive  Lifetimes')
 else
  disp('This  Fitting  Proceedure fits  to 2 lifetimes')
  if length(Input.tau)  == 1
   disp('Another  Lifetime  is required')
```

```
    elseif length(Input.tau) == 3
      disp('One less Lifetime is required')
    elseif length(Input.tau) > 3
      disp('Please reduce the number of lifetimes')
    end
    msg = 'Check length of tau';
    error(msg);
  end
elseif Control.Decay_Curves == 3
  if length(Input.tau) == 3
    disp('Assuming 3 Consecutive Lifetimes')
  else
    disp('This Fitting Proceedure fits to 3 lifetimes')
    if length(Input.tau) == 2
      disp('Another Lifetime is required')
    elseif length(Input.tau) == 1
      disp('More Lifetimes are required')
    elseif length(Input.tau) == 4
      disp('One fewer Lifetime is required')
    elseif length(Input.tau) > 4
      disp('Please reduce the number of lifetimes')
      disp(' ')
      disp('There''s a fine, fine line')
      disp('Between together and not.')
      disp('And there''s a fine, fine line')
```

```
      disp('Between what you wanted and what you got.')
      disp('You''ve got to go after the things you want')
      disp('While you''re still in your prime')
      disp('But there''s a fine, fine line')
      disp('Between a reasonable fit')
      disp('And a waste of your time')
    end
    msg = 'Check length of tau';
    error(msg);
  end
elseif Control.Decay_Curves == 4
  if length(Input.tau) > 2
    disp('Assuming 2 Consecutive Lifetimes, with additional lifetimes')
  else
    disp('More lifetimes are required')
    msg = 'Check length of tau';
    error(msg);
  end
elseif Control.Decay_Curves == 5
  if length(Input.tau) == 3
    disp('Assuming 3 Lifetimes, 2 consecutive to the first')
  else
    disp('Fewer lifetimes are required')
    msg = 'Check length of tau';
    error(msg);
```

```
 end
elseif Control.Decay_Curves == 6
 if length(Input.tau) < 4
  disp('Assuming 3 Consecutive Lifetimes, with additional lifetimes')
 else
  disp('More lifetimes are required')
  msg = 'Check length of tau';
  error(msg);
 end
else
 msg = 'Check Decay_Curves';
 error(msg);
end

if Control.POP_Output == 1
elseif Control.POP_Output == 0
 if Control.Plot_DAS == 1;
  Control.Plot_DAS = 0;
  disp('Outputs Suppressed - Check POP_Output')
 end
 if Control.TR_Data == 1;
  Control.TR_Data = 0;
  disp('Outputs Suppressed - Check POP_Output')
 end
 if Control.TR_Beta == 1;
```

```
    Control.TR_Beta  = 0;
    disp('Outputs  Suppressed  - Check POP_Output')
  end
  if Control.Figures  == 1;
    Control.Figures  = 0;
    disp('Outputs  Suppressed  - Check POP_Output')
  end
else
  msg = 'Check POP_Output';
  error(msg);
end

if Control.Plot_DAI  ~= 0 && Control.Plot_DAI  ~= 1
  msg = 'Check Plot_DAI';
  error(msg);
end

if Control.Plot_Decay_Curves  ~= 0 && Control.Plot_Decay_Curves  ~= 1
  msg = 'Check Plot_Decay_Curves';
  error(msg);
end

if Control.Plot_DAS  ~= 0 && Control.Plot_DAS  ~= 1
  msg = 'Check Plot_DAS';
  error(msg);
```

```
end

if Control.TR_Data  ~= 0 && Control.TR_Data  ~= 1
  msg = 'Check TR_Data';
  error(msg);
end

if Control.TR_Beta  ~= 0 && Control.TR_Beta  ~= 1
  msg = 'Check TR_Beta';
  error(msg);
end

if Control.Figures  ~= 0 && Control.Figures  ~= 1
  msg = 'Check Figures';
  error(msg);
end

%% Function  to extract  images  from  Base Directory

function  [times,specs,shape]  = Extract_Images(base_dir,AoI)
%   times  = Experimental  time  delays
%   specs = Matrix  of experimental  images.  Each image  is returned  as a
%       column  in the matrix.
% ion_counts  = If experiment  has been performed  using  ion normalisation,
%       the ion count  is extracted  from the image  and returned  here
```

```
%   shape = Shape of the original image file


 if ~exist('base_dir','var')  && isempty(base_dir)
   base_dir = uigetdir();
 end
 files_list  = dir(base_dir);
 times  = [];
 specs = cell(1,0);
 for f=files_list.'
   if ~f.isdir  && ~isempty(regexp(f.name,'[.]asc$','ignorecase'))
     disp(f.name)
     % Read the time from the filename
     time  = strsplit(f.name,'_');
       try
         time  = time(2);  %<<--- <<--- <<---
         % This value determines which part of the file name is read
         % to construct the time delays matrix. The file name is
         % split by the underscores.
         % For example: 1_~1000_RA_400+800nm_200V_TR_r2.asc
         %      1 2 3  4  5 6 7
       catch
         time  = time(1);
         time  = strsplit(time,'.');
         time  = time(1);
       end
```

```
        time = strrep(time,'~','-');
        time = str2double(time);
        image_array = dlmread([base_dir,'\',f.name]);
        image_array(335,416) = 0;
        image_array(354,425) = 0;
        image_array(75,304) = 0;
        % These identify dead pixels in our photoelectron spectrometer.
        % Please feel free to remove and add to them as needed.
        Crop_IR = image_array(AoI(2,2):AoI(1,2), AoI(2,1):AoI(1,1));
        shape = size(Crop_IR);
        Crop_IR = reshape(Crop_IR,prod(shape),1);
        times = [times,time];
        specs = [specs,Crop_IR];
    end
  end
  [times,idxs] = sort(times);
  specs = specs(idxs);
  specs = cell2mat(specs);
  clear image_array
end


%% Extract TRPES from Base Directory
% Set area of image to extract from files
AoI = [(Input.ImCentre(1) + Input.ImCentre(3))...
```

```
  (Input.ImCentre(2)  + Input.ImCentre(3));...
  (Input.ImCentre(1)  - Input.ImCentre(3))...
  (Input.ImCentre(2)  - Input.ImCentre(3))];

% Extracts  images  from the home directory
[delays,TRPEI,shape]  = Extract_Images(directory,AoI);
%   delays = Experimental  time  delays
%   TRPEI = Matrix of experimental  images.  Each image  is returned  as a
%       column  in the matrix.
% delays  = -delays;
%% Generate  Inputs
sigma  = Input.IRF/2.35;

% Generate  input  matrix
InMat = ones(2+length(Input.tau),1);
InMat(1)  = Input.t0;        % t0
InMat(2)  = sigma;          % IRF
InMat(3:end)  = Input.tau;      % Lifetimes

% Generate  eKE matrix
eKE = ones(shape(1),1);
for a = 1:length(eKE)
  eKE(a) = ((a-1)^2)*Input.eKE;
end
```

```
%% Various fitting functions, dependent on mode chosen

%% Fitting to Independent Lifetimes
% Function to generate the decay curves
function [delay_curve,TD] =
IndLife_Decay_Curves(Time_Delays,Tau,t0,Sigma)
 delay_curve = zeros(length(Time_Delays),(length(Tau)+1));
 TD = Time_Delays - t0;

 % Background
 % Constant amplitude set to 1
 for b = 1
  delay_curve(:,b) = ones(length(Time_Delays),1);
 end

 % Lifetimes
 for b=(2:(length(Tau)+1))
  B = (Sigma^2/(2*Tau(b-1)^2)) - (TD)/Tau(b-1);
  C = erfc((-1/sqrt(2)).*((TD)/Sigma - Sigma/Tau(b-1)));
  delay_curve(:,b) = exp(B).*C;
 end
end

% Function to generate the decay associated images
function [error,delay_curves,DAI,TD] = IndLife_Fitting_Function(x)
```

```
[delay_curves,TD] = IndLife_Decay_Curves(delays,x(3:end),x(1),x(2));
% DAS, TRPEI, delay_curves are matricies
% TRPEI = DAS*delay_curves
% solve for DAS
DAI = TRPEI/delay_curves.';
error = TRPEI - DAI*delay_curves.';
end


%% Fitting to 2 Sequential Lifetimes
% Function to generate the decay curves
function [delay_curve,TD] =
SeqLife2_Decay_Curves(Time_Delays,Tau,t0,Sigma)
delay_curve = zeros(length(Time_Delays),(length(Tau)+1));
TD = Time_Delays - t0;

% Background
delay_curve(:,1) = ones(length(Time_Delays),1);

% First Independent Lifetime
B = (Sigma^2/(2*Tau(1)^2)) - (TD)/Tau(1);
C = erfc((-1/sqrt(2)).*((TD)/Sigma - Sigma/Tau(1)));
delay_curve(:,2) = exp(B).*C;
```

```
  % Second lifetime, population dependent upon Tau(1)
  % [B] = (k1/(k2-k1))*(exp^(-k1t)-exp^(-k2t))
  B = (Sigma^2/(2*Tau(2)^2)) - (TD)/Tau(2);
  C = erfc((-1/sqrt(2)).*((TD)/Sigma - Sigma/Tau(2)));
  D = (Sigma^2/(2*Tau(1)^2)) - (TD)/Tau(1);
  E = erfc((-1/sqrt(2)).*((TD)/Sigma - Sigma/Tau(1)));
  delay_curve(:,3) = ...
    (Tau(2)/(Tau(1)-Tau(2)))*(exp(D).*E - exp(B).*C);
end

% Function to generate the decay associated images
function [error,delay_curves,DAI,TD] = SeqLife2_Fitting_Function(x)
  [delay_curves,TD] = SeqLife2_Decay_Curves(delays,x(3:end),x(1),x(2));
  % DAS, TRPEI, delay_curves are matricies
  % TRPEI = DAS*delay_curves
  % solve for DAS
  DAI = TRPEI/delay_curves.';
  error = TRPEI - DAI*delay_curves.';
end


%% Fitting to 3 Sequential Lifetimes
% Function to generate the decay curves
function [delay_curve,TD] =
SeqLife3_Decay_Curves(Time_Delays,Tau,t0,Sigma)
```

```
delay_curve  = zeros(length(Time_Delays),(length(Tau)+1));
TD = Time_Delays  - t0;

% Background
delay_curve(:,1)  = ones(length(Time_Delays),1);

% First  Independent  Lifetime
B = (Sigma^2/(2*Tau(1)^2))  - (TD)/Tau(1);
C = erfc((-1/sqrt(2)).*((TD)/Sigma  - Sigma/Tau(1)));
delay_curve(:,2)  = exp(B).*C;

% Second lifetime,  population  dependent  upon Tau(1)
B = (Sigma^2/(2*Tau(2)^2))  - (TD)/Tau(2);
C = erfc((-1/sqrt(2)).*((TD)/Sigma  - Sigma/Tau(2)));
D = (Sigma^2/(2*Tau(1)^2))  - (TD)/Tau(1);
E = erfc((-1/sqrt(2)).*((TD)/Sigma  - Sigma/Tau(1)));
delay_curve(:,3)  = ...
 (Tau(2)/(Tau(1)-Tau(2)))*(exp(D).*E  - exp(B).*C);

% Third  lifetime,  population  dependent  upon Tau(2)  and hence  Tau(1)
% ((k1/((k1-k2)(k1-k3)))*(exp^(-k1t)-exp^(-k3t)))
% +((k1/((k1-k2)(k3-k2)))*(exp^(-k2t)-exp^(-k3t)))

B = (Sigma^2/(2*Tau(1)^2))  - (TD)/Tau(1);  %Tau(1)
C = erfc((-1/sqrt(2)).*((TD)/Sigma  - Sigma/Tau(1)));  %(exp(B).*C)
```

```
 k1 = 1/Tau(1);
 D = (Sigma^2/(2*Tau(2)^2))  - (TD)/Tau(2);  %Tau(2)
 E = erfc((-1/sqrt(2)).*((TD)/Sigma  - Sigma/Tau(2)));  %(exp(D).*E)
 k2 = 1/Tau(2);
 F = (Sigma^2/(2*Tau(3)^2))  - (TD)/Tau(3);  %Tau(3)
 G = erfc((-1/sqrt(2)).*((TD)/Sigma  - Sigma/Tau(3)));  %(exp(F).*G)
 k3 = 1/Tau(3);
 H = (k1*((exp(D).*E).*(exp(F).*G)));
 I = (k2-k3)*((exp(B).*C).*(exp(D).*E)).*(exp(F).*G);
 J = ((k1-k2)*(exp(D).*E));
 K = (k3-k1)*(exp(F).*G);
 L = (k1-k2)*(k1-k3)*(k2-k3);
 M = I + J + K;
 N = H.*M;
 O = N/L;
 delay_curve(:,4)  = O;
end


% Function  to generate  the decay associated  images
function  [error,delay_curves,DAI,TD]  = SeqLife3_fitting_function(x)
 [delay_curves,TD]  = SeqLife3_Decay_Curves(delays,x(3:end),x(1),x(2));
 % DAS, TRPEI,  delay_curves  are matricies
 % TRPEI  = DAS*delay_curves
 % solve  for DAS
 DAI = TRPEI/delay_curves.';
```

```
 error = TRPEI - DAI*delay_curves.';
end


%% Fitting to 2 Sequential Lifetimes and additional independent lifetimes
% Function to generate the decay curves
function [delay_curve,TD] = SeqLife2_Ind_Decay_Curves(Time_Delays,...
   Tau,t0,Sigma)
 delay_curve = zeros(length(Time_Delays),(length(Tau)+1));
 TD = Time_Delays - t0;

 % Background
 delay_curve(:,1) = ones(length(Time_Delays),1);

 % First Independent Lifetime
 B = (Sigma^2/(2*Tau(1)^2)) - (TD)/Tau(1);
 C = erfc((-1/sqrt(2)).*((TD)/Sigma - Sigma/Tau(1)));
 delay_curve(:,2) = exp(B).*C;


 % Second lifetime, population dependent upon Tau(1)
 % [B] = (k1/(k2-k1))*(exp^(-k1t)-exp^(-k2t))
 B = (Sigma^2/(2*Tau(2)^2)) - (TD)/Tau(2);
 C = erfc((-1/sqrt(2)).*((TD)/Sigma - Sigma/Tau(2)));
 D = (Sigma^2/(2*Tau(1)^2)) - (TD)/Tau(1);
```

```
 E = erfc((-1/sqrt(2)).*((TD)/Sigma  - Sigma/Tau(1)));
 delay_curve(:,3)  = ...
  (Tau(2)/(Tau(1)-Tau(2)))*(exp(D).*E  - exp(B).*C);

 % Independent  Lifetimes
 for b=(4:(length(Tau)+1))
  B = (Sigma^2/(2*Tau(b-1)^2))  - (TD - t0)/Tau(b-1);
  C = erfc((-1/sqrt(2)).*((TD)/Sigma  - Sigma/Tau(b-1)));
  delay_curve(:,b)  = exp(B).*C;
 end
end

% Function  to generate  the decay associated  images
function  [error,delay_curves,DAI,TD]  = SeqLife2_Ind_Fitting_Function(x)
 [delay_curves,TD]  = SeqLife2_Ind_Decay_Curves(delays,x(3:end),...
  x(1),x(2));
 % DAS, TRPEI,  delay_curves  are matricies
 % TRPEI  = DAS*delay_curves
 % solve  for DAS
 DAI = TRPEI/delay_curves.';
 error = TRPEI  - DAI*delay_curves.';
end


%% Fitting  to 3 Lifetimes,  2 lifetimes  simultaneously  and sequentially
```

```
% following from the first
% Function to generate the decay curves
function [delay_curve,TD] =
Three2Seq_Decay_Curves(Time_Delays,Tau,t0,Sigma)
 delay_curve = zeros(length(Time_Delays),(length(Tau)+1));
 TD = Time_Delays - t0;

 % Background
 delay_curve(:,1) = ones(length(Time_Delays),1);

 % First Independent Lifetime
 B = (Sigma^2/(2*Tau(1)^2)) - (TD)/Tau(1);
 C = erfc((-1/sqrt(2)).*((TD)/Sigma - Sigma/Tau(1)));
 delay_curve(:,2) = exp(B).*C;


 % Second lifetime, population dependent upon Tau(1)
 % [B] = (k1/(k2-k1))*(exp^(-k1t)-exp^(-k2t))
 B = (Sigma^2/(2*Tau(2)^2)) - (TD)/Tau(2);
 C = erfc((-1/sqrt(2)).*((TD)/Sigma - Sigma/Tau(2)));
 D = (Sigma^2/(2*Tau(1)^2)) - (TD)/Tau(1);
 E = erfc((-1/sqrt(2)).*((TD)/Sigma - Sigma/Tau(1)));
 delay_curve(:,3) = ...
  (Tau(2)/(Tau(1)-Tau(2)))*(exp(D).*E - exp(B).*C);
```

```
  % Third lifetime, population dependent upon Tau(1)
  % [B] = (k1/(k2-k1))*(exp^(-k1t)-exp^(-k2t))
  B = (Sigma^2/(2*Tau(3)^2)) - (TD)/Tau(3);
  C = erfc((-1/sqrt(2)).*((TD)/Sigma - Sigma/Tau(3)));
  D = (Sigma^2/(2*Tau(1)^2)) - (TD)/Tau(1);
  E = erfc((-1/sqrt(2)).*((TD)/Sigma - Sigma/Tau(1)));
  delay_curve(:,4) = ...
    (Tau(3)/(Tau(1)-Tau(3)))*(exp(D).*E - exp(B).*C);
end

% Function to generate the decay associated images
function [error,delay_curves,DAI,TD] = Three2Seq_Fitting_Function(x)
  [delay_curves,TD] = Three2Seq_Decay_Curves(delays,x(3:end),x(1),x(2));
  % DAS, TRPEI, delay_curves are matricies
  % TRPEI = DAS*delay_curves
  % solve for DAS
  DAI = TRPEI/delay_curves.';
  error = TRPEI - DAI*delay_curves.';
end


%% Fitting to 3 Sequential Lifetimes and additional independent lifetimes
% Function to generate the decay curves
function [delay_curve,TD] =
SeqLife3_Ind_Decay_Curves(Time_Delays,Tau,t0,Sigma)
```

```
delay_curve  = zeros(length(Time_Delays),(length(Tau)+1));
TD = Time_Delays  - t0;

% Background
delay_curve(:,1)  = ones(length(Time_Delays),1);

% First  Independent  Lifetime
B = (Sigma^2/(2*Tau(1)^2))  - (TD)/Tau(1);
C = erfc((-1/sqrt(2)).*((TD)/Sigma  - Sigma/Tau(1)));
delay_curve(:,2)  = exp(B).*C;

% Second lifetime,  population  dependent  upon Tau(1)
B = (Sigma^2/(2*Tau(2)^2))  - (TD)/Tau(2);
C = erfc((-1/sqrt(2)).*((TD)/Sigma  - Sigma/Tau(2)));
D = (Sigma^2/(2*Tau(1)^2))  - (TD)/Tau(1);
E = erfc((-1/sqrt(2)).*((TD)/Sigma  - Sigma/Tau(1)));
delay_curve(:,3)  = ...
 (Tau(2)/(Tau(1)-Tau(2)))*(exp(D).*E  - exp(B).*C);

% Third  lifetime,  population  dependent  upon Tau(2)  and hence  Tau(1)
% ((k1/((k1-k2)(k1-k3)))*(exp^(-k1*t)-exp^(-k3*t)))
% +((k1/((k1-k2)(k3-k2)))*(exp^(-k2*t)-exp^(-k3*t)))

B = (Sigma^2/(2*Tau(1)^2))  - (TD)/Tau(1);  %Tau(1)
C = erfc((-1/sqrt(2)).*((TD)/Sigma  - Sigma/Tau(1)));  %(exp(B).*C)
```

```
k1 = 1/Tau(1);
D = (Sigma^2/(2*Tau(2)^2))  - (TD)/Tau(2);  %Tau(2)
E = erfc((-1/sqrt(2)).*((TD)/Sigma  - Sigma/Tau(2)));  %(exp(D).*E)
k2 = 1/Tau(2);
F = (Sigma^2/(2*Tau(3)^2))  - (TD)/Tau(3);  %Tau(3)
G = erfc((-1/sqrt(2)).*((TD)/Sigma  - Sigma/Tau(3)));  %(exp(F).*G)
k3 = 1/Tau(3);
H = (k1*((exp(D).*E).*(exp(F).*G)));
I = (k2-k3)*((exp(B).*C).*(exp(D).*E)).*(exp(F).*G);
J = ((k1-k2)*(exp(D).*E));
K = (k3-k1)*(exp(F).*G);
L = (k1-k2)*(k1-k3)*(k2-k3);
M = I + J + K;
N = H.*M;
O = N/L;
delay_curve(:,4)  = O;

% Independent  Lifetimes
for b=(5:(length(Tau)+1))
  B = (Sigma^2/(2*Tau(b-1)^2))  - (TD - t0)/Tau(b-1);
  C = erfc((-1/sqrt(2)).*((TD)/Sigma  - Sigma/Tau(b-1)));
  delay_curve(:,b)  = exp(B).*C;
end
end
```

```
% Function to generate the decay associated images
function [error,delay_curves,DAI,TD] = SeqLife3_Ind_fitting_function(x)
 [delay_curves,TD] = SeqLife3_Ind_Decay_Curves(delays,x(3:end),x(1),x(2));
 % DAS, TRPEI, delay_curves are matricies
 % TRPEI = DAS*delay_curves
 % solve for DAS
 DAI = TRPEI/delay_curves.';
 error = TRPEI - DAI*delay_curves.';
end


%% Analysis

% Fitting Controls
FC1 = 20000; % 'MaxFunEvals'
FC2 = 20000; % 'MaxIter'
FC3 = 1e-10; % 'TolFun'
FC4 = 1e-10; % 'TolX'

% Fitting Program
if Control.Fitting_Proc == 1
 switch Control.Decay_Curves
   case 1
     % Start with the default options
     options = optimset;
```

```
% Modify options setting
options = optimset(options,'Display', 'iter-detailed',...
          'ScaleProblem', 'Jacobian',...
          'MaxFunEvals',FC1,...
          'MaxIter',FC2,...
          'TolFun', FC3,...
          'TolX',FC4);
% Fitting
[OutMat,~,~,~,~,~,~] = ...
  lsqnonlin(@IndLife_Fitting_Function, InMat,[],[],options);


[~,delay_curves,DAI,TD] = IndLife_Fitting_Function(OutMat);


case 2
% Start with the default options
options = optimset;
% Modify options setting
options = optimset(options,'Display', 'iter-detailed',...
          'ScaleProblem', 'Jacobian',...
          'MaxFunEvals',FC1,...
          'MaxIter',FC2,...
          'TolFun', FC3,...
          'TolX',FC4);
% Fitting
[OutMat,~,~,~,~,~,~] = ...
```

```
    lsqnonlin(@SeqLife2_Fitting_Function, InMat,[],[],options);

  [~,delay_curves,DAI,TD] = SeqLife2_Fitting_Function(OutMat);

case 3
  % Start with the default options
  options = optimset;
  % Modify options setting
  options = optimset(options,'Display', 'iter-detailed',...
            'ScaleProblem', 'Jacobian',...
            'MaxFunEvals',FC1,...
            'MaxIter',FC2,...
            'TolFun', FC3,...
            'TolX',FC4);
  % Fitting
  [OutMat,~,~,~,~,~,~] = ...
    lsqnonlin(@SeqLife3_fitting_function, InMat,[],[],options);

  [~,delay_curves,DAI,TD] = SeqLife3_fitting_function(OutMat);
case 4
  % Start with the default options
  options = optimset;
  % Modify options setting
  options = optimset(options,'Display', 'iter-detailed',...
            'ScaleProblem', 'Jacobian',...
```

```
            'MaxFunEvals',FC1,...
            'MaxIter',FC2,...
            'TolFun', FC3,...
            'TolX',FC4);
  % Fitting
  [OutMat,~,~,~,~,~,~] = ...
    lsqnonlin(@SeqLife2_Ind_Fitting_Function, InMat,[],[],options);

  [~,delay_curves,DAI,TD] = SeqLife2_Ind_Fitting_Function(OutMat);
case 5
  % Start with the default options
  options = optimset;
  % Modify options setting
  options = optimset(options,'Display', 'iter-detailed',...
            'ScaleProblem', 'Jacobian',...
            'MaxFunEvals',FC1,...
            'MaxIter',FC2,...
            'TolFun', FC3,...
            'TolX',FC4);
  % Fitting
  [OutMat,~,~,~,~,~,~] = ...
    lsqnonlin(@Three2Seq_Fitting_Function, InMat,[],[],options);

  [~,delay_curves,DAI,TD] = Three2Seq_Fitting_Function(OutMat);
case 6
```

```
    % Start with the default options
    options = optimset;
    % Modify options setting
    options = optimset(options,'Display', 'iter-detailed',...
              'ScaleProblem', 'Jacobian',...
              'MaxFunEvals',FC1,...
              'MaxIter',FC2,...
              'TolFun', FC3,...
              'TolX',FC4);
    % Fitting
    [OutMat,~,~,~,~,~,~] = ...
     lsqnonlin(@SeqLife3_Ind_fitting_function, InMat,[],[],options);

    [~,delay_curves,DAI,TD] = SeqLife3_Ind_fitting_function(OutMat);
  end

  % Extracting results from raw input
elseif Control.Fitting_Proc == 0
  switch Control.Decay_Curves
    case 1
    [~,delay_curves,DAI,TD] = IndLife_Fitting_Function(InMat);
    OutMat = InMat;

    case 2
    [~,delay_curves,DAI,TD] = SeqLife2_Fitting_Function(InMat);
```

```
    OutMat = InMat;


  case 3
    [~,delay_curves,DAI,TD] = SeqLife3_fitting_function(InMat);
    OutMat = InMat;
  case 4
    [~,delay_curves,DAI,TD] = SeqLife2_Ind_Fitting_Function(InMat);
    OutMat = InMat;
  case 5
    [~,delay_curves,DAI,TD] = Three2Seq_Fitting_Function(InMat);
    OutMat = InMat;
  case 6
    [~,delay_curves,DAI,TD] = SeqLife3_Ind_fitting_function(InMat);
    OutMat = InMat;
 end
end

% Construct Output matrix
Output.tau = OutMat(3:end)';
Output.IRF = OutMat(2)*2.35;
Output.t0 = OutMat(1);
Output.DAI = DAI;
Output.TD = TD;
Output.shape = shape;
Output.delay_curves = delay_curves;
```

```
%% Extract Data


% Background subtraction loop
function [BKGSubSpec]=BKGSubtraction(input_TR_spectrum,delays)
 BKGIm = input_TR_spectrum(1,:);
 BKGSubSpec = ones(size(input_TR_spectrum));
 for c = 1:length(delays);
  BKGSubSpec(c,:) = input_TR_spectrum(c,:) - BKGIm;
 end
end



% Generate Time limits
if Input.Limits(2,1) == Input.Limits(2,2)
 Tlim(1,1) = min(TD);
 Tlim(1,2) = max(TD);
else
 Tlim(1,1) = Input.Limits(2,1);
 Tlim(1,2) = Input.Limits(2,2);
end


% POP Output
if Control.POP_Output == 1
```

```
% Output experimental TRPES and Betas
for n = 1:length(delays);
 if n == 1;
   ExIm = reshape(TRPEI(:,1),shape);
   ExImPOP = POP(ExIm,[2 4],[1 2 3 4],0);
   ExTRPES = ones(length(delays),length(ExImPOP.PESId));
   ExPOPBeta2 = ones(length(delays),length(ExImPOP.Betas));
   ExPOPBeta4 = ones(length(delays),length(ExImPOP.Betas));
   ExTRPES(n,:) = ExImPOP.PESId./(0:length(ExImPOP.PESId)-1);
   ExPOPBeta2(n,:) = ExImPOP.Betas(1,:);
   ExPOPBeta4(n,:) = ExImPOP.Betas(2,:);
 else
   ExIm = reshape(TRPEI(:,n),shape);
   ExImPOP = POP(ExIm,[2 4],[1 2 3 4],0);
   ExTRPES(n,:) = (ExImPOP.PESId)./(0:length(ExImPOP.PESId)-1);
   ExPOPBeta2(n,:) = ExImPOP.Betas(1,:);
   ExPOPBeta4(n,:) = ExImPOP.Betas(2,:);
 end
end
ExTRPES(:,1) = 0;
TRBeta2 = ExPOPBeta2;
TRBeta2(ExPOPBeta2<-1) = -1;
TRBeta2(ExPOPBeta2>2) = 2;
TRBeta4 = ExPOPBeta4;
TRBeta4(ExPOPBeta4<-1) = -1;
```

```
TRBeta4(ExPOPBeta4>2)  = 2;


% Output  POPped spectral components
for  n = 1:length(Input.tau)+1;
 if  n == 1;
   image  = reshape(DAI(:,n),shape);
   s = POP(image,[2  4],[1 2 3 4],0);
   POPcomponents  = ones(length(Input.tau)+1,length(s.PESId));
   POPBeta2 = ones(length(Input.tau)+1,length(s.Betas));
   POPBeta4 = ones(length(Input.tau)+1,length(s.Betas));
   POPcomponents(n,:)  = s.PESId./(0:length(s.PESId)-1);
   POPBeta2(n,:)  = s.Betas(1,:);
   POPBeta4(n,:)  = s.Betas(2,:);
 else
   image  = reshape(DAI(:,n),shape);
   s = POP(image,[2  4],[1 2 3 4],0);
   POPcomponents(n,:)  = s.PESId./(0:length(s.PESId)-1);
   POPBeta2(n,:)  = s.Betas(1,:);
   POPBeta4(n,:)  = s.Betas(2,:);
 end
end


POPcomponents(:,1)  = 0;
POPBeta2(:,1)  = 0;
DAIBeta2  = POPBeta2;
```

```
DAIBeta2(POPBeta2<-1) = -1;
DAIBeta2(POPBeta2>2) = 2;

POPBeta4(:,1) = 0;
DAIBeta4 = POPBeta4;
DAIBeta4(POPBeta4<-1) = -1;
DAIBeta4(POPBeta4>2) = 2;

% Producing all worked up spectra
FitTRPES = POPcomponents'*delay_curves.';
[BKGSubEx] = BKGSubtraction(ExTRPES,delays);
[BKGSubFit] = BKGSubtraction(FitTRPES',delays);

% Residuals
TRRes = BKGSubEx - BKGSubFit;

% Extract eKE vectors
PCeKE = eKE(1:length(POPcomponents));
EXeKE = eKE(1:length(ExTRPES));

% Generate eKE Limits
if Input.Limits(1,1) == Input.Limits(1,2)
  KElim(1,1) = Input.Limits(1,1);
  KElim(1,2) = max(EXeKE);
else
```

```
    KElim(1,1)  = Input.Limits(1,1);
    KElim(1,2)  = Input.Limits(1,2);
  end

  % Report to Output
  Output.eKE  = EXeKE;
  Output.Limits(1,1:2)  = KElim;
  Output.Limits(2,1:2)  = Tlim;
  Output.POPcomponents  = POPcomponents;
  Output.DAIBeta2  = DAIBeta2;
  Output.DAIBeta4  = DAIBeta4;
  Output.ExTRPES  = ExTRPES;
  Output.TRBeta2  = TRBeta2;
  Output.TRBeta4  = TRBeta4;
  Output.FitTRPES  = FitTRPES;
  Output.BKGSubEx  = BKGSubEx;
  Output.BKGSubFit  = BKGSubFit;

elseif  Control.POP_Output  == 0
  Output.POPcomponents  = 'Not Available  - Set POP_Output On';
  Output.DAIBeta2  = 'Not Available  - Set POP_Output On';
  Output.DAIBeta4  = 'Not Available  - Set POP_Output On';
  Output.ExTRPES  = 'Not Available  - Set POP_Output On';
  Output.TRBeta2  = 'Not Available  - Set POP_Output On';
  Output.TRBeta4  = 'Not Available  - Set POP_Output On';
```

```
 Output.FitTRPES  = 'Not Available  - Set POP_Output On';
 Output.BKGSubEx  = 'Not Available  - Set POP_Output On';
 Output.BKGSubFit  = 'Not Available  - Set POP_Output On';
end

% Define  Colour palette  for plotting
if length(Input.tau)  <= 12
 Colours  = [0 0 1; 0 0.4 0; 1 0 0; 1 0 1; 0 0 1; 0.5 0.5 0.5;...
   0.5 0 0.5; 0 0.5 0.5; 0.5 0.5 0; 0.5 0 0; 0 0.5 0; 0 0 0.5];
else
 Colours  = colormap(jet(length(Input.tau)));
end

% Output  fitting  parameters
if Control.Fitting_Proc  == 1
 if Control.Decay_Curves  == 1
   fprintf('Fit  for %0.0f independent  lifetimes\n',length(Input.tau))
   for n = 1:length(Input.tau);
     fprintf('Tau  %0.0f = %0.0f fs\n',(n),OutMat(n+2))
   end
   fprintf('The  IRFFWHM is %0.0f fs\n',(OutMat(2)*2.35))

 elseif  Control.Decay_Curves  == 2
   disp('Fit  for 2 consecutive  lifetimes')
   for n = 1:length(Input.tau);
```

```
    fprintf('Tau  %0.0f = %0.0f fs\n',(n),OutMat(n+2))
   end
   fprintf('The  IRFFWHM is %0.0f fs\n',(OutMat(2)*2.35))

  elseif  Control.Decay_Curves  == 2
   disp('Fit  for 3 consecutive  lifetimes')
   for  n = 1:length(Input.tau);
    fprintf('Tau  %0.0f = %0.0f fs\n',(n),OutMat(n+2))
   end
   fprintf('The  IRFFWHM is %0.0f fs\n',(OutMat(2)*2.35))
  end
end



%% Plot Results

% Extract  DAI and residuals
if Control.Plot_DAI  == 1

  % Extract  the Decay associated  images
  for  n=1:length(Input.tau)+1;
   figure;
   Image  = reshape(DAI(:,n),shape);
   A1 = 1:length(Input.tau)+1;
   Im_Title  = 'Tau %d, %0.0f fs';
```

```
    contourf(Image,150);
    set(gca,'PlotBoxAspectRatio',[1.0,1.0,1.0],...
       'PlotBoxAspectRatioMode','manual');
    if n == 1;
      title('Background','FontSize',12);
    else
      str = sprintf(Im_Title,A1(n-1),OutMat(n+1));
      title(str,'FontSize',12);
    end
    shading flat;
    colorbar('EastOutside');
  end

  % Plot residuals
  residuals = TRPEI - DAI*delay_curves.';
  residuals = sum(residuals.^2,2);
  figure;
  contourf(reshape(residuals,shape));
  shading flat;
  set(gca,'PlotBoxAspectRatio',[1.0,1.0,1.0],...
     'PlotBoxAspectRatioMode','manual');
end

% Plot Decay Curves and Integrals
if Control.Plot_Decay_Curves == 1
```

```
% Decay Curves
figure;
subplot(2,1,1);
plot(TD,delay_curves');
title('Fitted Exponential Decay Amplitudes','FontSize',12);
ylabel('Intensity');
xlabel('Delay (fs)');

if Control.Decay_Curves == 1
 if length(Input.tau) == 1
  legend('Background','Tau(1)');
 elseif length(Input.tau) == 2
  legend('Background','Tau(1)','Tau(2)');
 elseif length(Input.tau) == 3
  legend('Background','Tau(1)','Tau(2)','Tau(3)');
 elseif length(Input.tau) == 4
  legend('Background','Tau(1)','Tau(2)','Tau(3)','Tau(4)');
 elseif length(Input.tau) == 5
  legend('Background','Tau(1)','Tau(2)','Tau(3)','Tau(4)',...
     'Tau(5)');
 elseif length(Input.tau) == 6
  legend('Background','Tau(1)','Tau(2)','Tau(3)','Tau(4)',...
     'Tau(5)','Tau(6)');
 else
```

```
    disp('Plot  Decay Curves')
    disp('Legend  unsupported  for this  many lifetimes')
    disp(' ')
  end
  legend('boxoff');
end

if Control.Decay_Curves  == 2
  legend('BackGround','Tau(1)','Tau(2)');
  legend('boxoff');
end

if Control.Decay_Curves  == 3
  legend('BackGround','Tau(1)','Tau(2)','Tau(3)');
  legend('boxoff');
end

% Integrals
TR_Int  = sum(TRPEI);
DAI_Int  = ones(length(Input.tau)+2,length(TD));
for d = 1:(length(Input.tau)+1);
  Int  = sum((DAI(:,(d))*delay_curves(:,(d)).'));
  DAI_Int(d,:)  = Int;
end
for d = length(Input.tau)+2;
```

```
  if length(Input.tau)  == 1;
    DAI_Int(d,:)  = sum(DAI_Int(2,:),1);
  else
    DAI_Int(d,:)  = sum(DAI_Int(2:(length(Input.tau)+1),:));
  end
end

TR_Int  = TR_Int  - DAI_Int(1,:);

% Report to Output
Output.TR_Int  = TR_Int;
Output.DAI_Int  = DAI_Int;

subplot(2,1,2);
plot(TD,TR_Int,'ko');
hold on;
plot(TD,DAI_Int((length(Input.tau)+2),:),'k');
for m = 2:length(Input.tau)+1;
  plot(TD,DAI_Int(m,:),'color',Colours((m-1),:));
  hold on;
end
title('Overall Decay','FontSize',12);
ylabel('Intensity');
xlabel('Delay (fs)');
```

```
if Control.Decay_Curves  == 1
  if length(Input.tau)  == 1
    legend('Experimental  Data','Fit','Tau(1)');
  elseif  length(Input.tau)  == 2
    legend('Experimental  Data','Fit','Tau(1)','Tau(2)');
  elseif  length(Input.tau)  == 3
    legend('Experimental  Data','Fit','Tau(1)','Tau(2)','Tau(3)');
  elseif  length(Input.tau)  == 4
    legend('Experimental  Data','Fit','Tau(1)','Tau(2)','Tau(3)',...
        'Tau(4)');
  elseif  length(Input.tau)  == 5
    legend('Experimental  Data','Fit','Tau(1)','Tau(2)','Tau(3)',...
        'Tau(4)','Tau(5)');
  elseif  length(Input.tau)  == 6
    legend('Experimental  Data','Fit','Tau(1)','Tau(2)','Tau(3)',...
        'Tau(4)','Tau(5)','Tau(6)');
  else
    disp(...
      'Legend  is  still  unsupported  for this  number  of lifetimes')
  end
  legend('boxoff');
end

if Control.Decay_Curves  == 2
  legend('Experimental  Data','Fit','Tau(1)','Tau(2)');
```

```
  legend('boxoff');
 end

 if Control.Decay_Curves == 3
  legend('Experimental Data','Fit','Tau(1)','Tau(2)','Tau(3)');
  legend('boxoff');
 end

elseif Control.Plot_Decay_Curves == 0
 Output.TR_Int = 'Not Available - Set Plot_Decay_Curves On';
 Output.DAI_Int = 'Not Available - Set Plot_Decay_Curves On';
end

% Plot Background and DAS
if Control.Plot_DAS == 1

 % Plot Background
 figure;
 subplot(2,1,1);
 plot(PCeKE,POPcomponents(1,:));
 title('Background','FontSize',12);
 xlabel('Electron Kinetic Energy (eV)');
 xlim(KElim);

 % Plot DAS
```

```
subplot(2,1,2);
title('Decay Associated Spectra','FontSize',12);
xlabel('Electron Kinetic Energy (eV)');
for n = 1:length(Input.tau);
 plot(PCeKE,POPcomponents(n+1,:),'color',Colours((n),:));
 hold on;
end
Zero_Line  = zeros(1,length(PCeKE));
plot(PCeKE,Zero_Line,'k--');
title('Decay Associated Spectra','FontSize',12);
xlabel('Electron Kinetic Energy (eV)');
xlim(KElim);

if Control.Decay_Curves  == 1
 if length(Input.tau)  == 1
  legend('Tau(1)');
 elseif length(Input.tau)  == 2
  legend('Tau(1)','Tau(2)');
 elseif length(Input.tau)  == 3
  legend('Tau(1)','Tau(2)','Tau(3)');
 elseif length(Input.tau)  == 4
  legend('Tau(1)','Tau(2)','Tau(3)','Tau(4)');
 elseif length(Input.tau)  == 5
  legend('Tau(1)','Tau(2)','Tau(3)','Tau(4)','Tau(5)');
 elseif length(Input.tau)  == 6
```

```
    legend('Tau(1)','Tau(2)','Tau(3)','Tau(4)','Tau(5)','Tau(6)');
   else
    disp('Plot DAS')
    disp('Legend unsupported for this many lifetimes')
   end
   legend('boxoff');
  end

  if Control.Decay_Curves == 2
   legend('Tau(1)','Tau(2)');
   legend('boxoff');
  end

  if Control.Decay_Curves == 3
   legend('Tau(1)','Tau(2)','Tau(3)');
   legend('boxoff');
  end
end

% Plot all Time Resolved Data
if Control.TR_Data == 1
  figure;

  % Experimental Data
  subplot(3,2,1);
```

```
contourf(TD,EXeKE,ExTRPES',200);
shading flat;
title('Experimental Data','FontSize',12);
xlabel('Time Delay (fs)');
ylabel('Electron Kinetic Energy (eV)');
colorbar('EastOutside');
ylim(KElim);

% Fitted Data
subplot(3,2,2);
contourf(TD,PCeKE,FitTRPES,200);
shading flat;
title('Fit','FontSize',12);
xlabel('Time Delay (fs)');
ylabel('Electron Kinetic Energy (eV)');
colorbar('EastOutside');
ylim(KElim);

% Background Subtracted Experimental Data
subplot(3,2,3);
contourf(TD,EXeKE,BKGSubEx',200);
shading flat;
title('BKG-Sub Experimental Data','FontSize',12);
xlabel('Time Delay (fs)');
ylabel('Electron Kinetic Energy (eV)');
```

```
colorbar('EastOutside');
ylim(KElim);

% Background Subtracted Fitted Data
subplot(3,2,4);
contourf(TD,PCeKE,BKGSubFit',200);
shading flat;
title('BKG-Sub Fit','FontSize',12);
xlabel('Time Delay (fs)');
ylabel('Electron Kinetic Energy (eV)');
colorbar('EastOutside');
ylim(KElim);

% Residuals
subplot(3,2,[5 6]);
contourf(TD,PCeKE,TRRes',200);
shading flat;
title('Residuals','FontSize',12);
xlabel('Time Delay (fs)');
ylabel('Electron Kinetic Energy (eV)');
colorbar('EastOutside');
ylim(KElim);
end

% Plot Time Resolved Beta(2) Parameters
```

```
if Control.TR_Beta == 1
 % Time Resolved Experimental Data
 figure;
 contourf(TD,EXeKE,TRBeta2',200);
 shading flat;
 title('Beta2','FontSize',12);
 xlabel('Time Delay (fs)');
 ylabel('Electron Kinetic Energy (eV)');
 colorbar('EastOutside');
 ylim(KElim);

 % DAS Beta(2) Components
 figure;
 for n = 1:length(Input.tau);
  plot(PCeKE,DAIBeta2(n+1,:),'color',Colours((n),:));
  hold on;
 end
 title('DAI Beta2','FontSize',12);

 if Control.Decay_Curves == 1
  if length(Input.tau) == 1
   legend('Tau(1)');
  elseif length(Input.tau) == 2
   legend('Tau(1)','Tau(2)');
  elseif length(Input.tau) == 3
```

```
    legend('Tau(1)','Tau(2)','Tau(3)');
  elseif length(Input.tau) == 4
    legend('Tau(1)','Tau(2)','Tau(3)','Tau(4)');
  elseif length(Input.tau) == 5
    legend('Tau(1)','Tau(2)','Tau(3)','Tau(4)','Tau(5)');
  elseif length(Input.tau) == 6
    legend('Tau(1)','Tau(2)','Tau(3)','Tau(4)','Tau(5)','Tau(6)');
  else
    disp('Plot Beta2 Components')
    disp('Legend unsupported for this many lifetimes')
    disp(' ')
  end
  legend('boxoff');
end

if Control.Decay_Curves == 2
  legend('Tau(1)','Tau(2)');
  legend('boxoff');
end

if Control.Decay_Curves == 3
  legend('Tau(1)','Tau(2)','Tau(3)');
  legend('boxoff');
end
```

```
% Time Resolved Experimental Data
figure;
contourf(TD,EXeKE,TRBeta4',200);
shading flat;
title('Beta4','FontSize',12);
xlabel('Time Delay (fs)');
ylabel('Electron Kinetic Energy (eV)');
colorbar('EastOutside');
ylim(KElim);

% DAS Beta(4) Components
figure;
for n = 1:length(Input.tau);
  plot(PCeKE,DAIBeta4(n+1,:),'color',Colours((n),:));
  hold on;
end
title('DAI Beta4','FontSize',12);

if Control.Decay_Curves == 1
  if length(Input.tau) == 1
    legend('Tau(1)');
  elseif length(Input.tau) == 2
    legend('Tau(1)','Tau(2)');
  elseif length(Input.tau) == 3
    legend('Tau(1)','Tau(2)','Tau(3)');
```

```
    elseif length(Input.tau) == 4
      legend('Tau(1)','Tau(2)','Tau(3)','Tau(4)');
    elseif length(Input.tau) == 5
      legend('Tau(1)','Tau(2)','Tau(3)','Tau(4)','Tau(5)');
    elseif length(Input.tau) == 6
      legend('Tau(1)','Tau(2)','Tau(3)','Tau(4)','Tau(5)','Tau(6)');
    else
      disp('Plot Beta4 components')
      disp(...
        'Legend still unsupported for this many lifetimes')
    end
    legend('boxoff');
  end

  if Control.Decay_Curves == 2
    legend('Tau(1)','Tau(2)');
    legend('boxoff');
  end

  if Control.Decay_Curves == 3
    legend('Tau(1)','Tau(2)','Tau(3)');
    legend('boxoff');
  end
end
```

```
% Plotting for figures
if Control.Figures == 1
 fs = 30;

 % DAS
 figure;
 for n = 1:length(Input.tau);
  plot(PCeKE,POPcomponents(n+1,:),'color',...
   Colours((n),:),'linewidth',4);
  hold on;
 end
 Zero_Line = zeros(1,length(PCeKE));
 plot(PCeKE,Zero_Line,'k--','linewidth',4);
 xlim(KElim);
 title('Decay Associated Spectra','FontSize',fs);
 xlabel('Electron Kinetic Energy (eV)','FontSize',fs);
 set(gca,'FontSize',fs,'linewidth',4);

 if Control.Decay_Curves == 1
  if length(Input.tau) == 1
   legend('Tau(1)');
  elseif length(Input.tau) == 2
   legend('Tau(1)','Tau(2)');
  elseif length(Input.tau) == 3
   legend('Tau(1)','Tau(2)','Tau(3)');
```

```
  elseif length(Input.tau) == 4
    legend('Tau(1)','Tau(2)','Tau(3)','Tau(4)');
  elseif length(Input.tau) == 5
    legend('Tau(1)','Tau(2)','Tau(3)','Tau(4)','Tau(5)');
  elseif length(Input.tau) == 6
    legend('Tau(1)','Tau(2)','Tau(3)','Tau(4)','Tau(5)','Tau(6)');
  else
    disp('Figures DAS')
    disp('Legend unsupported for this many lifetimes')
  end
  legend('boxoff');
end

if Control.Decay_Curves == 2
  legend('Tau(1)','Tau(2)');
  legend('boxoff');
end

if Control.Decay_Curves == 3
  legend('Tau(1)','Tau(2)','Tau(3)');
  legend('boxoff');
end


 % Integrals
```

```
figure;
plot(TD,TR_Int,'ko','linewidth',4);
hold on;
plot(TD,DAI_Int((length(Input.tau)+2),:),'k','linewidth',4);
Colours = [0 0 1; 0 0.4 0; 1 0 0; 1 0 1; 0 0 1];
for m = 2:length(Input.tau)+1;
 plot(TD,DAI_Int(m,:),'color',Colours((m-1),:),'linewidth',4);
 hold on;
end
title('Overall Decay','FontSize',fs);
ylabel('Intensity','FontSize',fs);
xlabel('Delay (fs)','FontSize',fs);
xlim(Tlim);
set(gca,'FontSize',fs,'linewidth',4);
if Control.Decay_Curves == 1
 if length(Input.tau) == 1
  legend('Experimental Data','Fit','Tau(1)');
 elseif length(Input.tau) == 2
  legend('Experimental Data','Fit','Tau(1)','Tau(2)');
 elseif length(Input.tau) == 3
  legend('Experimental Data','Fit','Tau(1)','Tau(2)','Tau(3)');
 elseif length(Input.tau) == 4
  legend('Experimental Data','Fit','Tau(1)','Tau(2)','Tau(3)',...
     'Tau(4)');
 elseif length(Input.tau) == 5
```

```
    legend('Experimental Data','Fit','Tau(1)','Tau(2)','Tau(3)',...
        'Tau(4)','Tau(5)');
  elseif length(Input.tau) == 6
    legend('Experimental Data','Fit','Tau(1)','Tau(2)','Tau(3)',...
        'Tau(4)','Tau(5)','Tau(6)');
  else
    disp('Figures Decay Curves')
    disp(...
      'Legend is still unsupported for this number of lifetimes')
  end
  legend('boxoff');
end

if Control.Decay_Curves == 2
  legend('Experimental Data','Fit','Tau(1)','Tau(2)');
  legend('boxoff');
end

if Control.Decay_Curves == 3
  legend('Experimental Data','Fit','Tau(1)','Tau(2)','Tau(3)');
  legend('boxoff');
end

% Background Subtracted Time Resolved Experimental Data
figure;
```

```
contourf(TD,EXeKE,BKGSubEx',200);
shading flat;
title('BKG-Sub Experimental Data','FontSize',fs);
xlabel('Time Delay (fs)','FontSize',fs);
ylabel('Electron Kinetic Energy (eV)','FontSize',fs);
colorbar('EastOutside');
ylim(KElim);
xlim(Tlim);
set(gca,'FontSize',fs,'linewidth',4);

% Background Subtracted Time Resolved Fitted Data
figure;
contourf(TD,PCeKE,BKGSubFit',200);
shading flat;
title('BKG-Sub Fit','FontSize',fs);
xlabel('Time Delay (fs)','FontSize',fs);
ylabel('Electron Kinetic Energy (eV)','FontSize',fs);
colorbar('EastOutside');
ylim(KElim);
xlim(Tlim);
set(gca,'FontSize',fs,'linewidth',4);
end

end
```

```
% Comments and improvements are welcomed and should be sent to
% c.w.west@durham.ac.uk
```

10.2 Simulation of the Electrostatic Potential Energy Surface of the Antimony Tartrate Dianion

Generation of the photoelectron distribution that may surpass the RCB

```
function [Output] = Diff_Cross2(eKE)
% Function to generate the initial photoelectron distribution that can
% surpass the RCB. Generates a 3D raster of points at which to direct the
% initial photoelectrons, which are then used to run the trajectory
% simulation.

% eKE = Initial kinetic energy of the photoelectrons
Output = 0;
Output.x = 0;
Output.y = 0;
Output.z = 0;
Output.xt = 0;
Output.yt = 0;
Output.zt = 0;
Shift = [-2 0 0];
for n = 1:8
   for nn = 1:8
      for nnn = 1:8
         Shift(end+1,:) = [(-2+(n-1)*0.5) (-2+(nn-1)*0.5) (-2+(nnn-1)*0.5)];
      end
   end
```

```
end
Shift = Shift(2:end,:);
for n = 1:length(Shift)
   [Out] = Sim3D_Move_Charge_17(eKE,Shift(n,:));
   for nn = 1:30
      if Out.Repul(nn,11000) < 0
         if Output.x == 0
            Output.x = Out.x(nn,1);
         else
            Output.x(end+1,:) = Out.x(nn,1);
         end;
      end
      if Out.Repul(nn,11000) < 0
         if Output.y == 0
            Output.y = Out.y(nn,1);
         else
            Output.y(end+1,:) = Out.y(nn,1);
         end;
      end
      if Out.Repul(nn,11000) < 0
         if Output.z == 0
            Output.z = Out.z(nn,1);
         else
            Output.z(end+1,:) = Out.z(nn,1);
         end;
```

```
        end
        if Out.Repul(nn,11000) < 0
            if Output.xt == 0
                Output.xt = Out.xt(nn,1);
            else
                Output.xt(end+1,:) = Out.xt(nn,1);
            end;
        end
        if Out.Repul(nn,11000) < 0
            if Output.yt == 0
                Output.yt = Out.yt(nn,1);
            else
                Output.yt(end+1,:) = Out.yt(nn,1);
            end;
        end
        if Out.Repul(nn,11000) < 0
            if Output.zt == 0
                Output.zt = Out.zt(nn,1);
            else
                Output.zt(end+1,:) = Out.zt(nn,1);
            end;
        end
    end
    save('Outputmat','Output');
end
```

```
end
```

Calculation of the trajectories of electrons on the electrostatic potential energy surface and whether the electrons become bound.

```
function [Out] = Sim3D_Move_Charge_17(eKE,Shift)
% Classical electron trajectory simulation on the electrostatic potential
% energy surface of the antimony tartrate monoanion.

% eKE - Initial kinetic energy of the photoelectrons (eV, minimum value 1.4
% eV)
% Shift - Point at which the electrons are initially directed
%% Definitions
Perm = 1.11265*10^-10; % Vacuum Permittivity, 4PiE0, C^2/ J m
ec = 1.602176*10^-19; % Elementary Charge, C
Me = 9.10938*10^-31; % Mass of an Electron, kg
eVJ = 1.602176*10^-19; % 1 eV = 1.602*10^-19 J
% Define poisitions of atoms
ATPos = [0. 0. 2.4632480534;...
   0. 0. -2.4632480534;...
   -1.6528628965 1.3185836011 2.0732613868;...
   1.6528628965 -1.3185836011 2.0732613868;...
   1.6528628965 1.3185836011 -2.0732613868;...
   -1.6528628965 -1.3185836011 -2.0732613868;...
   0.8349925512 1.2745995862 1.211292942;...
   -0.8349925512 -1.2745995862 1.211292942;...
   -0.8349925512 1.2745995862 -1.211292942;...
```

```
    0.8349925512 -1.2745995862 -1.211292942;...
    0.0573912119 2.3538174664 0.764159112;...
    0.5362450874 3.3005612155 1.0434734001;...
    -0.0573912119 2.3538174664 -0.764159112;...
    -0.5362450874 3.3005612155 -1.0434734001;...
    0.0573912119 -2.3538174664 -0.764159112;...
    0.5362450874 -3.3005612155 -1.0434734001;...
    -0.0573912119 -2.3538174664 0.764159112;...
    -0.5362450874 -3.3005612155 1.0434734001;...
    1.3668559184 2.3590875494 -1.3547475296;...
    -1.3668559184 2.3590875494 1.3547475296;...
    -1.3668559184 -2.3590875494 -1.3547475296;...
    1.3668559184 -2.3590875494 1.3547475296;...
    -2.1044815908 -3.3074908875 -1.1496233225;...
    2.1044815908 3.3074908875 -1.1496233225;...
    2.1044815908 -3.3074908875 1.1496233225;...
    -2.1044815908 3.3074908875 1.1496233225];
% Define positions of charges
% Mulliken Charges
ATChg = [0.943641;...
    0.943641;...
    -0.483333;...
    -0.483333;...
    -0.483333;...
    -0.483333;...
```

```
    -0.446774;...
    -0.446774;...
    -0.446774;...
    -0.446774;...
    0.079815;...
    0.103839;...
    0.079815;...
    0.103839;...
    0.079815;...
    0.103839;...
    0.079815;...
    0.103839;...
    0.470939;...
    0.470939;...
    0.470939;...
    0.470939;...
    -0.446307;...
    -0.446307;...
    -0.446307;...
    -0.446307];
ts = 0.00005; % Time step factor
NoInc = 30; % Number of electrons in model
Init_Dist = 1000; % Initial distance
%% Generating starting positions
Init_Pos = ones(NoInc,3);
```

```
for n = 1:NoInc
   theta = 2*pi()*rand(1,1);
   Init_Pos(n,3)  = rand(1,1);
   Init_Pos(n,1)  = sqrt(1-Init_Pos(n,3)^2)*cos(theta);
   Init_Pos(n,2)  = sqrt(1-Init_Pos(n,3)^2)*sin(theta);
   if mod(n,2) == 0
      Init_Pos(n,3)  = Init_Pos(n,3)*-1;
   end
end
Init_Pos = Init_Pos.*(ones(NoInc,3)*Init_Dist);
a = ones(NoInc,3);
a(:,1) = a(:,1).*Shift(1);
a(:,2) = a(:,2).*Shift(2);
a(:,3) = a(:,3).*Shift(3);
NoIter = 11000; % Number of iterations in each run
% Define output matrix
Out.x = zeros(length(Init_Pos),NoIter);
Out.xt = zeros(length(Init_Pos),NoIter);
Out.y = zeros(length(Init_Pos),NoIter);
Out.yt = zeros(length(Init_Pos),NoIter);
Out.z = zeros(length(Init_Pos),NoIter);
Out.zt = zeros(length(Init_Pos),NoIter);
% Set initial positions
Out.x(:,1) = Init_Pos(:,1);
Out.y(:,1) = Init_Pos(:,2);
```

```
Out.z(:,1) = Init_Pos(:,3);
% Determine initial repulsion
PESStart = zeros(NoInc,1);
for n = 1:NoInc
   DistancesS(:,1) = Out.x(n,1) - ATPos(:,1);
   DistancesS(:,2) = Out.y(n,1) - ATPos(:,2);
   DistancesS(:,3) = Out.z(n,1) - ATPos(:,3);
   DistancesS(:,4) = sqrt(sum(DistancesS(:,1:3).^2,2));
   EStart = bsxfun(@rdivide,ATChg*-1*ec^2,(Perm*abs(DistancesS(:,4)*1e-
10)));
   PESStart(n) = sum(EStart);
end
% Determine initial kinetic energy
eKE = ones(NoInc,1).*eKE - PESStart;
Velocity = sqrt((2*eKE*eVJ)/Me); % m/s
Vel_Corr = ones(length(Init_Pos),3);
Vel_Corr_2 = ones(length(Init_Pos),3);
Vel_Corr(Init_Pos<0) = Vel_Corr(Init_Pos<0)*-1;
Vel_Corr_2(Init_Pos>0) = Vel_Corr_2(Init_Pos>0)*-1;
Init_Pos = Init_Pos.*Vel_Corr;
% Determine initial speed in each direction
Out.xt(:,1) = sqrt(((Velocity(:,1).^2).*((Init_Pos(:,1)-a(:,1)).^2)./((Init_Pos(:,1)-
a(:,1)).^2+(Init_Pos(:,2)-a(:,2)).^2+(Init_Pos(:,3)-a(:,3)).^2))).*Vel_Corr_2(:,1);
Out.yt(:,1) = sqrt(((Velocity(:,1).^2).*((Init_Pos(:,2)-a(:,2)).^2)./((Init_Pos(:,1)-
a(:,1)).^2+(Init_Pos(:,2)-a(:,2)).^2+(Init_Pos(:,3)-a(:,3)).^2))).*Vel_Corr_2(:,2);
```

```
Out.zt(:,1) = sqrt(((Velocity(:,1).^2).*((Init_Pos(:,3)-a(:,3)).^2)./((Init_Pos(:,1)-
a(:,1)).^2+(Init_Pos(:,2)-a(:,2)).^2+(Init_Pos(:,3)-a(:,3)).^2))).*Vel_Corr_2(:,3);
% Out.ts = ones(NoInc,NoIter);
% Out.eKE = eKE;
% Out.Velocity = Velocity;
Out.Repul = zeros(length(Init_Pos),NoIter);
% Iteration of the trajectories
for n = 1:length(Init_Pos) % Particle idx
  for nn = 1:NoIter % Iteration
    if sqrt(Out.x(n,nn)^2 + Out.y(n,nn)^2 + Out.z(n,nn)^2)...
        < (Init_Dist + 0.1) % Repelled particle end condition
      DistancesS = zeros(length(ATChg),4);
      DistancesS(:,1) = Out.x(n,nn) - ATPos(:,1);
      DistancesS(:,2) = Out.y(n,nn) - ATPos(:,2);
      DistancesS(:,3) = Out.z(n,nn) - ATPos(:,3);
      DistancesS(:,4) = sqrt(sum(DistancesS(:,1:3).^2,2));
      % End condition for crossing the barrier
      RepulE = bsxfun(@rdivide,...
                ATChg*-1*ec^2,...
                (Perm*abs(DistancesS(:,4)*1e-10)));
      Out.Repul(n,nn) = sum(RepulE);
      if sum(RepulE) < 0
        Out.xt(n,nn+1:end) = Out.xt(n,nn);
        Out.x(n,nn+1:end) = Out.x(n,nn);
        Out.yt(n,nn+1:end) = Out.yt(n,nn);
```

```
    Out.y(n,nn+1:end)  = Out.y(n,nn);
    Out.zt(n,nn+1:end)  = Out.zt(n,nn);
    Out.z(n,nn+1:end)  = Out.z(n,nn);
    Out.Repul(n,nn+1:end)  = sum(RepulE);
    break
end
% Determine  force acting  on the particle  in each dimension
RepulS  = bsxfun(@rdivide,...
            bsxfun(@times,(DistancesS(:,1:3)*1e-10),...
            ATChg)*-1*ec^2,...
            (Perm*abs(DistancesS(:,4)*1e-10).^3));
Force = sum(RepulS,1);
% Determine  acceleration  in each dimension
Accel = Force./Me;
% Determine  time  step
Out.ts(n,nn)  = ts*(Out.x(n,nn)^2  + Out.y(n,nn)^2  +...
    Out.z(n,nn)^2)/(2.4^2);
% Verlet  integration
Out.xt(n,nn+1)  = (Out.xt(n,nn)  +...
    Accel(1)*(Out.ts(n,nn)*10^-15));
Out.x(n,nn+1)  = Out.x(n,nn)  +...
    (Out.xt(n,nn)*Out.ts(n,nn)*10^-15  +...
    0.5*Accel(1)*(Out.ts(n,nn)*10^-15)^2)*10^10;
Out.yt(n,nn+1)  = (Out.yt(n,nn)  +...
    Accel(2)*(Out.ts(n,nn)*10^-15));
```

```
            Out.y(n,nn+1)  = Out.y(n,nn)  +...
                (Out.yt(n,nn)*Out.ts(n,nn)*10^-15  +...
                0.5*Accel(2)*(Out.ts(n,nn)*10^-15)^2)*10^10;
            Out.zt(n,nn+1)  = (Out.zt(n,nn)  +...
                Accel(3)*(Out.ts(n,nn)*10^-15));
            Out.z(n,nn+1)  = Out.z(n,nn)  +...
                (Out.zt(n,nn)*Out.ts(n,nn)*10^-15  +...
                0.5*Accel(3)*(Out.ts(n,nn)*10^-15)^2)*10^10;
        else % When repelled particle end condition met, exits loop
            Out.xt(n,nn+1:end)  = Out.xt(n,nn);
            Out.x(n,nn+1:end)  = Out.x(n,nn);
            Out.yt(n,nn+1:end)  = Out.yt(n,nn);
            Out.y(n,nn+1:end)  = Out.y(n,nn);
            Out.zt(n,nn+1:end)  = Out.zt(n,nn);
            Out.z(n,nn+1:end)  = Out.z(n,nn);
            % Crude method to track progress of simulation
            n
            break
        end
    end
end
end
```

Convolution to simulate the photoelectron images

```
function [Convoluted_Dist,bins,h] = CartesianToPolar12(Output,dist)
```

```
%% Generate bound distribution
Theta = 0;
% Extract angle from z axis if repulsion becomes negative
for n = 1:length(Output.x)
    Theta(end+1) =
acos(Output.zt(n)/sqrt((Output.xt(n))^2+(Output.yt(n))^2+(Output.zt(n))^2));
end
Theta = Theta(2:end);
% Account for C(infinity) symmetry about z axis of transt dipole moment
Phi = zeros(1,1440);
for n = 1:1440
  Phi(n) = -pi()+((n-1)*pi())/720;
end
x = zeros(length(Theta),length(Phi));
y = zeros(length(Theta),length(Phi));
z = zeros(length(Theta),length(Phi));
for n = 1:length(Theta)
  for nn = 1:length(Phi)
    x(n,nn) = 100*sin(Theta(n))*cos(Phi(nn));
    y(n,nn) = 100*sin(Theta(n))*sin(Phi(nn));
    z(n,nn) = 100*cos(Theta(n));
  end
end
% Extract out outer ring of distribution in yz plane
OuterRing.x = 0;
```

```
OuterRing.y  = 0;
OuterRing.z  = 0;
% ThetaSin  = (1+(0*(3*cos(Theta).*cos(Theta)-1))/2);
for n = 1:length(Theta)
   for nn = 1:length(Phi)
      if -1 < x(n,nn)  && x(n,nn)  < 1
         OuterRing.x(end+1)  = x(n,nn);
         OuterRing.y(end+1)  = y(n,nn);
         OuterRing.z(end+1)  = z(n,nn);
      end
   end
end
OuterRing.x  = OuterRing.x(2:end);
OuterRing.y  = OuterRing.y(2:end);
OuterRing.z  = OuterRing.z(2:end);
% Extract  angle  relative  to z axis
OuterRing.Theta  = atan2(OuterRing.y,OuterRing.z);
% Bin  the distribution  into  1 degree bins
[h,bins]=hist(OuterRing.Theta,500);
h = h./dist;
Convoluted_Dist  = zeros(1,length(h));
% Convolute  with cos^2(Theta)  distribution
for n = 1:500
   Convoluted_Dist  = Convoluted_Dist  + ((ones(1,length(h))*h(n))).*...
      (1+((2*((3*cos(bins-bins(n)).*cos(bins-bins(n)))-1))/2));
```

```
end
```